UNIVERSITY OF CALIFORNIA, SAN DIEGO

One- and Two-Point Particle Tracking Microrheology of Complex Viscoelastic Fluids

A dissertation submitted in partial satisfaction of the
requirements for the degree
Doctor of Philosophy

in

Engineering Sciences (with a specialization in Multi-Scale Biology)

by

Manuel Gómez-González

Committee in charge:

Professor Juan Carlos del Álamo, Chair
Professor Juan C. Lasheras
Professor Vishal Nigam
Professor David Saintillan
Professor Daniel M. Tartakovsky
Professor Qiang Zhu

2015

The dissertation of Manuel Gómez-González is approved, and it is acceptable in quality and form for publication on microfilm and electronically:

_____

_____

_____

_____

_____

_____

Chair

University of California, San Diego

2015

DEDICATION

To Bego, to my parents Manuel and Constantina

and to my sisters Tina, Alicia and Encina.

EPIGRAPH

Observar sin pensar es tan peligroso como pensar sin observar.

—Santiago Ramón y Cajal

To observe without thinking is as dangerous as to think without observing.

—Santiago Ramón y Cajal

TABLE OF CONTENTS

LIST OF FIGURES

LIST OF SYMBOLS AND ABBREVIATIONS

D Diffusion coefficient.

E_K Kinetic energy.

Er Ericksen number.

E Total energy.

F Force.

I Induced.

L Characteristic length.

N_t Number of time points.

N Number of particles.

T Absolute temperature.

U Characteristic velocity.

$\Delta\theta$ Displacement of a particle orthogonal to the line that connects its center with the center of a second particle.

Δr Displacement of a particle along the line that connects its center with the center of a second particle.

Γ Gamma function.

$\boldsymbol{Re}$ Reynolds number.

$\alpha(s)$ Logarithmic slope.

α_i Leslie viscosity coefficients.

α Particle identifier.

β Particle identifier.

δ Dirac delta function.

η_a First Miesowicz viscosity coefficient.

η_b Second Miesowicz viscosity coefficient.

η_c Third Miesowicz viscosity coefficient.

η Viscosity coefficient.

$\langle ... \rangle$ Ensemble average.

$\langle \Delta \tilde{r}^2_\Gamma(s) \rangle$ Fit of the MSD with the Γ-approximation.

$\mathcal{G}$ Greens function for the velocity.

$\mathcal{L}$ Laplace transform.

$\mathcal{P}$ Greens function for the pressure.

$\mathbf{R}$ White noise random process.

eff Effective.

μ Elasticity coefficient.

ω Frequency.

$\overline{\overline{\gamma}}$ Hydrodynamic mobility.

$\overline{\overline{\mathcal{Z}}}$ Multiparticle resistance tensor.

$\overline{\overline{\tau}}$ Stress tensor.

$\parallel$ Direction parallel to the nematic director.

$\perp$ Direction perpendicular to the nematic director.

ρ Density.

σ Shear stress.

τ Time step.

$\tilde{G}''$ Loss modulus.

$\tilde{G}'$ Storage modulus.

$\tilde{G}_a$ First generalized Miesowicz shear modulus.

$\tilde{G}_b$ Second generalized Miesowicz shear modulus.

$\tilde{G}_c$ Third generalized Miesowicz shear modulus.

$\tilde{G}_f$ Shear modulus of a fluid surrounding the membrane.

$\tilde{G}_m$ Shear modulus of a membrane.

$\tilde{G}_{2P}$ Shear modulus calculated with 2PPTM.

$\tilde{G}_\Gamma$ Shear modulus calculated with the Γ-approximation.

$\tilde{G}$ Shear modulus.

$\tilde{\alpha}_k^*$ Generalized Leslie viscoelasticity coefficients.

ε Shear strain.

$\vec{N}$ Rate of change of the director.

$\vec{\omega}$ Vorticity vector.

$\vec{n}$ Director of the nematic.

$\vec{r}$ Position vector.

ξ Mesh size.

ζ Memory function.

a Particle radius.

f_R External force.

h Thickness of the membrane.

i Imaginary unit.

j Counter.

k_B Boltzmann constant.

k Space wavenumber.

m Mass.

n Number of degrees of freedom.

p Pressure.

$r_{\alpha,\beta}$ Separation between the centers of particle α and β.

s Laplace complex frequency.

t Time.

u Displacement.

v Velocity.

x Space coordinate.

y Space coordinate.

z Space coordinate.

$\overline{\overline{\Sigma}}$ Covariance matrix.

1PPTM One-Point Particle Tracking Microrheology.

2PPTM Two-Point Particle Tracking Microrheology.

AFM Atomic Force Microscopy.

D2PTM Directional Two-Point Particle Tracking Microrheology.

DGSER Directional Generalized Stokes Einstein Relationship.

F-actin Filamentous actin.

FFT Fast Fourier Transform.

GSER Generalized Stokes Einstein Relationship.

MSD Mean Squared Displacements.

PTM Particle Tracking Microrheology.

RBC Red Blood Cells.

WBC White Blood Cells.

ACKNOWLEDGEMENTS

I am deeply greatful to Professor Juan C. del Álamo for offering me the once-in-a-lifetime oportunity to join his research group. He led the transition of my career from aerospace engineering to biphysics, allowing me to be a part in the beginning of his research group. I will always be thankful for the professional and scientific advice he has offered me throughout these years, as well as his full personal support.

I also want to thank Professor Juan Lasheras, who has shared with me inspiring scientific discussions and provided me with his personal guidance.

I want to thank the people who helped me learn experimental techniques, specially Begoña Álvarez-González, Shun Zhang and Aereas Aung. I am also indebted to the UCSD Interfaces Graduate Program for providing me support in a multidisciplinary traning, and all the proffessional staff that allow the MAE department and the whole UCSD to work.

I also want to thank the many friends that I have met in San Diego. Most of us were far away from our homes and families, and their constant support made this experience trully extraordinary. I will always hold a special place in my heart for Katie Osterday. We began this scientific adventure together, but the missfortune took her from us too early.

I am truly thankful to my friends in Spain, who have supported me in the distance and have always comforted for me when I most needed them.

I am sincerely thankful to my parents Manuel and Constantina and my sisters Tini, Ali and Enci, who have always been there for me, as far back as my memory can recall. My parents have given everything to provide us with an opportunity in live, and I hope to make them proud in this day and the days to come. A special thanks to my nephew Samuel and my niece Lucía, who where borned while I was in the distance, and who have brought immense hapiness to the family.

And finaly, thanks to Begoña Álvarez-González, the person around whom my live revolves. Nothing of this would be possible if you hadn't shared this journey with me. You have been of constant help and inspiration, thanks for being there for me.

Chapter 2 is currently being prepared for publication under the provisional title "On the Laplace transform of Particle Tracking measurements into Microrheology data", by M. Gómez-González and J. C. del Álamo. The dissertation author is the primary investigator in this publication.

Chapter 3 has been published in the *Journal of Fluid Mechanics* under the title "Flow of a Viscous Nematic Fluid around a Sphere", by M. Gómez-González and J. C. del Álamo (2013), 725, 299-331. The dissertation author is the primary investigator in this publication.

Chapter 4 has been in part submitted for peer review under the title "Two-Point Particle Tracking Microrheology of Nematic Complex Viscoelastic Fluids", by M. Gómez-González and J. C. del Álamo. The dissertation author is the primary investigator in this publication.

Chapter 5 is currently being prepared for publication under the provisional title "Dynamic viscoelasticity of individual human RBCs measured by video-particle tracking microrheology", by Y.F. Tseng, Y.Q. Chen, M. Gómez-González, J. C. del Álamo and A. Chiou.

This investigation was partially funded by the U.S. National Science Foundation.

I also acknowledge the support of the Ibercaja Foundation Fellowship, the Interfaces Graduate Training Fellowship and the Howard Hughes Medical Institute.

VITA

2007	Ingeniero Aeronáutico. Escuela Técnica Superior de Ingenieros Aeronáuticos. Polytechnic University of Madrid, Spain.
2008-2009	Mission Analysis Engineer. GMV, S. A., Madrid, Spain.
2009-2010	Awarded Ibercaja Foundation Fellowship.
2009-2015	Research Assistant. Department of Mechanical and Aerospace Engineering. University of California, San Diego. USA.
2010-2013	Teaching Assistant. Departments of Mechanical and Aerospace Engineering and Bioengineering. University of California, San Diego. USA.
2009-2010	M. S. in Aerospace Engineering. University of California, San Diego. USA.
2011-2012	Interfaces Graduate Training Fellowship.
2015	Ph. D. in Engineering Sciences (with specialization in Multi-Scale Biology). University of California, San Diego. USA.

PUBLICATIONS

K. Osterday, T. Chew, P. Loury, J. Haga, **M. Gómez-González**, J. C. del Álamo and S. Chien. "Viscoelastic Properties of Vascular Endothelial Cells Exposed to Stretch". *ICTAM 2012*. Beijing. China. August 19-24, 2012.

M. Gómez-González and J. C. del Álamo. "Flow of a viscous nematic fluid around a sphere". *Journal of Fluid Mechanics*. Vol. 725, pages 299-331, June 2013.

M. Gómez-González and J. C. del Álamo. "Two-Point Particle Tracking Microrheology of Nematic Complex Fluids". (Under review).

M. Gómez-González and J. C. del Álamo. "Accurate Laplace Transform of Experimental Particle Tracking Microrheology Measurements". (In preparation).

Y.F. Tseng, Y.Q. Chen, **M. Gómez-González**, J. C. del Álamo and A. Chiou. "Dynamic Viscoelasticity of Individual Human RBCs Measured by Video-Particle Tracking Microrheology". (In preparation).

S. Zhang, **M. Gómez-González**, R. Meili, J. Lasheras and J. C. del Álamo. "Intracellular Rheology and Traction Forces Driving Physarum Plasmodia Migration". (In preparation).

FIELDS OF STUDY

Major Field: **Engineering Science**

Studies in Biomechanics
Professors Juan C. del Álamo and Juan C. Lasheras.

Studies in Tissue Engineering
Professor Karen L. Christman.

Studies in Fluid Mechanics
Professors Daniel M. Tartakovsky, James W. Rottman and Stefan G. Llewellyn Smith.

Studies in Computational Methods
Professors Alison L. Marsden and Juan C. del Álamo.

Studies in Applied Mathematics
Professors Eric Lauga, Stefan G. Llewellyn Smith and William R. Young.

Studies in Cardiovascular Fluid Mechanics
Professor Alison L. Marsden.

Studies in Biomedical Imaging
Professor Thomas R. Nelson.

Studies in Microscopy
Professors Gina Sosinsky, Mark Ellisman and Hiroyuki Hakozaki.

Studies in Biophysical Techniques
Professor Philbert S. Tsai.

ABSTRACT OF THE DISSERTATION

One- and Two-Point Particle Tracking Microrheology of Complex Viscoelastic Fluids

by

Manuel Gómez-González

Doctor of Philosophy in Engineering Sciences (with a specialization in Multi-Scale Biology)

University of California, San Diego, 2015

Professor Juan Carlos del Álamo, Chair

The mechanical properties of the cell cytoplasm, individual cell constituents and their surrounding medium play a determinant role in many cell functions, including migration, mechanotransduction, disease, etc. Several methods have been developed to measure the shear moduli of microscopic materials, being Passive Particle Tracking Microrheology one of the most prominent. It employs embedded microparticles subjected to Brownian thermal motion. From the statistics of the particles' motion, we extract the shear modulus of the sample. Particle Tracking Microrheology presents practical limitations when applied to complex materials. In this dissertation, we analyze two of these limitations: the Laplace transform of the microrheology data,

and the anisotropy of the sample under study. In the first part, we examine the numerical Laplace transform techniques currently used and their limitations. We then provide a new alternative and show that it yields more accurate results than the methods currently in use. In the second part we focus on a type of anisotropy ubiquitously present in nature and technology: directionality. We describe the mechanical properties of a directional nematic fluid, and calculate the dynamics of interacting particles embedded in a directional medium. We use this result to formulate the directional particle tracking microrheology. We conclude that the motion of single particles don't provide enough information to fully characterize the rheology of a directional material. However, we design a protocol to extract the directional rheology of a sample by correlating the motion of pairs of distant particles, naming it Directional Two-Point Particle Tracking Microrheology. We assess the accuracy of the method by simulating the motion of groups of particles embedded in a directional viscoelastic fluid, and applying the method to them. We then apply this technique to a nematic F-actin gel, in the first report of the directional microrheological properties of F-actin. In the final part of this dissertation, we study the rheology of a different anisotropic system: a viscoelastic membrane embedded in a different fluid. By using this model system, we study the viscoelastic properties of the membrane-cortex complex of red blood cells, obtaining results that are consistent with reported data acquired through independent techniques.

Chapter 1

Introduction

1.1 Background

The mechanical properties of the cell cytoplasm, individual cell constituents and their surrounding medium play a determinant role in many cell functions, including migration, mechanotransduction, development, differentiation, disease, regeneration, etc. Perhaps the most intuitive example of the importance of cell rheology is the effect of the cytoplasm viscoelasticity in the motion and distribution of organelles [80, 109], which is specially determinant during the cell-division cycle [133].

The motile *Amoeba proteus* has been shown to locally and globally tune its viscoelasticity, creating stiffness gradients used to generate the required traction forces [126]. In the same vein, migrating fibroblasts are known to polarize and reorganize their cytoskeleton, assembling filamentous actin (F-actin) in the leading lamella, effectively increasing the stiffness of the leading edge [75].

Individual cells and tissues are known to sense external mechanical stimuli and generate electro-chemical and mechanical responses through mechanisms globally known as *mechanotransduction*. Tissue cells are known to feel and respond to the stiffness of the external substrate [36], developing different phenotypes according to the cell type and the substrate they are in contact with. Furthermore, stem cells have been reported to differentiate in a lineage directed by the

stiffness of their surrounding matrix [40]. Additionally, embryonic stem cells have been shown to display qualitatively different viscoelasticity than differentiated cells [31], *i.e.* while differentiated cells present a complex elastic and viscous behaviour, the cytoplasm of embryonic stem cells do not exhibit measurable elasticity, behaving as a purely viscous fluid. Moreover, characteristic differences have been found between the mechanical properties of embryonic stem cells and induced pluripotent stem cells [32]. On the other hand, cells are not only able to sense isotropic mechanical stimuli, but they can detect directional stimuli such as stiffness gradients [92] and directional shear flows [34] and provide a directional response.

Of particular significance is the viscoelasticity of cells that need to withstand large deformations in order to perform their correct function. Characteristic examples are white blood cells (WBC) and red blood cells (RBC). WBC are the cellular elements of the immune system in humans and other animals. They traverse the body seeking potential sources of infection. Neutrophils, which are one of the WBC types, circulate the blood, penetrate the capillaries and migrate to the extravascular sites of infection where they phagocyte the infecting organisms [69]. Consequently, the deformability of the cytoplasm and nucleus of neutrophils is key for their ability to invade and penetrate towards the sites of infection. Furthermore, due to their size and viscoelastic properties, WBC are often temporarily trapped in the smallest capillaries, and need to deform in order to traverse them. Thus, a reduction in the WBC deformability can locally obstruct the capillaries and reduce the hematocrit [69]. On the other hand, RBC are the cells that deliver oxygen to the body tissues, by using the oxygen-binding protein hemoglobin. Adult human RBC maximize the oxygen they transport by lacking a nucleus and most organelles. Much like WBC, RBC flow in the blood and deform to penetrate the body capillaries. However, the only structural elements present in the RBC are the cell membrane and the underlying spectrin cortex, that confer them rigidity and structural integrity [19]. Given the delicate balance between deformability and stability needed for the correct function of WBC and RBC, variations of their mechanical properties may lead into different disease states.

Of extreme importance to medicine are the microrheological properties of metastatic cancer cells, that need to develop an optimal balance between stiffness and deformability in

order to migrate in three-dimensional matrices [159]. They need to be stiff enough to be able to deform the extracellular matrix while being deformable enough to migrate efficiently. Similarly, a delicate balance between cortical tension and contractility has been found to enable amoeboid migration [2].

Due to the importance of the rheological properties in cell and tissue function, different methods have been used to measure their characteristic viscoelasticity. Simple elastic solids, modeled as an elastic spring, withstand deformations when a force is applied to them, *i.e.* they store elastic energy, and they are characterized by an elastic constant. Conversely, simple viscous fluids flow when a force is applied to them, *i.e.* they dissipate energy through viscous flow, and they are characterized by a viscosity constant. On the other hand, complex viscoelastic fluids present both solid- and viscous-like behaviour that depend on the frequency and time scale of the excitation [83, 51]. Macroscopically, the viscoelastic rheology of a material can be measured with a rheometer by applying an oscillatory shear stress, $\sigma(t)$ at constant frequency and measuring the resultant shear strain $\varepsilon(t)$, or vice versa [43]. In the frequency domain, shear strain and stress are linearly related by the shear moduli of the material, $\tilde{G}(s)$

$$\tilde{\sigma}(s) = \tilde{G}(s) \cdot \tilde{\varepsilon}(s), \tag{1.1}$$

where $\tilde{\cdot}$ represents the Laplace transform and s the Laplace complex frequency. The shear modulus is a complex number,

$$\tilde{G}(s) = \tilde{G}'(s) + i \cdot \tilde{G}''(s), \tag{1.2}$$

whose real part $\tilde{G}'(s)$ is known as the storage modulus and quantifies the elastic energy stored in the deformation, and whose imaginary part $\tilde{G}''(s)$ is the loss modulus and measures the energy viscously dissipated during flow. However, certain limitations hinder the applicability of macroscopic rheology to study the live cell rheology. When applying a probing shear stress, only one frequency is explored, and thus the study of a large frequency spectrum becomes complicated. On the other hand, typical rheometers are able to explore samples no smaller than a

few millimeters in size, making it difficult if not impossible to probe individual cells. Furthermore, cells are known to be complex entities with heterogeneous structures and subdomains of varying mechanical properties, and the use of a rheometer will, at most, provide a bulk shear modulus that averages the measurements over the whole cellular domain. Due to these limitations, a lot of effort has been directed towards designing methods able to study the complex microrheology of microscopic materials such as the cell cytoplasm. All these methods are based on applying either a known force or displacement on the sample by means of a microscopical probe, and measuring the subsequent displacement or stress on the probe. Finally, through an analytical model of the relation between stress and strain on the sample, equivalent to (1.1), the shear modulus of the material is calculated. The earliest implementations of microrheological measurements date from the 1920's, when rudimentary iron microparticles where inserted in gelatin and the cell cytoplasm, manipulated by means of magnetic fields and their motion recorded [59, 45]. This method was later refined in [28, 27]. However, insufficient accuracy in the detection of the particle motion and inadequate control on the probing particles' shape prevented the quantitatively accurate application of the method at that early time.

Typically, microrheology methods fall into two broad categories. In *active* microrheology the probing is driven by an external force applied on the system, while in *passive* microrheology the forcing is provided by the dynamics of the system under study. A first example of active microrheology technique is the micro-pipette aspiration [21, 144, 42], probably inspired by the passage of the blood cells through narrow capillaries. Thin micropipettes with internal diameter of a few microns are used to suction on small regions or in whole cells. A known pressure is applied on the pipette, and the length of the sample that is aspired into the pipette is measured. A simple relation between the applied pressure and the deformation is applied in order to calculate the effective deformability of the cell. More complex analytical models can be used in order to refine the measurements. Limitations of this technique include the need for physical access to the measured cell, the reduced throughput, *i.e.* only one cell is analyzed in each measurement, and the fact that the measured properties are bulk viscoelasticities of a relatively large area and ensemble of cell structures.

A second active microrheology method is the Atomic Force Microscopy (AFM). Small known forces in the order of tenths of piconewtons, or small deformations in the order of nanometers, are applied with a probing tip attached to a soft cantilever [10], and the surface of the sample is indented according to the shape of the tip. The subsequent deformations on the cantilever, or the forces on the cantilever base, are measured. A relation between the applied force and the deformation of the sample, equivalent to (1.1), is modelled according to the shape of the indentation that the probing tip induces on the sample, and from it the microrheological properties of the sample are calculated. This technique allows for high spacial resolution of the measurements, and it can be used to provide a mapping of the heterogeneous mechanical properties of the cell. However, much like micropipette aspiration, AFM requires mechanical access to the sample. Furthermore, the AFM probing of cells is always applied on the cellular membrane, what complicates the probing of the internal structure of the cell.

An extensive group of microrheology methods employs probing micron sized particles to both apply a force on the sample and measure the sample deformation. As a whole, they are named Particle Tracking Microrheology (PTM) techniques, and they encompass both active and passive methods. We refer to *one-point* methods to those that use the same particle to both excite the material and measure the material deformations, while we call *two-point* methods to those that use different particles to excite the medium and to measure the deformations. One-particle microrheology methods typically employ spherical probing particles and model their motion in agreement to Stokesian dynamics, *i.e.*

$$\tilde{\vec{F}}(s) = 6\pi a \frac{\tilde{G}(s)}{s} \tilde{\vec{v}}(s), \tag{1.3}$$

where a is the particle radius, $\tilde{\vec{F}}(s)$ is the exciting force and $\tilde{\vec{v}}(s)$ is the velocity of the particle. It is important to know that equation (1.3) assumes, among others, a low Reynolds number flow and isotropy of the fluid. On the other hand, two-particle methods exploit the fact that a particle α

undergoing a force $\tilde{\vec{F}}_\alpha(s)$ will induce a velocity $\tilde{\vec{v}}^{\,I}_{\alpha,\beta}(s)$ on a distant particle β such that

$$\tilde{\vec{v}}^{\,I}_{\alpha,\beta} = \frac{s}{8\pi\tilde{G}(s)r_{\alpha,\beta}} \cdot \begin{bmatrix} 1+\left(\frac{x}{r_{\alpha,\beta}}\right)^2 & \frac{xy}{r^2_{\alpha,\beta}} & \frac{xz}{r^2_{\alpha,\beta}} \\ \frac{yx}{r^2_{\alpha,\beta}} & 1+\left(\frac{y}{r_{\alpha,\beta}}\right)^2 & \frac{yz}{r^2_{\alpha,\beta}} \\ \frac{zx}{r^2_{\alpha,\beta}} & \frac{zy}{r^2_{\alpha,\beta}} & 1+\left(\frac{z}{r_{\alpha,\beta}}\right)^2 \end{bmatrix} \cdot \tilde{\vec{F}}_\alpha(s), \qquad (1.4)$$

where $\vec{r}_{\alpha,\beta} = (x,y,z)$ is the vector that connects the centers of the interacting particles. It should be noted that equation (1.4) is valid for distant particles, *i.e.* $r_{\alpha,\beta} = \left|\vec{r}_{\alpha,\beta}\right| \gg a_\alpha, a_\beta$. Both equations (1.3) and (1.4) have been modified to be used with non-spherical probing particles [137], and in this dissertation we provide equivalent equations applicable to non-isotropic materials such as nematic fluids. Some of the advantages of PTM techniques are that they do not require mechanical access to the sample, only an optical path, and they can be used to locally probe the material under study, obtaining a mapping of its mechanical properties.

Among the active PTM techniques we find the "magnetic bead microrheometers" or "magnetic tweezers" that were introduced above. They are based on the injection of magnetic microparticles in the sample of interest, and the excitation through applied external magnetic fields that induce known driving forces on the particles [51]. The displacements of the excited particles are recorded, and the shear modulus of the fluid is measured by applying either equation (1.3) in one-particle experiments or equation (1.4) in two-particle assays. A second active PTM technique is known as "Optical Tweezers". It makes use of highly focused laser beams to trap an optical particle in the laser focus. The laser beam is accurately calibrated and the force that it applies on the particle is know as a function of the particle position with respect to the laser focus [4, 11]. Similarly to magnetic tweezers, the excitation force is known, the particle displacement is recorded and the fluid shear modulus is calculated. However, the forcing applied by the optical tweezers is highly local, and they provide a higher control on the particle manipulation.

In a similar manner, passive PTM techniques track the motion of probing particles that display Brownian motion due to thermal excitation. The instantaneous thermal force acting on

the probing particle is not known, but the statistical description of its motion is well characterized mathematically, and thus we can measure the shear modulus of the fluid from the statistical properties of the problem. An important characteristic of PTM is that the thermal driving force provides a broad spectrum of excitation frequencies, allowing to probe the material simultaneously in a wide range of frequencies. The following section introduces passive PTM in more detail.

1.2 Passive Particle Tracking Microrheology

Due to the atomic nature of matter, microparticles suspended in a soft material experience a continuous random motion due to thermal excitations. In brief, the molecular constituents of matter are continuously vibrating and bouncing in a motion that is proportional to their thermal energy content. These molecules randomly collide with the embedded microparticles, inducing an exchange of momentum that translates into the random Brownian thermal motion of the particles. This motion was first reported in 1828 by the Scottish botanist Robert Brown, in a work later collected in [14] and further extended in [13]. Almost a century was necessary until this phenomenon was mathematically described by Albert Einstein in [38, 39]. The simplest model of Brownian motion predicts [9] that the microparticles move according to

$$\dot{x}(t) = \sqrt{2D} \cdot \mathrm{R}(t), \tag{1.5}$$

where $x(t)$ indicates the displacement of the particle in any direction, $\dot{x}(t)$ is the velocity of that degree of freedom, t is the time, D is the diffusion coefficient and $\mathrm{R}(t)$ is any white noise process, the simplest of which follow, for all t and τ

$$\langle \mathrm{R}(t) \rangle = 0, \tag{1.6}$$

$$\langle \mathrm{R}(t), \mathrm{R}(t+\tau) \rangle = \delta(\tau) \tag{1.7}$$

where $\langle ... \rangle$ represents an ensemble average and δ the Dirac delta. Einstein made use of the *equipartition theorem* [104, 155], that states that the energy content of each degree of freedom of

any microscopical system in equilibrium is on average equal to

$$E = \frac{1}{2} k_B T \tag{1.8}$$

where E is the total energy of the system, $k_B = 1.3806488 \times 10^{-23}$ m^2 kg s^{-2} K^{-1} is the Boltzmann constant and T is the absolute temperature of the system, and he further identified the total energy of the particle with its kinetic energy

$$E_K = \frac{1}{2} n \sum_{\forall j} \dot{x}_j^2(t), \tag{1.9}$$

where $\dot{x}_j(t)$ represents the velocity of the particle in each one of its n degrees of freedom. Finally, he calculated that the diffusion constant of a spherical particle of radius a embedded in a fluid of viscosity η takes the form

$$D = \frac{k_B T}{6\pi a \eta}. \tag{1.10}$$

In 1995, Mason and Weitz [102] extended this theory to be able to measure the viscoelastic response of soft materials. They model the hydrodynamics of a microparticle embedded in a viscoelastic fluid by means of a generalized Langevin equation [62, 16]

$$m\dot{v}(t) = f_R(t) - \int_{\tau=0}^{\tau=t} \zeta(t-\tau) v(\tau) d\tau, \tag{1.11}$$

where m is the particle mass, $v(t)$ its velocity, $\dot{v}(t)$ its acceleration, $f_R(t)$ the external force applied on the particle and $\zeta(t-\tau)$ a memory function, also known as *response function*, that quantifies the hydrodynamic force applied on the particle as a function of the current velocity and the previous history of velocities. By transforming equation (1.11) into Laplace space, multiplying it for the velocity at the initial instant of time, taking an ensemble average and applying the

equipartition theorem, we obtain the following equation

$$\langle v(0), \tilde{v}(s) \rangle = \frac{k_B T}{\tilde{\zeta}(s) + m \cdot s}. \tag{1.12}$$

For very small particles that move slowly in a very viscous fluid the inertial terms are negligible when compared to the viscoelastic terms, *i.e.* $m \cdot s \ll \tilde{\zeta}(s)$, and equation (1.12) simplifies into

$$\tilde{\zeta}(s) = \frac{k_B T}{\langle v(0), \tilde{v}(s) \rangle}, \tag{1.13}$$

which is an alternative expression of the *fluctuation-dissipation* theorem [114, 76]. We define the one-dimensional Mean Squared Displacements (MSD) of an ensemble of particles in the direction x as the ensemble average of the particle jumps in the coordinate x for each time τ

$$MSD_x(\tau) = \langle \Delta x^2(\tau) \rangle = \frac{1}{N_t} \sum_{\forall t} \left[x(t+\tau) - x(t) \right]^2, \tag{1.14}$$

where N_t represents the number of times considered in the sum. It can be shown that, in the frequency domain, the MSD are related to the velocity correlation as

$$\langle \Delta x^2(s) \rangle = \frac{2}{s^2} \langle v(0), \tilde{v}(s) \rangle, \tag{1.15}$$

and thus, we obtain a relation between the response function of the fluid and the MSD of microparticles embedded in it

$$\tilde{\zeta}(s) = \frac{2 k_B T}{s^2 \langle \Delta x^2(\tau) \rangle}, \tag{1.16}$$

that is known as the generalized Einstein equation.

Mason and Weitz [102] combined the generalized Einstein (1.16) and the generalized Stokes (1.3) equations into a formula that relates the MSD of embedded microparticles with the

complex shear modulus of the probed material

$$\tilde{G}(s) = \frac{nk_BT}{3\pi as\langle\Delta\tilde{r}^2(s)\rangle}, \tag{1.17}$$

where n is the number of dimensions of the motion of the particle and $\langle\Delta\tilde{r}^2(s)\rangle$ are the n-dimensional MSD of the particle

$$\langle\Delta\tilde{r}^2(s)\rangle = \sum_{j=1}^{j=n}\langle\Delta\tilde{x}_j^2(s)\rangle. \tag{1.18}$$

The equation (1.17) is known as the Generalized Stokes Einstein Relationship (GSER), and is the base of Passive One-Point Particle Tracking Microrheology.

Passive one-point PTM has many advantages, which we summarized in the previous section, that make it specially suitable to probe soft materials. However, this technique also presents certain limitations that we need to know in order to correctly apply it, and even to overcome them, as we will do in the following chapters of this dissertation. Due to the fact that the driving force of the probing particles is very small, in the order of k_BT, only very soft materials can be probed with passive PTM. Furthermore, the displacements of the probing particles will be very small, and extremely precise tracking algorithms, able to detect bead displacements of the order of tenths of nanometers, become essential. On the bright side, such small energies are unlikely to distort the material or to induce non-linear hydrodynamic effects, a concern commonly associated to active microrheology techniques.

An important characteristic of the Einstein equation (1.16) is that it assumes thermodynamic equilibrium. This is a safe hypothesis for many soft materials, where the only energy present is in the form of thermal excitations, but it might be inappropriate for active materials, such as the cell cytoplasm, where the presence of random active motors might induce an excitation with a white noise spectrum different than (1.10) [55].

On the other hand, the generalized Stokes equation (1.3) rely on several assumptions that need to be assessed in order to correctly apply PTM. For once, it is only applicable to spherical particles, although advances have been made in order to study the dynamic of non-spherical probing particles [137]. In addition, it assumes a homogeneous probed material that behaves as a

continuum. This implies that the probing microparticle must be larger than any structural element of the probed material, such as the mesh size, persistence length, etc. In contrast, the Stokes flow assumption is only applicable to low Reynolds number flows, where $Re = \rho UL/\eta \ll 1$ is the Reynolds number, ρ is the density of the material, U and L are characteristic velocity and length of the flow and η is a characteristic viscosity. This implies that the particle must be smaller than the relevant length scale of the flow around the particle. These two conditions impose an upper and lower bound for the radius of the probing particle, and we need to asses their compatibility in order to perform a PTM measurement.

At the same time, the Stokes equation assumes that the probed fluid is isotropic and its dynamics can be described by just one complex shear modulus $\tilde{G}(s)$. However, many materials of interest display complex dynamics that prevent us from directly using equation (1.3), and thus we need to correctly model the dynamics of the probing microparticles in order to extract the actual microrheology information of the material. In the following chapters of this dissertation we will focus on studying two examples of great practical interest: directional materials, that cannot be described by just one shear modulus, and membranes, that don't follow the linear Stokes equation.

The final limitations of the Stokes model that we will mention in this introduction are the physico-chemical interactions between the probing particle and the surrounding medium. As an example, microparticles embedded in a polymer solution can locally create depletion zones around it and thus modifying the local diffusivity. Additionally, the particle motion can induce local compressibility on an otherwise incompressible polymer. Furthermore, the Stokes equation assumes no slip on the particle surface, and electrically charged or chemically reacting particles can induce partial or total slip on the particle surface. Even more, probing microparticles can induce molecular anchoring on their surface, locally modifying the polymer structure. All of these phenomena are restricted to a small region around the particle surface and will modify its dynamics. As a consequence, they might prevent us from accurately measuring the material properties of the sample, and affected one-point PTM experiment will render effective diffusivities of the particles instead of the actual shear modulus of the probed material.

In order to overcome this local effects, in 2000 Crocker *et al.* introduced a technique

called Two-Point Particle Tracking Microrheology (2PPTM) [30], that was later mathematically justified by Levine and Lubensky [87, 88]. It is based on the correlation of the motion of pairs of distant hydrodynamically interacting particles (1.4), and its formulation takes the form

$$\tilde{G}_{2P}(s) = \frac{k_B T}{2\pi r_{\alpha,\beta} s \langle \Delta\tilde{r}_\alpha(s), \Delta\tilde{r}_\beta(s) \rangle} = \frac{k_B T}{4\pi r_{\alpha,\beta} s \langle \Delta\tilde{\theta}_\alpha(s), \Delta\tilde{\theta}_\beta(s) \rangle}, \tag{1.19}$$

where Δr_α and $\Delta\theta_\theta$ represent the displacements of particle α along the line that connects the centers of both particles, and the perpendicular direction respectively. Here, we have used the definition of the cross-MSD between any two degrees of freedom x and y

$$\langle \Delta x(\tau), \Delta y(\tau) \rangle = \frac{1}{N_t} \sum_{\forall t} \left[x(t+\tau) - x(t) \right] \left[y(t+\tau) - y(t) \right]. \tag{1.20}$$

It is important to note that, while the GSER (1.17) uses one particle to locally probe the surrounding medium, equation (1.19) correlates the motion of pairs of distant particles and provides an average shear modulus in the region between the particles. Furthermore, equation (1.19) is not dependent on any of the particles radii and as long as the particles are far apart, *i.e.* $\left|\vec{r}_{\alpha,\beta}\right| \gg a_\alpha, a_\beta$, the shear modulus it provides is insensitive to the local interactions of the probing particles with the medium [30, 87, 88]. For this reason, the use of 2PPTM is preferred over One-Point Particle Tracking Microrheology (1PPTM) when studying complex materials where the mere presence of the probing particles introduce distortions to the material and to its local rheology. On the other hand, the hydrodynamic interactions between pairs of distant particles are weaker than each own particle's thermal motion, *i.e.* they decay as $r_{\alpha,\beta}^{-1}$, and thus they are more sensitive to experimental noise and more experimental measurements need to be performed in order to obtain statistically significant results.

1.3 Outline of the Dissertation

In the preceding sections we provided a short introduction to the importance of the mechanical properties of the cell cytoplasm and cell constituents, and their relation to the correct

cell function. We then summarized the different microrheological methods used to measure their shear moduli. We concluded by providing an overview of passive particle tracking microrheology and provided the formulation and limitations of both the one- and two-point variants. In the following, we will address different mechanical limitations of PTM when applied to complex materials. We provide suitable models for certain materials that cannot be regarded as isotropic, we modify the existing PTM to take into account the particularities of such media, and we apply the obtained formulation to experimental samples.

In **chapter 2** we focus on a limitation that hinders the accurate application of current PTM implementations to complex materials. In a typical PTM experiment we measure the displacement of the probing microparticles, and calculate their MSD in the time domain (2.1). However, the GSER formulation (1.17) requires us to provide the Laplace transform of the MSD and it yields the shear modulus in the frequency domain. Because the MSD are measured on a finite time interval and over a discrete set of time points, the numerical Laplace transform methods that are currently used provide results that contain high numerical errors. In this dissertation, we provide a method based on a least-square fit of the MSD to a physically satisfactory sum of functions that have a known Laplace transforms. We analyze the accuracy of this novel approach and compare it to the *de facto* approximation used in experimental PTM, and we find that the our approach renders results that are highly more accurate.

In **chapter 3** we study a characteristic of many biological and technological materials that is not accounted for in the current microrheology formulations: directionality. We first provide the fluid equations that direct the motion of a spherical particle moving at low Reynolds number in a directional fluid, and from them we calculate the drag force experienced by the particle, providing a generalization of the Stokes equation (1.3) for directional fluids. We find that the motion of the particle is described by three complex shear moduli, as opposed to isotropic materials that are described by just one. We then generalize the GSER to account for the directionality of the probed material, defining the Directional GSER (DGSER). We find that, even for particles that are able to move in three-dimensions, the DGSER is able to provide, at most, two independent equations that are not enough to calculate the three independent viscoelastic shear moduli of a

directional fluid. Nevertheless, we use the DGSER to provide an estimation of the errors rendered by previous PTM methods when applied to directional materials.

In **chapter 4** we study the interacting motion of pairs of distant particles embedded in a directional viscoelastic fluid. We calculate the form of the velocity that one particle induces on the other, in a generalization of equation (1.4). We then use this formula to generalize the form of 2PPTM (1.19) when applied to directional fluids, in a method called Directional Two-Point Particle Tracking Microrheology (D2PTM). We find that D2PTM provides three independent equations that allows us to calculate the three complex shear moduli of a directional viscoelastic material. In order to test the applicability of the method, we first simulate the motion of groups of interacting particles embedded in a directional viscoelastic fluid. From their motion, we calculate their MSD and the shear moduli of the simulated fluid, finding a good agreement with the actual values initially prescribed to the simulation. In order to illustrate the applicability of D2PTM to experimental samples, we studied the microrheology of nematic F-actin gels. Through the application of shear flow to the samples, the molecules of the F-actin gels align in the direction of the flow, conferring directional mechanical properties to the sample. By applying D2PTM to these directional gels, we were able to measure, for the first time, the directional shear moduli of nematic F-actin.

In **chapter 5** we study the applicability of Live-Cell PTM to another type of samples that are not isotropic: we analyze the mechanical properties of the membrane-cortex complex of RBC. Their membrane-cortex complex is a thin layer bounded by other fluids above and bellow, and the probing microparticles used in the PTM experiment are not free to move in three-dimensions, but they are restricted to move in the membrane-cortex complex. We model the motion of the probing microparticles in this viscoelastic anisotropic environment, and review the formulation of 1PPTM and 2PPTM when applied to this medium. We then apply both formulations to particles embedded in the membrane-cortex complex of RBC and compare the results to the effective shear moduli provided by isotropic PTM.

Chapter 2

On the Laplace Transform of Particle Tracking Measurements into Microrheology Data

2.1 Introduction

In a PTM experiment, we track the motions of individual or groups of probing particles, and from them we calculate the shear moduli of the material. This process entails the measurement of the time evolution of the location of the center of each particle, $\vec{r}_\alpha(t)$, the calculation of the average MSD as a function of the time steps, the transformation from the time domain into frequency space, and the connection of this mobility data with the shear moduli of the material. For each coordinate x of a particle, the MSD are defined as the ensemble average over N particles

$$MSD_x(\tau) = \langle \Delta x^2(\tau) \rangle = \frac{1}{N} \sum_{\alpha=0}^{\alpha=N} \sum_{\forall t} \left[x_\alpha(t+\tau) - x_\alpha(t) \right]^2, \tag{2.1}$$

and the cross-MSD of two degrees of freedom x and y

$$MSD_{x,y}(\tau) = \langle \Delta x(\tau), \Delta y(\tau) \rangle = \frac{1}{N} \sum_{\alpha=0}^{\alpha=N} \sum_{\forall t} \left[x_\alpha(t+\tau) - x_\alpha(t) \right] \left[y_\alpha(t+\tau) - y_\alpha(t) \right], \tag{2.2}$$

where these degrees of freedom are typically either two coordinates of a particle, or two coordinates of two interacting particles. In passive one-point PTM of isotropic materials, the MSD are related to the shear moduli of the material through the *Generalize Stokes-Einstein Relationship* [102], provided in equation (1.17). On the other hand, in passive two-point PTM of isotropic materials, the shear moduli is related to the cross-MSD as of interacting particles through equation (1.19). In active microrheology these formulas need to be adapted to take into account the shape of the driving force.

In this chapter, we will focus on the transformation from the time domain to the Laplace frequency space, the problems and particularities of the process, the approaches taken in previous studies, and a proposed method to highly improve the results.

2.2 The Γ-Approximation to the Laplace Transform

In [102], Mason and Weitz firstly introduced the formulation of one-point PTM, and suggested to transform $\Delta r^2(\tau)$ into $\Delta \tilde{r}^2(s)$ by performing a numerical Laplace transform, *i.e.* by performing the numerical integral

$$\langle \Delta \tilde{r}^2(s) \rangle = \int_{\tau=0}^{\tau=\infty} \langle \Delta r^2(\tau) \rangle e^{-s\tau} d\tau \tag{2.3}$$

for each complex frequency $s = c + i\omega$. On the other hand, in [53, 132] the authors propose to apply a standard Fast Fourier Transform (FFT), obtain $\langle \Delta \tilde{r}^2(\omega) \rangle$ from the coefficients calculated, and identify $s = i \cdot \omega$. However, since $\langle \Delta r^2(\tau) \rangle$ is only known at discrete time points of a finite time interval, the two methods will introduce numerical errors in the frequency extremes due to the truncation of the temporal data set [100, 101].

In order to solve this issue, in [103, 101] the authors propose the Γ-approximation to the

Laplace transform. It consists in locally approximate $\langle \Delta r^2(\tau) \rangle$, around each frequency s, by a power law and substitute $\langle \Delta \tilde{r}^2(s) \rangle$ by the analytic Laplace transform of the approximation. The MSD are locally approximated around a complex frequency s as

$$\langle \Delta r^2(\tau) \rangle \approx A \cdot (s\tau)^{\alpha(s)}, \tag{2.4}$$

that has the exact analytic Laplace transform

$$\mathcal{L}\left[A \cdot (s\tau)^{\alpha(s)}; \tau \to s\right] = A \cdot s^{\alpha(s)} \frac{\Gamma[1+\alpha(s)]}{s^{1+\alpha(s)}}. \tag{2.5}$$

The coefficient A is given by

$$\langle \Delta r^2(\tau = \tfrac{i}{s}) \rangle = A \cdot i^{\,\alpha(s)}, \tag{2.6}$$

and the exponent is calculated as

$$\alpha(s) = \left. \frac{\partial \ln\left[\langle \Delta r^2(\tau) \rangle\right]}{\partial \ln(\tau)} \right|_{\tau = i/s}. \tag{2.7}$$

It is important to note here that $\langle \Delta r^2(\tau) \rangle$ is known at discrete time points and typically contains experimental noise. In order to calculate the logarithmic slope $\alpha(s)$, $\ln\left[\langle \Delta r^2(\tau) \rangle\right]$ is typically fitted, as a function of $\ln(\tau)$, by a polynomial [30]. By using equations (2.4)-(2.7) we can approximate the Laplace transform of the MSD as

$$s\langle \Delta \tilde{r}^2(s) \rangle \approx \langle \Delta r^2(\tau = \tfrac{i}{s}) \rangle i^{\,-\alpha(s)} \Gamma\left[1 + \left. \frac{\partial \ln\left[\langle \Delta r^2(\tau) \rangle\right]}{\partial \ln(\tau)} \right|_{\tau = i/s}\right]. \tag{2.8}$$

The slope of the MSD of a particle thermally diffusing in a viscoelastic material, $\alpha(s)$, is physically bounded between 0 for an elastic medium and 1 for a viscous fluid. For this range of slopes, Mason [101] provides a polynomial approximation of the gamma function, $\Gamma[1+\alpha] \approx 0.457(1+\alpha)^2 - 1.36(1+\alpha) + 1.90$, with a maximum error of 12%. However, given the widespread availability of the gamma function in most modern programing environments, we

will not consider the polynomial approximation in this analysis. The shear moduli provided by one-point PTM when the Γ-approximation is used is

$$\tilde{G}_\Gamma(s) = \frac{nk_BTi^{\,\alpha(s)}}{3\pi a\langle\Delta r^2(\tau=\frac{i}{s})\rangle\Gamma[1+\alpha(s)]}. \tag{2.9}$$

The Γ-approximation has the advantage of being algebraic and not requiring the calculation of integrals, while retaining a maximum error of around 15% in the absolute value of the shear modulus [101], and has become the *de facto* method used in microrheology analysis. On the other hand, it comes with its drawbacks. Since it is a local transform, not a global integral, it neglects the important contributions from distant time points. Furthermore, the small error in the absolute value doesn't guarantee a similar small error in the storage and loss moduli. The argument of the complex shear moduli (2.9) is given by $\frac{\pi}{2}\cdot\alpha(s)$ rad. When either storage or loss modulus is larger than the other, a small variation on $\alpha(s)$ will have a small effect in the larger moduli, and a comparatively large effect in the smaller. In order to study the impact of an error in $\alpha(s)$ on the storage and loss moduli, we define a non-dimensional shear modulus

$$\overline{G}_\Gamma(s) = \tilde{G}_\Gamma(s)\cdot\frac{3\pi a\langle\Delta r^2(\tau=\frac{i}{s})\rangle\Gamma[1+\alpha(s)]}{nk_BT} = i^{\,\alpha(s)} = \cos\left[\tfrac{\pi}{2}\cdot\alpha(s)\right] + i\cdot\sin\left[\tfrac{\pi}{2}\cdot\alpha(s)\right]. \tag{2.10}$$

It is a complex number with the same complex argument than the shear modulus, and unity absolute value. Thus, it is a great benchmark for the distinct impact that small errors have on the storage and loss moduli. An error $\Delta\alpha(s)$ in the determination of the slope will induce an error $\Delta\overline{G}(s)$ in the non-dimensional shear modulus such that

$$\overline{G}_\Gamma(s) + \Delta\overline{G}_\Gamma(s) = \frac{\Gamma[1+\alpha(s)]}{\Gamma[1+\alpha(s)+\Delta\alpha(s)]}\cdot i^{\,\alpha(s)+\Delta\alpha(s)}. \tag{2.11}$$

For small errors, equation (2.11) can be linearized as

$$\begin{aligned}\overline{G}_\Gamma(s) + \Delta\overline{G}_\Gamma(s) \approx{}& \cos\left[\tfrac{\pi}{2}\cdot\alpha(s)\right] - \tfrac{\pi}{2}\Delta\alpha(s)\sin\left[\tfrac{\pi}{2}\cdot\alpha(s)\right] \\ &+ i\cdot\left\{\sin\left[\tfrac{\pi}{2}\cdot\alpha(s)\right] + \tfrac{\pi}{2}\Delta\alpha(s)\cos\left[\tfrac{\pi}{2}\cdot\alpha(s)\right]\right\}.\end{aligned} \tag{2.12}$$

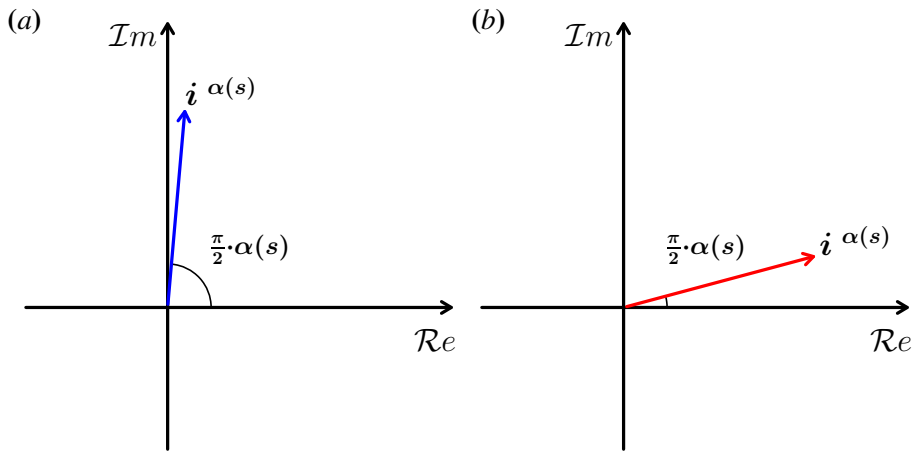

Figure 2.1: Schematic representation of the complex number $i^{\alpha(s)}$ that defines the ratio between storage and loss moduli in the Γ-approximation. We depict (*a*) a material with high viscosity and low elasticity and (*b*) a material with low viscosity and high elasticity. Its argument (angle with the real axis) is determined by $\frac{\pi}{2}\cdot\alpha(s)$.

Here, we can consider two extreme cases: a very viscous fluid and a very elastic material, that will help us understand why small errors differently affect the storage and loss moduli. In **Figure 2.1** we provide a visual representation of the issue. A fluid with high viscosity and low elasticity, and thus $\alpha(s) \lesssim 1$, is depicted in **Figure 2.1 (*a*)**. Under this simplification, equations (2.11)-(2.12) approximate to

$$\overline{G}_\Gamma(s) \approx \frac{\pi}{2}\Big(1-\alpha(s)\Big) + i\cdot\Big[1-\frac{\pi^2}{8}\Big(1-\alpha(s)\Big)^2\Big], \tag{2.13}$$

$$\overline{G}_\Gamma(s) + \Delta\overline{G}_\Gamma(s) \approx \frac{\pi}{2}\Big[\big(1-\alpha(s)\big) - \Delta\alpha(s)\Big] + i\cdot\Big[1-\frac{\pi^2}{8}\Big(\big(1-\alpha(s)\big) - \Delta\alpha(s)\Big)^2\Big]. \tag{2.14}$$

By inspecting the above equations, one can see that the relative importance of the error in the storage modulus is much higher than the influence in the loss modulus. Both errors grow with $\Delta\alpha(s)$ and with $\alpha(s)$ approaching 1. Furthermore, when $\Delta\alpha(s) > 1-\alpha(s)$, the storage modulus becomes unphysically negative. Correspondingly, in **Figure 2.1 (*b*)** we show a material with low elasticity and high viscosity, *i.e.* $\alpha(s) \lesssim 0$. In the presence of small errors, equations (2.11)-(2.12) approximate to

$$\overline{G}_\Gamma(s) \approx 1 - \frac{\pi^2}{8}\alpha(s)^2 + i\cdot\frac{\pi}{2}\alpha(s), \tag{2.15}$$

$$\overline{G}_\Gamma(s)+\Delta\overline{G}_\Gamma(s)\approx 1-\frac{\pi^2}{8}\left(\alpha(s)+\Delta\alpha(s)\right)^2+i\cdot\frac{\pi}{2}\big(\alpha(s)+\Delta\alpha(s)\big). \tag{2.16}$$

For this material, the relative influence of the error in the storage and loss moduli increases with increasing $\Delta\alpha(s)$ and with decreasing $\alpha(s)$. Furthermore, when $\Delta\alpha(s) < -\alpha(s)$, the loss modulus becomes unphysically negative.

In the following sections, we apply the Γ-approximation to four typical materials, an isotropic viscous liquid, an isotropic elastic solid, a viscoelastic Kelvin-Voigt gel and a viscoelastic Maxwell gel, and assess the errors introduced by the approximation.

2.2.1 Isotropic Viscous and Elastic Materials

Isotropic viscous liquids are characterized by a zero elasticity coefficient and a constant viscosity η. They are represented by a viscous damper with viscosity constant η, as shown in

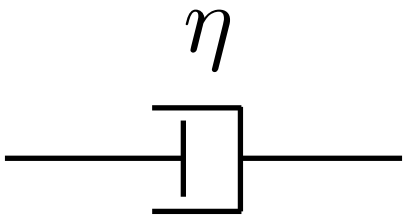

Figure 2.2: Schematic representation for isotropic viscous fluids. It consists on a damper with viscosity constant η.

Figure 2.2. Their complex shear moduli have the form

$$\tilde{G}(s)=s\cdot\eta. \tag{2.17}$$

The mean squared displacements of probing microparticles embedded in them are, according to the *GSER* (1.17),

$$\langle\Delta\tilde{r}^2(s)\rangle=\frac{nk_BT}{3\pi as^2\eta}. \tag{2.18}$$

The above equations has the exact analytic inverse Laplace transform

$$\langle \Delta r^2(\tau) \rangle = \frac{nk_BT}{3\pi a\eta}\tau. \tag{2.19}$$

By applying equation (2.7) to equation (2.19) we find $\alpha(s) = 1$, and equation (2.9) matches exactly equation (2.18). Thus, isotropic viscous materials are perfectly described by the gamma approximation.

At the other end of the spectrum, isotropic elastic solids are described by a constant elasticity coefficient μ and a zero viscosity constant. They are represented by a spring, as depicted in **Figure 2.3**. Their complex shear moduli are described by

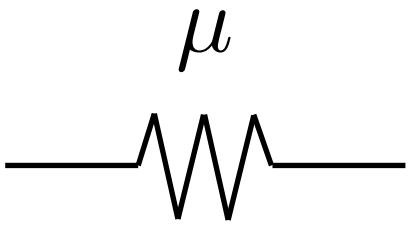

Figure 2.3: Schematic representation for isotropic elastic materials. It consists on a spring with elasticity constant μ.

$$\tilde{G}(s) = \mu, \tag{2.20}$$

and the MSD of embedded microparticles have the form

$$\langle \Delta \tilde{r}^2(s) \rangle = \frac{nk_BT}{3\pi as\mu}, \tag{2.21}$$

with exact analytical inverse Laplace transform

$$\langle \Delta r^2(\tau) \rangle = \frac{nk_BT}{3\pi a\mu}. \tag{2.22}$$

The application of equation (2.7) to (2.22) provides a slope $\alpha(s) = 0$ and thus equation (2.9) also provides an exact description of the material's microrheology.

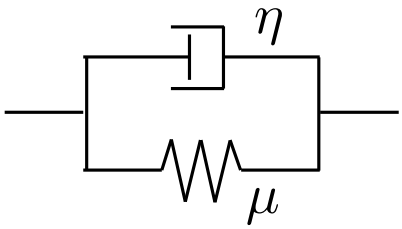

Figure 2.4: Schematic representation of the Kelvin-Voigt model for viscoelastic fluids. It consists on a damper with viscosity constant η in parallel with a spring of elasticity constant μ.

2.2.2 Isotropic Kelvin-Voigt Viscoelastic Fluids

The Kelvin-Voigt model describes one of the simplest cases of viscoelastic fluids. It consists on a purely viscous damper, with viscosity constant η, connected in parallel to a purely elastic spring, with elasticity constant μ, as illustrated in **Figure 2.4**. The shear modulus of the group takes the form

$$\tilde{G}(s) = \mu + s \cdot \eta, \tag{2.23}$$

with the MSD of embedded probing particles being, as a function of the frequency,

$$\langle \Delta \tilde{r}^2(s) \rangle = \frac{nk_BT}{3\pi a\eta} \frac{1}{s} \frac{1}{s+\mu/\eta}, \tag{2.24}$$

and as a function of time,

$$\langle \Delta r^2(\tau) \rangle = \frac{nk_BT}{3\pi a\mu} \left(1 - e^{-\frac{\mu}{\eta}\tau}\right). \tag{2.25}$$

In **Figure 2.5** we illustrate the MSD, as a function of the time separation, of microparticles embedded in a Kelvin-Voigt fluid and subjected to Brownian thermal motion. The example was chosen with the viscoelastic parameters $\mu/\eta = 1$. Two features of the plot become readily apparent. For short time separations, $\tau \ll \frac{\eta}{\mu}$, (*i.e.* high frequencies $\omega \gg \frac{\mu}{\eta}$), the material asymptotically behaves as a viscous fluid, *i.e.* the slope of the MSD approaches 1. At long time separations $\tau \gg \frac{\eta}{\mu}$ (low frequencies $\omega \ll \frac{\mu}{\eta}$), the material asymptotically approaches to an elastic solid behaviour,

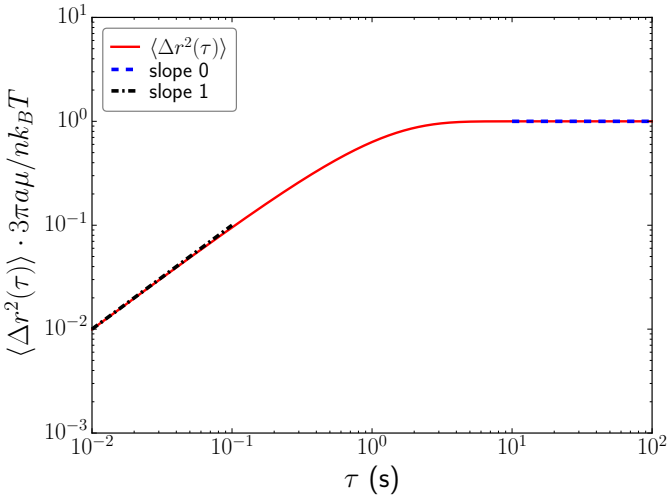

Figure 2.5: Normalized MSD, as a function of the time separation τ, of particles embedded in a Kelvin-Voigt viscoelastic fluid and subjected to Brownian thermal motion (——). The slope 0 trend (– –) is plotted at high frequencies, and the slope 1 trend (– · –) at low frequencies. The material is defined by the parameter ratio $\mu/\eta = 1$.

i.e. the slope of the MSD approaches 0.

The logarithmic slope (2.7) of equation (2.25) takes the form

$$\alpha(s) = \frac{\mu}{\eta}\frac{i}{s}\frac{e^{-\frac{\mu}{\eta}\frac{i}{s}}}{1-e^{-\frac{\mu}{\eta}\frac{i}{s}}}, \tag{2.26}$$

and the Γ-approximation of the MSD (2.8) and the shear modulus (2.9) become

$$\langle \Delta\tilde{r}^2_\Gamma(s) \rangle = \frac{nk_BT}{3\pi a\mu}\frac{1-e^{-\frac{\mu}{\eta}\frac{i}{s}}}{s}\cdot i^{\,-\alpha(s)}\cdot\Gamma\left[1+\alpha(s)\right], \tag{2.27}$$

$$\tilde{G}_\Gamma(s) = \frac{\mu\cdot i^{\,\alpha(s)}}{\left(1-e^{-\frac{\mu}{\eta}\frac{i}{s}}\right)\cdot\Gamma\left[1+\alpha(s)\right]}. \tag{2.28}$$

In the panel (*a*) of **Figure 2.6** we show the real and imaginary part of the MSD, as a function of frequency, of microparticles embedded in a Kelvin-Voigt fluid and subjected to Brownian thermal motion (2.24), as well as the results provided by the Γ-approximation (2.27). In panel (*b*), we show the percentage error of the Γ-approximation in the real and imaginary parts as well as in the absolute value. One can see that the maximum error in the absolute value is never higher than 20%, being the maximum near the "knee" region of the MSD (see **Figure 2.5**) while for most frequencies the error lies below 10%. The Γ-approximation generally

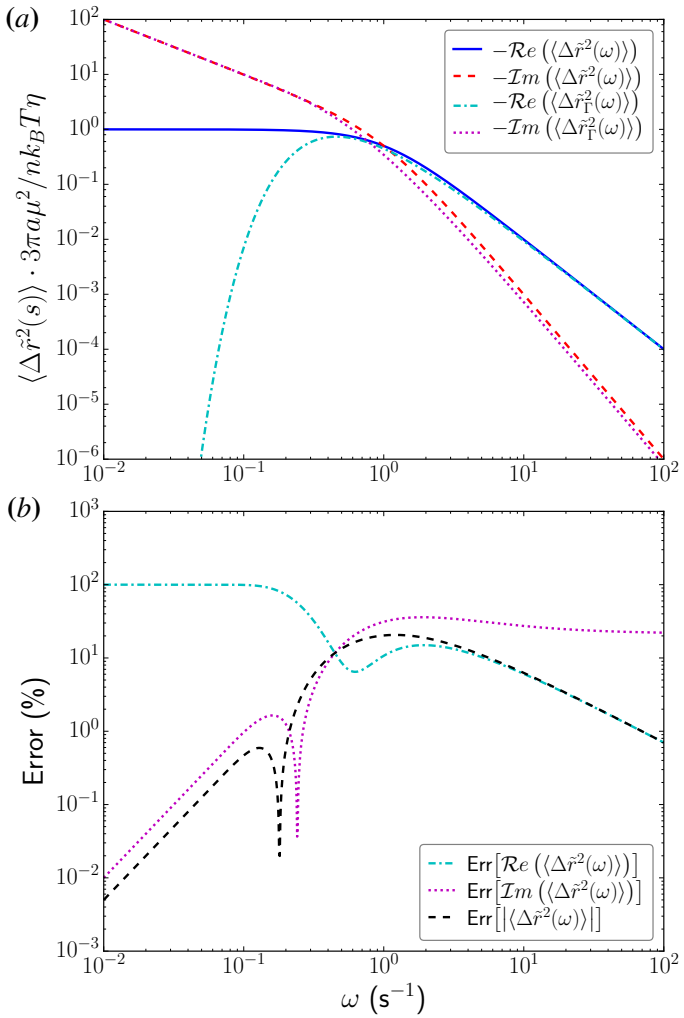

Figure 2.6: Normalized MSD and their Γ-approximation, as a function of frequency ω, of particles embedded in a Kelvin-Voigt viscoelastic fluid, with the parameter ratio $\mu/\eta = 1$, and subjected to Brownian thermal motion. (*a*) Exact real (——) and imaginary (– –) components of the MSD, and the Γ-approximation of the real (– · –) and imaginary (· · ·) parts. (*b*) Percentage error of the real (– · –) and imaginary (· · ·) parts, and the absolute value (——) of the Γ-approximation with respect to the exact value.

accurately describes, at each individual frequency, the biggest component of the MSD (the real or the imaginary parts), while failing to accurately model the smallest component. This is patent at low frequencies, where the error in the real part reaches 100% in the real component while tending towards 0% in the imaginary component. Correspondingly, at high frequencies the real part is larger than the imaginary part, and thus the error in the imaginary part is much larger.

In **Figure 2.7** we depict similar graphs for the exact shear moduli and its Γ-approximation. We can also see here that the maximum error in the absolute value of the shear modulus is 26%,

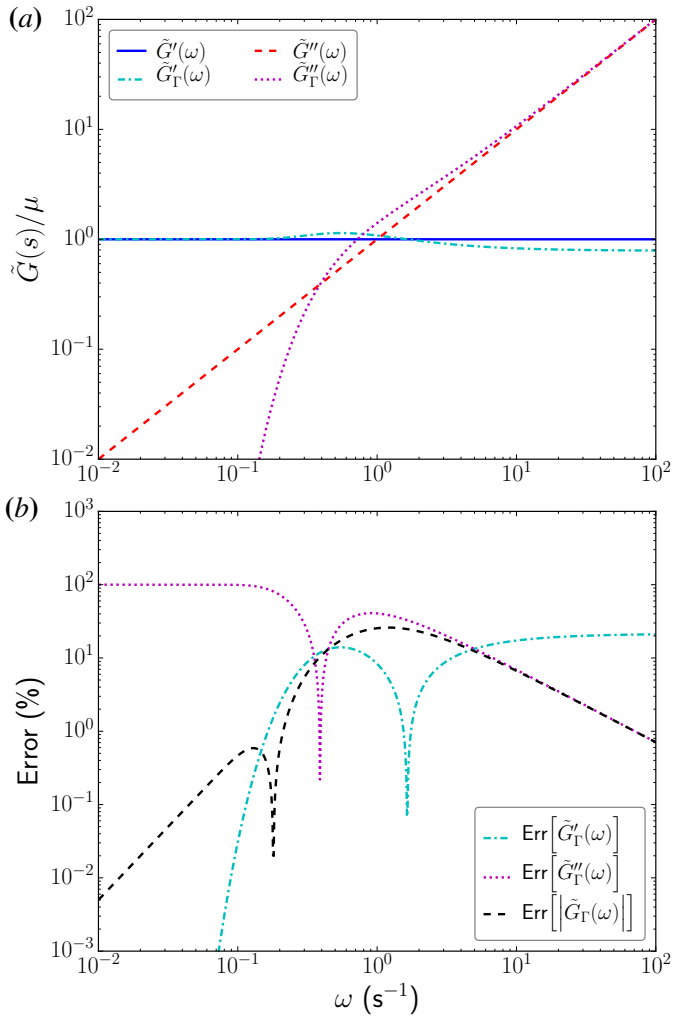

Figure 2.7: Normalized shear modulus and its Γ-approximation, as a function of frequency ω, of a Kelvin-Voigt viscoelastic fluid with the parameter ratio $\mu/\eta = 1$. (*a*) Exact storage $\tilde{G}'$ (——) and loss modulus $\tilde{G}''$ (– –), and the Γ-approximation of the real (– · –) and imaginary (· · · ·) parts. (*b*) Percentage error of the storage (– · –) and loss (· · · ·) modulus, and the absolute value (– –) of the Γ-approximation with respect to the exact value.

while the error stays below 10% for most frequencies. At low frequencies, the storage modulus is much higher than the loss modulus, *i.e.* the material behaves more like an elastic solid than a viscous fluid but the viscosity is never zero, and the error in the loss modulus tends towards 100% while the error in the loss modulus is negligible. On the other hand, at higher frequencies the loss modulus is much higher than the storage modulus, *i.e.* the material behaviour is viscous-like, the error in the storage modulus reaches a 20% plateau while the error in the loss modulus decrease with increasing frequencies.

2.2.3 Isotropic Maxwell Viscoelastic Fluids

The Maxwell model is a representation of a viscoelastic fluid which consists on a purely viscous damper, with viscosity constant η, connected in series to a purely elastic spring, with elasticity constant μ, as illustrated in **Figure 2.8**. Despite having the same individual constituents

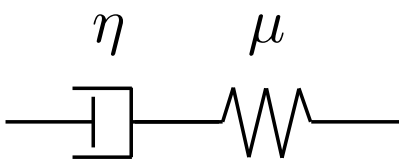

Figure 2.8: Schematic representation of the Maxwell model for viscoelastic fluids. It consists on a damper of viscosity constant η in series with a spring of elastic constant μ.

than a Kelvin-Voigt material, its mechanical characteristics are very different. The assembly presents a shear modulus

$$\tilde{G}(s) = \frac{\mu \cdot s}{s + \mu/\eta}. \tag{2.29}$$

The MSD of embedded particles subjected to thermal motion take the form, as a function of the frequency,

$$\langle \Delta\tilde{r}^2(s) \rangle = \frac{nk_BT}{3\pi a\mu} \frac{s + \mu/\eta}{s^2}, \tag{2.30}$$

whose analytic inverse Laplace transform is

$$\langle \Delta r^2(\tau) \rangle = \frac{nk_BT}{3\pi a\mu} \left(1 + \frac{\mu}{\eta}\tau\right). \tag{2.31}$$

Figure 2.9 shows the MSD, as a function of time separation, of microparticles embedded in a Maxwell viscoelastic fluid and subjected to Brownian thermal motion. The fluid is characterized by a ratio of viscoelasticity constants $\mu/\eta = 1$. By comparing with **Figure 2.5** one can see a qualitative difference in the dynamics of both models. At high frequencies $\omega \gg \frac{\mu}{\eta}$ (*i.e.* short time separations $\tau \ll \frac{\eta}{\mu}$), the MSD in a Maxwell material present a slope approaching 0, *i.e.* it

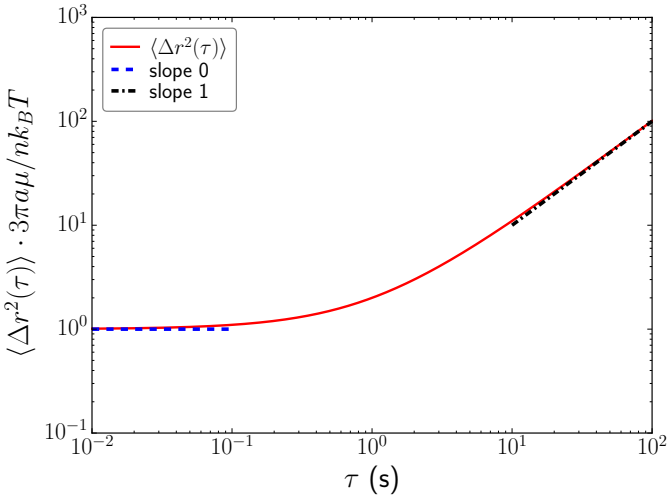

Figure 2.9: Normalized MSD, as a function of the time separation τ, of particles embedded in a Maxwell viscoelastic fluid and subjected to Brownian thermal motion (——). The slope 0 trend (– –) is plotted at low frequencies, and the slope 1 trend (– · –) at high frequencies. The material is defined by the parameter ratio $\mu/\eta = 1$.

asymptotically approaches an elastic material. On the other hand, for low frequencies $\omega \ll \frac{\mu}{\eta}$ (*i.e.* long time separations $\tau \gg \frac{\eta}{\mu}$), the slope of the MSD asymptotically go toward 1, *i.e.* it asymptotically behaves as a viscous fluid.

The logarithmic slope (2.7) of equation (2.31) and the Γ-approximation of the MSD (2.8) and shear moduli (2.9) of a Maxwell viscoelastic fluid take the form

$$\alpha(s) = \frac{\mu}{\eta}\frac{i}{s}\frac{1}{1+\frac{\mu}{\eta}\frac{i}{s}}, \tag{2.32}$$

$$\langle \Delta \tilde{r}^2_\Gamma(s) \rangle = \frac{nk_BT}{3\pi a\mu}\frac{1+\frac{\mu}{\eta}\frac{i}{s}}{s}\cdot i^{\,-\alpha(s)}\cdot\Gamma\left[1+\alpha(s)\right], \tag{2.33}$$

$$\tilde{G}_\Gamma(s) = \frac{\mu\cdot i^{\,\alpha(s)}}{\left(1+\frac{\mu}{\eta}\frac{i}{s}\right)\cdot\Gamma\left[1+\alpha(s)\right]}. \tag{2.34}$$

Panel (*a*) of **Figure 2.10** shows the real and imaginary parts of the MSD, as a function of frequency, of microparticles embedded in a Maxwell fluid and subjected to Brownian thermal motion (2.30), as well as the results provided by the Γ-approximation (2.33). Panel (*b*), shows the percentage error of the Γ-approximation in the real and imaginary parts as well as in the absolute value. We can see that the Γ-approximation yields a worse result for a Maxwell material than a Kelvin-Voigt material. The maximum error is around 26%, and the portion of the frequency

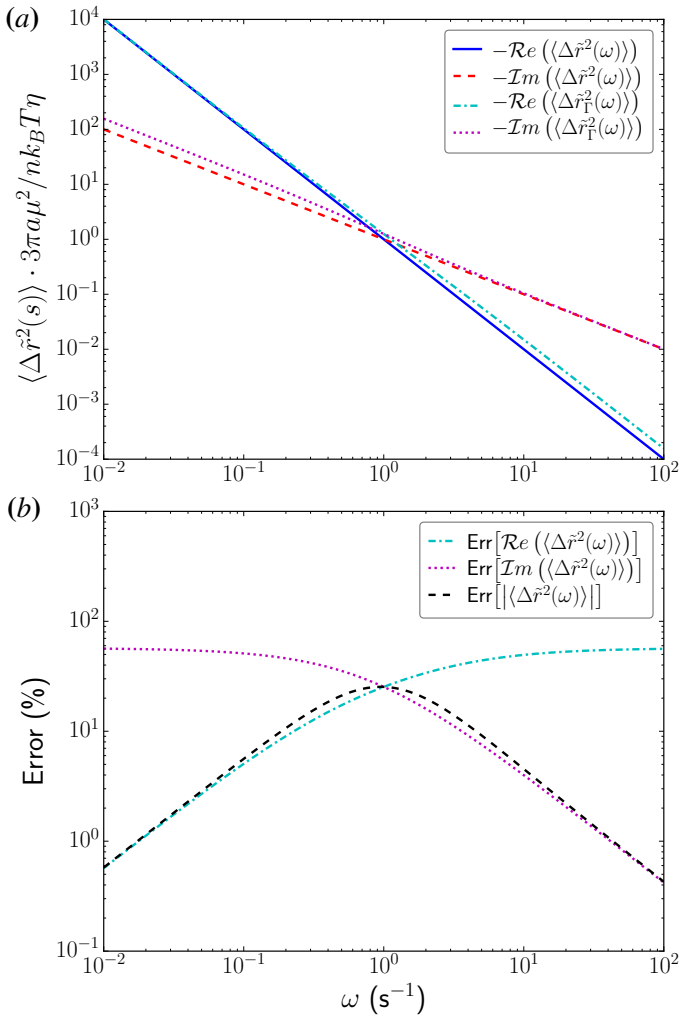

Figure 2.10: Normalized MSD and their Γ-approximation, as a function of frequency ω, of particles embedded in a Maxwell viscoelastic fluid, with the parameter ratio $\mu/\eta = 1$, and subjected to Brownian thermal motion. (*a*) Exact real (——) and imaginary (– –) components of the MSD, and the Γ-approximation of the real (– – –) and imaginary (· · · · ·) parts. (*b*) Percentage error of the real (– · – · –) and imaginary (· · · · ·) parts, and the absolute value (— —) of the Γ-approximation with respect to the exact value.

domain with errors higher than 10% is now larger. As expected, the Γ-approximation produces a better result for the biggest component of the MSD than for the smallest component. At low frequencies, the error in the imaginary part grows larger than 50% while the error in the real part falls bellow 1%. Likewise, at high frequencies the error in the real part exceeds 50% while the error in the imaginary part goes bellow 1%.

Figure 2.11 shows analogous graphs for the exact shear moduli and its Γ-approximation. The maximum error in the absolute value of the shear modulus is 20%, lower than the correspond-

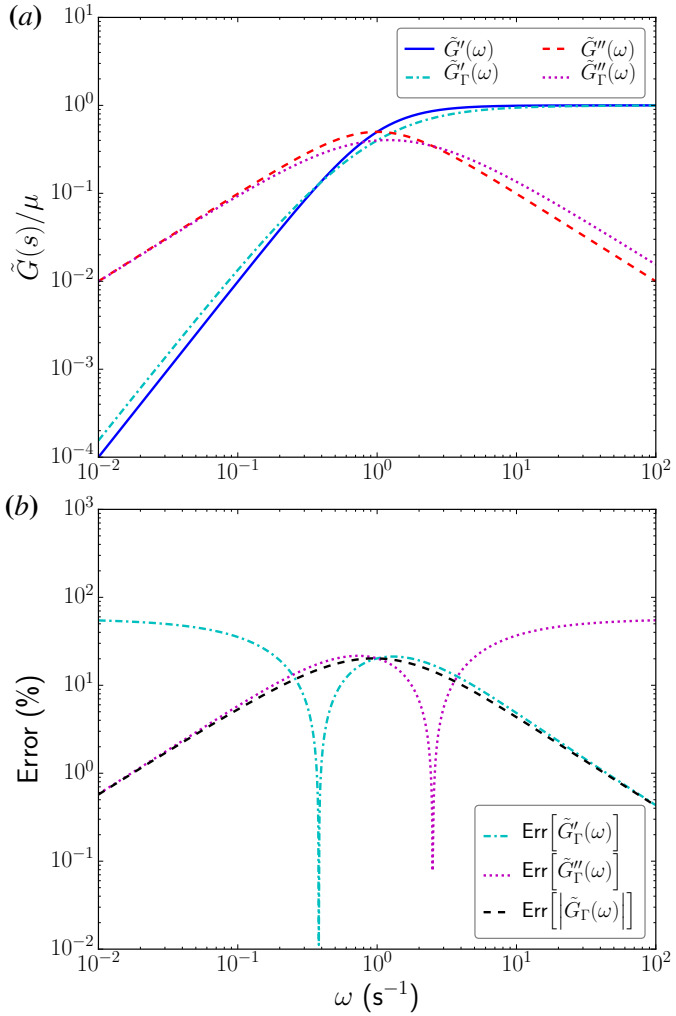

Figure 2.11: Normalized shear modulus and its Γ-approximation, as a function of frequency ω, of a Maxwell viscoelastic fluid with the parameter ratio $\mu/\eta = 1$. (*a*) Exact storage $\tilde{G}'$ (——) and loss modulus (– –), and the Γ-approximation of the real (– · –) and imaginary (· · · · ·) parts. (*b*) Percentage error of the storage (– · –) and loss (· · · · ·) modulus, and the absolute value (– –) of the Γ-approximation with respect to the exact value.

ing value of a Kelvin-Voigt material, while the portion of the frequency domain with errors below 10% is wider. The storage modulus at low frequencies is much smaller than the loss modulus, and the error in the former goes above 50% while the error in the later falls bellow 1%. On the other hand, for high frequencies the loss modulus is larger than the storage modulus, and thus the error in the real part exceeds 50% while the error in the imaginary part goes under 1%.

2.3 The Power-Exp-Approximation to the Laplace Transform

In the preceding sections we showed that, despite being an useful tool for purely viscous and purely elastic materials, the Γ-approximation renders high qualitative and quantitative errors when applied to viscoelastic fluids. Consequently, here we propose a more accurate approximation to the Laplace transform of experimental data. Our approach has the advantage of being global, not local, whilst not requiring the evaluation of numerical integrals.

Here, we propose to perform a least square fit of the experimentally measured $\langle \Delta r^2(\tau) \rangle$ to a series of power-exponential functions

$$\langle \Delta r^2(\tau) \rangle \approx \sum_j A_j \cdot \tau^{B_j} \cdot e^{-C_j \cdot \tau}, \tag{2.35}$$

where A_j, B_j and C_j are free parameters. This approach has the advantage of being global, *i.e.* the fit describes the whole τ domain, and the choice of functions present a known exact analytical Laplace transform

$$\langle \Delta \tilde{r}^2(s) \rangle \approx \sum_j A_j \cdot \frac{\Gamma[B_j+1]}{[s+C_j]^{B_j+1}}, \tag{2.36}$$

that is valid for $B_j > -1$. An interesting feature of this method is that we can constrain the fitted constants by making use of known physical information about the system, such as restricting the slope of the MSD between 0 and 1. For simple fluids, the fit will be accurate with one or two terms, while for materials with complex rheology, we can start the fit with two parameters and iteratively increase their number in order to achieve a better approximation in the whole domain. Unless otherwise stated, all the fits shown in this chapter were performed with exactly two terms, *i.e.* six parameters A_0, A_1, B_0, B_1, C_0 and C_1.

In the following sections, we will assess the accuracy of the power-exponential fit, and compare it to the results provided by the Γ-approach. We will consider a purely viscous, a purely elastic, a Kelvin-Voigt and a Maxwell viscoelastic fluids. We fit their MSD to equation (2.35) by using the general purpose Least-Square fit algorithm provided by SciPy [67], use the

calculated coefficients to calculate the Laplace transform of the MSD (2.36), and finally apply the GSER (1.17) to calculate the material's shear moduli.

2.3.1 Isotropic Viscous and Elastic Materials

In **§2.2.1** we introduced the isotropic viscous and elastic materials, we provided the form of their shear moduli (equations 2.17 and 2.20), and the MSD of embedded microparticles subjected to Brownian thermal motion in the time domain (equations 2.19 and 2.22) and in the frequency domain (equations 2.18 and 2.21). We also justified that the Γ-approximation provides exact results for these types of materials. In this section, we illustrate the use of the Power-Exp approach, analyze the obtained results and compare them with the Γ-approach, finding a virtually equivalent accuracy for purely viscous and elastic materials.

In **Figure 2.12** we show the normalized MSD, as a function of time separation τ, of microparticles subjected to Brownian thermal motion and embedded in a purely viscous fluid (panel *a*) and in a purely elastic material (panel *c*), together with their Power-Exp approximation. In panels (*b*) and (*d*) we report the percentage error of the approximation. We can see that the Power-Exp approximation provides very low numerical errors, and the results for simple viscous and elastic materials are highly accurate. Even though these are reasonable errors for most applications, the accuracy of the fit can be further increased by optimizing the fitting algorithm. As important as the local value of the MSD is their local slope, since the slope greatly affects their Laplace transform. In **Figure 2.13** we show the exact MSD in Laplace space, and the predictions given by the Γ-approach and the Power-Exp fit, together with the percentage error of the later. The Γ-approach provides exact results for these simple materials, while the Power-Exp fit provides similarly good results, with maximum errors of around $10^{-2}\%$, that, as we stated before, could even be reduced with a better optimization of the fit algorithm.

In **Figure 2.14** we plot the exact shear moduli of a viscous fluid (panel *a*) and an elastic material (panel *c*) and the values provided by the Γ-approximation and the Power-Exp fit. In panels (*b*) and (*c*), we show the error of the Power-Exp approximation. As with the MSD, the Γ-approach privies exact values for the shear moduli of purely viscous and purely elastic materials.

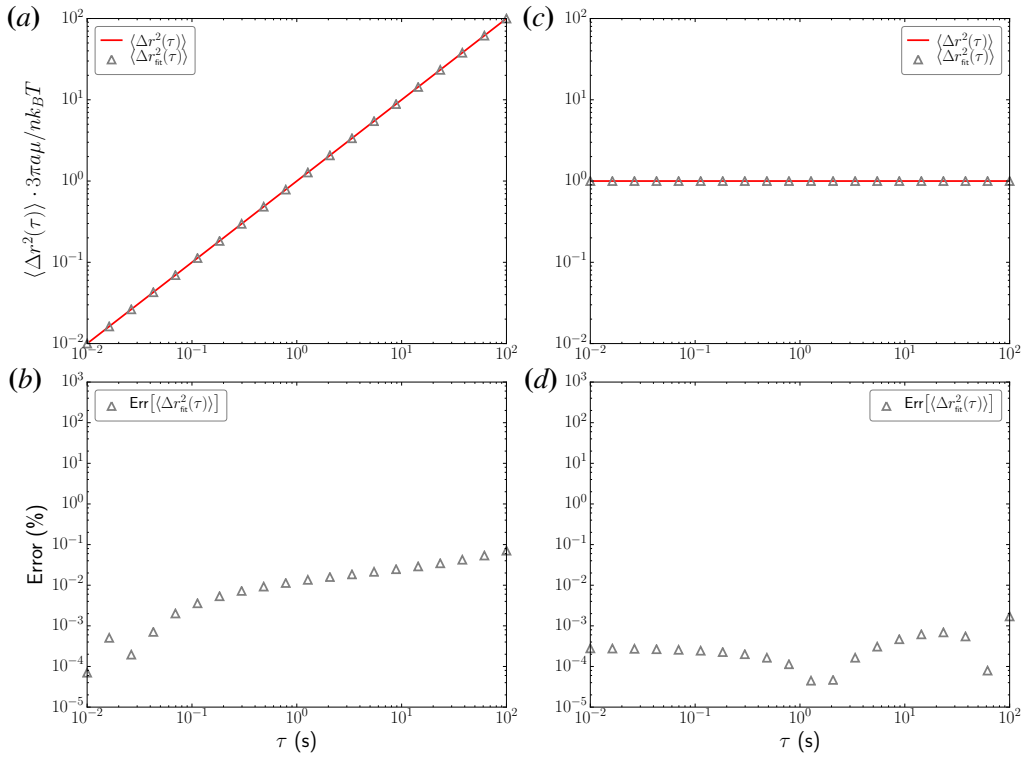

Figure 2.12: Normalized MSD and their Power-Exp approximation, as a function of the time separation τ, of microparticles subjected to Brownian thermal motion and embedded in purely viscous (*a*) and elastic (*c*) materials. Lines: exact values (—). Symbols: Power-Exp approximation (Δ). Percentage error of the Power-Exp approximation (Δ) when applied to purely viscous (*b*) and elastic (*d*) materials.

On the other hand, the Power-Exp approximation provides a very accurate approximation.

In this section, we have seen that the Power-Exp approximation, when applied to purely viscous and purely elastic materials, provides results that are virtually as accurate as the Γ-approximation. In the next section we will analyze how the two approximations compare for more complex viscoelastic materials.

2.3.2 Isotropic Kelvin-Voigt and Maxwell Viscoelastic Fluids

Isotropic Kelvin-Voigt and Maxwell viscoelastic fluids were described in **§2.2.2** and **§2.2.3**. The form of their shear moduli was given in equations (2.23) and (2.29), the MSD of embedded microparticles subjected to Brownian thermal motion were described, in the time domain, by equations (2.25) and (2.31), and in the frequency domain by equations (2.24) and (2.30). The Γ-approximation to the MSD and shear modulus was also assessed, finding varying

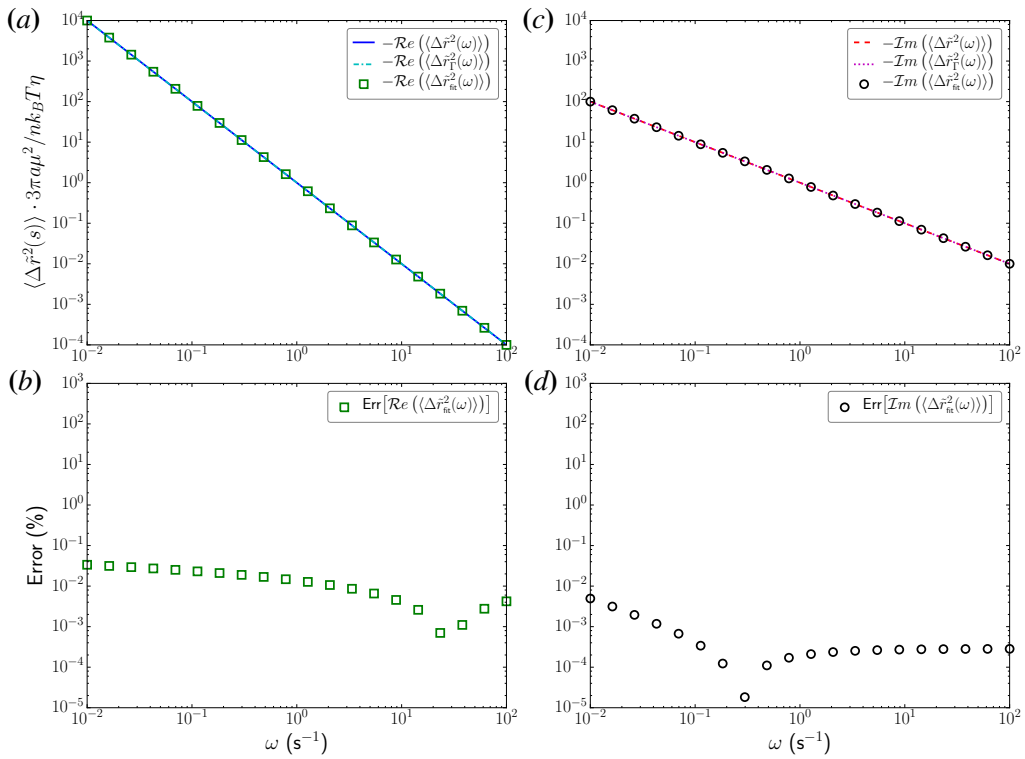

Figure 2.13: Normalized MSD and their Γ and Power-Exp approximations, as a function of frequency ω, of microparticles subjected to Brownian thermal motion and embedded in purely viscous (*a*) and elastic (*c*) materials. Lines: exact values of the real (——) and imaginary (– –) parts, real (– · –) and imaginary (· · · · ·) parts of the Γ-approximation. Symbols: real (□) and imaginary (○) parts of the Power-Exp approximation. Percentage error of the real (□) and imaginary (○) parts of the Power-Exp approximation when applied to purely viscous (*b*) and elastic (*d*) materials.

errors depending the relative values of the storage and loss moduli. In this section, we apply the Power-Exp approximation, we compare it with the Γ-approach, and we find consistently more accurate results with our proposed method.

In **Figure 2.15** we show the normalized MSD, as a function of time separation τ, of microparticles subjected to Brownian thermal motion and embedded in a Kelvin-Voigt (panel *a*) and Maxwell (panel *c*) viscoelastic fluid, together with their Power-Exp approximation. In panels (*b*) and (*d*) we report the percentage error of the Power-Exp approximation. It can be seen that the numerical errors of the Power-Exp approach are very low, and thus, it can be used to accurately fit the MSD in Kelvin-Voigt and Maxwell viscoelastic fluids.

In **Figure 2.16** we show the exact MSD in Laplace space, and the predictions given by the Γ-approach and the Power-Exp fit, together with the percentage error of the later. As

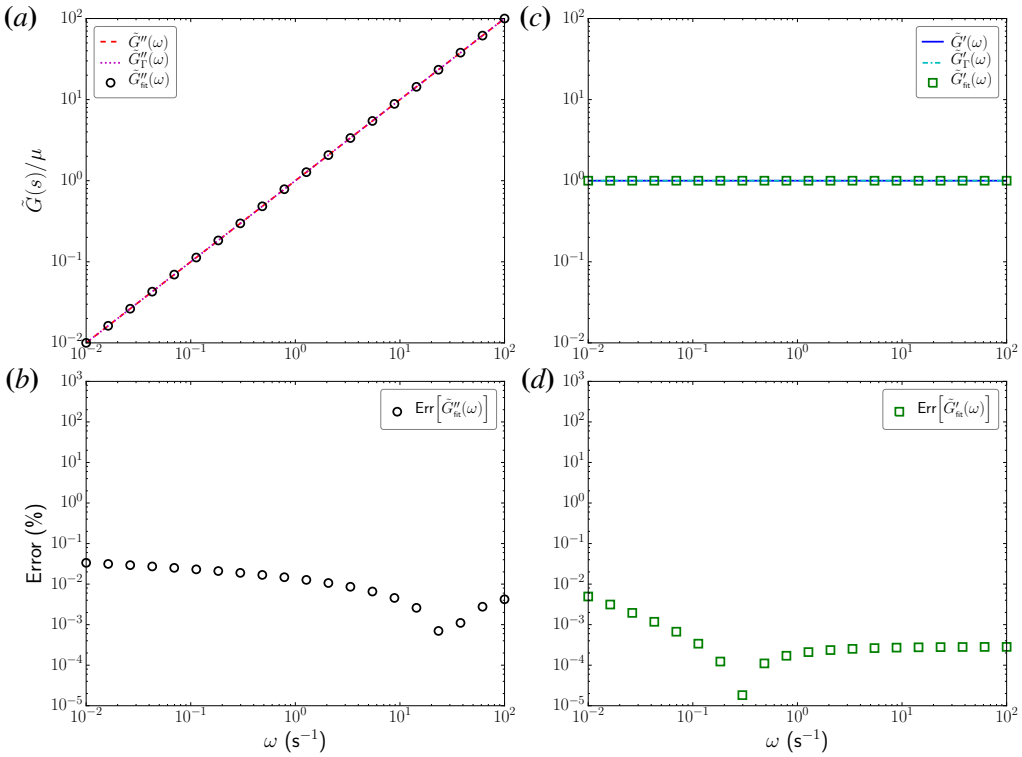

Figure 2.14: Normalized shear moduli and their Γ and Power-Exp approximations, as a function of frequency ω, of purely viscous (*a*) and elastic (*c*) materials. Lines: exact values of the storage $\tilde{G}'$ (——) and loss $\tilde{G}''$ (– – –) moduli, real (– · –) and imaginary (· · · · ·) parts of the Γ-approximation. Symbols: storage (□) and loss (○) moduli provided by the Power-Exp approximation. Percentage error of the real (□) and imaginary (○) parts of the Power-Exp approximation when applied to purely viscous (*b*) and elastic (*d*) materials.

explained in **§2.2.2** and **§2.2.3**, the Γ-approximation provides fairly accurate results in the largest component of the MSD, either the real or the imaginary part, and a very poor approximation for the smallest, reaching errors of around 100%. In contrast, the Power-Exp approximation provides a consistently more accurate approximation, with a maximum error of around 1% at the lowest frequencies, and errors of around or less than 10^{-2}% for most other frequencies.

In **Figure 2.17** we depict the exact shear moduli of a Kelvin-Voigt (panel *a*) and a Maxwell viscoelastic fluid (panel *c*) and the values provided by the Γ-approximation and the Power-Exp fit. In panels (*b*) and (*c*), we show the error of the Power-Exp approximation. Much like with the MSD, the Γ-approximation provides a much better fit for the largest storage or loss modulus, and a poor fit for the smallest. On the other hand, the Power-Exp fit render consistently more accurate results, with errors typically much lower than 1%.

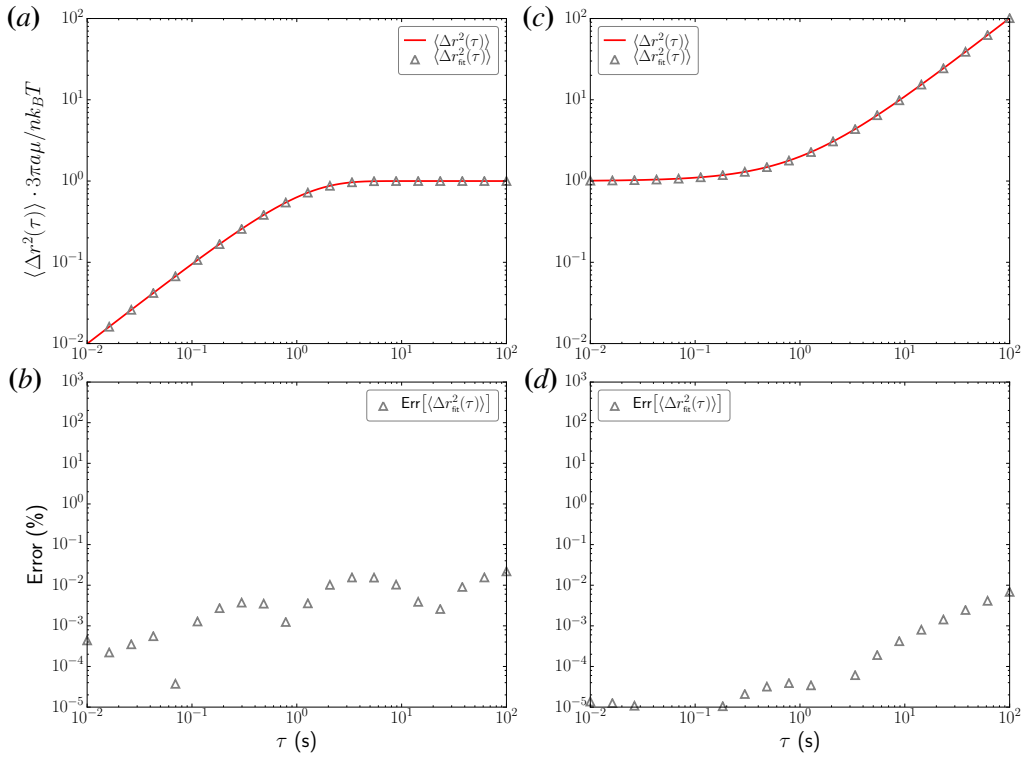

Figure 2.15: Normalized MSD and their Power-Exp approximation, as a function of the time separation τ, of microparticles subjected to Brownian thermal motion and embedded in a Kelvin-Voigt (*a*) and Maxwell (*c*) viscoelastic fluid. Lines: exact values (—). Symbols: Power-Exp approximation (△). Percentage error of the Power-Exp approximation (△) when applied to Kelvin-Voigt (*b*) and Maxwell (*d*) viscoelastic fluids.

In summary, in this section we have shown that, for typical viscoelastic fluids, the Power-Exp approximation performs exceptionally well, even at the frequencies where the Γ-approach breaks, and not performing worse, at any frequency, than the later. Furthermore, the Power-Exp approach inherently has the needed flexibility to accurately fit viscoelastic fluids that are more complex than the ones shown in this chapter.

2.4 Conclusions

Due to the nature of the PTM experiments, the measured MSD are acquired in the time domain, but the calculated quantity of interest, the shear modulus, needs to be prescribed in the frequency domain. Consequently, a key step to connect those quantities is to accurately perform a numerical Fourier or Laplace transform of the experimental data. Several approaches have

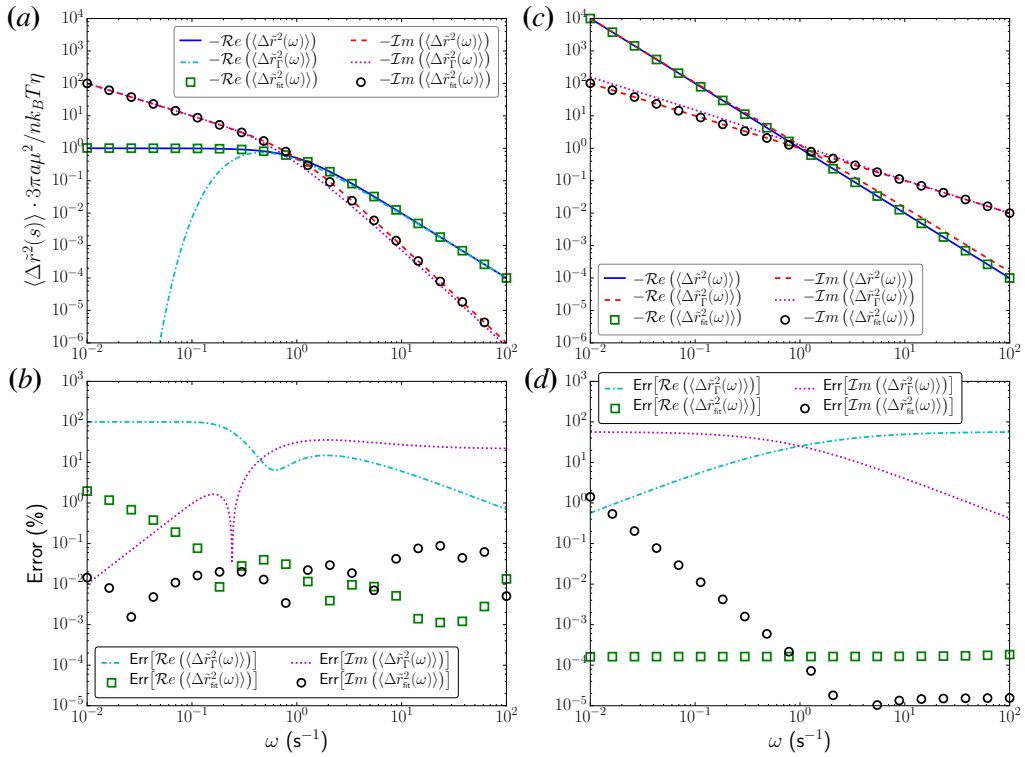

Figure 2.16: Normalized MSD and their Γ and Power-Exp approximations, as a function of frequency ω, of microparticles subjected to Brownian thermal motion and embedded in a Kelvin-Voigt (*a*) and Maxwell (*c*) viscoelastic fluid. Lines: exact values of the real (▬) and imaginary (▬ ▬) parts, real (▬ · ▬) and imaginary (▪ ▪ ▪) parts of the Γ-approximation. Symbols: real (□) and imaginary (○) parts of the Power-Exp approximation. Percentage error of the real (□) and imaginary (○) parts of the Power-Exp approximation when applied to Kelvin-Voigt (*b*) and Maxwell (*d*) viscoelastic fluids.

been proposed in the literature, such as a numerically performing the Laplace transform integral, the use of an FFT routine, and the *de facto* standard in microrheology analysis, the Γ-approach. In this chapter, we have studied the accuracy of the later, finding that it is highly accurate for simple viscous and elastic materials, while introducing high quantitative and qualitative errors for complex viscoelastic fluids. As a consequence, we proposed a new method, based on globally fitting the measured MSD to a series of power-exponential functions, that have a known analytical Laplace transform. We have studied the accuracy of this approximation, providing some examples of application. We have found that, for purely viscous and elastic materials, as well as for complex Kelvin-Voigt and Maxwell viscoelastic fluids, the Power-Exp approximation provides consistently highly accurate results, shaping up as a powerful tool in microrheology analysis. Throughout this chapter, all of the presented examples were fitted by keeping only two terms in the Power-Exp

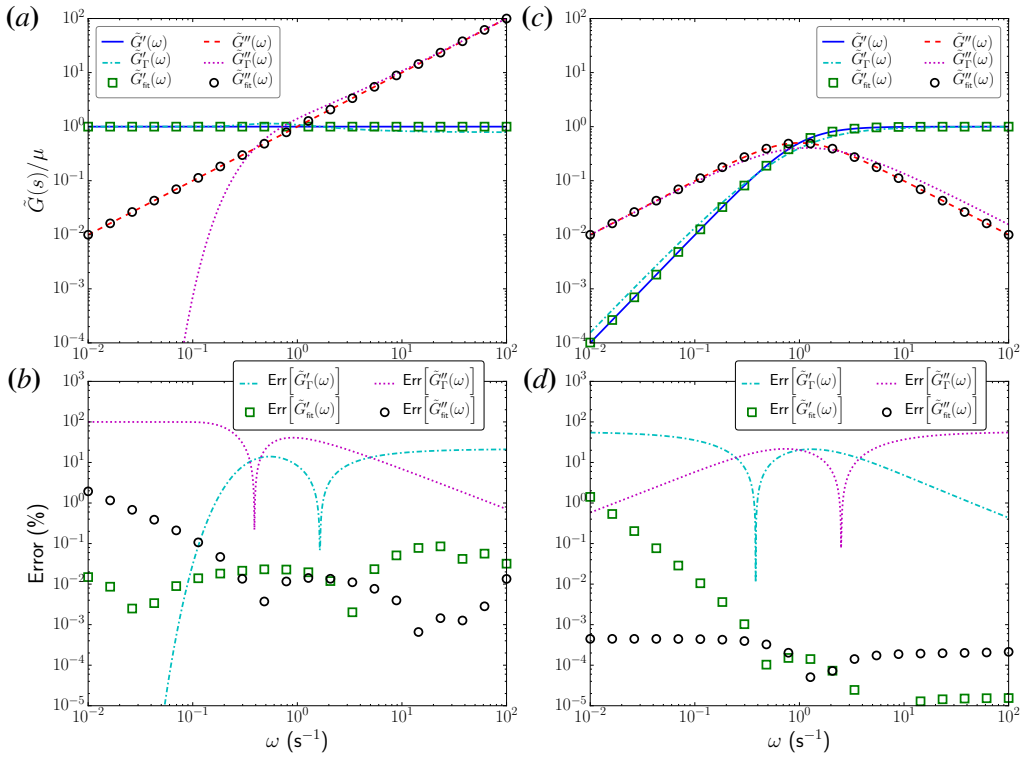

Figure 2.17: Normalized shear moduli and their Γ and Power-Exp approximations, as a function of frequency ω, of Kelvin-Voigt (*a*) and Maxwell (*c*) viscoelastic fluids. Lines: exact values of the storage $\tilde{G}'$ (—) and loss $\tilde{G}''$ (– –) moduli, real (– · –) and imaginary (· · ·) parts of the Γ-approximation. Symbols: storage (□) and loss (○) moduli provided by the Power-Exp approximation. Percentage error of the real (□) and imaginary (○) parts of the Power-Exp approximation when applied to purely Kelvin-Voigt (*b*) and Maxwell (*d*) viscoelastic fluids.

series. This allowed for reduced complexity in the calculation of the fit. However, due to the great flexibility of this tool, one can fit more complex fluids by keeping as many terms in the series as needed to reach the desired accuracy.

Chapter 2 is currently being prepared for publication under the provisional title "On the Laplace transform of Particle Tracking measurements into Microrheology data", by M. Gómez-González and J. C. del Álamo. The dissertation author is the primary investigator in this publication.

Chapter 3

Flow of a Viscous Nematic Fluid Around a Sphere

3.1 Introduction

Nematic fluids exhibit molecular or supramolecular alignment along a director vector field, leading to anisotropic rheology. These fluids often appear in industrial applications and in biology. For instance, nematic liquid crystals are a key component in a vast variety of displays for their high resolution and energy efficiency. The interaction between flow, topological defects and nematic orientation in liquid crystals are exploited in particle self-assembly [123, 93] and sensing applications [12]. Anisotropic rheology is also observed in reconstituted gels when the polymer phase is aligned [57, 58] and, perhaps more importantly, the cytoplasm of animal cells is far from being isotropic. The filaments that make up the cytoskeleton can experience spatial order and alignment both at the level of the mesh size ($\sim$ 10 nm) and of the whole cell ($\sim$ 10 μm), leading to short- and long-range directionality [95]. Intracellular rheology has been proposed to modulate important cell functions such as mechanotransduction, [20, 153, 17], cell migration [75, 122, 161] and intracellular organelle transport [79, 85, 109]. Recent studies suggest that intracellular anisotropy may play an important role in controlling the directionality

of these cellular processes [130, 126, 34]. In short, anisotropy is purpose.

Particle Tracking Microrheology (PTM) determines the viscoelastic shear modulus of a medium from the measured motion of embedded microparticles [102, 103, 101]. This technique is particularly suitable for probing minute quantities of biological materials, including live cells [147, 29, 34]. In active PTM, the motion of the probing particle is forced with magnetic or laser tweezers, whereas in passive PTM this motion is caused by the thermal excitation of the medium. These two approaches estimate the complex response function $\tilde{\zeta}(s)$ that relates the drag force experienced by the probing particle and the particle velocity as $\tilde{\mathbf{f}}(s) = \tilde{\zeta}(s)\tilde{\mathbf{v}}(s)$, where $\tilde{\cdot}$ indicates Laplace transform and s is the Laplace frequency. A crucial step in both active and passive PTM is to connect the measured response function to the underlying rheological properties of the medium, which is usually accomplished by assuming that the particle experiences a generalized Stokes's resistance. For a sphere of radius a moving in a single-phase no-slip isotropic continuum, the response function is modeled as $\tilde{\zeta}(s) = 6\pi a\tilde{\eta}(s)$ [102, 138], where $\tilde{\eta}(s)$ is the frequency dependent viscosity of the medium.

The application of the generalized Stokes's law in complex biomaterials (e.g. gels) is complicated by their multiphase nature as well as by interactions between the material and the probing particle. For instance, the Stokes's flow assumption can break down in live cells when tracking endogenous particles that are anchored to the cytoskeleton [90]. Furthermore, the mobility of injected microspheres has been reported to vary dramatically depending on their surface charge [147]. Chemical interactions, polymer depletion near the microsphere and network compressibility can also introduce substantial deviations from Stokes's flow [136, 105, 149, 53].

Theoretical studies have analyzed the effect of both network compressibility and slip between the probing particle and the material in two-fluid gels composed by a polymer network viscously coupled to a solvent [87, 48]. These studies have provided frequency-dependent corrections to the generalized Stokes's law that can be used to better interpret PTM experiments. The introduction of two-point PTM [30, 88] has allowed investigators to account for most non-Stokesian effects in the vicinity of the probing particle by cross-correlating the motion between pairs of distant probing particles.

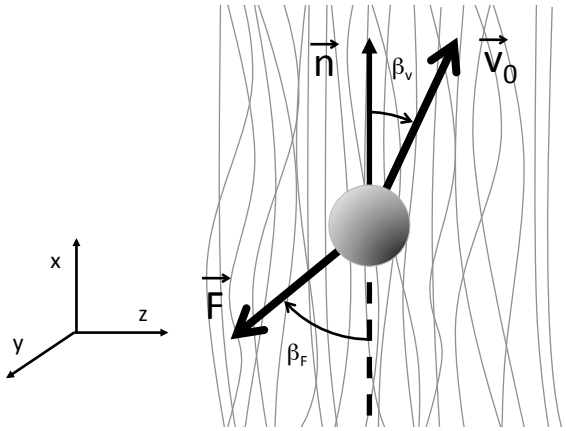

Figure 3.1: We consider an orthotropic gel with constant and homogeneous nematic. The motion of the sphere is assumed to not alter the nematic.

Despite these advances, little is known about the effect of anisotropy in the response function of a microrheology probe. This lack of knowledge affects both the active and passive modalities of PTM, as well as both single-particle and two-particle microrheology. Previous studies have provided directional diffusivity coefficients (effective viscosities) of microrheological probes in nematic fluids, $\eta_{\parallel}^{\text{eff}}$ and $\eta_{\perp}^{\text{eff}}$, where $\parallel$ and $\perp$ denote, respectively, the directions parallel and perpendicular to the nematic director. Although these measurements provide useful information about anisotropic diffusion processes, it is not clear how to relate $\eta_{\parallel/\perp}^{\text{eff}}$ with the directional viscosities of anisotropic fluids because the Stokes's formula is not applicable in this case.

In this chapter, we address the limitations of PTM in anisotropic fluids by calculating an analytical expression for the response function of a microsphere moving through an orthotropic two-fluid gel. In **§3.2**, we formulate the mathematical problem under the assumptions that the director remains constant and is not altered by the motion of the sphere (see **Figure 3.1**) and that there is strong viscous coupling between the network phase and the liquid phase. The anisotropy of the medium is modeled through the Leslie-Ericksen constitutive equations [41, 86]. Interestingly, the resulting flow equations are also valid for the case of a nematic fluid with high bending elastance and free of defects, thereby conferring a broader reach to the results of this theoretical study.

The Green's function of the problem is obtained in **§3.3** and is used in **§3.4** to determine an explicit analytical expression for the anisotropic response function that depends on up to four

viscosity coefficients. This solution is compared with numerical solutions that have previously been obtained for particular combinations of the viscosity coefficients [63], obtaining excellent agreement. We find that the anisotropy of the Leslie-Ericksen constitutive relation affects the response function through two independent mechanisms. One is the anisotropy in the stress-strain relationship and the other is the bending of the fluid with respect to the nematic director. These mechanisms are studied in isolation by considering rotationally pseudo-isotropic fluids in which the bending stresses are zero, and strain pseudo-isotropic fluids in which the stress-strain relation is isotropic.

Analysis of our results and experimental data from nematic biopolymer networks in **§3.5** reveals that the application of Stokes's drag law can lead to errors of orders of magnitude in PTM measurements even for moderate levels of anisotropy. **§3.6** illustrates the effect of anisotropy on the flow velocity field showing that, in some cases, it leads to streamline patterns that challenge our intuition about creeping flow.

3.2 Problem Formulation

This section introduces the equations to be solved in subsequent sections. We start by considering a two-fluid gel formed by a dilute polymer network that is permeated by a liquid. We illustrate the possible sources of anisotropy in this model before performing a number of simplifying assumptions that hold under the conditions of a live-cell PTM experiment. The simplified equations are still of general scope, as they also describe the flow in other anisotropic fluids such as nematic liquid crystals. We conclude the section by providing a physical interpretation of the different viscosity terms appearing in the flow equations.

As mentioned above, we consider a two-fluid gel composed of a polymer network viscously coupled to a solvent similar to previous PTM studies [87, 88, 48]. The viscoelastic network is characterized by its displacement field $\vec{u}$, and the viscous solvent by its velocity field $\vec{v}$. We assume that the network is dilute as the polymer network fraction ϕ in the eukaryotic cytoskeleton is very small [$\phi \sim 0.01 - 0.02$, see 143]. For a dilute network, the two-fluid equations

take the form

$$\rho\ddot{\vec{u}} - \nabla\cdot\bar{\bar{\tau}}_N = -\bar{\bar{\Gamma}}\cdot(\dot{\vec{u}} - \vec{v}) + \vec{f}_u, \tag{3.1}$$

$$\rho_F\dot{\vec{v}} - \eta\nabla^2\vec{v} + \nabla p = \bar{\bar{\Gamma}}\cdot(\dot{\vec{u}} - \vec{v}) + \vec{f}_v, \tag{3.2}$$

$$\nabla\cdot\vec{v} = 0, \tag{3.3}$$

where $\bar{\bar{\tau}}_N$ is the Cauchy stress tensor in the network, $\bar{\bar{\Gamma}}$ is a tensor that represents the viscous coupling between the network and the solvent and $\vec{f}_u$ and $\vec{f}_v$ model the stresses caused by the sphere on the gel.

The directional order in the network may cause anisotropic dynamics not only through constitutive equations of the polymer but also through the viscous coupling between the polymer and the solvent, even if the solvent is isotropic. For instance, if we idealise the polymer phase in a nematic network as a square array of circular cylinders, then the coupling tensor is defined by the two coefficients

$$\Gamma_{\parallel} = \frac{\pi\eta}{\xi^2\log(A/\phi)}, \tag{3.4}$$

$$\Gamma_{\perp} = \frac{2\pi\eta}{\xi^2\log(A/\phi)}, \tag{3.5}$$

where ξ is the distance between neighbouring filaments and A is a non-dimensional shape factor that takes the value $A \approx 0.23$ under dilute conditions [$\phi < 0.02$, see 151]. Note that, in this case, the viscous coupling is weaker in the nematic direction than in the perpendicular directions by a factor of two.

An order-of-magnitude analysis of equation (3.2) after eliminating the pressure indicates that viscous coupling is dominant for $(k\xi)^2 \ll 1$ and $s\xi^2\rho_F/\eta \ll 1$, where k and s are respectively a characteristic wavenumber and frequency. These conditions are often met in live cell cytoplasmic microrheology, where the network (cytoskeleton) mesh size is $\xi \sim 0.02$ μm, and the density and viscosity of the cytosol (the solvent) are approximately equal to those of water [96, 95]. Using the inverse radius of the probing particle $1/a$ as an upper bound to k, the strong coupling limit is

found for $a \gg \xi \sim 0.02$ μm and $s \ll 10^4$ s^{-1}. In the forthcoming analysis, we assume that these conditions hold so that $\dot{\vec{u}} = \vec{v}$, and equations (3.1) and (3.2) combine into

$$\rho\dot{\vec{v}} - \nabla \cdot \bar{\bar{\tau}} = \vec{f}, \tag{3.6}$$

where $\bar{\bar{\tau}}$ is prescribed, as a function of $\vec{v}$, by the constitutive relations for the strongly coupled two-fluid gel. Interestingly, this simplification makes the flow equations applicable to single-phase fluids such as nematic liquid crystals as well. Note that, due to the strong coupling and the incompressibility of the solvent (3.3), the network motion in this model is also divergence-free, even if the network is compressible.

Equation 4.1 is completed with the Leslie-Ericksen constitutive relation, which is generally used for anisotropic fluids with nematic order [41, 86, 33],

$$\tau_{ij} = -p\delta_{ij} + \alpha_1 n_k n_p \varepsilon_{kp} n_i n_j + \alpha_2 n_i N_j + \alpha_3 n_j N_i + \alpha_4 \varepsilon_{ij} + \alpha_5 n_i n_k \varepsilon_{kj} + \alpha_6 n_j n_k \varepsilon_{ki}. \tag{3.7}$$

This constitutive relation depends on the six Leslie viscosity coefficients, α_i. It relates the stress tensor τ_{ij} with the strain rate tensor $\varepsilon_{ij} = (v_{i,j} + v_{j,i})/2$, the director n_i and the rate of change of the director with respect to the background fluid. The latter is written as

$$\vec{N} = \partial_t \vec{n} + (\vec{v} \cdot \nabla)\vec{n} - (\nabla \wedge \vec{v}) \wedge \vec{n}/2, \tag{3.8}$$

where the first two terms represent the substantial derivative of $\vec{n}$ and the third one represents the rotation of the fluid with respect to $\vec{n}$.

In general, the director field $\vec{n}$ can be obtained by imposing the elastic and viscous torques to be in equilibrium. For simplicity, however, we assume that the viscous torque is much smaller than the elastic one, so that the director remains uniform and constant throughout the fluid and $\vec{N} = -(\nabla \wedge \vec{v}) \wedge \vec{n}/2$. This assumption is known as the small Ericksen number limit [140] and is likely reasonable to model passive PTM experiments, where the thermal energy driving the motion, $k_B T$, is extremely low and not expected to alter the nematic configuration. We further

assume that the Reynolds number, $Re = \rho U a/\alpha_4$, is very small. Typical parameter values in PTM are $\rho \sim 10^3\,\mathrm{kg\,m^{-3}}$, $U \sim 10^{-6}\,\mathrm{m\,s^{-1}}$, $a \sim 10^{-6}\,\mathrm{m}$, $\alpha_4 \sim 10^{-3}\,\mathrm{Pa\,s^{-1}}$ and $Re \sim 10^{-6}$, so the low-Reynolds-number simplification is reasonable in this problem. These simplifications make the resulting equations analogous to those describing the dynamics of nematic visco-elastomers [141] when only the viscous terms are retained in the latter.

It is possible to reduce the number of independent viscosity coefficients from the six that appear in the Leslie-Ericksen constitutive equation (3.7) to four by introducing the Miesowicz coefficients [107],

$$\eta_a = \alpha_4/2, \tag{3.9}$$

$$\eta_b = (\alpha_3 + \alpha_4 + \alpha_6)/2, \tag{3.10}$$

$$\eta_c = (-\alpha_2 + \alpha_4 + \alpha_5)/2, \tag{3.11}$$

and by using Parodi's relation [119],

$$\alpha_6 = \alpha_2 + \alpha_3 + \alpha_5. \tag{3.12}$$

Under these simplifications and, using a Cartesian coordinate system in which $\vec{n} = (1,0,0)$, the momentum balance equation (4.1) can be written as

$$\partial_x p' = \eta_b \nabla^2 u + \alpha_1 \partial_{xx} u + f_x, \tag{3.13}$$

$$\partial_y p' = \eta_a \nabla^2 v + (\eta_c - \eta_a)\partial_x \omega_z + f_y, \tag{3.14}$$

$$\partial_z p' = \eta_a \nabla^2 w - (\eta_c - \eta_a)\partial_x \omega_y + f_z, \tag{3.15}$$

where $\vec{r} = (x,y,z)$ is the position vector, $\vec{v} = (u,v,w)$ is the velocity vector, $\vec{\omega} = (\omega_x, \omega_y, \omega_z)$ is the vorticity vector and $p' = p - \alpha_5 \partial_x u$ is a modified pressure. This form of the momentum balance equations is not the most suitable one to solve for the flow around a sphere, but it is included here to facilitate the physical interpretation of the Miesowicz viscosity coefficients. The

equations suggest that the two first Miesowicz coefficients, η_a and η_b, govern the diffusion of the momentum components perpendicular ($\perp$) and parallel ($||$) to $\vec{n}$, respectively. In particular, η_a is equivalent to the viscosity in an isotropic fluid and the difference $\eta_b - \eta_a$ indicates the level of anisotropy in the stress-strain relation due to the nematic order of the fluid. Apart from the momentum diffusion Laplacians, equations (3.13)-(3.15) have contributions from $||$-derivatives of the vorticity. These terms represent bending of the fluid with respect to the nematic and are proportional to $\eta_c - \eta_a$. This second source of anisotropy is perhaps less intuitive than the anisotropy of the stress-strain relation but it can modify significantly the response function of a sphere, as shown in **§3.4**.

Taking the curl of equations (3.13)-(3.15) yields the vorticity equation,

$$\left[\eta_a \nabla^2 + (\eta_c - \eta_a)\partial_{xx}\right] \vec{\omega} + \left[(\eta_b - \eta_a)\nabla^2 + \alpha_1 \partial_{xx}\right] \{\nabla \wedge [(\vec{u}\cdot\vec{n})\vec{n}]\} = \vec{0}, \tag{3.16}$$

which is analogous to Laplace's vorticity equation for an isotropic, low-*Re* flow, and where terms in addition to $\nabla^2\vec{\omega}$ clearly show the two anisotropy mechanisms mentioned above: the anisotropy in the stress-strain relationship, which is proportional to $\eta_b - \eta_a$, and the bending resistance of the fluid, which is proportional to $\eta_c - \eta_a$. Unfortunately, the physical interpretation of α_1 appears to be less clear. This parameter bears relation to the compressibility of the fluid in the direction of the nematic, as it can be deduced by inspecting the constitutive equation (3.7). Nevertheless, our results suggest that α_1 affects the response function of a sphere less than the other viscosity coefficients (see **§3.4**).

3.3 Green's Function for the Flow in an Orthotropic Fluid

The response function of a particle in the linear regime can be calculated by using a multipole expansion [70, 91, 77]. The first step is to calculate the Green's function for the flow. This task is simplified by defining a second modified pressure,

$$\overline{p} = p' + (\eta_c - \eta_a)\partial_x u = p + (\eta_c - \eta_a - \alpha_5)\partial_x u, \tag{3.17}$$

so that equations (3.13) to (3.15) become separated in u, v and w,

$$\partial_x \overline{p} = (\eta_c + \eta_b - \eta_a + \alpha_1)\partial_{xx} u + \eta_b(\partial_{yy} + \partial_{zz})u + f_x, \tag{3.18}$$

$$\partial_y \overline{p} = \eta_c \partial_{xx} v + \eta_a(\partial_{yy} + \partial_{zz})v + f_y, \tag{3.19}$$

$$\partial_z \overline{p} = \eta_c \partial_{xx} w + \eta_a(\partial_{yy} + \partial_{zz})w + f_z. \tag{3.20}$$

In these equations, the boundary conditions introduced by the sphere are replaced by a point force at the origin before shifting to Fourier space. Because the problem is linear, we assume a solution of the form

$$\vec{v} = \frac{\overline{\overline{\mathcal{G}}} \cdot \vec{F}}{8\pi} = \frac{1}{8\pi} \begin{Bmatrix} \mathcal{G}_{1j} F_j \\ \mathcal{G}_{2j} F_j \\ \mathcal{G}_{3j} F_j \end{Bmatrix}, \tag{3.21}$$

$$\overline{p} = \frac{\vec{\mathcal{P}} \cdot \vec{F}}{8\pi} = \frac{1}{8\pi} \mathcal{P}_j F_j, \tag{3.22}$$

where $\mathcal{G}_{ij}$ is the Green's function for the velocity (also called the Oseen tensor) and $\mathcal{P}_j$ is the Green's function for the pressure. Solving for the Green's function in Fourier space renders (see **Appendix 3.8** for more details)

$$\frac{\widehat{\mathcal{P}}_j}{\sqrt{8/\pi}} = ik_j \left[\frac{1-\delta_{1j}}{k^2} + \frac{\frac{1-\delta_{1j}}{k^2}(\alpha_1 k_1^4 - \eta_a k^4) + \eta_a k^2 + (\eta_b - \eta_a)k_1^2 + (\eta_c - \eta_b)k_1^2 \delta_{1j}}{\alpha_1 k_1^2(k_2^2 + k_3^2) + \eta_b k^4 + (\eta_c - \eta_b)k_1^2 k^2} \right], \tag{3.23}$$

and

$$\frac{\widehat{\mathcal{G}}_{1j}}{\sqrt{8/\pi}} = \frac{\delta_{1j} k^2 - k_1 k_j}{\alpha_1 k_1^2(k_2^2 + k_3^2) + \eta_b k^4 + (\eta_c - \eta_b)k_1^2 k^2}, \tag{3.24}$$

$$\frac{\widehat{\mathcal{G}}_{2j}}{\sqrt{8/\pi}} = \frac{\delta_{2j}}{(\eta_c - \eta_a)k_1^2 + \eta_a k^2} - k_2 k_j \frac{(1-\delta_{1j})\frac{\alpha_1 k_1^2 + (\eta_b - \eta_a)k^2}{(\eta_c - \eta_a)k_1^2 + \eta_a k^2} + 1}{\alpha_1 k_1^2(k_2^2 + k_3^2) + \eta_b k^4 + (\eta_c - \eta_b)k_1^2 k^2}, \tag{3.25}$$

$$\frac{\widehat{\mathcal{G}}_{3j}}{\sqrt{8/\pi}} = \frac{\delta_{3j}}{(\eta_c - \eta_a)k_1^2 + \eta_a k^2} - k_3 k_j \frac{(1-\delta_{1j})\frac{\alpha_1 k_1^2 + (\eta_b - \eta_a)k^2}{(\eta_c - \eta_a)k_1^2 + \eta_a k^2} + 1}{\alpha_1 k_1^2(k_2^2 + k_3^2) + \eta_b k^4 + (\eta_c - \eta_b)k_1^2 k^2}, \tag{3.26}$$

In this formulation, $\vec{k} = (k_1, k_2, k_3) = (k_x, k_y, k_z)$ is the wavenumber vector in the Fourier domain, δ_{ij} is the Dirac delta function and i the imaginary unit. In the isotropic limit case where $\eta_a = \eta_b = \eta_c = \eta$ and $\alpha_1 = 0$, we recover the Green's functions for isotropic fluids as expected.

3.4 Response Function of a Spherical Particle in a Nematic Fluid

In the low-Reynolds-number limit, the velocity of a particle moving in an orthotropic fluid and the drag force exerted on it are related as

$$\vec{F} = \overline{\overline{\zeta}} \cdot \vec{v}(\vec{x} = \vec{0}) = \overline{\overline{\zeta}} \cdot \vec{v}_0, \tag{3.27}$$

where $\overline{\overline{\zeta}}$ is a tensorial response function, also known as hydrodynamic resistance [70]. The aim of this section is to obtain analytical expressions for the different elements of $\overline{\overline{\zeta}}$. Given the singularity at the origin, the response function cannot be directly calculated from equation (3.21) but it can be obtained by regularizing the solution and assuming that the force applied by the sphere is not a point force but a compact force distribution $\vec{F}(\vec{x})$ [88, 91]. The velocity at the origin can be obtained from the Fourier transform of the Green's function as

$$\vec{v}_0 = \frac{1}{(2\pi)^{3/2}} \iiint \frac{\widehat{\overline{\overline{\mathcal{G}}}}}{8\pi} \cdot \widehat{\vec{F}}(\vec{k}) d^3k = \overline{\overline{\gamma}} \cdot \vec{F}, \tag{3.28}$$

where $\widehat{\vec{F}}(\vec{k}) = \vec{F}\,\widehat{\mathcal{F}}(\vec{k})$ is the Fourier transform of $\vec{F}(\vec{x})$, the function $\widehat{\mathcal{F}}(\vec{k})$ is a regularization kernel that localized the drag force in physical and/or Fourier space, and $\overline{\overline{\gamma}}$ is the hydrodynamic mobility. Note that equation (3.28) is just the inverse Fourier transform of $\widehat{\vec{v}}(\vec{k})$ particularized at the origin, and that equations (3.27)-(3.28) imply that $\overline{\overline{\zeta}} = \overline{\overline{\gamma}}^{-1}$.

In [88] the authors propose a volume localization approach to simplify the calculation of $\overline{\overline{\gamma}}$ in the isotropic case by considering that the particle radius limits the spectrum of allowed fluctuations in the flow field. Hence, they only consider wavenumbers smaller than $k_{max} = \pi/2a$.

This approximation is written as

$$\widehat{\mathcal{F}}(k) = H\left(\frac{\pi}{2a} - k\right), \tag{3.29}$$

where H is the Heaviside function. It leads to the following expression for the inverse response function tensor

$$\gamma_{ij} = \frac{1}{4\sqrt{2\pi}a}\int_{\theta=0}^{\theta=\pi} \sin\theta \left(\int_{\varphi=0}^{\varphi=2\pi} \frac{k^2\widehat{\mathcal{G}}_{ij}}{8\pi} d\varphi\right) d\theta, \tag{3.30}$$

where θ and φ are the inclination and azimuth angles in spherical coordinates, respectively. Note that $\widehat{\mathcal{G}}_{ij}$ is inversely proportional to k^2, so that the whole expression is independent of k. While it holds a clear physical meaning, the sharp Fourier cut-off of the Heaviside regularization function leads to a non-localized force distribution in physical space and a velocity field with Gibbs oscillations in the radial direction. For this reason, the Gaussian regularization function

$$\widehat{\mathcal{F}}(k) = e^{-a^2k^2/\pi} \tag{3.31}$$

is preferred in this study. This choice yields the same equation for γ_{ij} and has the advantage of providing a localized Gaussian force distribution and a smooth velocity field in physical space (see **§3.6**). This approach is analogous to the regularized Stokeslet method [5, 26].

Owing to the symmetry of the Green's function (3.24)-(3.26), we obtain that $\gamma_{ij} = 0$ for $i \neq j$, and both $\overline{\overline{\gamma}}$ and $\overline{\overline{\zeta}}$ are diagonal tensors. In particular,

$$\vec{F} = \begin{bmatrix} \zeta_{||} & 0 & 0 \\ 0 & \zeta_{\perp} & 0 \\ 0 & 0 & \zeta_{\perp} \end{bmatrix} \cdot \vec{v}_0, \tag{3.32}$$

where $\zeta_{||}$ is the response function in the direction parallel to the nematic and $\zeta_{\perp}$ is the response function in all transverse directions. These principal values can be determined independently by measuring the drag force of a particle in the directions parallel and perpendicular to $\vec{n}$. For any other direction of motion, the drag force acting on a particle is not parallel to $\vec{v}_0$. In general, if

$\vec{v}_0$ forms an angle β_v with $\vec{n}$, the angle between the drag force vector and the nematic director is $\beta_F = \arctan[\tan(\beta_v)\zeta_\perp/\zeta_{||}]$ (see **Figure 3.1**).

Armed with some tenacity, one can find an explicit analytical solution to the integrals in equation (3.30), leading to the following expressions for the diagonal components of the response function,

$$\zeta_{||} = \frac{1}{\gamma_{11}} = \frac{8\pi a \eta_b B(\vec{\eta})}{D_+(\vec{\eta})\frac{\arctan[C_+(\vec{\eta})]}{C_+(\vec{\eta})} - D_-(\vec{\eta})\frac{\arctan[C_-(\vec{\eta})]}{C_-(\vec{\eta})}}, \tag{3.33}$$

$$\zeta_\perp = \frac{1}{\gamma_{22}} = \frac{1}{\gamma_{33}} = \frac{8\pi a \eta_a \left(\frac{\eta_b}{\alpha_1}\right)^2 C_-(\vec{\eta})^8 \frac{E_+(\vec{\eta})}{E_-(\vec{\eta})}}{\frac{\arctan\left(\sqrt{\eta_c/\eta_a - 1}\right)}{\sqrt{\eta_c/\eta_a - 1}} + \frac{1}{B(\vec{\eta})}\frac{\eta_a}{\eta_b}\left[\frac{\arctan[C_-(\vec{\eta})]}{C_-(\vec{\eta})} - \frac{\arctan[C_+(\vec{\eta})]}{C_+(\vec{\eta})}\right]}, \tag{3.34}$$

where $B(\vec{\eta})$, $C_\pm(\vec{\eta})$, $D_\pm(\vec{\eta})$ and $E_\pm(\vec{\eta})$ are non-dimensional functions of the viscosity vector $\vec{\eta} = (\alpha_1, \eta_a, \eta_b, \eta_c)$. These functions are given in **Appendix 3.9**. Equations (3.33) and (3.34) have a weak singularity at $\alpha_1 = 0$ that can be removed by taking the limit $\alpha_1 \to 0$, leading to

$$\zeta_{||,\alpha_1=0} = \frac{4\pi a(\eta_c - \eta_b)}{\frac{\eta_c}{\eta_b}\frac{\arctan\left(\sqrt{\eta_c/\eta_b - 1}\right)}{\sqrt{\eta_c/\eta_b - 1}} - 1}, \tag{3.35}$$

$$\zeta_{\perp,\alpha_1=0} = \frac{8\pi a(\eta_c - \eta_b)}{1 - \frac{\arctan\left(\sqrt{\eta_c/\eta_b - 1}\right)}{\sqrt{\eta_c/\eta_b - 1}} + \frac{\eta_c - \eta_b}{\eta_a}\frac{\arctan\left(\sqrt{\eta_c/\eta_a - 1}\right)}{\sqrt{\eta_c/\eta_a - 1}}}. \tag{3.36}$$

The isotropy point is of particular interest because diluted networks should not be too far from it. Taylor expanding equations (3.33) and (3.34) around the point $\alpha_1 = 0$, $\eta_a = \eta_b = \eta_c = \eta$, and keeping only the first order term we obtain

$$\frac{\zeta_\parallel}{6\pi a \eta} \approx 1 + \frac{4}{35}\frac{\alpha_1}{\eta} + \frac{4}{5}\left(\frac{\eta_b}{\eta} - 1\right) + \frac{1}{5}\left(\frac{\eta_c}{\eta} - 1\right), \tag{3.37}$$

$$\frac{\zeta_\perp}{6\pi a \eta} \approx 1 + \frac{3}{70}\frac{\alpha_1}{\eta} + \frac{1}{2}\left(\frac{\eta_a}{\eta} - 1\right) + \frac{1}{10}\left(\frac{\eta_b}{\eta} - 1\right) + \frac{2}{5}\left(\frac{\eta_c}{\eta} - 1\right). \tag{3.38}$$

This Taylor expansion is consistent with previous results by Pokrovskii & Tskhai [121], who studied the motion of a particle in a weakly anisotropic fluid with $\eta_b = \eta_c$.

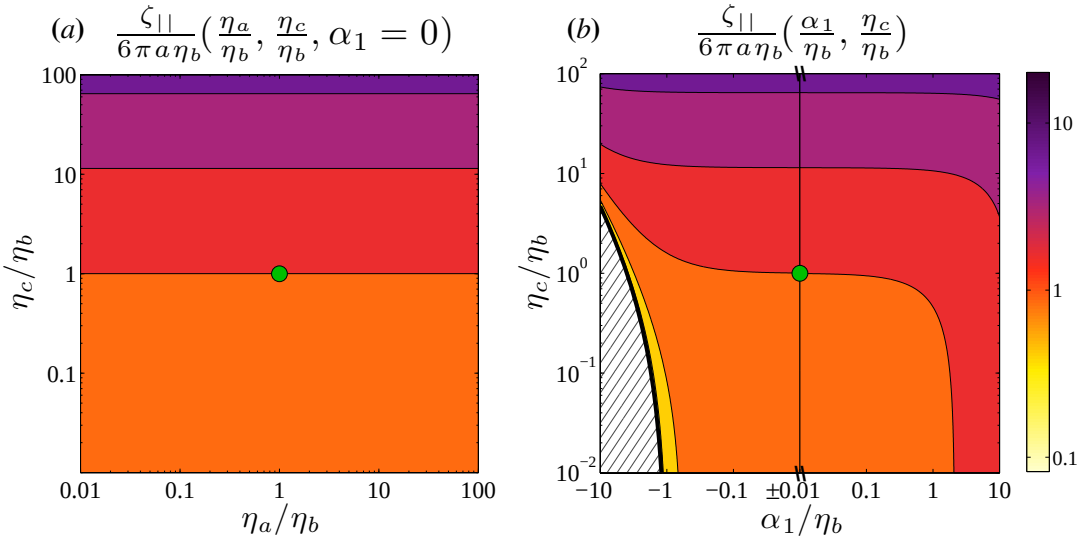

Figure 3.2: Contour maps of the response function in the nematic direction, $\zeta_{||}$, obtained from equation (3.33): (*a*), $\zeta_{||}(\eta_a/\eta_b, \eta_c/\eta_b)$ for $\alpha_1 = 0$, showing that this response function is independent of η_a; (*b*), $\zeta_{||}(\alpha_1/\eta_b, \eta_c/\eta_b)$. Note that the *x*-axis is broken between $\alpha_1 = -0.01\eta_b$ and $\alpha_1 = 0.01\eta_b$. The thick black curve indicates the locus where $\zeta_{||} = 0$. The hatched region to the left of this curve yields unphysical, complex-valued results for the response function. In both panels, the response functions have been normalized with $6\pi a\eta_b$. The green circle represents the isotropic case with $\eta_a = \eta_b = \eta_c$ and $\alpha_1 = 0$.

In general, both components of the response function increase with increasing the viscosity coefficients but there are several aspects of this dependence that deserve especial attention. **Figure 3.2** displays the response function in the nematic direction, $\zeta_{||} = \zeta_{11}$. Interestingly, this component is independent of the first Miesowicz viscosity η_a, as shown in **Figure 3.2** (*a*) for $\alpha_1 = 0$, and in agreement with [73]. This degeneracy can be explained by realizing that the flow elicited by a sphere that translates parallel to the nematic director is axially symmetric. Working in polar cylindrical coordinates (r, θ, x) and taking into account this symmetry, the momentum balance equations (3.13)-(3.15) can be rewritten as

$$\partial_x p' = \eta_b \nabla^2 u_x + \alpha_1 \partial_{xx} u_x, \tag{3.39}$$

$$\partial_r p' = \eta_c \left(\nabla^2 u_r - u_r/r^2\right) - (\eta_c - \eta_a)\partial_r(\nabla \cdot \vec{v}), \tag{3.40}$$

where $\eta_c - \eta_a$ acts as a dilatational viscosity in the radial direction that disappears when the velocity field is divergence-free. It is recognized that the resulting divergence-free, axially symmetric velocity field has a stream function but this function is not pursued here for the sake

of consistency with the perpendicular problem, which is not axially symmetric. Note also that the Green's function derived in **§3.3** can be easily extended to networks with significant volume fractions, where network compressibility leads to $\nabla \cdot \vec{v} \neq 0$, and there is no stream function.

Figure 3.2 (*b*) depicts the dependence of the parallel response function on the remaining three viscosity coefficients by displaying $\zeta_{||}/(a\eta_b)$ as a function of α_1/η_b and η_c/η_b. This non-dimensionalization is chosen because the viscous shear stresses in the $||$ direction are proportional to η_b (see equation 3.13). In this scaling, the parallel response function shows a moderate dependence on the ratio η_c/η_b. In fact, the limiting values of $\zeta_{||}(\alpha_1 = 0)$ for $\eta_c/\eta_b \to 0, \infty$ are $4\pi a\eta_b$ and $8a\sqrt{\eta_b\eta_c}$, respectively, only differing by a factor of order $(\eta_c/\eta_b)^{1/2}$.

The dependence of the parallel response function on α_1 is even weaker, especially in the case $\eta_c \gg \eta_b$, which is dominated by the viscous stresses in the $\perp$ directions. Near the isotropy point, the parallel response function is relatively insensitive to α_1, consistent with the small factor multiplying this coefficient in the Taylor expansion of equation (3.37). **Figure 3.2** (*b*) also considers $\alpha_1 < 0$ as this viscosity coefficient has been reported to be negative in some nematic liquid crystals [72]. Our analysis indicates that lowering α_1 below zero causes the response function to decrease. This decrease is moderate everywhere but near the curve

$$\frac{\eta_c}{\eta_b} = 1 - \frac{\alpha_1}{\eta_b} - 2\sqrt{\frac{-\alpha_1}{\eta_b}}, \quad \alpha_1 < -\eta_b, \tag{3.41}$$

where the function $B(\vec{\eta})$ that multiplies the right-hand side of equation (3.33) becomes zero and so does the parallel response function (see **Appendix 3.9**). The region to the left of this curve in the $(\alpha_1/\eta_b, \eta_c/\eta_b)$ plane produces complex values of $\zeta_{||}$ and, thus, is physically impossible.

The transverse response function, $\zeta_\perp = \zeta_{22}$ (equation 3.34), has a more complicated dependence on the viscosity coefficients than its parallel counterpart because the flow elicited by $\vec{v}_0$ is not axially symmetric. In order to analyze this dependence, it is convenient to plot $\zeta_\perp/(a\eta_a)$ as a function of η_b/η_a, η_c/η_a and α_1/η_a. This representation allows us to evaluate the relative importance of the different sources of anisotropy in the Leslie-Ericksen constitutive equation (3.7), namely bending of the fluid with respect to the nematic and anisotropy in the

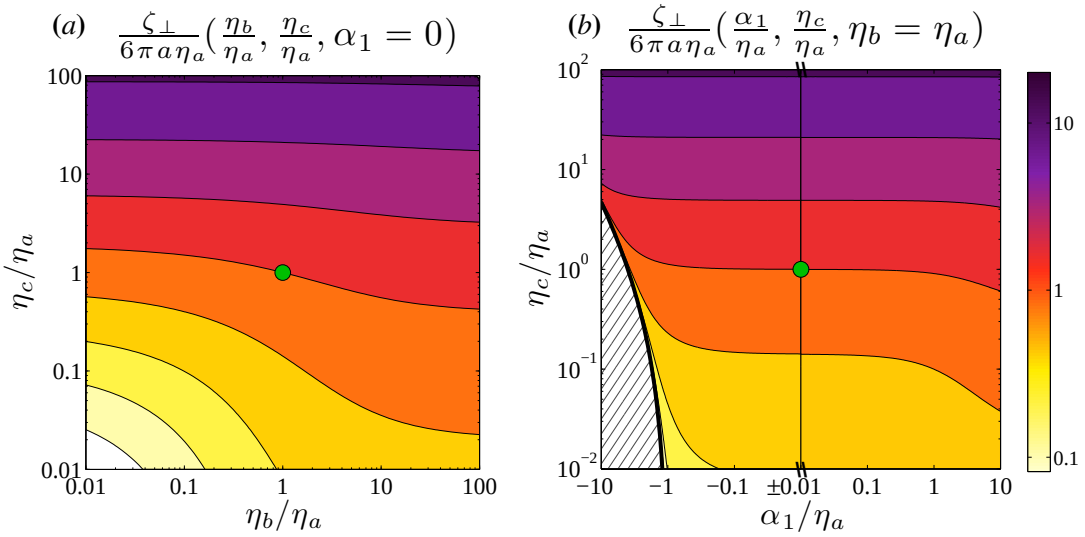

Figure 3.3: Contour maps of the response function perpendicular to the nematic, $\zeta_\perp$, obtained from equation (3.34): (*a*), $\zeta_\perp(\eta_b/\eta_a, \eta_c/\eta_a)$ for $\alpha_1 = 0$; (*b*), $\zeta_\perp(\eta_b/\eta_a, \alpha_1/\eta_a)$ for $\eta_b = \eta_a$. Note that the *x*-axis is broken between $\alpha_1 = -0.01\eta_a$ and $\alpha_1 = 0.01\eta_a$. The thick black curve indicates the locus where $\zeta_\perp = 0$. The region to the left of this curve yields unphysical, complex-valued results for the response function. In both panels, the response functions have been normalized with $6\pi a\eta_a$. The green circle represents the isotropy point, $\eta_a = \eta_b = \eta_c$ and $\alpha_1 = 0$.

stress-strain relationship.

Figure 3.3 (*a*) displays the transverse response function in the case $\alpha_1 = 0$. The plot reveals that $\zeta_\perp/(a\eta_a)$ is more sensitive to η_c/η_a than to η_b/η_a. This is especially true in the limit $\eta_c \gg \eta_a$, in which the bending stresses become dominant in the equations of motion, and the response function has a concise limit that is independent of the second Miesowicz viscosity,

$$\zeta_\perp \to 16a\eta_a\sqrt{\frac{\eta_c}{\eta_a}}. \tag{3.42}$$

The response function also becomes independent of η_b in the limit $\eta_b \gg \eta_a$, in which the anisotropic momentum diffusivity dominates the flow dynamics, and

$$\zeta_\perp \to 8\pi a\eta_a \frac{\sqrt{\eta_c/\eta_a - 1}}{\arctan\left(\sqrt{\eta_c/\eta_a - 1}\right)}. \tag{3.43}$$

The α_1-dependence of $\zeta_\perp$ is similar to that of $\zeta_{||}$, as shown in **Figure 3.3** (*b*) for the case $\eta_a = \eta_b$. The transverse response function is fairly insensitive to α_1 for the most part of the parameter

space, particularly near the isotropy point and for large η_c/η_a. Much like the $||$ case, the effect of α_1 only becomes strong near the curve defined by equation (3.41), where the transverse response function is zero. In the scaling used to plot **Figure 3.3** (*b*), this curve has an asymptote at $(\alpha_1/\eta_a, \eta_c/\eta_a) = (-\eta_b/\eta_a, 0)$. Thus, as η_b increases, the asymptote moves towards larger negative values of α_1/η_a and the influence of α_1 becomes less important.

3.4.1 Pseudo-Isotropic Conditions

The analysis of the equations of motion (3.13)-(3.16) suggests that the anisotropy in the Leslie-Ericksen constitutive relation (3.7) may influence the response function by means of two separate mechanisms. One is the anisotropy of the stress-strain relationship, which is proportional to the viscosity difference $\eta_b - \eta_a$, while the other is the resistance to the bending of the fluid, which is proportional to the viscosity difference $\eta_c - \eta_a$. The aim of this section is to dissect the effects of the two anisotropy mechanisms. We first study the response function in a rotationally pseudo-isotropic fluid where anisotropy comes exclusively from the anisotropic momentum diffusivity, and which corresponds to the horizontal line $\eta_c = \eta_a$ in **Figures 3.2** (*a*) and **3.3** (*a*). We then consider a strain pseudo-isotropic fluid, where the anisotropy comes solely from the resistance to bending of the fluid with respect to the nematic, and which corresponds to the vertical line $\eta_b = \eta_a$ in **Figures 3.2** (*a*) and **3.3** (*a*).

The response functions derived in this section also provide with distinct two-viscosity benchmarks to test the accuracy of existing PTM methods when applied to anisotropic fluids (see **§3.5**). This assessment needs to be performed on two-viscosity fluids as only two of the principal components of the response functions are independent in a nematic fluid (see equation 3.32). This limitation can be circumvented by considering two-point response functions, and such approach will be addressed in **Chapter 4**.

An aspect of particular interest that is evaluated on pseudo-isotropic fluids is the accuracy of the directional effective viscosity approximation. Based on the principal components of the response function, one can define two effective directional viscosities $\eta^{\text{eff}}_{||,\perp} = \zeta_{||,\perp}/(6\pi a)$, similar to [140]. This phenomenological approach has been previously used by experimentalists to

characterise different types of nematic fluids [94, 57, 126, 34, 58] but it has not been justified yet.

3.4.1.1 Rotationally Pseudo-Isotropic Fluid ($\eta_a = \eta_c$)

Consider a fluid where α_1 is very small and $\alpha_2 = \alpha_5$. Under these conditions, the last term in the transverse components of the momentum balance equation (equations 3.14-3.15) disappears, yielding the rotationally isotropic pseudo-Stokes problem

$$\nabla p' = \begin{bmatrix} \eta_{||} & 0 & 0 \\ 0 & \eta_{\perp} & 0 \\ 0 & 0 & \eta_{\perp} \end{bmatrix} \cdot \nabla^2 \vec{v}, \tag{3.44}$$

where $\eta_{||} = \eta_b$ denotes the viscosity parallel to the director and $\eta_{\perp} = \eta_a$ is the viscosity in the transverse directions. In this case, the directionality of the problem is solely due to the anisotropic diffusion of momentum along different directions (i.e. anisotropy in the stress-strain relationship).

Taking the limit $\eta_a \to \eta_c$ on equations (3.33)-(3.34), and introducing the anisotropy ratio $\Lambda = \eta_{||}/\eta_{\perp}$, we find that

$$\frac{\zeta_{||}}{6\pi a \eta_{||}} = \frac{\frac{2}{3}(1-\Lambda)}{-\Lambda + \frac{\arctan\left(\sqrt{1/\Lambda - 1}\right)}{\sqrt{1/\Lambda - 1}}}, \tag{3.45}$$

$$\frac{\zeta_{\perp}}{6\pi a \eta_{\perp}} = \frac{\frac{4}{3}(1-\Lambda)}{-\Lambda + 2 - \frac{\arctan\left(\sqrt{1/\Lambda - 1}\right)}{\sqrt{1/\Lambda - 1}}}. \tag{3.46}$$

These response functions are plotted in **Figure 3.4** (*a*) together with their tangent lines at the isotropy point $\Lambda = 1$ and their asymptotes for highly anisotropic conditions ($\Lambda \gg 1$ and $\Lambda \ll 1$). This figure shows 1D cuts of **Figures 3.2** (*a*) and **3.3** (*a*) along the horizontal line $\eta_c = \eta_a$.

The behavior of the $||$ and $\perp$ response functions near the isotropy point is given by their

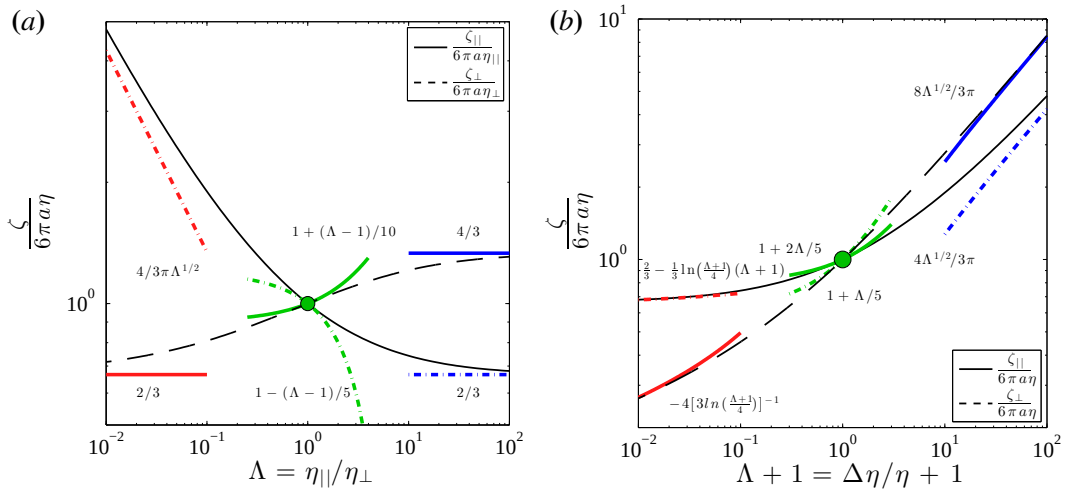

Figure 3.4: Principal component of the response function in a rotationally pseudo-isotropic and a strain pseudo-isotropic fluids, as a function of the viscosity ratios. (*a*) Rotationally pseudo-isotropic fluid, $\alpha_1 = 0$, $\eta_b = \eta_{||}$ and $\eta_a = \eta_c = \eta_\perp$, represented as a function of the viscosity ratio $\Lambda = \eta_{||}/\eta_\perp$ and (*b*) strain pseudo-isotropic fluid $\alpha_1 = 0$, $\eta_a = \eta_b = \eta$ and $\eta_c = \Delta\eta + \eta$, represented as a function of the viscosity ratio $\Lambda = \Delta\eta/\eta$: ——, $\zeta_{||}/6\pi a\eta_{||}$: – – –, $\zeta_\perp/6\pi a\eta_\perp$. The green circle marks the isotropy point: (*a*) $\Lambda = 1$ and (*b*) $\Lambda = 0$. The thick color segments mark the asymptotic behavior of the response function for (*a*) $\Lambda \ll 1$ (red), $\Lambda \approx 1$ (green) and $\Lambda \gg 1$ (blue), and (*b*) $\Lambda \to -1$ (red), $\Lambda \approx 0$ (green) and $\Lambda \gg 1$ (blue).

Taylor expansion

$$\frac{\zeta_{||}}{6\pi a\eta_{||}} = 1 - \frac{1}{5}(\Lambda-1) + \frac{27}{175}(\Lambda-1)^2 + O[(\Lambda-1)^3], \tag{3.47}$$

$$\frac{\zeta_{\perp}}{6\pi a\eta_{\perp}} = 1 + \frac{1}{10}(\Lambda-1) - \frac{33}{700}(\Lambda-1)^2 + O[(\Lambda-1)^3], \tag{3.48}$$

where the leading-order terms correspond to the expected isotropic result $\zeta = 6\pi a\eta$, and the higher-order terms are the corrections introduced by the anisotropy of the fluid. The numerical values of the coefficients in these expansions indicate that the anisotropic corrections are weaker in the transverse response function than in the parallel one, consistent with the weaker variation of $\zeta_\perp$ observed in **Figure 3.4** (*a*).

In order to determine whether the effects of anisotropy are bounded in a rotationally pseudo-isotropic fluid, we consider the asymptotic behavior of the response function for $\Lambda \gg 1$,

where

$$\frac{\zeta_{||}}{6\pi a\eta_{||}} \simeq \frac{2}{3}, \tag{3.49}$$

$$\frac{\zeta_{\perp}}{6\pi a\eta_{\perp}} \simeq \frac{4}{3}. \tag{3.50}$$

Interestingly, these expressions are equivalent to those of a prolate ellipsoid moving along its principal axes in an isotropic liquid [70]. It is important to note that the two components of the response function are decoupled from each other, so that increasing $\eta_{||}$ does not affect $\zeta_{\perp}$ and vice versa. Thus, the ratio of effective diffusivities becomes proportional to the ratio of actual viscosities of the fluid for $\Lambda \gg 1$,

$$\frac{\eta_{||}^{\text{eff}}}{\eta_{\perp}^{\text{eff}}} = \frac{\zeta_{||}}{\zeta_{\perp}} \simeq \frac{1}{2}\frac{\eta_{||}}{\eta_{\perp}}, \tag{3.51}$$

although these ratios differ by a factor of two.

The second asymptotic limit is $\Lambda \ll 1$, which results in

$$\frac{\zeta_{||}}{6\pi a\eta_{||}} \simeq \frac{4}{3\pi\sqrt{\Lambda}}, \tag{3.52}$$

$$\frac{\zeta_{\perp}}{6\pi a\eta_{\perp}} \simeq \frac{2}{3}. \tag{3.53}$$

It can be seen that, in this limit, the $||$ component of the response function not only depends on $\eta_{||}$ but also on $\eta_{\perp}$, so that the ratio of effective diffusivities,

$$\frac{\eta_{||}^{\text{eff}}}{\eta_{\perp}^{\text{eff}}} = \frac{\zeta_{||}}{\zeta_{\perp}} \simeq \frac{2}{\pi}\sqrt{\frac{\eta_{||}}{\eta_{\perp}}} \gg \frac{\eta_{||}}{\eta_{\perp}}, \tag{3.54}$$

becomes a rather poor measure of the ratio of actual viscosities of the fluid.

3.4.1.2 Strain Pseudo-Isotropic Fluid ($\eta_a = \eta_b$)

Consider a fluid where α_1 and α_3 are very small and $\alpha_2 = -\alpha_5$. Under these conditions, the equations of motion (3.13)-(3.15) become

$$\nabla p' = \eta \nabla^2 \vec{v} + \Delta\eta \partial_{||}(\vec{\omega} \times \vec{n}), \tag{3.55}$$

where $\eta = \eta_a$ and $\Delta\eta = \eta_c - \eta_a$. The Laplacian term on the right hand side of equation (3.55) can be seen as coming from isotropic momentum diffusion with viscosity η. On the other hand, the last term in the equation represents the resistance of the fluid to bending with respect to the nematic, and this is the only source of anisotropy in the strain pseudo-isotropic condition. The coefficient $\Delta\eta$ can be interpreted as a rotational viscosity.

Taking the limit $\eta_b \to \eta_a$ on equations (3.33)-(3.34), and introducing the anisotropy ratio $\Lambda = \Delta\eta/\eta$, we find that

$$\frac{\zeta_{||}}{6\pi a \eta} = \frac{\frac{2}{3}\Lambda}{(\Lambda+1)\frac{\arctan(\sqrt{\Lambda})}{\sqrt{\Lambda}} - 1}, \tag{3.56}$$

$$\frac{\zeta_{\perp}}{6\pi a \eta} = \frac{\frac{4}{3}\Lambda}{(\Lambda-1)\frac{\arctan(\sqrt{\Lambda})}{\sqrt{\Lambda}} + 1}. \tag{3.57}$$

Note that, in this case, the anisotropy ratio ranges between $\Lambda = -1$ ($\eta_c \ll \eta_a$) and $\Lambda = \infty$ ($\eta_c \gg \eta_a$), and the isotropy point corresponds to $\Lambda = 0$.

Similar to **Figure 3.4** (*a*), the parallel and perpendicular response functions for a strain pseudo-isotropic fluid are plotted in **Figure 3.4** (*b*), along with their tangent lines at the isotropy point and their asymptotes for highly anisotropic conditions. In this case, the plotted curves are one-dimensional sections of **Figures 3.2** (*a*) and **3.3** (*a*) along the vertical line $\eta_a = \eta_b$.

The behavior of the response function near the isotropy point is given by its Taylor

expansion,

$$\frac{\zeta_{||}}{6\pi a\eta} = 1 + \frac{1}{5}\Lambda - \frac{8}{175}\Lambda^2 + O[\Lambda^3], \tag{3.58}$$

$$\frac{\zeta_{\perp}}{6\pi a\eta} = 1 + \frac{2}{5}\Lambda - \frac{17}{175}\Lambda^2 + O[\Lambda^3], \tag{3.59}$$

which shows that, in contrast to the rotationally pseudo-isotropic condition, the anisotropy corrections are stronger in the transverse direction than in the parallel direction. This result is consistent with the intuitive notion that particle motion in the $\perp$ direction bends the nematic more than particle motion in the $||$ direction.

In the limit $\Lambda \gg 1$, the asymptotic behavior of the response function is

$$\frac{\zeta_{||}}{6\pi a\eta} \simeq \frac{4}{3\pi}\sqrt{\Lambda}, \tag{3.60}$$

$$\frac{\zeta_{\perp}}{6\pi a\eta} \simeq \frac{8}{3\pi}\sqrt{\Lambda}, \tag{3.61}$$

whereas, in the limit $\Lambda \to -1$, we have

$$\frac{\zeta_{||}}{6\pi a\eta} \simeq \frac{2}{3} - \frac{2}{3}\left[1 + \frac{1}{2}\ln\left(\frac{\Lambda+1}{4}\right)\right](\Lambda+1), \tag{3.62}$$

$$\frac{\zeta_{\perp}}{6\pi a\eta} \simeq -\frac{4}{3}\frac{1}{\ln\left(\frac{\Lambda+1}{4}\right)+1}. \tag{3.63}$$

Comparing these asymptotic responses with those in **Figure 3.4** (*a*) reveals that the effects of anisotropy in the stress-strain relationship are fundamentally different from those arising from nematic bending. In rotationally pseudo-isotropic fluids, the response function becomes independent of the anisotropy ratio for high levels of anisotropy, leading to horizontal asymptotes in **Figure 3.4** (*a*), and rendering upper bounds to the effect of anisotropy. The only exception to this behavior is $\zeta_{||}(\eta_{||} \ll \eta_{\perp})$, which has a square-root dependence on $\eta_{\perp}$ due to the fact that the flow is still infinitesimally deflected in the $\perp$ direction by the sphere in this limit, as will be shown in **§3.6.1**.

In contrast, the strain pseudo-isotropic response function remains dependent on both η

and $\Delta\eta$ even at high levels of anisotropy, suggesting a strong interaction between the anisotropic stresses caused by bending and the diffusion of momentum by strain. These two mechanisms only appear to decouple from each other for $\zeta_{||}(\Delta\eta \to -\eta)$, which is consistent with the independence of the parallel response with respect to the first Miesowicz coefficient (**Figure 3.2** *a*), as $\Delta\eta = -\eta_a$ in this limit. These results inevitably call for caution in employing the concept of effective directional viscosities. This notion may be qualitatively useful in rotationally pseudo-isotropic fluids where the effect of anisotropy can be partially separated in different directions. However, its usefulness becomes limited in fluids with resistance to bending, where the anisotropy appears to act in all directions concurrently and in a non-trivial manner.

3.4.2 Comparison with Numerical Results

This section uses data from existing numerical simulations to validate the analytical procedures employed to determine $\overline{\overline{\zeta}}$. Owing to the relatively high number of different viscosities involved in the problem, it is difficult to find simulation studies that cover a significant part of the parameter space. The most comprehensive set of simulations is [63], where the authors compute the steady creeping flow of a nematic liquid of uniform director around a sphere using finite differences and a relaxation time integrator. They provide empirical formulae for both $\zeta_{||}$ and $\zeta_{\perp}$ that fit their simulation results near the isotropy point.

Figure 3.5 (*a*) compares the analytical expression for $\zeta_{||}$ (3.33) with Heuer *et al.*'s empirical fit in the parameter range where these authors find the fit to be accurate, that is $0.05 < \eta_c/\eta_b < 10$ and $-1/2 < \alpha_1/\eta_b < 1$ [63]. Both results are in an excellent agreement, not only around the isotropy point but in the whole domain, including its boundaries $\alpha_1 = -\eta_b/2$ and $\alpha_1 = \eta_b$.

Figure 3.5 (*b*) displays a similar comparison for $\zeta_{\perp}$ (3.34), this time in the domain $0.2 < \eta_c/\eta_b < 5$, $0.2 < \eta_c/\eta_a < 5$ and $\alpha_1 = 0$, which is the range of accuracy of Heuer *et al.*'s empirical fit to their simulation data [63]. The agreement is again perfect near the isotropy point and for low values of η_b/η_a and η_c/η_a (bottom left corner of **Figure 3.5** (*b*)). However, it worsens slightly for high values of η_b/η_a and η_c/η_a (top right corner of the figure), where the

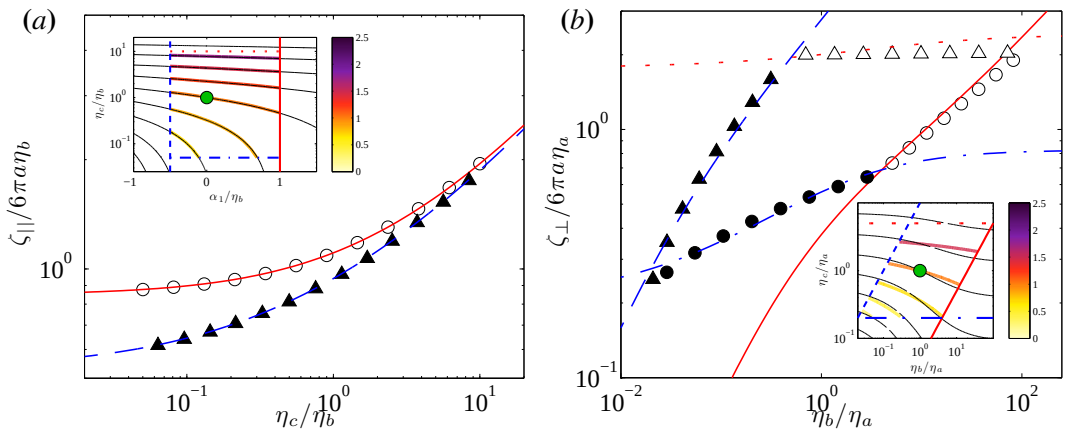

Figure 3.5: Comparison between our analytical expression for the response function (lines) and numerical simulations by [63] (symbols). The two line plots on each figure represent the lower and upper limits of the parameter ranges provided in [63]. These limits and the entire parameter ranges are represented in the inset contour maps, where the thick colour contours come from the simulations, the thin black contours come from equations (3.33) and (3.34), and the green circle denotes the isotropic case. (*a*) Response function in the nematic direction, $\zeta_{||}$, normalized with $a\eta_b$ and represented as a function of η_c/η_b and α_1/η_b: – – and ▲, $\alpha_1 = -0.5\eta_b$; ——— and ○, $\alpha_1 = \eta_b$; – · – ·, $\eta_c = 0.05\eta_b$; ····· , $\eta_c = 10\eta_b$. (*b*) Response function perpendicular to the nematic direction, $\zeta_\perp$, computed for $\alpha_1 = 0$, normalized with $a\eta_a$ and represented as a function of η_b/η_a and η_c/η_a: – – and ▲, $\eta_c = 10\eta_b$; ——— and ○, $\eta_b = 0.05\eta_c$; – · – · and ●, $\eta_c = 0.2\eta_a$; ····· and Δ, $\eta_c = 5\eta_a$.

simulation results seem to underestimate $\zeta_\perp$. These differences are however small and remain below 12%. The observed divergence may be due to imprecisions in Heuer *et al.* 's fit to their own simulation results far from the isotropy point. This hypothesis is supported by comparing their simulation results to the prediction from the empirical fit for the one case in their paper where both are available, *i.e.* $(\eta_b/\eta_a, \eta_c/\eta_a, \alpha_1/\eta_a) = (1/3,\ 10/3,\ 0)$. For this combination of viscosities, the simulation yields $\zeta_\perp/6\pi a\eta_a = 5.28$, which is in excellent agreement with our calculation of $\zeta_\perp/6\pi a\eta_a = 5.27$. However, the empirical fit predicts $\zeta_\perp/6\pi a\eta_c = 5.47$, which differs by 4% from the simulation result.

3.5 Assessing Particle Tracking Microrheology of Nematic Bio-Polymer Networks

This section employs the expressions for the response function derived in **§3.4.1** to evaluate the accuracy of existing PTM formulae when applied to pseudo-isotropic nematic fluids.

This analysis allows us to separately determine the ability of those formulae to estimate strain directional viscosities or bending viscosities.

PTM determines the viscosity of a fluid from the measured response function of embedded microparticles. Whether the motion of the particles is spontaneously driven by the thermal excitation of the fluid (passive PTM) or externally forced (active PTM), the fluid viscosity is estimated by fitting the measured response function to a model for the drag of a canonical particle. The simplest possible model is the Stokes's formula $\zeta = 6\pi a\eta$, which is valid for isotropic fluids [102, 103, 101]. A second, more recent approach that is applied to nematic biogels and liquid crystals consists of applying Stokes's equation separately in the two principal directions of the motion to obtain two effective viscosity coefficients [140, 94, 57, 126, 34, 58],

$$\zeta_{||,\perp} = 6\pi a\eta^{\text{eff}}_{||,\perp}. \tag{3.64}$$

From the statistical mechanics perspective, this approach has been justified on the grounds that the motion of the particle in one principal direction is uncorrelated from its motion in the second principal direction [34]. From the point of view of fluid mechanics, the effective viscosities were proposed as friction coefficients that quantify overall directional diffusivity in a nematic fluid [140]. However, their relation to the actual directional viscosities of the fluid has not been characterized yet. **Figure 3.6** sheds light into this question with the aid of experimental data coming from reconstituted biopolymer gels [57, 58] and live cells [34]. The figure displays the ratio of viscosity coefficients in pseudo-isotropic fluids as a function of the ratio $\zeta_\perp/\zeta_{||}$ calculated in this study, together with the predictions from the isotropic Stokes's law and the effective viscosity approach (3.64). The range of values of $\zeta_\perp/\zeta_{||}$ measured in experiments is included in the plots. In passive PTM experiments, this ratio is equal to the ratio of mean squared displacements of the particles $\langle\Delta x^2\rangle_\perp/\langle\Delta x^2\rangle_{||}$ [34].

A first interesting observation that can be made from comparing **Figures 3.6** (*a*) and **3.6** (*b*) is that biopolymer networks, both reconstituted and inside live cells, behave closer to a rotationally pseudo-isotropic fluid than to a strain pseudo-isotropic one. In fact, **Figure 3.6** (*b*)

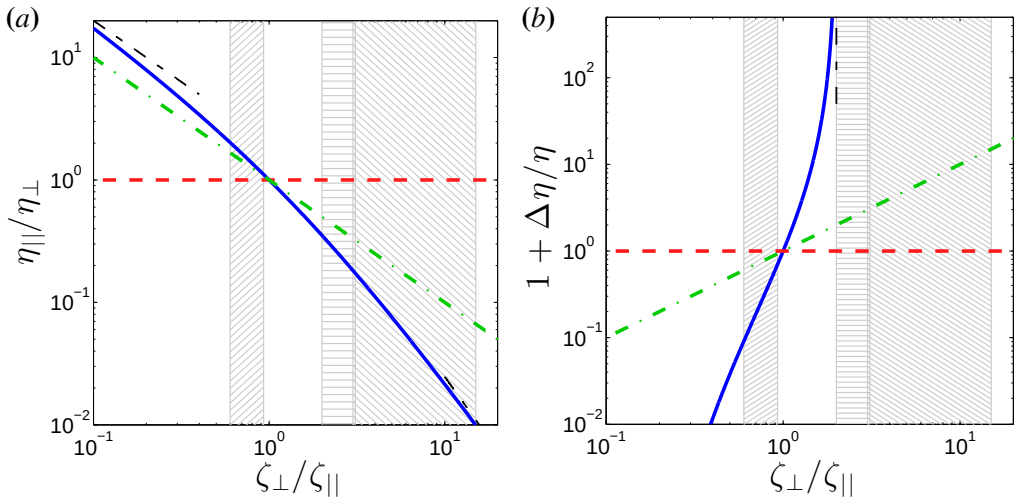

Figure 3.6: Ratio of viscosity coefficients as a function of the ratio of directional response functions, $\zeta_{\perp}/\zeta_{||}$, for rotationally pseudo-isotropic and strain pseudo-isotropic fluids. (*a*) Ratio of viscosity coefficients, $\eta_{||}/\eta_{\perp}$. Each curve is obtained by using a different model for the response function: – –, isotropic Stokes's formula; – · –, effective viscosity approach (equation 3.64); ——, rotationally pseudo-isotropic fluid (see **§3.4.1.1**); – · · –, asymptotes. The hatched areas represent experimental ranges of $\zeta_{\perp}/\zeta_{||}$ for biopolymer networks: left hatched, sheared DNA solutions [57]; horizontally hatched, nematic reconstituted actin networks [58]; right hatched, cytoplasm of live bovine aortic endothelial cells [34]. (*b*) Same as panel (*a*) for a strain pseudo-isotropic fluid (see **§3.4.1.2**) where the relevant ratio of viscosities is $\Delta\eta/\eta$

reveals that most of the reported values of $\zeta_{\perp}/\zeta_{||}$ for these materials are disallowed by the strain pseudo-isotropic model. In this model, $\zeta_{\perp}/\zeta_{||}$ has a vertical asymptote at 2 and, thus, fluids where $\zeta_{\perp}/\zeta_{||}$ is measured to be > 2 are necessarily strain anisotropic. The only exception is the sheared DNA solution [57], which shows a nearly isotropic behavior that can be in principle consistent with both the rotationally pseudo-isotropic and the strain pseudo-isotropic conditions.

If, in consonance with the previous observation, one assumes that the rheology of nematic biopolymer networks is relatively close to rotationally pseudo-isotropic, **Figure 3.6** (*a*) can be used to estimate the accuracy of previous response function models when applied to those biomaterials. Note that this estimation is not expected to be very precise as we merely proved that these fluids are not strain pseudo-isotropic, which is not exactly equivalent to proving that they are rotationally pseudo-isotropic. Nevertheless, we proceed with this estimation for lack of a better measure. Comparing the different curves in **Figure 3.6** (*a*) within the range of experimental values of $\zeta_{\perp}/\zeta_{||}$ obtained from the literature indicates that previous models render errors of up to one

order (effective viscosity) or two orders of magnitude (isotropic Stokes). In both cases, the actual anisotropy of the fluid, given by the ratio $\eta_\perp/\eta_{||}$, is underestimated, with the effective viscosity approach predicting $0.8 \lesssim \eta_\perp/\eta_{||} \lesssim 9$, and the present results predicting $0.5 \lesssim \eta_\perp/\eta_{||} \lesssim 100$. Thus, researchers should exercise caution when interpreting directional PTM data.

3.6 Influence of Anisotropy on the Far Velocity Field

Anisotropy does not alter the r^{-1} decay of the velocity far away from the sphere but it does modify the dependence of $\vec{v}$ on the azimuth and inclination angles. The velocity in the far field of the sphere can be calculated from equations (3.21) and (3.32), yielding

$$\vec{v}(\vec{x}) = \frac{\overline{\overline{\mathcal{G}}}(\vec{x})}{8\pi} \cdot \begin{bmatrix} \zeta_{||} & 0 & 0 \\ 0 & \zeta_\perp & 0 \\ 0 & 0 & \zeta_\perp \end{bmatrix} \cdot \vec{v}_0, \tag{3.65}$$

where $\vec{v}_0$ is the velocity of the particle. Similar to **§3.4**, the Green's function is obtained by Fourier transforming equations (3.24)-(3.26) after regularizing with the Gaussian (3.31). This section focuses on the two basic flow configurations in which $\vec{v}_0$ is parallel and perpendicular to $\vec{n}$. All other possible configurations are linear combinations of these two basic flows.

3.6.1 Velocity Field Caused by a Sphere Moving Parallel to the Nematic Director ($\vec{v}_0 \,||\, \vec{n}$)

Figure 3.7 displays velocity profiles around a sphere that translates parallel to the nematic director (*i.e.* northwards) and experiences a resistance equal to $\zeta_{||}$. The velocity components parallel and perpendicular to the director, $v_{||}$ and $v_\perp$ respectively, are shown. These components fully define the axially symmetric velocity field elicited by the sphere. For illustrative purposes, we have represented $v_{||}$ and $v_\perp$ at a distance $r = 5a$ from its centre but similar results are obtained at other radial locations.

As noted above, the flow generated by $\vec{v}_0 \,||\, \vec{n}$ is independent of the first Miesowicz

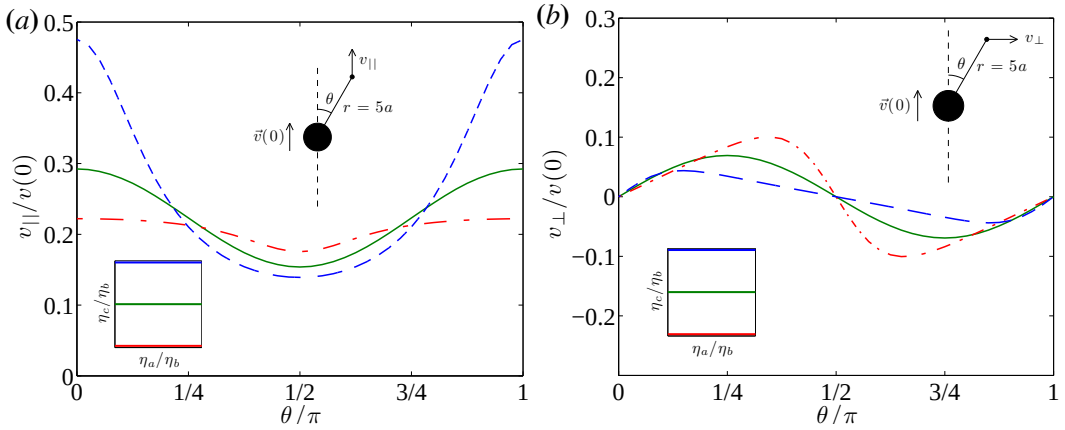

Figure 3.7: Longitudinal ($v_{||}$, panel *a*) and transverse ($v_\perp$, panel *b*) flow velocity components elicited by a sphere moving parallel to the nematic director. The velocities are calculated at a distance $r = 5a$ away from the sphere centre, represented as a function of the inclination angle θ. Each line type corresponds to a different value of η_c/η_b, as indicated in the inset map at the lower left corner of each figure: – –, $\eta_c = 10\eta_b$; ——, $\eta_c = \eta_b$; – · –, $\eta_c = \eta_b/10$.

viscosity, so we restrict our analysis to the effect of the other two Miesowicz coefficients. For simplicity, we focus on the case $\alpha_1 = 0$ in which the equations governing the flow (3.39)-(3.40) become

$$\partial_x p' = \eta_b \nabla^2 u_x, \tag{3.66}$$

$$\partial_r p' = \eta_c \left(\nabla^2 u_r - u_r/r^2\right). \tag{3.67}$$

These equations are similar to Stokes's equations but have different viscosity coefficients in the axial and radial directions. The resulting flow is therefore rotationally pseudo-isotropic, and η_b and η_c represent the viscosities in the $||$ and $\perp$ directions, respectively (see equation 3.44). Curiously enough, invoking axial symmetry allows us to recast the very same equations as

$$\partial_x p' = \eta_b \nabla^2 u_x, \tag{3.68}$$

$$\partial_r p' = \eta_b(\nabla^2 u_r - u_r/r^2) + (\eta_c - \eta_b)\partial_x \omega_\theta, \tag{3.69}$$

which are now consistent with strain pseudo-isotropic conditions with $\eta_b = \eta$ and $\eta_c = \eta + \Delta\eta$ (see equation 3.55). The equivalence of these two formulations implies that the flow generated

by a sphere moving parallel to the director is both strain pseudo-isotropic and rotationally isotropic. However, it is important to note that this conjunction arises exclusively from the flow geometry and not from the fluid properties, and that it does not mean that the flow is isotropic. In this configuration, the bending stresses are still different than zero and momentum diffuses differently in the $||$ and $\perp$ directions unless $\eta_c = \eta_a$ and $\eta_b = \eta_a$, respectively. This is possible because the axial symmetry of the flow imposes a connection between the two types of anisotropic stresses, which is reflected by the equivalence $\eta_{||} = \eta$ and $\eta_{\perp} = \eta + \Delta\eta$ that follows from comparing equations (3.66)-(3.67) with equations (3.68)-(3.69). Consistent with this idea, the change of variables $(\eta_{||}, \eta_{\perp}) = (\eta, \eta + \Delta\eta)$ transforms the rotationally pseudo-isotropic $\zeta_{||}$ (3.45) into the strain pseudo-isotropic one (3.56). Of course, the same does not happen for $\zeta_{\perp}$ (equations 3.46 and 3.57) because the flow elicited by $\vec{v}_0 \perp \vec{n}$ is not axially symmetric.

Probably due to this enhanced pseudo-isotropy, the velocity profiles in the $\vec{v}_0 \,||\, \vec{n}$ configuration conserve many isotropic features and the streamlines are not substantially affected by the viscosity ratio η_c/η_b. In particular, **Figure 3.7** (a) shows that, regardless of the value of η_c/η_b, the longitudinal velocity component has a single maximum on the polar axis ($\theta = 0$) and a single minimum on the equatorial plane ($\theta = \pi/2$). The viscosity ratio η_c/η_b, however, has a marked effect on the peak-to-valley variation of $v_{||}$. For $\eta_c/\eta_b \ll 1$, the spatial distribution of $v_{||}$ is nearly uniform. However, for $\eta_c \gg \eta_b$, there is a significant enhancement of the flow velocity on the polar axis, which is accompanied by a slight velocity damping on the equatorial plane.

The transverse velocity component is shown in **Figure 3.7** (b). Owing to the symmetry of this flow configuration, $v_{\perp}$ is zero both on the polar axis and the equatorial plane. We find that the ratio η_c/η_b influences both the maximum value of $v_{\perp}$ and its azimuthal location, which is $\theta = \pi/4$ in the isotropic case. For $\eta_c < \eta_b$ the peak value of $v_{\perp}$ increases and its location is displaced towards the equator, whereas the opposite happens for $\eta_c > \eta_b$.

Figure 3.8 displays the flow streamlines obtained by integrating the far velocity field after subtracting the speed of the sphere. In order to illustrate the effect of anisotropy, the integration is performed for different values of η_c/η_b from a common initial point far upstream of the sphere. It is found that anisotropy only has a modest influence on the flow streamlines when the sphere

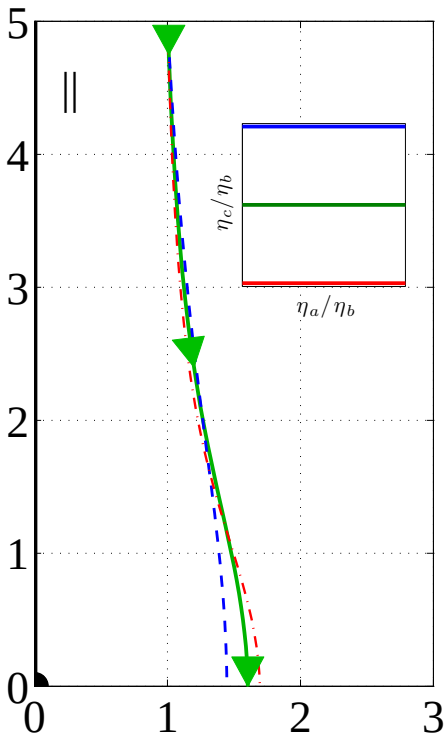

Figure 3.8: Streamlines on the meridional plane of a sphere that translates parallel to the nematic director (thick black vertical axis). The arrows indicate the flow direction in a reference frame moving with the sphere. The spatial coordinates are normalized with the sphere radius. One streamline is plotted for each value of η_c/η_b considered in **Figure 3.7**: – –, $\eta_c = 10\eta_b$; ——, $\eta_c = \eta_b$; – · –, $\eta_c = \eta_b/10$.

moves parallel to the nematic. Consistent with η_b and η_c acting as $\eta_{||}$ and $\eta_\perp$, respectively, in equations (3.66)-(3.67) and with the observed decrease of $v_\perp$ with η_c/η_b (**Figure 3.7** *b*), fluid particles approaching the sphere are deflected somewhat more in the $\perp$ direction for $\eta_c < \eta_b$ than in isotropic conditions, and the opposite happens for $\eta_c > \eta_b$. However, the level of deflection in this axially symmetric configuration is considerably smaller than when the sphere is moving perpendicular to the nematic (**Figure 3.11**).

3.6.2 Velocity Field Caused by a Sphere Moving Perpendicular to the Nematic Director ($\vec{v}_0 \perp \vec{n}$)

The flow generated by a sphere moving perpendicular to the nematic director (*e.g.* eastwards) is more complex than its $\vec{v}_0 || \vec{n}$ counterpart because axial symmetry is bro-

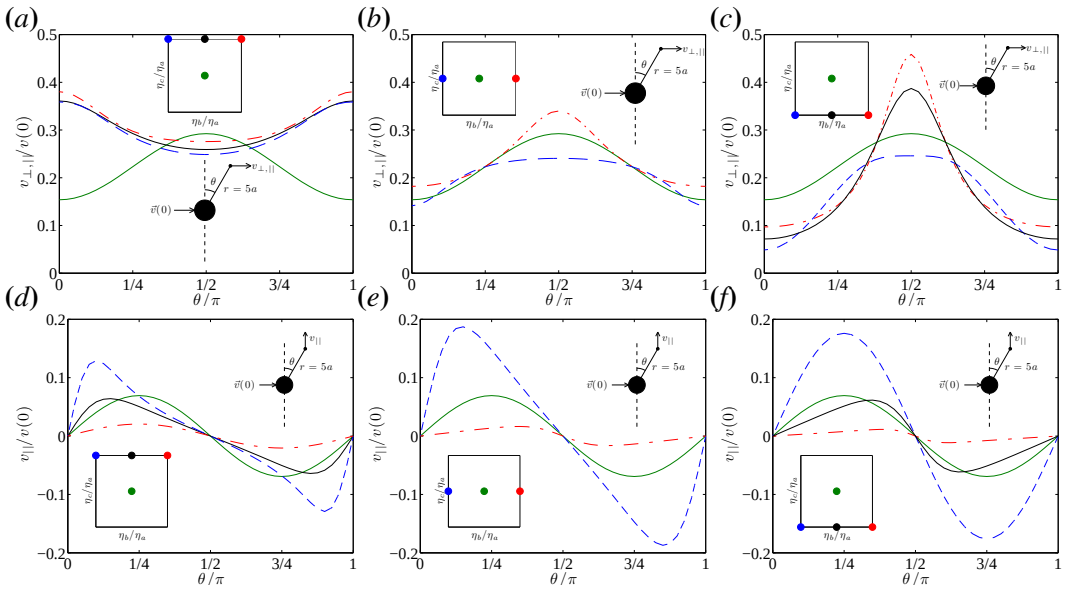

Figure 3.9: Flow velocity elicited by a sphere moving perpendicular to the nematic director. The velocities are calculated on the meridional plane $\phi = 0$ at a distance $r = 5a$ away from the sphere centre, and represented as a function of the inclination angle θ: (*a*)-(*c*), $v_{\perp,||}$; (*d*)-(*f*), $v_{||}$. (*a*) and (*d*), $\eta_a = \eta_c/10$; (*b*) and (*e*), $\eta_a = \eta_c$; (*f*) and (*g*), $\eta_a = 10\eta_c$. Each line type corresponds to a different value of η_b/η_c, as indicated in the inset maps: – – –, $\eta_b = \eta_c/10$; ——, $\eta_b = \eta_c$; – · – ·, $\eta_b = 10\eta_c$. The isotropic case is also plotted for reference (——).

ken, the velocity field is three-dimensional and all four viscosity coefficients affect the flow. In this section, we study this dependence by plotting velocity profiles and streamlines for all of the possible combinations of the viscosity ratios defined by η_b/η_a and $\eta_c/\eta_a \ll, =, \gg 1$ (0.1, 1, 10), and consistent with the scaling of the response function chosen to plot **Figure 3.3**. For simplicity, we restrict our analysis to $\alpha_1 = 0$ similar to the $\vec{v}_0 \,||\, \vec{n}$ configuration.

Figures 3.9 and **3.10** display angular profiles of the velocity at a constant distance $r = 5a$ from the origin, similar to **Figure 3.7**. To characterise the spatial organization of the velocity field in the present three-dimensional configuration, we plot data on two planes. The first is the meridional plane $\phi = \pi/2$ (**Figure 3.9**) and the second is the equatorial plane $\theta = \pi/2$ (**Figure 3.10**). These planes intersect along the west-east axis of translation of the sphere. On them, $v_{||}$ is the velocity component parallel to the nematic director (*i.e.* northward), whereas $v_{\perp,||}$ is perpendicular to the director and parallel to the sphere's trajectory (*i.e.* eastward). The remaining velocity component, $v_{\perp,\perp}$, is perpendicular to both the director and the sphere's trajectory.

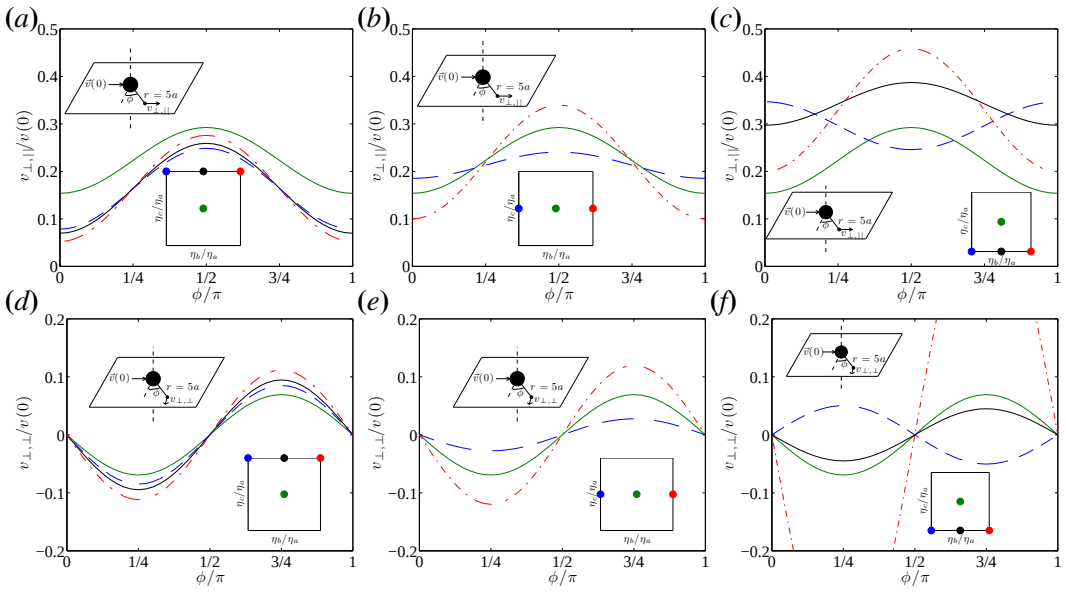

Figure 3.10: Same as **Figure 3.9** for the equatorial plane $\theta = 0$. Velocities are represented as a function of the azimuth angle ϕ: (*a*)-(*c*), $v_{\perp,||}$; (*d*)-(*f*), $v_{\perp,\perp}$.

Figure 3.11 demonstrates the effect of anisotropy on the streamline pattern. The streamlines in each panel are obtained by integrating the far velocity field relative to the sphere from a common initial point in the far east, upstream of the sphere. They are represented on the same meridional and equatorial planes used in **Figure 3.9** and **3.10**. Apart from allowing direct comparison between velocity profiles and streamlines, the choice of these two planes has the additional advantage that the local cross-plane flow velocity is zero, so that the streamlines remain in-plane. The same is not true for other initial points of integration given the three-dimensional nature of the flow when $\vec{v}_0 \perp \vec{n}$.

3.6.2.1 Case $\eta_a = \eta_c$

A first look into **Figures 3.9** and **3.10** indicates that, for $\eta_a = \eta_c$, the velocity profiles are qualitatively similar to the isotropic condition (panels *b* and *e*). The reason for this behavior is that the bending stresses in the equations of fluid motion are zero for $\eta_a = \eta_c$, and the flow becomes rotationally pseudo-isotropic with η_b and η_c acting respectively as $\eta_{||}$ and $\eta_\perp$ (see equation 3.44). Comparing **Figures 3.7** and **3.8** with panels (*b*), (*e*) of **Figures 3.9** and **3.10** and **Figure 3.11** (*b*) suggests that anisotropy influences the flow organization more deeply in the present rotationally

pseudo-isotropic configuration than in the $\vec{v}_0 \,||\, \vec{n}$ case, consistent with the fact that the bending stresses are not zero in that configuration.

The response function of a sphere in the case $\eta_a = \eta_c$ is characterized in **§3.4.1.1** above. Here we focus on the effect of the ratio η_b/η_a on the flow organization. We find that $v_{\perp,||}$ increases with η_b/η_a on the axis of translation of the sphere, $\theta = \pi/2$, whereas it decreases or varies little on the perpendicular axes (**Figures 3.9** *b* and **3.10** *b*). Thus, the profile of this velocity component becomes sharper as η_b/η_a increases. More importantly, the magnitude of $v_{||}$ decreases with η_b/η_a on the meridional plane (**Figure 3.9** *e*), while the magnitude of $v_{\perp,\perp}$ increases on the equatorial plane (**Figure 3.10** *e*). Overall, these velocity profiles suggest that the motion of the sphere leads to an asymmetric deflection of the fluid particles that is larger in the plane of lower viscosity and vice versa. This behavior can be easily appreciated by looking at the streamline pattern in **Figure 3.11** (*b*). Note also that these streamlines resemble the streamlines in the flow of isotropic fluid around a prolate ellipsoid, consistent with the results in **§3.4.1.1**.

3.6.2.2 Case $\eta_c \gg \eta_a$

For large values of η_c/η_a, the viscous bending stresses become important in the equations of motion (3.13)-(3.15), causing changes in the anisotropic velocity field that depend little on the other viscosity ratio, η_b/η_a. This result is consistent with the fact that $\zeta_\perp/(a\eta_a)$ is almost independent of η_b/η_a in the limit $\eta_c \gg \eta_a$ (see **Figure 3.3** *a*). The largest variations in the velocity profiles occur on the meridional plane, where the east-west velocity component $v_{\perp,||}$ increases substantially near the polar axis (**Figure 3.9** *a*). This is also the region where the anisotropic stresses are maximum (data not shown). The northward velocity $v_{||}$ behaves qualitatively similar to the $\eta_c = \eta_a$ case. It experiences a moderate increase in magnitude and shifts towards the polar axis as η_b/η_a decreases (**Figure 3.9** *d*). As a consequence, the streamlines on the meridional plane are deflected more as η_b/η_a decreases, and this deflection occurs closer to the location of the sphere (**Figure 3.11** *a*).

The flow in the equatorial plane is even less sensitive to the ratio η_b/η_a, remaining very close to the isotropic case (**Figures 3.10** *a*,*d*). In particular, the streamlines on this plane are almost

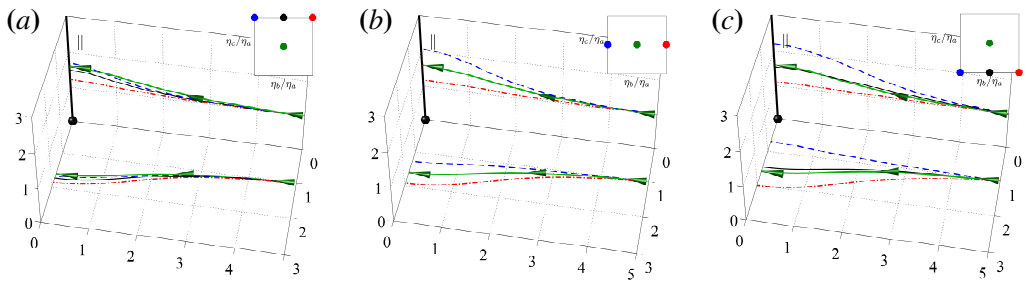

Figure 3.11: Streamlines on the meridional and equatorial planes of a sphere moving perpendicular to the nematic director (thick black vertical axis). The arrows indicate the flow direction in a reference frame moving with the sphere. The spatial coordinates are normalized with the sphere radius. Each panel corresponds to one value of the first viscosity ratio: (*a*) $\eta_a = \eta_c/10$; (*b*) $\eta_a = \eta_c$; (*c*) $\eta_a = 10\eta_c$. Each line type corresponds to a different value of η_b/η_c, as indicated in the inset map at the upper right corner of each figure: – –, $\eta_b = \eta_c/10$; ——, $\eta_b = \eta_c$; – · –, $\eta_b = 10\eta_c$. The isotropic case is also plotted for reference (——).

identical to the isotropic ones, with a slight increase in deflection with η_b/η_a (**Figure 3.11** *a*).

3.6.2.3 Case $\eta_c \ll \eta_a$

Similar to the rotationally pseudo-isotropic condition, the flows with $\eta_c \ll \eta_a$ are rather sensitive to the ratio of momentum diffusivities in the $||$ and $\perp$ directions, η_b/η_a. For large values of this ratio, $v_{||}$ decreases to virtually zero on the meridional plane (**Figure 3.9** *f*), where the viscosity is higher (η_b). Conversely, $v_{\perp,\perp}$ increases significantly on the equatorial plane (**Figure 3.10** *f*), where the viscosity is lower (η_a). Accordingly, the flow streamlines remain almost straight on the meridional plane whereas they are highly deflected away from the sphere on the equatorial plane (**Figure 3.11** *c*).

The velocity field corresponding to $\eta_c \ll \eta_a = \eta_b$ is comparable to the isotropic velocity field. The only remarkable difference is that the profile of $v_{\perp,||}$ is sharper than the isotropic one on the meridional plane and flatter on the equatorial plane (**Figures 3.9** *c* and **3.10** *c*). Apart from that, anisotropy affects little the velocity components perpendicular to axis of translation of the sphere in this case ($v_{\perp,||}$ and $v_{||}$, **Figures 3.9** *f* and **3.10** *f*), and the streamline pattern remains similar to the isotropic one (**Figure 3.11** *c*).

Finally, we consider the flow elicited by a sphere moving perpendicular to the nematic director in a fluid with $\eta_c \ll \eta_b \ll \eta_a$. As expected, $v_{||}$ significantly increases in the meridional

plane because of the $\eta_b \ll \eta_a$ condition (**Figure 3.9** *f*), and the flow streamlines are highly deflected away from the sphere on this plane (**Figure 3.11** *c*). However, this flow has a remarkable characteristic which separates it from all other cases studied above, including the isotropic one; its streamlines converge towards the sphere on the equatorial plane (**Figure 3.11** *c*). Consequently, the sign of $v_{\perp,\perp}$ on this plane is opposite to that of all of the other flow conditions (**Figure 3.10** *f*). This somewhat counterintuitive behavior can be partially understood by inspecting the balance of the different terms in the vorticity equation (3.16) at constant η_b/η_a and varying η_c/η_a (not shown). It is found that the angular profiles of the torques coming from the anisotropy of the stress-strain relation remain similar when varying η_c/η_a. However, the torques coming from the bending of the fluid with respect to the nematic change sign at $\eta_c = \eta_a$, attenuating the effect of the stress-strain anisotropy for $\eta_c > \eta_a$ and magnifying it for $\eta_c < \eta_a$.

3.6.2.4 A Remark on the η_b/η_a Dependence of the Flow

It should be noted that the above classification in terms of η_c/η_a is exclusively intended to facilitate the presentation of the nine flows obtained by combining $\eta_c/\eta_a = 0.1, 1, 10$ and $\eta_b/\eta_a = 0.1, 1, 10$ in the $\vec{v}_0 \perp \vec{n}$ configuration. Likewise, one may choose to classify these flows in relation to the order of magnitude of η_b/η_a. Such classification is indeed implicit in **Figures 3.9** to **3.11**, where the strain pseudo-isotropic condition is depicted with solid (black) lines, whereas the $\eta_b/\eta_a \ll 1$ and $\eta_b/\eta_a \gg 1$ cases are depicted respectively by dashed (blue) and chain-dotted (red) lines. In broad strokes, although the general shape of the velocity profiles is mainly dependent on η_c/η_a, the velocity magnitudes in the direction perpendicular to the sphere's motion and, therefore, the asymmetry in streamline deflection, are mostly dependent on η_b/η_a.

3.7 Conclusions

3.7.1 Summary of Findings

One of the greatest challenges that hinders the application of PTM to complex anisotropic fluids is the lack of knowledge about the dynamics of the probing particle. This paper studies the

creeping flow generated by the motion of a point particle in a nematic incompressible fluid defined by the Leslie-Ericksen constitutive relation. The equations governing this flow are generally applicable to a broad range of nematic systems, ranging from liquid crystals to aligned biopolymer networks that are strongly coupled to their solvent, and nematic visco-elastomers.

The response function $\overline{\overline{\zeta}}$ of a sphere in a nematic fluid is a 3×3 tensor that provides the drag force $\vec{F}$ experienced by the particle as

$$\vec{F} = \overline{\overline{\zeta}} \cdot \vec{v}_0, \tag{3.70}$$

where $\vec{v}_0$ is the velocity of the particle. This tensor only has two independent values, $\zeta_{||}$ and $\zeta_{\perp}$, which respectively represent the resistance of the fluid to the motion of the particle in the directions parallel and perpendicular to the nematic director, $\vec{n}$ [33]. In this work, we provide explicit analytical expressions for $\zeta_{||}$ and $\zeta_{\perp}$, *i.e.* the equivalent of Stokes' drag formula for a nematic fluid, by performing a multipole expansion in Fourier space. These formulae depend on up to four viscosity coefficients: the three Miesowicz viscosities η_a, η_b and η_c, and the first Leslie viscosity α_1. Our solution compares well with the results from previous numerical simulations [63] in the limited region of the parameter space where the simulation data are available. Similar to [73], we observe that the flow caused by a particle moving parallel to the nematic ($\vec{v}_0 || \vec{n}$) is axially symmetric and $\zeta_{||}$ is independent of the first Miesowicz viscosity. On the other hand, the flow originated by a particle moving perpendicular to the nematic ($\vec{v}_0 \perp \vec{n}$) is three-dimensional and $\zeta_{\perp}$ depends on all four viscosity coefficients. It is important to note, however, that the $\vec{v}_0 || \vec{n}$ flow is independent of η_a only if the velocities of the network and the solvent are divergence-free. This requirement is only satisfied when the viscous coupling between the network and the solvent is strong and the network velocity matches that of the incompressible solvent.

In a nematic two-fluid gel, anisotropy can present itself through the viscous coupling between the network and the solvent, as well as through the network's constitutive equations. The anisotropy arising from the coupling has been illustrated by considering an idealized network formed by a square array of circular cylinders, which opposes twice as much resistance to the

relative motion of the solvent in the $\perp$ direction than in the $||$ direction. Further analysis of the effect of anisotropic coupling will require relaxing the strong coupling assumption and is beyond the scope of this study. The anisotropy of the Leslie-Ericksen constitutive relation can, however, be thoroughly studied in the present formulation. We find that the response function is affected mainly by the anisotropic diffusion of momentum along different directions (*i.e.* anisotropy in the stress-strain relationship), and by the resistance of the fluid to bending. Analysis of the equations of fluid motion indicates that momentum diffusivity is anisotropic when $\eta_a \neq \eta_b$ and that the fluid opposes resistance to bending when $\eta_a \neq \eta_c$. We have studied these two mechanisms independently from each other by examining the response function in a rotationally pseudo-isotropic fluid where the bending stresses are zero and in a strain pseudo-isotropic fluid where the stress-strain relation is isotropic. The first of these fluids is governed by a pseudo-Stokes equation with different viscosities $\eta_{||} = \eta_b$ and $\eta_\perp = \eta_a$ in the directions parallel and perpendicular to the nematic director. The second fluid is characterized by an isotropic momentum diffusivity $\eta = \eta_a$ plus a resistance to bending $\Delta\eta = \eta_c - \eta_a$. A comparative analysis of these two "pure" conditions indicates that anisotropic momentum diffusivity leads to greater changes in $\zeta_{||}$, whereas $\zeta_\perp$ is more influenced by the bending resistance of the fluid.

It is also found that directional momentum diffusivity has a limited effect on the response function in rotationally pseudo-isotropic fluids, so that $\zeta_{||}/\eta_{||}$ and $\zeta_\perp/\eta_\perp$ reach constant asymptotic values for high levels of anisotropy with the only exception of $\zeta_{||}/\eta_{||}(\eta_{||} \ll \eta_\perp)$. In fluids with zero resistance to bending, this result provides some level of justification for the qualitative usage of effective directional viscosities, which are defined by applying Stokes's drag law separately along the $||$ and $\perp$ directions. However, it is important to note that the thus estimated effective viscosities differ from the actual viscosities of the fluid by over one order of magnitude for moderate levels of anisotropy like those observed in reconstituted biopolymer networks and the cytoskeleton of cultured animal cells. Furthermore, the very notion of directional effective viscosities may be misleading in fluids with an appreciable resistance to bending because the effect of $\Delta\eta$ is felt in both components of the response function for all levels of anisotropy.

The present study is finalized by a parametric description of the far velocity field around

a spherical particle under different anisotropy conditions. For simplicity and due to the observed small influence of the first Leslie viscosity on the response function, the analysis is restricted to zero values of this coefficient ($\alpha_1 = 0$). When the particle moves parallel to the nematic director, the axial symmetry of the flow establishes a constraint between the bending stresses in the fluid and the directional diffusion of momentum, which cannot vary independently of each other in this flow configuration. As a consequence, the flow pattern varies little with respect to the isotropic case although the level of streamline deflection increases when $\eta_b = \eta_{||} > \eta_\perp = \eta_c$ and vice versa. When the sphere moves perpendicular to the nematic director, the flow is three-dimensional and the directional diffusion of momentum can be varied independently of the bending resistance of the fluid through the viscosity ratios η_b/η_a and η_c/η_a. When $\eta_c/\eta_a \gg 1$, the fluid opposes high resistance to bending and the flow differs little from the isotropic case, similar to the $\vec{v}_0||\vec{n}$ flow. However, when η_c/η_a is of order unity, anisotropic momentum diffusivity can lead to large changes in the flow structure which essentially consist of asymmetric streamline deflection; for $\eta_b > \eta_a$, the streamlines are deflected more in the equatorial plane than in the meridional ones, and the opposite happens for $\eta_b < \eta_a$. Intriguingly, when $\eta_c/\eta_a \ll 1$, the resistance to bending enhances the flow asymmetry caused by anisotropic momentum diffusivity rather than reducing it, so much as to cause the streamlines to converge towards the sphere in the equatorial plane when $\eta_b \ll \eta_a$.

The parametric study of anisotropic viscosity effects on the flow of a nematic fluid around a sphere would be incomplete without a survey of the experimental values of the viscosity coefficients reported in the literature. Such a survey is useful in determining which of the conditions explored in this chapter are more likely to be observed experimentally and, at the same time, it can offer new insight about the dynamics of those fluids. Unfortunately, there is little information about the anisotropic rheology of nematic biopolymer gels, and most of this information comes from effective viscosity approaches that suffer from the limitations described above. Our analysis suggests that these biopolymers are relatively close to a rotationally pseudo-isotropic fluids with $0.5 \lesssim \eta_\perp/\eta_{||} \lesssim 100$ but these values should only be taken as rough estimations. For nematic liquid crystals, the situation is better and we find values of the Miesowicz

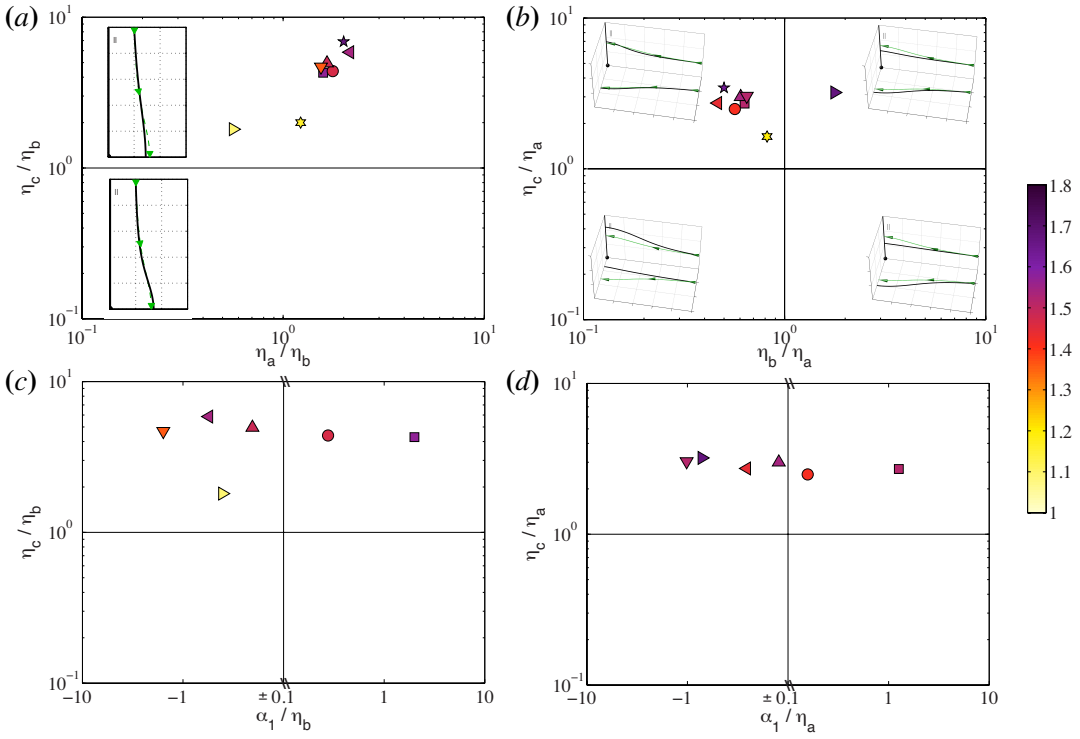

Figure 3.12: Survey of Miesowicz viscosity coefficients reported for nematic liquid crystals in the literature, plotted in the scaling of **Figures 3.2** and **3.3**: (*a*, *c*) $\zeta_{||}/6\pi a\eta_b$; (*b*, *d*) $\zeta_{\perp}/6\pi a\eta_a$. Each symbol represents a different compound and has been coloured according to the corresponding value of the response function as predicted by equations (3.33)-(3.34), and according to the colorbar on the right hand side of the figure: □, PPA [146, 116, 108]; ○, MBBA [49, 82]; △, 5CB [135, 61]; ▽, MBPP [61]; ◁, E7 [152]; ▷, UCF-02 [152]; ★, N4 [6]; ∗, 8OCB [66]. (*a*, *b*) also include the representative streamline pattern corresponding to each region of the parameter space. For reference, the isotropic streamlines are also included in green.

viscosities for eight different compounds. This information is summarized in **Figure 3.12** using the same scaling as **Figures 3.2** and **3.3**. The vast majority of the compounds have $\eta_c/\eta_a \approx 3$ and $0.5 \lesssim \eta_b/\eta_a \lesssim 0.8$, which implies that their bending resistance is relatively high and that, in contrast to biopolymer networks, nematic liquid crystals can be considered to behave somewhat closer to a strain pseudo-isotropic fluid than to a rotationally pseudo-isotropic fluid. Interestingly, all of the liquid crystals considered are in the range where α_1 has a small effect on the flow.

Although the main motivation for this study is to provide fundamental understanding of the dynamics of a microrheology probe in nematic fluids, many of the results presented here have broader applications. Modelling the motility of spermatozoa in the cervical mucus is just one example of such applications. This mucus varies through different phases along the ovulatory

cycle, including one in which the mucin network aligns parallel to the direction of the reproductive tract thereby favouring the directed migration of spermatozoa [22]. This anisotropic synergy could be studied in more detail by modeling each swimmer as a superposition of regularized point forces using the anisotropic Green's functions derived in this study.

3.7.2 Model Limitations

The present formulation is linear, incompressible and assumes affine deformations. Thus, the results in this dissertation are valid only for small deformations and do not apply to regimes displaying strain-stiffening, negative normal stresses and other non-linear effects.

A potential limitation of the results presented in this chapter is that we consider the response of the fluid to be purely viscous. However, most biopolymer gels have viscoelastic properties defined by a dependence of their stress field on their deformation at previous instants of time. A standard procedure to model these effects is to replace the constant viscosity coefficients in equation (3.7) by time-dependent memory functions, and the products by temporal convolutions. Owing to the linear nature of the problem, Fourier transforming in time renders similar equations in which the constant, real-valued viscosity coefficients are replaced by complex-valued functions of the frequency, $\alpha_i \rightarrow \widehat{\alpha}_i(s)$. From there, the calculation of the response function in the frequency domain follows the same steps as in the purely viscous case, although its analysis is complicated by the fact that both the viscosity coefficients and the response function are complex numbers. Such analysis will be performed when we study the Directional Two-Point Particle Tracking Microrheology of Complex Viscoelastic Fluids in **Chapter 4**.

One of the main potential limitations of this study is our assumption that the particle does not distort the nematic director field. Molecular anchoring at the particle surface may distort the director in liquid crystals, leading to dipole or Saturn ring configurations next to the particle. The drag force of a sphere in these configurations has been numerically calculated and reported in [127], and [140], showing considerable differences with respect to results obtained for a uniform nematic. The influence of surface anchoring on the local director topology and particle diffusion has been determined experimentally [74] and numerically [112]. These near-field effects

disappear in two-point PTM [30, 88], which is based on measurements of the correlated motion of distant particles.

Particle motion can also distort the director in the far field due to the finite elastance of the nematic. We have hypothesized that this effect is negligible in passive PTM of biopolymer networks because the thermal energy that drives particle motion is extremely low. However, this energy can be several orders of magnitude higher in active PTM. In that case, the methodology presented here can be extended by prescribing a suitable spatio-temporal nematic distribution [140], including the Frank elasticity constants into the formulation [44] or by calculating the dynamics of the nematic through the Poisson-bracket approach [139].

Finally, assuming a uniform director is relatively reasonable for live cell PTM experiments. Adherent cells are known to align their cytoskeletal fibers in response to directional mechanical stimuli [50, 68] and substratum stiffness [84]. Even in the absence of global alignment, the cytoskeleton will organize in smaller nematic domains in which the director remains locally uniform.

3.8 Appendix A - Green's Functions

In this appendix, we outline the procedures to obtain the Green's functions for the flow velocity and pressure from the equations of motion (3.18), (3.19), (3.20) and (3.3). In Fourier space, these equations of motion become

$$ik_1\widehat{p}+\left(\frac{1}{2\pi}\right)^{3/2}\widehat{f_x}=(\eta_c+\eta_b-\eta_a+\alpha_1)k_1^2\widehat{u}+\eta_b(k_2^2+k_3^2)\widehat{u}, \tag{3.71}$$

$$ik_2\widehat{p}+\left(\frac{1}{2\pi}\right)^{3/2}\widehat{f_y}=\eta_c k_1^2\widehat{v}+\eta_a(k_2^2+k_3^2)\widehat{v}, \tag{3.72}$$

$$ik_3\widehat{p}+\left(\frac{1}{2\pi}\right)^{3/2}\widehat{f_z}=\eta_c k_1^2\widehat{w}+\eta_a(k_2^2+k_3^2)\widehat{w}, \tag{3.73}$$

$$k_1\widehat{u}+k_2\widehat{v}+k_3\widehat{w}=0. \tag{3.74}$$

Assuming a linear solution of the form (3.21)-(3.22), equations (3.71)-(3.74) simplify to

$$\left[(\alpha_1+\eta_c-\eta_a)k_1^2+\eta_b k^2\right]\frac{\widehat{\mathcal{G}}_{1j}}{8\pi}=ik_1\frac{\widehat{\mathcal{P}}_j}{8\pi}+\left(\frac{1}{2\pi}\right)^{3/2}\delta_{1j}, \tag{3.75}$$

$$\left[(\eta_c-\eta_a)k_1^2+\eta_a k^2\right]\frac{\widehat{\mathcal{G}}_{2j}}{8\pi}=ik_2\frac{\widehat{\mathcal{P}}_j}{8\pi}+\left(\frac{1}{2\pi}\right)^{3/2}\delta_{2j}, \tag{3.76}$$

$$\left[(\eta_c-\eta_a)k_1^2+\eta_a k^2\right]\frac{\widehat{\mathcal{G}}_{3j}}{8\pi}=ik_3\frac{\widehat{\mathcal{P}}_j}{8\pi}+\left(\frac{1}{2\pi}\right)^{3/2}\delta_{3j}, \tag{3.77}$$

$$k_i\widehat{\mathcal{G}}_{ij}=0. \tag{3.78}$$

After applying the divergence of equations (3.75)-(3.77) and using (3.78), we obtain

$$\frac{\widehat{\mathcal{P}}_j}{8\pi}=\left(\frac{1}{2\pi}\right)^{3/2}\frac{ik_j}{k^2}-\left[\alpha_1k_1^2+(\eta_b-\eta_a)k^2\right]\frac{ik_1}{k^2}\frac{\widehat{\mathcal{G}_{1j}}}{8\pi}. \tag{3.79}$$

Finally, plugging this result into equations (3.75)-(3.77) and (3.79) we obtain the Green's functions for the velocity and pressure,

$$\frac{\widehat{\mathcal{G}}_{1j}}{\sqrt{8/\pi}}=\frac{\delta_{1j}k^2-k_1k_j}{\alpha_1k_1^2(k_2^2+k_3^2)+\eta_bk^4+(\eta_c-\eta_b)k_1^2k^2}, \tag{3.80}$$

$$\frac{\widehat{\mathcal{G}}_{2j}}{\sqrt{8/\pi}}=\frac{\delta_{2j}}{(\eta_c-\eta_a)k_1^2+\eta_ak^2}-k_2k_j\frac{(1-\delta_{1j})\frac{\alpha_1k_1^2+(\eta_b-\eta_a)k^2}{(\eta_c-\eta_a)k_1^2+\eta_ak^2}+1}{\alpha_1k_1^2(k_2^2+k_3^2)+\eta_bk^4+(\eta_c-\eta_b)k_1^2k^2}, \tag{3.81}$$

$$\frac{\widehat{\mathcal{G}}_{3j}}{\sqrt{8/\pi}}=\frac{\delta_{3j}}{(\eta_c-\eta_a)k_1^2+\eta_ak^2}-k_3k_j\frac{(1-\delta_{1j})\frac{\alpha_1k_1^2+(\eta_b-\eta_a)k^2}{(\eta_c-\eta_a)k_1^2+\eta_ak^2}+1}{\alpha_1k_1^2(k_2^2+k_3^2)+\eta_bk^4+(\eta_c-\eta_b)k_1^2k^2}, \tag{3.82}$$

$$\frac{\widehat{\mathcal{P}}_j}{\sqrt{8/\pi}}=ik_j\left[\frac{1-\delta_{1j}}{k^2}+\frac{\frac{1-\delta_{1j}}{k^2}(\alpha_1k_1^4-\eta_ak^4)+\eta_ak^2+(\eta_b-\eta_a)k_1^2+(\eta_c-\eta_b)k_1^2\delta_{1j}}{\alpha_1k_1^2(k_2^2+k_3^2)+\eta_bk^4+(\eta_c-\eta_b)k_1^2k^2}\right]. \tag{3.83}$$

3.9 Appendix B - Expressions for the Functions Appearing in the Response Function

Equations (3.33) and (3.34) for the response function of a sphere in a nematic fluid refer to the non-dimensional functions

$$A(\vec{\eta}) = \frac{\alpha_1}{\eta_b} + \frac{\eta_c}{\eta_b} - 1, \tag{3.84}$$

$$B(\vec{\eta}) = \sqrt{A(\vec{\eta})^2 + 4\frac{\alpha_1}{\eta_b}}, \tag{3.85}$$

$$C_+(\vec{\eta}) = \sqrt{\frac{A(\vec{\eta}) + B(\vec{\eta})}{2}}, \tag{3.86}$$

$$C_-(\vec{\eta}) = \sqrt{\frac{A(\vec{\eta}) - B(\vec{\eta})}{2}}, \tag{3.87}$$

$$D_+(\vec{\eta}) = A(\vec{\eta}) + 2 + B(\vec{\eta}), \tag{3.88}$$

$$D_-(\vec{\eta}) = A(\vec{\eta}) + 2 - B(\vec{\eta}), \tag{3.89}$$

$$E_+(\vec{\eta}) = A(\vec{\eta})D_+(\vec{\eta}) - 2\left(\frac{\eta_c}{\eta_b} - 1\right), \tag{3.90}$$

$$E_-(\vec{\eta}) = A(\vec{\eta})D_-(\vec{\eta}) - 2\left(\frac{\eta_c}{\eta_b} - 1\right), \tag{3.91}$$

which arise from the integrals in equation (3.30).

These equations degenerate in the limit $B(\vec{\eta}) \longrightarrow 0$, which occurs whenever

$$\frac{\eta_c}{\eta_b} \longrightarrow 1 - \frac{\alpha_1}{\eta_b} \pm 2\sqrt{\frac{-\alpha_1}{\eta_b}}. \tag{3.92}$$

In this limit, $C_+ \to C_-$, $D_+ \to D_-$ and $E_+ \to E_-$, and the expressions that determine the two components of the response function (equations 3.33-3.34) become undefined. Solving the limit yields that $\zeta_{||} = \zeta_\perp = 0$ along the branch associated with the $-$ sign in the square root of equation (3.92), and the same happens for the $-$ branch when $\alpha_1 > \eta_b$. As a consequence, the region of parameter space corresponding to

$$\eta_c < \eta_b - \alpha_1 - 2\sqrt{-\alpha_1\eta_b}, \quad \alpha_1 < -\eta_b \tag{3.93}$$

is associated with unphysical complex values of the response functions and cannot be realized. On the other hand, the signs of $\zeta_{||}$ and $\zeta_{\perp}$ do not change along the branch associated with the $+$ sign in the square root of equation (3.92).

Chapter 3 has been published in the *Journal of Fluid Mechanics* under the title "Flow of a Viscous Nematic Fluid around a Sphere", by M. Gómez-González and J. C. del Álamo (2013), 725, 299-331. The dissertation author is the primary investigator in this publication.

Chapter 4

Two-Point Particle Tracking Microrheology of Nematic Complex Viscoelastic Fluids

4.1 Introduction

Particle tracking microrheology (PTM)[102, 103] is a useful experimental technique to determine the rheological properties of soft materials that exhibit complex mechanical behaviors and are available only in minute amounts [158, 138]. In PTM, micron-sized particles are embedded in a material sample, excited with a known force, and their displacements are measured as a function of time. From these measurements one can determine the material's frequency-dependent shear modulus $G(\omega)$. PTM methods can be classified as active or passive depending on the nature of the excitation force that drives particle motion. Active PTM methods apply an external force on the probing particle whereas in passive PTM methods, the embedded microparticles undergo random motion due to thermal and possibly non-thermal excitations. Active and passive PTM have been applied to characterize, among other systems, colloidal suspensions [15, 106, 157], reconstituted protein gels [3, 53, 110], and the cytoplasm of live cells [147, 34, 56].

Regardless of the mechanism driving particle motion, a key step of PTM is to connect the measured motion with the underlying rheological properties of the medium. This step requires theoretical knowledge of the relation between excitation force and particle velocity as a function of $G(\omega)$. This relation is usually idealized as Stokesian, *i.e.* $F = 6\pi G a/\omega$ where a is the particle radius, but there is a number of near field phenomena that generate deviations from Stokesian behavior. Examples of these are partial slip at the particle surface [48], compressibility [88] and electrochemical surface interactions [149]. To eliminate these short-range effects, Crocker *et al.* [30] introduced two-point PTM, which analyzes the cross-correlated motion of pairs of distant particles.

The vast majority of existing PTM protocols (active and passive, single-point and two-point) assume that the probed medium is isotropic. However, there is a substantial number of soft materials that exhibit molecular or supramolecular alignment leading to anisotropic rheology. Anisotropic particle diffusion has been reported in nematic liquid crystals [94, 148], reconstituted polymer networks [57, 58], and the cytoplasm of cells [34, 117, 84, 18, 98]. Currently, there is not any microrheological method to measure the viscoelastic response of nematic complex fluids. Previous efforts analyzed particle motion in the principal directions of minimum and maximal motion, and applied Stokes' law in each direction [57, 34, 58]. This approach provides effective shear moduli that quantify the viscoelastic resistance experienced by the particle in different directions, but these effective shear moduli could significantly differ from the actual directional viscosities of the fluid (see **Chapter 3** and [54]). To address this limitation, in **Chapter 3** we studied the flow of a nematic fluid around a sphere using the Leslie-Ericksen constitutive relation (see also [54]). We calculated the two drag coefficients in the directions parallel and perpendicular to the nematic as functions of the three directional shear moduli of the fluid. Yet, incorporating this knowledge to one-point PTM leads to an undetermined problem.

In this chapter, we resolve this indetermination by analyzing the cross-correlated motion of a pair of distant spheres in a nematic fluid. Specifically, we derive a closed-form analytical solution for the spheres' mutually induced velocity, *i.e.* the *multiparticle mobility tensor*. We show that this approach provides three independent equations, so that two-point PTM, with the Leslie-

Ericksen constitutive relation can be used to determine the rheological properties of a nematic fluid. To validate and illustrate this novel directional two-Point PTM (D2PTM) formulation, we perform numerical simulations and experiments in a nematic solution of filamentous actin. The results presented in this chapter represent the first report of the measurement of the directional shear moduli of F-actin, enabling future applications of D2PTM to other soft materials.

4.2 Theoretical Foundation of Directional Two-Point Particle Tracking Microrheology

This section describes the motion of spherical PTM probes embedded in a nematic complex fluid defined by the director $\vec{n}$ (**Figure 4.1**). The drag force experienced by the particles, and the interaction between pairs of distant particles (**Figure 4.2**), are calculated. These results are used to develop analysis algorithms for D2PTM.

4.2.1 Mathematical Formulation

The velocity field of an incompressible complex fluid can be described [81] by the Cauchy's momentum equation

$$\rho\dot{\vec{v}} - \nabla\cdot\bar{\bar{\tau}} = \vec{f}, \tag{4.1}$$

together with the continuity equation $\nabla\cdot\vec{v} = 0$, where $\vec{f}$ represents the applied external forces, $\vec{v} = \partial_t\vec{u}$ is the velocity field, $\vec{u}$ is the deformation field, ρ is the density and $\bar{\bar{\tau}}$ is the stress tensor. These equations rely on the assumption of a continuum material and are equally valid for homogeneous one-component materials and semidiluted bio-polymer networks that conform to certain conditions [87], *i.e.* low volume fraction ϕ of the solute, characteristic length of the displacements a larger than the mesh size ξ, and frequencies $\omega \ll 10^4 \mathrm{s}^{-1}$. These conditions are often met in microrheology studies of biological samples, such as the eukaryotic cytoplasm ($\phi \sim 0.01 - 0.02$ [143]) and reconstituted bio-polymer networks ($\phi \sim 0.001 - 0.01$ [132, 53, 58]), where the length scale is the radius of the probing particle $a \gg \xi$ and the frequencies are usually

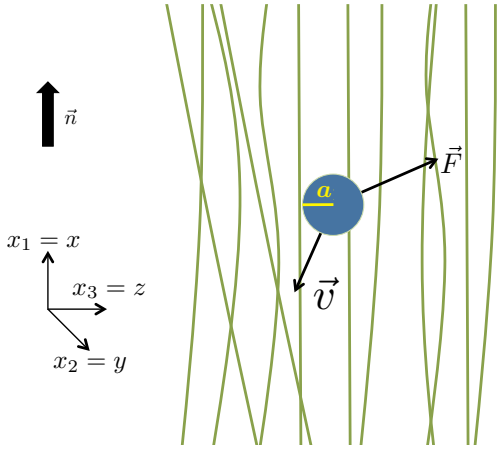

Figure 4.1: Particle of radius a embedded in a nematic complex fluid with director $\vec{n}$. The particle moves with velocity $\vec{v}$ and experiences a resistance force $\vec{F}$.

well below the specified limit.

We estimate a Reynolds number $Re = \rho U a/\eta \sim 10^{-6}$ in PTM experiments [54] and thus neglect inertial terms in the equations of motion. We relate the stress and strain ($\bar{\bar{\varepsilon}}$) tensors via a generalization of the Leslie-Ericksen constitutive equations [41, 86, 33] in the frequency domain,

$$\begin{aligned}\tilde{\tau}_{ij} = &-\tilde{p}\delta_{ij} + \tilde{\alpha}_1^*(s)\tilde{n}_k\tilde{n}_p\tilde{\varepsilon}_{kp}\tilde{n}_i\tilde{n}_j + \tilde{\alpha}_2^*(s)\tilde{n}_i\tilde{N}_j + \tilde{\alpha}_3^*(s)\tilde{n}_j\tilde{N}_i \\ &+ \tilde{\alpha}_4^*(s)\tilde{\varepsilon}_{ij} + \tilde{\alpha}_5^*(s)\tilde{n}_i\tilde{n}_k\tilde{\varepsilon}_{kj} + \tilde{\alpha}_6^*(s)\tilde{n}_j\tilde{n}_k\tilde{\varepsilon}_{ki},\end{aligned} \tag{4.2}$$

where $\tilde{\cdot}$ indicates Laplace transform and s is the frequency. This expression is analogous to the generalized Stokes' formula proposed by Mason and Weitz [102]. It depends on six complex viscoelasticity coefficients $\tilde{\alpha}_k^*(s)$, the director of the nematic $\tilde{n}_i$, and the rate of change of the director with respect to the background gel, $\tilde{N}_i$. The viscoelasticity coefficients are a generalization of the Leslie viscosity coefficients α_k through analytical continuation, and depend on the complex frequency s. The vector $\tilde{N}_i$ is defined as the sum of the substantial derivative of $\tilde{n}_i$ and the rotation of the gel with respect to the nematic, and is more conveniently expressed in real space as

$$\vec{N} = \partial_t\vec{n} + (\vec{v}\cdot\nabla)\vec{n} - (\nabla\wedge\vec{v})\wedge\vec{n}/2. \tag{4.3}$$

The nematic field $\vec{n}$ is determined by the equilibrium of moments of the viscoelastic stresses on the gel and the elastic forces on the nematic. We define the Ericksen number, Er, as the ratio of viscoelastic forces on the gel to elastic forces on the nematic. In the limit of $Er \ll 1$, the viscoelastic forces on the gel generated by the motion of the particle are small enough to not perturb the nematic field, and $\vec{n}$ will be equal to the equilibrium distribution [33]. In a typical PTM experiment the low Ericksen number hypothesis is reasonable far away from the particle. Thus, for the sake of studying the correlated motion of pairs of distant particles to formulate D2PTM, we assume the director field to be uniform in space and constant in time, $\vec{n} = (1,0,0)$.

To reduce the number of free material parameters, we group the viscoelasticity coefficients into three generalized Miesowicz [107] shear moduli,

$$\tilde{G}_a = \tilde{\alpha}_4^*/2, \tag{4.4}$$

$$\tilde{G}_b = (\tilde{\alpha}_3^* + \tilde{\alpha}_4^* + \tilde{\alpha}_6^*)/2, \tag{4.5}$$

$$\tilde{G}_c = (-\tilde{\alpha}_2^* + \tilde{\alpha}_4^* + \tilde{\alpha}_5^*)/2, \tag{4.6}$$

and make use of Parodi's relation [119], $\tilde{\alpha}_6^* = \tilde{\alpha}_2^* + \tilde{\alpha}_3^* + \tilde{\alpha}_5^*$. Under these simplifications, equation (4.1) becomes

$$\partial_x \tilde{\tilde{p}} = (\tilde{G}_c - \tilde{G}_a + \tilde{\alpha}_1^*)\partial_{xx}\tilde{u}_x + \tilde{G}_b \nabla^2 \tilde{u}_x + \tilde{f}_x, \tag{4.7}$$

$$\partial_y \tilde{\tilde{p}} = \quad (\tilde{G}_c - \tilde{G}_a)\partial_{xx}\tilde{u}_y + \tilde{G}_a \nabla^2 \tilde{u}_y + \tilde{f}_y, \tag{4.8}$$

$$\partial_z \tilde{\tilde{p}} = \quad (\tilde{G}_c - \tilde{G}_a)\partial_{xx}\tilde{u}_z + \tilde{G}_a \nabla^2 \tilde{u}_z + \tilde{f}_z, \tag{4.9}$$

where $\tilde{\tilde{p}} = \tilde{p} + (\tilde{G}_c - \tilde{G}_a - \tilde{\alpha}_5^*)\partial_x \tilde{u}_x$ is a modified pressure, and $\vec{r} = (x,y,z)$ and $\vec{\tilde{u}} = (\tilde{u}_x, \tilde{u}_y, \tilde{u}_z)$ are the position and displacement vectors in a Cartesian coordinate system.

4.2.2 Derivation of the Response Function

A spherical particle of radius a, moving at low Reynolds number, experiences a drag force that is proportional to its velocity

$$\tilde{\vec{F}} = -\tilde{\overline{\overline{\zeta}}} \cdot \tilde{\vec{v}}(\vec{x} = \vec{0}) = -\tilde{\overline{\overline{\zeta}}} \cdot \tilde{\vec{v}}_0 = -s\tilde{\overline{\overline{\zeta}}} \cdot \tilde{\vec{u}}_0, \tag{4.10}$$

where $\tilde{\overline{\overline{\zeta}}}$ is the tensorial *Response Function*, also known as *Hydrodynamic Resistance* [70] or *Self-Resistance* [137]. Note that $\vec{v}_0$ and $\vec{F}$ are not parallel to each other in an anisotropic fluid as $\tilde{\overline{\overline{\zeta}}}$ is not proportional to the identity matrix.

To calculate the response function of the particle, we perform a multipole expansion [70, 91, 77]. We first calculate the Green's function of the problem in the Fourier wavenumber domain, and then integrate the Green's function to obtain the velocity of the particle as a function of the driving force. Due to the linearity of the problem, we look for a solution of equations (4.7)-(4.9) of the form

$$\widehat{\vec{v}} = \frac{\widehat{\overline{\overline{\mathcal{G}}}} \cdot \widehat{\vec{f}}}{8\pi} = \frac{1}{8\pi} \left\{ \begin{array}{c} \widehat{\mathcal{G}}_{1j} \widehat{f}_j \\ \widehat{\mathcal{G}}_{2j} \widehat{f}_j \\ \widehat{\mathcal{G}}_{3j} \widehat{f}_j \end{array} \right\}, \tag{4.11}$$

$$\widehat{\overline{p}} = \frac{\widehat{\vec{\mathcal{P}}} \cdot \widehat{\vec{f}}}{8\pi} = \frac{1}{8\pi} \widehat{\mathcal{P}}_j \widehat{f}_j, \tag{4.12}$$

where $\widehat{\cdot}$ denotes Fourier transform along the spatial coordinates, $\widehat{\mathcal{G}}_{ij}$ and $\widehat{\mathcal{P}}_j$ are the Green's functions for the velocity and the pressure, and $\widehat{\vec{f}}$ is the driving force applied on the fluid. Solving for the Green's functions of the problem yields (see **Chapter 3** and [54] for more details)

$$\frac{\widehat{\mathcal{P}}_j}{\sqrt{8/\pi}} = \sqrt{-1} k_j \frac{(1 - \delta_{1j})c + b}{d}, \tag{4.13}$$

and

$$\frac{\widehat{\mathcal{G}}_{1j}}{s\sqrt{8/\pi}} = \frac{\delta_{1j}k^2 - k_1k_j}{d}, \tag{4.14}$$

$$\frac{\widehat{\mathcal{G}}_{lj}}{s\sqrt{8/\pi}} = \frac{\delta_{lj}}{b} - k_lk_j\frac{(1-\delta_{1j})c+b}{db}, \tag{4.15}$$

with $l = 2,3$, and where

$$b(\vec{\mu};\vec{k}) = (\tilde{G}_c - \tilde{G}_a)k_1^2 + \tilde{G}_a k^2, \tag{4.16}$$

$$c(\vec{\mu};\vec{k}) = \tilde{\alpha}_1^* k_1^2 + (\tilde{G}_b - \tilde{G}_a)k^2, \tag{4.17}$$

$$d(\vec{\mu};\vec{k}) = \tilde{\alpha}_1^* k_1^2(k_2^2+k_3^2) + \tilde{G}_b k^4 + (\tilde{G}_c - \tilde{G}_b)k_1^2k^2, \tag{4.18}$$

$\vec{k} = (k_1,k_2,k_3) = (k_x,k_y,k_z)$ is the wavenumber vector, $\vec{\mu} = (\tilde{\alpha}_1^*, \tilde{G}_a, \tilde{G}_b, \tilde{G}_c)$ is the viscoelasticity vector, and δ_{ij} is the Kronecker delta.

The particle velocity is calculated by performing the inverse Fourier transform of equation (4.11) particularized at $\vec{x} = \vec{0}$,

$$\tilde{\vec{v}}_0 = \frac{1}{(2\pi)^{3/2}}\iiint \frac{\widehat{\widehat{\mathcal{G}}}}{8\pi}\cdot\widehat{\vec{f}}(\vec{k})d^3k = -\tilde{\tilde{\zeta}}^{-1}\cdot\tilde{\vec{F}}, \tag{4.19}$$

where $\widehat{\vec{f}}(\vec{k}) = \vec{f}\cdot\widehat{H}(\vec{k})$ is the Fourier transform of $\vec{f}(\vec{x})$ and the function $\widehat{H}(\vec{k})$ is a regularization kernel that localizes the drag force in physical and/or Fourier space. We choose to distribute the force as a Gaussian around the origin [5, 26], so that

$$\widehat{H}(k) = e^{-a^2k^2/\pi}. \tag{4.20}$$

The response function is thus given by

$$\tilde{\tilde{\zeta}}^{-1}\Big|_{ij} = \frac{s}{4\sqrt{2\pi}a}\int_{\theta=0}^{\theta=\pi}\sin\theta\left(\int_{\varphi=0}^{\varphi=2\pi}\frac{k^2\widehat{\mathcal{G}}_{ij}}{8\pi}d\varphi\right)d\theta, \tag{4.21}$$

where $\vec{k} = (k, \phi, \theta)$ is the Fourier wavenumber vector in spherical coordinates. Due to the symmetry of $\widehat{\mathcal{G}}_{ij}$, the tensor $\tilde{\tilde{\zeta}}^{-1}$ is diagonal and equation (4.10) becomes

$$\tilde{\vec{F}} = -s \begin{bmatrix} \tilde{\zeta}_{||} & 0 & 0 \\ 0 & \tilde{\zeta}_{\perp} & 0 \\ 0 & 0 & \tilde{\zeta}_{\perp} \end{bmatrix} \cdot \tilde{\vec{u}}_0, \tag{4.22}$$

where $\tilde{\zeta}_{\parallel}$ and $\tilde{\zeta}_{\perp}$ are respectively the components of the response function in the directions parallel and perpendicular to the nematic. Their general form is provided in **Appendix 4.6** (equations 4.49 and 4.50) together with its singularities and Taylor expansion around the isotropy point.

The influence of the parameter $\tilde{\alpha}_1^*$ in the response function has been shown to be weak compared to that of the other coefficients [54], and its value has been measured to be very small for many nematic materials [146, 49, 61, 152, 6]. Thus, we focus on the limit case $\tilde{\alpha}_1^* \to 0$, for which the principal components of the response function are defined by

$$s\tilde{\zeta}_{||}\Big|_{\tilde{\alpha}_1^* \to 0} = \frac{4\pi a(\tilde{G}_c - \tilde{G}_b)}{\frac{\tilde{G}_c}{\tilde{G}_b} \frac{\arctan\left(\sqrt{\tilde{G}_c/\tilde{G}_b - 1}\right)}{\sqrt{\tilde{G}_c/\tilde{G}_b - 1}} - 1}, \tag{4.23}$$

$$s\tilde{\zeta}_{\perp}\Big|_{\tilde{\alpha}_1^* \to 0} = \frac{8\pi a(\tilde{G}_c - \tilde{G}_b)}{1 - \frac{\arctan\left(\sqrt{\tilde{G}_c/\tilde{G}_b - 1}\right)}{\sqrt{\tilde{G}_c/\tilde{G}_b - 1}} + \frac{\tilde{G}_c - \tilde{G}_b}{\tilde{G}_a} \frac{\arctan\left(\sqrt{\tilde{G}_c/\tilde{G}_a - 1}\right)}{\sqrt{\tilde{G}_c/\tilde{G}_a - 1}}}, \tag{4.24}$$

which exclusively depend on the three generalized Miesowicz shear moduli.

4.2.3 Particle-Particle Hydrodynamic Interactions in a Nematic Complex Fluid

Consider two distant particles denoted α and β, embedded in a nematic complex fluid as shown in **Figure 4.2**, where a_α and a_β represent the particle radii, $\vec{r}_{\alpha,\beta}$ is the vector that connects the center of the particles, and $\|\vec{r}_{\alpha,\beta}\| \gg a_\alpha,\ a_\beta$.

When particle β moves with velocity $\tilde{\vec{v}}_\beta^{\,0}$ it displaces the fluid around itself and induces a

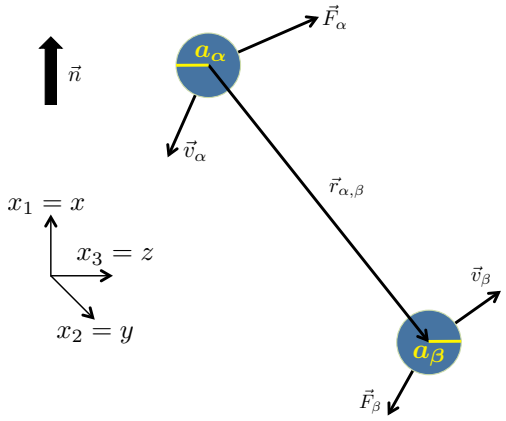

Figure 4.2: Hydrodynamic interaction between two particles separated by a vector $\vec{r}_{\alpha,\beta}$.

velocity

$$\tilde{\vec{v}}^{\,I}_{\alpha,\beta} = \frac{\tilde{\tilde{\mathcal{G}}} \cdot \tilde{\tilde{\zeta}}}{8\pi} \cdot \tilde{\vec{v}}^{\,0}_{\beta} \tag{4.25}$$

on particle α. Contrary to the isotropic case, the induced velocity depends not only on the distance between particles, $|\vec{r}_{\alpha,\beta}|$, but also on the orientation of $\vec{r}_{\alpha,\beta}$ with respect to the nematic director. This induced velocity will create an additional drag force on particle α. Up to first order, the drag force acting on particle α is

$$\tilde{\vec{F}}_\alpha = -\tilde{\tilde{\zeta}} \cdot \left(\tilde{\vec{v}}^{\,0}_{\alpha} + \frac{\tilde{\tilde{\mathcal{G}}}}{8\pi} \cdot \tilde{\tilde{\zeta}} \cdot \tilde{\vec{v}}^{\,0}_{\beta} \right). \tag{4.26}$$

Reciprocally, the total velocity of particle α is

$$\tilde{\vec{v}}_\alpha = -\tilde{\tilde{\zeta}}^{-1} \cdot \tilde{\vec{F}}^{\,0}_{\alpha} - \frac{\tilde{\tilde{\mathcal{G}}}}{8\pi} \cdot \tilde{\vec{F}}^{\,0}_{\beta}. \tag{4.27}$$

The dependence between the velocities and drag forces of both particles can be expressed

in matrix form [137] as

$$\begin{bmatrix} \tilde{\vec{F}}_\alpha \\ \hdashline \tilde{\vec{F}}_\beta \end{bmatrix} = -\tilde{\tilde{\tilde{\mathcal{Z}}}} \cdot \begin{bmatrix} \tilde{\vec{v}}_\alpha \\ \hdashline \tilde{\vec{v}}_\beta \end{bmatrix}, \tag{4.28}$$

where $\tilde{\tilde{\tilde{\mathcal{Z}}}}(\vec{r};s)$ is the *multiparticle resistance tensor* and its inverse, the *multiparticle mobility tensor*. When the two particles are far apart from each other their long range interaction is very weak, and each particle's self-induced drag force dominates over their mutually-induced force. Thus, the resistance and mobility tensors can be simplified up to first order as

$$\tilde{\tilde{\tilde{\mathcal{Z}}}} \approx \begin{bmatrix} \tilde{\tilde{\zeta}} & \dfrac{\tilde{\tilde{\zeta}} \cdot \tilde{\tilde{\tilde{\mathcal{G}}}} \cdot \tilde{\tilde{\zeta}}}{8\pi} \\ \hdashline \dfrac{\tilde{\tilde{\zeta}} \cdot \tilde{\tilde{\tilde{\mathcal{G}}}} \cdot \tilde{\tilde{\zeta}}}{8\pi} & \tilde{\tilde{\zeta}} \end{bmatrix}, \tag{4.29}$$

and

$$\tilde{\tilde{\tilde{\mathcal{Z}}}}^{-1} \approx \begin{bmatrix} \tilde{\tilde{\zeta}}^{-1} & \dfrac{\tilde{\tilde{\tilde{\mathcal{G}}}}}{8\pi} \\ \hdashline \dfrac{\tilde{\tilde{\tilde{\mathcal{G}}}}}{8\pi} & \tilde{\tilde{\zeta}}^{-1} \end{bmatrix}. \tag{4.30}$$

This result is essential to derive D2PTM formulae in **§4.2.5** below. To this end, it is necessary to transform the Fourier expressions (4.14)-(4.15) of the Green's function back into the physical domain. For a nematic fluid, it is sufficient to obtain the inverse transform particularized at $z = 0$ due to the axial symmetry of the nematic configuration. To exploit this symmetry, we work on the plane defined by $\vec{n}$ and $\vec{r}_{\alpha,\beta}$ and apply a simple rotation of the coordinate system to transform this

plane into $z=0$. The general form $\overline{\overline{\mathcal{G}}}(x,y,z=0)$ is given in **Appendix 4.7** (equations 4.69-4.74), along with its singularities and Taylor expansion around the isotropy condition. In the limit $\tilde{\alpha}_1^* \to 0$, the components of the Green's function are

$$\frac{\tilde{\mathcal{G}}_{11}}{s}\Big|_{\substack{z=0\\ \tilde{\alpha}_1^*\to 0}} = \frac{2}{\tilde{G}_b-\tilde{G}_c}\left(\frac{1}{\sqrt{x^2+y^2}} - \frac{\tilde{G}_c}{\tilde{G}_b}\frac{1}{\sqrt{x^2+\frac{\tilde{G}_c}{\tilde{G}_b}y^2}}\right), \tag{4.31}$$

$$\frac{\tilde{\mathcal{G}}_{12}}{s}\Big|_{\substack{z=0\\ \tilde{\alpha}_1^*\to 0}} = \frac{2}{\tilde{G}_b-\tilde{G}_c}\frac{x}{y}\left(\frac{-1}{\sqrt{x^2+y^2}} + \frac{1}{\sqrt{x^2+\frac{\tilde{G}_c}{\tilde{G}_b}y^2}}\right), \tag{4.32}$$

$$\frac{\tilde{\mathcal{G}}_{22}}{s}\Big|_{\substack{z=0\\ \tilde{\alpha}_1^*\to 0}} = \frac{2}{\tilde{G}_b-\tilde{G}_c}\frac{x^2}{y^2}\left[\frac{1}{\sqrt{x^2+y^2}} - \frac{\tilde{G}_b}{\tilde{G}_c}\frac{1}{\sqrt{x^2+\frac{\tilde{G}_c}{\tilde{G}_b}y^2}} + \frac{1}{x^2}\left(\frac{\tilde{G}_b}{\tilde{G}_c}-1\right)\sqrt{x^2+\frac{\tilde{G}_c}{\tilde{G}_a}y^2}\right], \tag{4.33}$$

$$\frac{\tilde{\mathcal{G}}_{33}}{s}\Big|_{\substack{z=0\\ \tilde{\alpha}_1^*\to 0}} = \frac{2}{\tilde{G}_b-\tilde{G}_c}\frac{1}{y^2}\left[-\sqrt{x^2+y^2} + \frac{\tilde{G}_b}{\tilde{G}_c}\sqrt{x^2+\frac{\tilde{G}_c}{\tilde{G}_b}y^2} - \left(\frac{\tilde{G}_b}{\tilde{G}_c}-1\right)\frac{x^2}{\sqrt{x^2+\frac{\tilde{G}_c}{\tilde{G}_a}y^2}}\right]. \tag{4.34}$$

4.2.4 Directional One-Point Particle Tracking Microrheology: An Undetermined Problem

The Einstein relation between the one-dimensional mean squared displacements (MSD) of a particle undergoing Brownian motion and its hydrodynamic drag is

$$\tilde{\zeta} = \frac{2k_BT}{s^2\langle \Delta x(0), \Delta\tilde{x}(s)\rangle}, \tag{4.35}$$

where k_B is the Boltzmann constant, T the temperature and $\langle \Delta x(0), \Delta\tilde{x}(s)\rangle$ the Laplace transform of the MSD. This Einstein equation can be adapted to describe the motion of a particle embedded in a nematic complex fluid using the results derived in **§4.2.1** and **§4.2.2**. In the principal directions defined by the nematic and its orthogonal plane, the response function tensor is diagonal (see equation 4.22). Thus, the MSD measured in these principal directions are independent of each other (zero cross-correlation) and equation (4.35) can be applied separately along each

principal direction [57, 34, 58], yielding

$$6\pi a\tilde{G}_{\text{eff},||} = s\tilde{\zeta}_{||} = \frac{2k_BT}{s\langle \Delta x_{||}(0), \Delta\tilde{x}_{||}(s)\rangle}, \tag{4.36}$$

$$6\pi a\tilde{G}_{\text{eff},\perp} = s\tilde{\zeta}_{\perp} = \frac{2k_BT}{s\langle \Delta x_{\perp}(0), \Delta\tilde{x}_{\perp}(s)\rangle}. \tag{4.37}$$

However, it is important to note that these two equations together with (4.23)-(4.24), are not sufficient to determine the three Miesowicz shear moduli $\tilde{G}_a$, $\tilde{G}_b$ and $\tilde{G}_c$ [54]. Next section shows that analyzing the correlated motion of pairs of distant particles resolves this indetermination.

4.2.5 Directional Two-Point Particle Tracking Microrheology

Consider two distant particles whose coordinates and velocity components are represented by $x_{\alpha,i}$ and $v_{\alpha,i}$ in a Cartesian coordinate system with its $x_1 = x_{||}$ direction parallel to the nematic, its $x_2 = x_\perp$ direction contained in the plane defined by the two particles and the nematic, and the $x_3 = z$ direction perpendicular to said plane (see **Figure 4.2**). The two particles are thus contained in the plane $z = 0$ and equations (4.31)-(4.34) hold. Following Squires and Mason [137], we obtain that

$$\langle \Delta x_{\alpha,i}(0), \Delta\tilde{x}_{\beta,j}(s)\rangle = \frac{2k_BT}{s^2}\left[\tilde{\mathcal{Z}}^{-1}(\vec{r}_{\alpha,\beta};s)\right]_{i,j}, \tag{4.38}$$

where $\overline{\overline{\tilde{\mathcal{Z}}}}(\vec{r};s)$ is the multiparticle resistance tensor derived in **§4.2.3**, whose inverse is given in equation (4.30). The upper left and lower right blocks of (4.30) provide the one-point directional PTM formula derived by Gómez-González and del Álamo [54] (presented in **Chapter 3** and summarized in **§4.2.4**). The off-diagonal blocks of the tensor provide the two-point formulae

$$\langle \Delta x_{\alpha,i}(0), \Delta\tilde{x}_{\beta,j}(s)\rangle = \frac{k_BT}{4\pi s^2}\tilde{\mathcal{G}}_{ij}, \qquad \alpha \neq \beta. \tag{4.39}$$

This symmetric tensor relation provides with six equations for $\tilde{G}_a$, $\tilde{G}_b$ and $\tilde{G}_c$ but these equations are not linearly independent. The incompressibility condition $\nabla \cdot \overline{\overline{\mathcal{G}}} = \vec{0}$ provides three relations

between the elements $\tilde{\mathcal{G}}_{ij}$, effectively reducing the number of independent equations (4.39) to three.

In the ideal experimental scenario where one could measure 3D particle displacements as a function of time, it would be convenient to use diagonal equations of (4.39) to solve for the Miesowicz shear moduli from the measured two-point mobility tensor. However, typical experiments only provide accurate measurements of 2D particle displacements. In this scenario, it is still possible to calculate the three Miesowicz shear moduli from the equations corresponding to $\tilde{\mathcal{G}}_{11}$, $\tilde{\mathcal{G}}_{12}$ and $\tilde{\mathcal{G}}_{22}$, but it is advisable to precondition the equations as described below to minimize numerical error.

The cross-correlated displacements in the left hand side of (4.39) have very low values due to the low energy and long range of the particle-particle interactions. Thus, it is necessary to compile averages over a large number of particle pairs to obtain statistically meaningful results. Because $\tilde{\mathcal{G}}_{ij} \sim r_{\alpha,\beta}^{-1}$, the averaging procedure converges faster if (4.39) is renormalized by $r_{\alpha,\beta}$. Additionally, $\tilde{\mathcal{G}}_{12}$ is typically much smaller than $\tilde{\mathcal{G}}_{11}$ and $\tilde{\mathcal{G}}_{22}$, which can lead to numerical errors when jointly solving the three equations. Considering that $\tilde{\mathcal{G}}_{12} \sim x/(y\sqrt{x^2+y^2})$, we use this factor to renormalize the corresponding equation. The resulting system of equations for the calculation of the Miesowicz shear moduli is

$$\sum_{\alpha,\beta} r_{\alpha,\beta}\langle \Delta x_{\alpha,||}(0), \Delta\tilde{x}_{\beta,||}(s)\rangle = \frac{k_B T}{4\pi s^2}\cdot\sum_{\alpha,\beta} r_{\alpha,\beta}\tilde{G}_{11}(\vec{r};s), \tag{4.40}$$

$$\sum_{\alpha,\beta} \frac{y}{x} r_{\alpha,\beta}\langle \Delta x_{\alpha,||}(0), \Delta\tilde{x}_{\beta,\perp}(s)\rangle = \frac{k_B T}{4\pi s^2}\cdot\sum_{\alpha,\beta} \frac{y}{x} r_{\alpha,\beta}\tilde{G}_{12}(\vec{r};s), \tag{4.41}$$

$$\sum_{\alpha,\beta} r_{\alpha,\beta}\langle \Delta x_{\alpha,\perp}(0), \Delta\tilde{x}_{\beta,\perp}(s)\rangle = \frac{k_B T}{4\pi s^2}\cdot\sum_{\alpha,\beta} r_{\alpha,\beta}\tilde{G}_{22}(\vec{r};s), \tag{4.42}$$

Equations (4.40)-(4.42) form a system of non-linear equations that must be solved iteratively for each Laplace frequency.

Figure 4.3 presents a flow chart summarizing the D2PTM analysis. We first track the embedded probing particles in two random orthogonal directions x and y. The geometry of the experiment must be such that x and y define a plane containing the director of the gel, $\vec{n}$. We

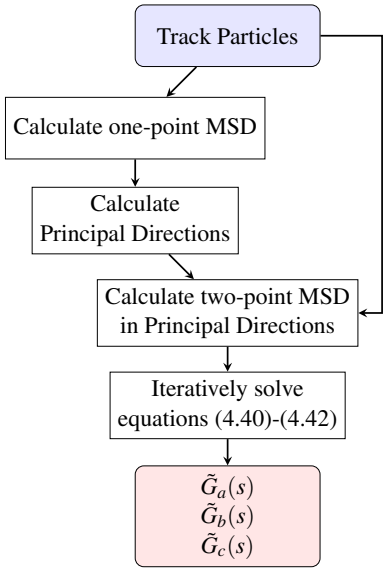

Figure 4.3: Flow diagram summarizing the D2PTM analysis procedures.

then calculate the average of their 1P MSD, *i.e.* $\langle \Delta x^2(\tau) \rangle$, $\langle \Delta y^2(\tau) \rangle$ and $\langle \Delta x, \Delta y(\tau) \rangle$. From them, we calculate their principal directions $x_{||}$ and $x_{\perp}$, *i.e.* the two orthogonal directions where the cross-MSD term $\langle \Delta x_{||}, \Delta x_{\perp}(\tau) \rangle$ is minimum. One of the principal directions is parallel to $\vec{n}$. After that, we calculate the two-point MSD of each pair of probing particles, in principal directions, and from them we solve equations (4.40)-(4.42) iteratively. Their solution will provide the values of $\tilde{G}_a(s)$, $\tilde{G}_b(s)$ and $\tilde{G}_c(s)$.

4.3 Validation of D2PTM by Numerical Simulation

This section assesses the feasibility and accuracy of our D2PTM analysis procedures. To this end, we simulate the Brownian motion of particles embedded in a directional viscoelastic fluid of known Miesowicz viscoelasticity coefficients, including the particle-particle hydrodynamic interactions. We then analyze the simulated particle trajectories using the method presented in **§4.2.5** above, and compare the shear moduli values obtained from this analysis with those initially prescribed in the Brownian motion simulation.

4.3.1 Simulation Methodology

In our simulations, we prescribe the Miesowicz shear moduli using a Kelvin-Voigt model $\tilde{G}_k = \mu_k + s \cdot \eta_k$ with constant μ_k and η_k. The Brownian motion experienced by each particle is defined as a Gaussian process with average and autocorrelation consistent with the fluctuation-dissipation theorem [76, 114]:

$$\langle v_x(t) \rangle = \langle v_y(t) \rangle = \langle v_z(t) \rangle = 0, \tag{4.43}$$

$$\langle v_x(t), v_x(t+\tau) \rangle = \mathcal{L}^{-1} \left(\frac{2k_B T}{ms + \tilde{\zeta}_{||}(s)}; s \to \tau \right), \tag{4.44}$$

$$\langle v_y(t), v_y(t+\tau) \rangle = \langle v_z(t), v_z(t+\tau) \rangle = \mathcal{L}^{-1} \left(\frac{2k_B T}{ms + \tilde{\zeta}_{\perp}(s)}; s \to \tau \right), \tag{4.45}$$

where $\mathcal{L}^{-1}(\cdot; s \to t)$ represents the inverse Laplace transform. A key step of the simulations is to calculate direct and inverse Laplace transforms. The numerical implementation of these transforms is explained in detail in **Appendix 4.8**. Since the particles are small, we assume that inertial forces are negligible compared with the hydrodynamic forces acting on them, i.e. $ms \ll \tilde{\zeta}_j(s)$. This assumption has been shown to be valid for the frequencies accessible to PTM experiments [54, 88].

By virtue of the central limit theorem, it can be shown that equations (4.43), (4.44) and (4.45) describe three multivariate normal distributions, one for the velocity in each direction [113]. Each distribution is completely defined by a zero average vector and a covariance matrix $\overline{\overline{\Sigma}}_{||}$ or $\overline{\overline{\Sigma}}_{\perp}$ with components

$$\Sigma_{||,kl} = 2k_B T \cdot \mathcal{L}^{-1} \left(\tilde{\zeta}_{||}^{-1}(s); s \to \tau \right) \Big|_{\tau = t_k - t_l}, \tag{4.46}$$

$$\Sigma_{\perp,kl} = 2k_B T \cdot \mathcal{L}^{-1} \left(\tilde{\zeta}_{\perp}^{-1}(s); s \to \tau \right) \Big|_{\tau = t_k - t_l}. \tag{4.47}$$

We prescribe fixed values for μ_a, μ_b, μ_c, and η_a η_b, η_c, and calculate the covariance matrices (4.46) and (4.47). The time distribution of velocities for each particle, $\vec{v}_\alpha^{\,0}(t)$, is drawn from a Multivariate Random Number generator. **Figure 4.4** shows the parallel and perpendicular covariance kernels calculated from (4.46)-(4.47) for $\mu_a = 0.5$ Pa, $\mu_b = 0.01$ Pa, $\mu_c = 1$ Pa and

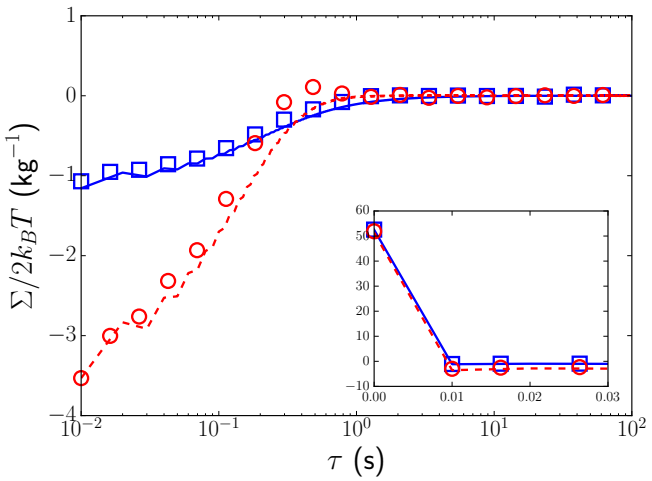

Figure 4.4: Covariance of the velocity components of the simulated particles, represented as a function of time separation τ. Symbols: averaged autocorrelation of the $||$ (□) and $\perp$ (○) velocity components of the simulated particles, represented as a function of time separation τ. Lines: covariance kernels $\Sigma_{||}$ (——) and $\Sigma_{\perp}$ (– – –) (equations 4.46-4.47), represented as a function of the time separation. The vicinity of $\tau = 0$ is shown in the inset.

$\eta_a = \eta_b = \eta_c = 0.1$ Pa·s, compared to the average of the autocorrelation of the velocity samples drawn from the multivariate random number generator, for $10,000$ time steps and $3,325$ particles. The plot shows that the autocorrelation closely follows the prescribed covariance kernels, indicating that the simulation procedures are self-consistent.

In each simulation we consider five particles randomly located at a distance not smaller than ten radii from their neighbors, which is representative of the F-actin experiments presented in **§4.4.3**. From the simulated Brownian motion of the particles, we calculate the hydrodynamic interactions between pairs of particles as described in **§4.2.3**. The computation of these interactions can be accelerated by exploiting the fact that the jumps in particle position are negligible compared to the inter-particle distance, which allows us to assume constant $\vec{r}(s)$. Thus, for each pair of particles it is only necessary to evaluate once the Green's functions (4.31)-(4.33) to calculate the induced velocity from (4.25).

Once the hydrodynamic interactions are calculated, the velocity of each particle is obtained as the sum of its own Brownian motion and the particle-particle interaction terms,

$$\tilde{\vec{v}}_\alpha = \tilde{\vec{v}}_\alpha^{\,0} + \sum_{\forall \beta \neq \alpha} \tilde{\vec{v}}_{\alpha,\beta}^{\,I}. \tag{4.48}$$

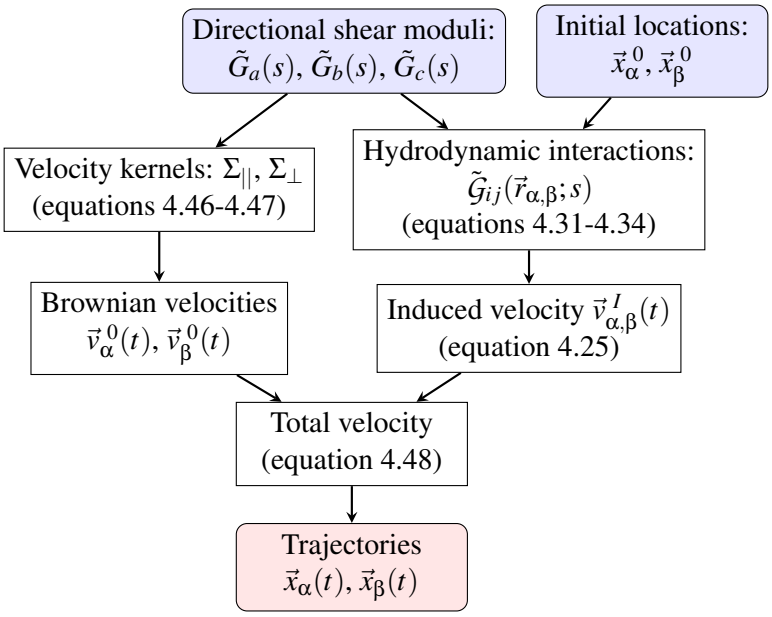

Figure 4.5: Flow diagram of the numerical simulations of the probing particles moving in a nematic viscoelastic fluid.

The final step of the simulation is to calculate the particle trajectories by integrating in time their velocity vector. As a summary, in **Figure 4.5** we outline the steps of the numerical simulations of the Brownian thermal motion of groups of distant interacting particles. All the analysis and simulation tools used in this chapter were written in the general-purpose programming language Python [125], using the numerical and scientific packages Numpy [150] and Scipy [67] and the plotting library Matplotlib [64]. The most computationally intensive functions were compiled in C by using Cython [7], and sped up by using Memoryview objects and the linear algebra module Ceygen [78].

Figure 4.6 (*a*) shows the random evolution of the velocity of a representative particle in the directions parallel and perpendicular to the nematic. The blue and red lines represent respectively the total velocity of the particle and the velocity induced by its four neighboring particles. The particle-particle interaction is a weak, higher order effect, and the total influence of the four neighbouring particles is very small compared with the Brownian thermal particle velocity. **Figure 4.6** (*b*) shows the trajectories of the five particles in the same simulation. As noted above the inter-particle distance is much greater than the particle displacement, which

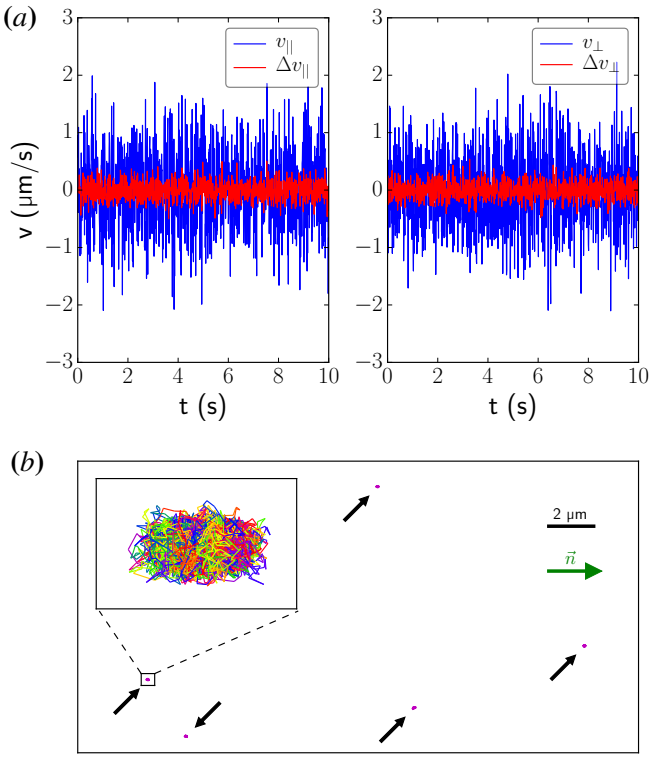

Figure 4.6: Trajectories and velocity components of a representative numerical simulation containing five interacting particles embedded in a nematic Kelvin-Voigt fluid and subjected to Brownian motion. (*a*) || and ⊥ velocity components of the simulated Brownian motion of an example simulated particle moving through a nematic Kelvin-Voigt fluid with $\mu_a = 0.5$ Pa, $\mu_b = 0.01$ Pa, $\mu_c = 1$ Pa and $\eta_a = \eta_b = \eta_c = 0.1$ Pa·s. The total velocity is shown in blue (—) while the velocity contribution from hydrodynamic interactions is shown in red (—). (*b*) Trajectories of a representative numerical simulation containing five interacting particles. The nematic is aligned in the horizontal direction. For reference, each trajectory is marked with a black arrow. The inset zooms in the trajectory of one of the particles.

justifies our assumption of constant particle-particle separation in the calculation of the Green's functions (4.31)-(4.33). The inset of **Figure 4.6** (*b*) zooms into the trajectory of one particle, whose envelope is an ellipse with its major axis aligned along the nematic, consistent with the anisotropic rheological properties of the simulated fluid.

4.3.2 D2PTM on Simulated Particle Trajectories

To determine the mean square displacement tensor, we simulate the trajectories of 200 particle groups each containing 5 particles (*i.e.* 2,000 particle pairs). For consistency, we consider the same nematic Kelvin-Voigt fluid with $\mu_a = 0.5$ Pa, $\mu_b = 0.01$ Pa, $\mu_c = 1$ Pa and

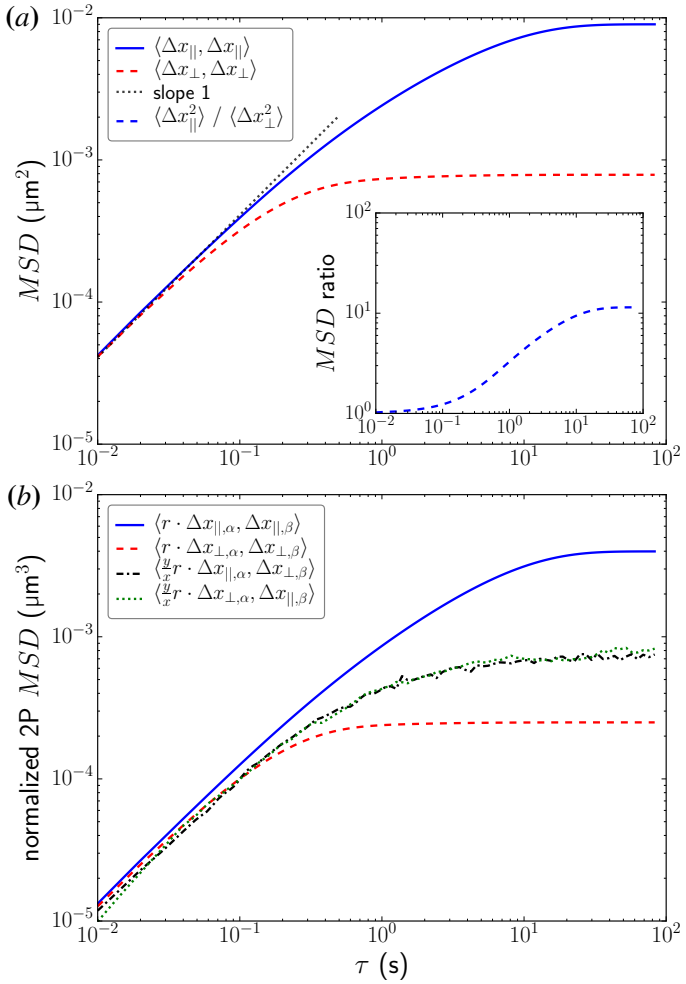

Figure 4.7: One- and two-point MSD of $N = 1{,}000$ simulated particles and $M = 2{,}000$ particle pairs in the principal directions of a nematic Kelvin-Voigt fluid. (*a*) One-point MSD in the principal directions of a nematic Kelvin-Voigt fluid with $\mu_a = 0.5$ Pa, $\mu_b = 0.01$ Pa, $\mu_c = 1$ Pa and $\eta_a = \eta_b = \eta_c = 0.1$ Pa·s, projected along the $||$ (——) and $\perp$ (– –) directions. A line of unit slope is plotted as reference (▪▪▪▪▪▪). The inset shows the MSD ratio, $\langle \Delta x_{||}, \Delta x_{||} \rangle / \langle \Delta x_{\perp}, \Delta x_{\perp} \rangle$. (*b*) Renormalized two-point cross-MSD of the same simulated trajectories: $\langle r \cdot \Delta x_{||,\alpha}, \Delta x_{||,\beta} \rangle$ (——), $\langle r \cdot \Delta x_{\perp,\alpha}, \Delta x_{\perp,\beta} \rangle$ (– –), $\langle \frac{y}{x} r \cdot \Delta x_{||,\alpha}, \Delta x_{\perp,\beta} \rangle$ (– ▪ –) and $\langle \frac{y}{x} r \cdot \Delta x_{\perp,\alpha}, \Delta x_{||,\beta} \rangle$ (▪▪▪▪▪▪). The data is plotted versus the time separation τ.

$\eta_a = \eta_b = \eta_c = 0.1$ Pa·s used for **Figures 4.4** and **4.6**. The directional one-point MSD of the simulated particles are plotted in **Figure 4.7** (*a*) in principal directions of the fluid. Due to the particular choice of parameters for the Kelvin-Voigt model, these MSD have a characteristic shape. At low values of τ, the MSD are dominated by the high-frequency viscous response of the fluid and thus increase linearly with τ. Furthermore, since we prescribed the same value for η_a, η_b and η_c, at short τ the MSD are isotropic (*i.e.* $\langle \Delta x_{||}^2 \rangle = \langle \Delta x_{\perp}^2 \rangle$). In contrast with this behavior, the

MSD are dominated by the low-frequency elastic response of the fluid at high values of τ, thereby reaching a plateau. Additionally, since we prescribed different values for μ_a, μ_b and μ_c, the MSD are different along different directions. It is important to note that the MSD ratio $\langle \Delta x_{||}^2 \rangle / \langle \Delta x_{\perp}^2 \rangle$ is non-trivially related to the ratios between the three shear moduli [54] (see also **Chapter 3**).

Figure 4.7 (*b*) displays the two-point MSD of the simulated 2,000 particle pairs. The dependence of these data on τ is similar to that of their one-point counterparts, although as we had anticipated, the noise content of the cross-directional MSD (*i.e.* $||-\perp$) is higher. Also as expected, the renormalization proposed in (4.40)-(4.42) makes the values of the different two-point and one-point MSD components comparable to each other. Using the two-point MSD as inputs, we solve equations (4.40)-(4.42) to determine the three Miesowicz complex shear moduli.

Figure 4.8 shows the loss (panel *a*) and storage (panel *b*) components of the complex moduli recovered from the simulated trajectories, together with the functional forms of these parameters initially prescribed in our simulations. The agreement between recovered and prescribed moduli is fairly good for the whole range of frequencies considered. A similarly good agreement between prescribed and recovered shear moduli is found for different combinations of viscoelastic parameters (see **Appendix 4.9** for an additional example). Thus, we conclude that the D2PTM analysis framework presented in this chapter can be used to accurately determine the rheological properties of nematic complex fluids. Next section focuses on the experimental implementation of D2PTM.

4.4 Experimental Application of D2PTM to Nematic F-actin Solutions

This section illustrates the experimental application of D2PTM to characterize the rheological properties of a nematic complex fluid formed by a solution of filamentous actin (F-actin). Actin is the most abundant cytoskeletal protein in eukaryotic cells, and forms elongated fibers that can display a nematic ordering and anisotropic rheology [34]. He *et al.* [58] showed that the mobility of microscopic particles in reconstituted nematic F-actin solutions is anisotropic. Thus,

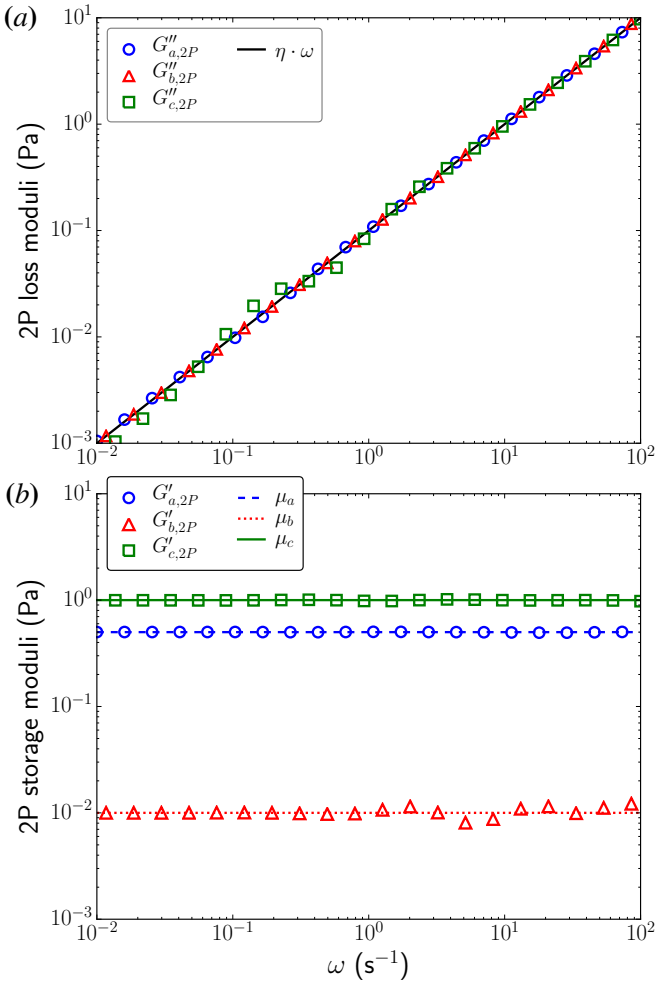

Figure 4.8: Prescribed and recovered loss and storage moduli of the simulated fluid, calculated by applying the D2PTM analysis. (*a*) Symbols: Miesowicz loss moduli; G''_a (O), G''_b (Δ) and G''_c (□). Solid line: prescribed loss moduli of the material; $\omega\eta_a = \omega\eta_b = \omega\eta_c$ (——). (*b*) Symbols: Miesowicz storage moduli; G'_a (O), G'_b (Δ) and G'_c (□). Lines: prescribed storage moduli of the material; μ_a (– –), μ_b (·····) and μ_c (——). The data are plotted versus the frequency ω.

this system is an ideal benchmark for D2PTM.

4.4.1 Sample Preparation

F-actin samples were prepared following well-established protocols [58, 118]. Preformed actin filaments from rabbit skeletal muscle were purchased from Cytoskeleton, Inc. (Denver, CO). This F-actin mixture was diluted in Milli-Q water at room temperature to a concentration of 0.4 mg/ml. The resulting F-actin solution contained 5 mM Tris-HCl pH 8.0, 0.2

mM $CaCl_2$, 0.2 mM ATP, 2 mM $MgCl_2$ and 5% (w/v) sucrose. The samples were incubated for 10 minutes at room temperature, allowing the filaments to completely dissociate from each other. In order to protect the samples from bacterial growth, ampicillin was added to a final concentration of 100 μg/ml. This salt concentration of the buffer produces an average filament length of 8 μm, which is substantially smaller than the persistence length of F-actin, $\xi_p \sim 20$ μm [52]. Thus, the actin filaments in our experiments can be safely assumed to be straight. To induce the nematic transition of the samples, the F-actin concentration was increased to 4 mg/ml while keeping constant the salt concentration and filament length by dialyzing the sample, *i.e.* the sample was centrifuged at 2,000 g and 19°C in an Amicon Ultra-4 Centrifugal Filter Unit (EMD Millipore, Billerica, MA) until the target concentration was reached. The protein concentration was monitored using a spectrophotometer to measure the absorbance at 650 nm.

Carboxylate modified red latex beads with 0.5 μm nominal diameter (Fluospheres, Invitrogen, Carlsbad CA) were diluted in the supernatant solution and then added to the protein solution. The protein solution with beads was stored at 4°C for no more than a week. Rectangular capillary tubes with internal dimensions 0.1 mm × 1 mm × 50 mm (VitroCom, Mountain Lakes, NJ) were filled through capillarity with the protein solution. The filling flow provides enough shear to align the F-actin filaments parallel to the capillary axis (**Figure 4.11** *a* and ref. [58]). The tubes were sealed with two-component epoxy resin to avoid evaporation and internal currents, and attached to a microscope glass slide. The samples were kept at room temperature for at least 2 hours to reach thermal equilibrium in preparation for imaging.

4.4.2 Microscopy and Image Processing

Fluorescent light image sequences of the samples were captured at 50 Hz using a Leica DMI6000 B inverted microscope (Leica Microsystems, Inc., Buffalo Grove, IL), equipped with a Zyla 4.2 sCMOS camera (Andor Technology Ltd., Belfast, UK) and a 63x oil immersion objective lens, and mounted on a Micro-g 63-543 optical air table (TMC - AMETEK, Inc.) that damped vibrations. The imaging setup was controlled by the open source microscopy software Micro-Manager [1, 142, 37].

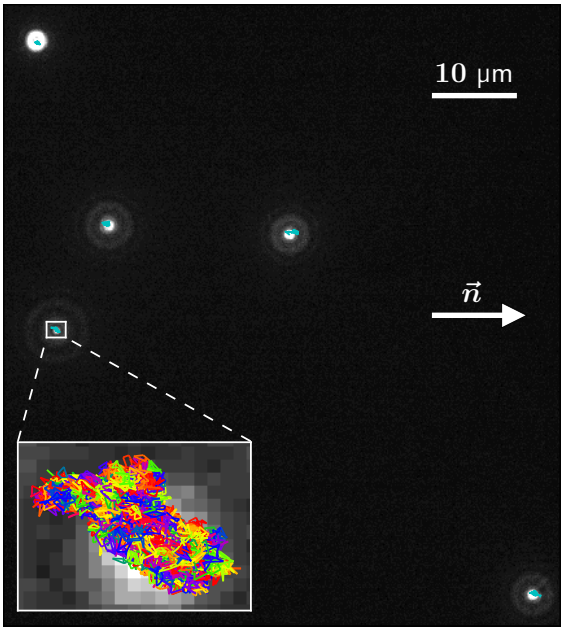

Figure 4.9: Fluorescence images of the microparticles embedded in a nematic F-actin gel with their trajectories superimposed. The inset represents a zoom in one of the particles. The nematic of the gel is parallel to the horizontal axis.

The centers of the fluorescent particles were tracked by implementing a previously reported algorithm [120] that we validated for Newtonian fluids (see **Appendix 4.10**). From the trajectories of the particles, we calculated the one-point MSD in the directions parallel and perpendicular to the nematic, and the two-point cross-MSD for pairs of distant particles. **Figure 4.9** shows particle trajectories obtained in a typical experiment. We then analyzed the cross MSD as described in **§4.2.5** to determine the directional shear moduli of the F-actin solution (see **Figure 4.3**). A total of 20 F-actin samples were analyzed. For each sample, images from different regions were taken, capturing the motion of 2 to 10 particles in each image, for a total of 2,346 particles and 6,105 particle pairs.

4.4.3 Experimental Results and Discussion

The qualitative anisotropic rheology of nematic F-actin solutions can be observed by plotting the histograms of the tracked particle jumps in the directions parallel and perpendicular to the nematic, $P[\Delta x_{||}(\Delta t)]$ and $P[\Delta x_{\perp}(\Delta t)]$ (see ref. [58] and **Figure 4.10**). Both histograms

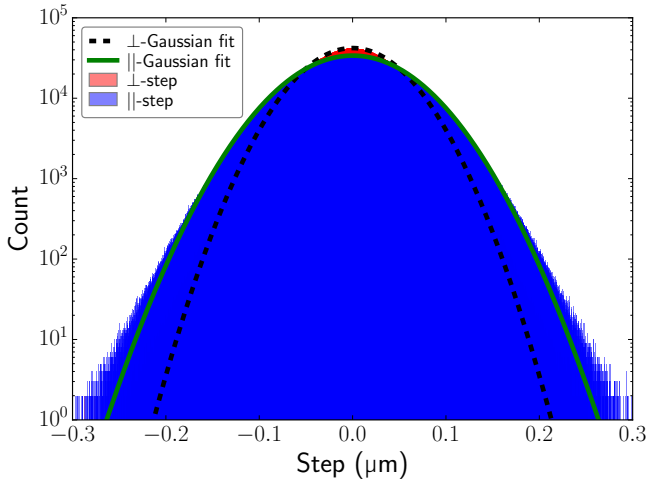

Figure 4.10: Histograms of the experimental particle jumps in the $||$ and $\perp$ directions for $\tau = \delta t = 0.02$ s. Two Normal histograms with the same average and standard deviation than the $||$ (– –) and $\perp$ (——) experimental distributions are included for reference.

have similar skewness (S) and kurtosis (K) coefficients, namely $S_{||} = -2.4 \times 10^{-3}$, $K_{||} = 3.25$, and $S_{\perp} = 9 \times 10^{-4}$, $K_{\perp} = 3.22$. These values are also approximately consistent with a Normal distribution ($S = 0$, $K = 3$). The widths of these histograms are however markedly different, indicating that particle mobility is anisotropic. The nematic of the F-actin solution has been shown to correspond with the direction of highest mobility of the probing particles [58]. Thus, we define the $||$ direction as the principal direction of maximal mobility in our experiments, and the $\perp$ direction as the orthogonal direction corresponding to minimal mobility. This assignment is confirmed by **Figure 4.11** (a), which shows one-point MSD of the tracked particles along the axis of the capillary tube (x direction), the orthogonal direction (y), and the principal $||$ and $\perp$ directions determined by diagonalizing the MSD tensor. The data shows that the MSD in the x and y directions respectively agree with the MSD in the $||$ and $\perp$ directions, implying that the actin fibers were successfully aligned parallel to the capillary axis during sample preparation.

As expected, the MSD curves in **Figure 4.11** (a) have slopes between 0 and 1, suggesting that the rheology of the F-actin solutions was neither elastic nor viscous in the range of time scales considered. The MSD ratio $\langle \Delta x_{||}^2 \rangle / \langle \Delta x_{\perp}^2 \rangle$, shown in the inset of **Figure 4.11** (a), ranges between 2 at low values of τ and 4 at high τ values, confirming the anisotropic behavior observed in the histograms of **Figure 4.10**. Overall, these one-point MSD are in fair agreement with previously

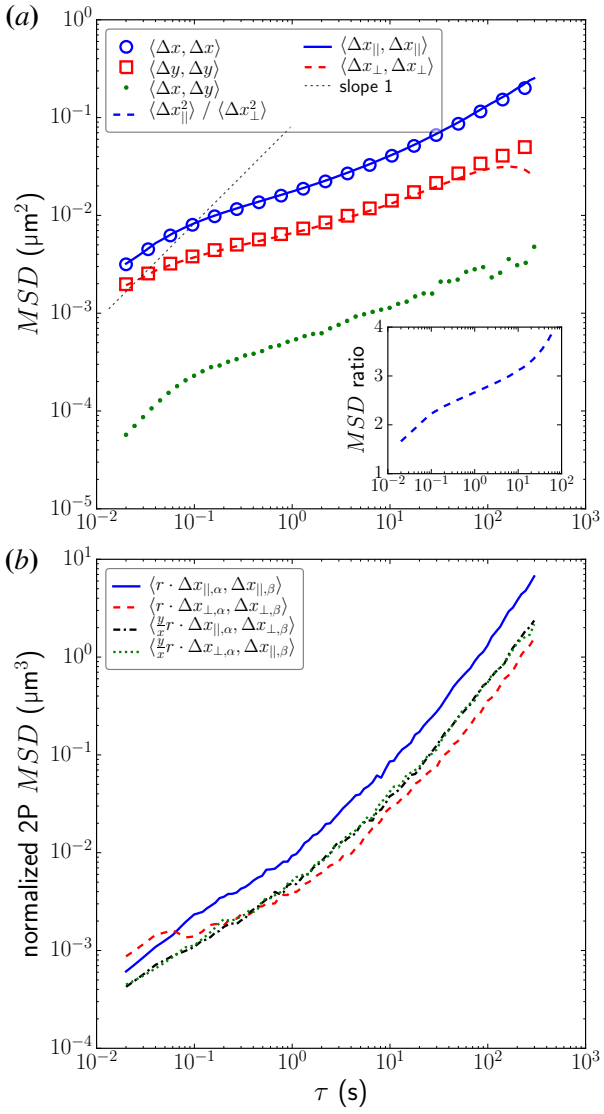

Figure 4.11: One- and two-point MSD of $N = 2,346$ experimental particles and $M = 6,105$ particle pairs in the principal directions of an F-actin nematic solution. (*a*) One-point MSD. Symbols: MSD along the direction of the capillary tube axis x (○) and the perpendicular direction y (□). Lines: MSD along the principal directions of maximal ($||$, ——) and minimal ($\perp$, – –) particle mobility. The dotted green line (• • •) represents the $||$-$\perp$ cross-correlation of the particle displacements. For reference, a line with unit slope has been included (· · · · · ·). The inset shows the MSD ratio $\langle \Delta x_{||}, \Delta x_{||} \rangle / \langle \Delta x_{\perp}, \Delta x_{\perp} \rangle$. (*b*) Renormalized two-point MSD: $\langle r \cdot \Delta x_{||,\alpha}, \Delta x_{||,\beta} \rangle$ (——), $\langle r \cdot \Delta x_{\perp,\alpha}, \Delta x_{\perp,\beta} \rangle$ (– –), $\langle \frac{y}{x} r \cdot \Delta x_{||,\alpha}, \Delta x_{\perp,\beta} \rangle$ (– · –) and $\langle \frac{y}{x} r \cdot \Delta x_{\perp,\alpha}, \Delta x_{||,\beta} \rangle$ (· · · · · ·). The data are plotted versus the time separation τ.

reported data [58].

In **Figure 4.11** (*b*) we plot the two-point directional MSD of the 6,105 tracked particle pairs, expressed in principal directions and normalized as indicated in (4.40)-(4.42). These data

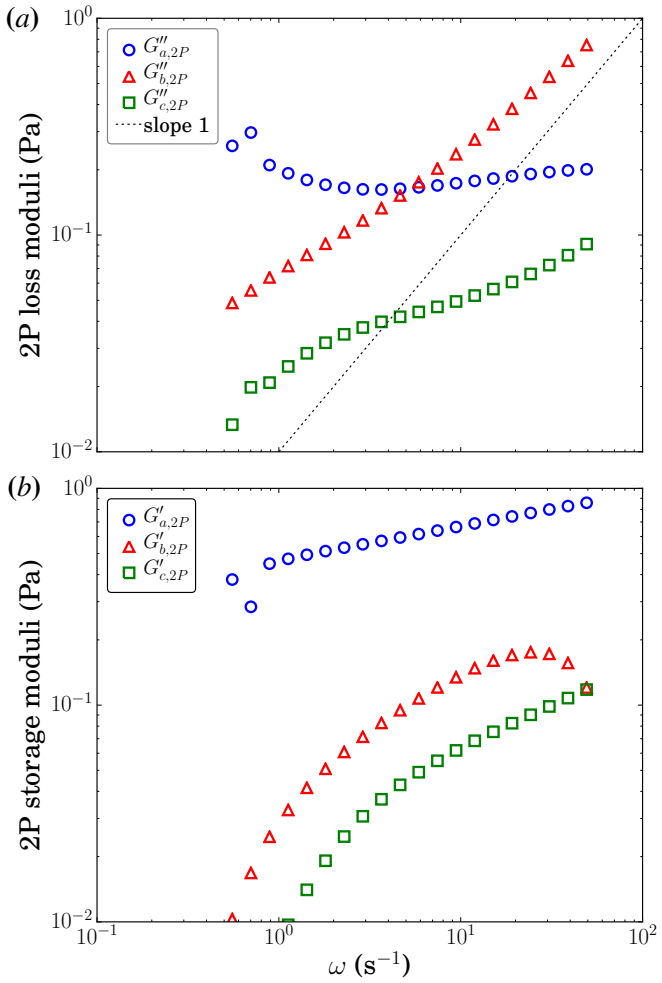

Figure 4.12: Directional loss and storage moduli of the F-actin gel, calculated by applying the D2PTM analysis. (*a*) G''_a (O), G''_b (Δ) and G''_c (□), calculated with the two-particle data. (*b*) G'_a (O), G'_b (Δ) and G'_c (□), calculated with the two-particle data.

are noisier than the one-point MSD in agreement with our simulations (**Figure 4.7**), and with previous experiments on isotropic fluids [30]. This explains why it was necessary to compile data from a relatively large number of particle pairs to obtain converged statistics. The D2PTM analysis of the two-point MSD allowed us to calculate the complex shear moduli of the nematic F-actin solutions from our experimental measurements. These shear moduli are plotted in **Figure 4.12** as a function of frequency. For the whole range of frequencies considered, the smallest loss modulus is G''_c (see **Figure 4.12** *a*). On the other hand, $G'_a > G'_b > G'_c$ (**Figure 4.12** *b*). We also observe that $G''_b > G''_a$ for high frequencies while the opposite happens for low frequencies. It is notable that, while all the loss moduli have a slope lower than 1, G''_b has the highest slope.

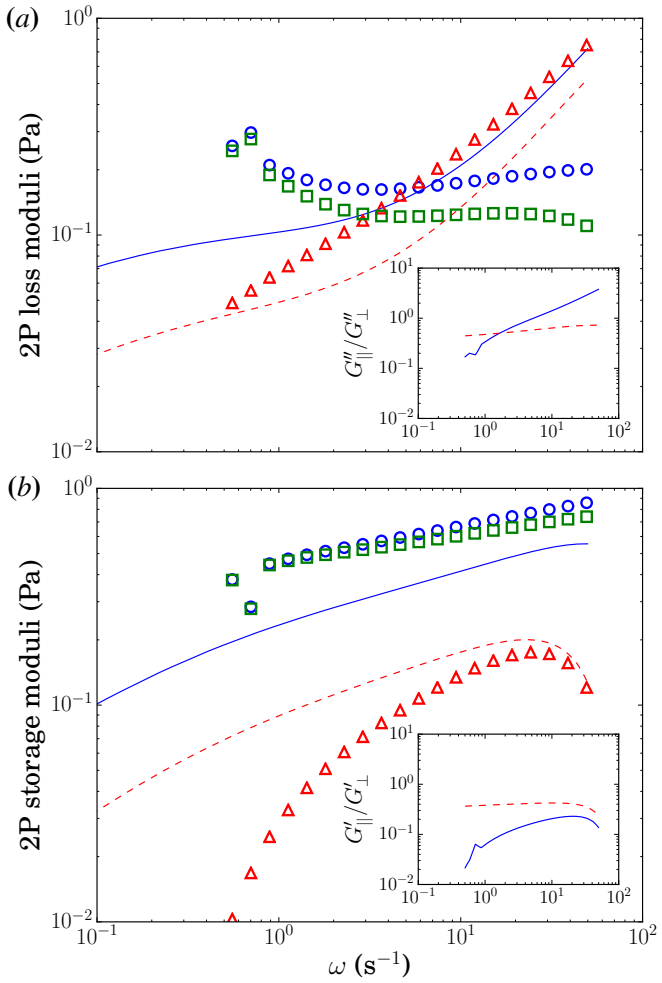

Figure 4.13: Comparison of the directional shear moduli of the nematic F-actin gel calculated with D2PTM and the effective directional shear moduli predicted from one-point PTM. (*a*) Symbols: loss moduli $G''_{\perp} = G''_a$ (○), $G''_{||} = G''_b$ (△), $-G''_{\Delta} = -(G''_c - G''_a)$ (□). Lines: effective loss moduli $G''_{\text{eff},\perp}$ (——), $G''_{\text{eff},||}$ (– –). Inset: ratio $G''_{||}/G''_{\perp}$ (——) and $G''_{\text{eff},||}/G''_{\text{eff},\perp}$ (– –). (*b*) Symbols: storage moduli $G'_{\perp} = G'_a$ (○), $G'_{||} = G'_b$ (△), $-G'_{\Delta} = -(G'_c - G''_a)$ (□). Lines: effective storage moduli $G'_{\text{eff},\perp}$ (——), $G'_{\text{eff},||}$ (– –). Inset: ratio $G'_{||}/G'_{\perp}$ (——) and $G'_{\text{eff},||}/G'_{\text{eff},\perp}$ (– –).

To facilitate the interpretation of these results, **Figure 4.13** replots the Miesowicz moduli as $G_{||} = G_b$, $G_{\perp} = G_a$ and $G_{\Delta} = G_c - G_a$, based on the form of the equations of motion (4.7)-(4.9). In this representation, $G_{||}$ and $G_{\perp}$ reflect the anisotropy in the strain-stress relationship, while G_{Δ} indicates the bending resistance with respect to the nematic (see **Chapter 3** and [54]). The data suggest that fluctuations perpendicular to the nematic likely generate distortions of the F-actin fibers including fiber bending, which trigger an elastic-like response, *i.e.* the storage components

of $G_\perp$ and G_Δ are dominant. Conversely, fluctuations parallel to the nematic generate a viscous response dominated by $G''_{||}$, and likely caused by filament-solvent sliding.

The anisotropic rheology of a nematic complex fluid can be fully characterized by one-point microrheology only in two particular pseudo-isotropic cases (see **Chapter 3** and [54]) in which the number of independent Miesowicz shear moduli is reduced to two. These cases are $G_a = G_b$, which corresponds with isotropic momentum diffusivity ($G_{||} = G_\perp$), and $G_a = G_c$, which corresponds with zero resistance to bending ($G_\Delta = 0$). Our experimental results indicate that neither of these conditions are satisfied for nematic F-actin solutions. **Figure 4.13** compares the shear moduli obtained by D2PTM with the effective moduli obtained by one-point directional PTM, $G_{\text{eff},||}$ and $G_{\text{eff},\perp}$ (equations 4.36-4.37 and refs. [57, 34, 58]). Apart from the obvious differences in magnitude, there is a number of notable qualitative differences between the effective one-point moduli and actual two-point ones. We observe that $|G_\Delta| \sim |G_\perp|$ suggesting that the response to nematic bending, which cannot be captured by one-point PTM, makes an important contribution to the microrheology of nematic F-actin solutions. More importantly, the one-point data would suggest that $G''_{\text{eff},||} < G''_{\text{eff},\perp}$ despite that $G''_{||} > G''_\perp$ (**Figure 4.13** *a*), implying that one-point PTM may fail to identify the direction of maximum viscosity in nematic complex fluids. Additionally, one-point PTM underestimates $G'_\perp$ while it overestimates $G'_{||}$ (**Figure 4.13** *b*), thus severely under-predicting the level of anisotropy in the elastic response.

4.5 Conclusions

Many technological and biological soft viscoelastic materials exhibit microstructural alignment along a common direction leading to anisotropic rheological properties. Examples of these are liquid crystals [24], nematic viscoelastomers [154], the cell cytoplasm [50, 34], and the extracellular matrix [99]. For small distortions of the nematic direction field (*i.e.* low Ericksen number limit), the anisotropic rheology of nematic complex fluids can be approximately described by three frequency-dependent Miesowicz complex shear moduli [140, 141, 54]. These coefficients can be macroscopically measured by subjecting the sample to simple shear in different

geometrical configurations [108, 134], by propagating ultrasound waves or electromagnetic fields, and by light scattering techniques [8]. However, there is a lack of microscopic methods to characterize the rheological properties of nematic complex fluids. This chapter introduces a novel particle tracking microrheology method to address this limitation: directional two-point particle tracking microrheology (D2PTM). Compared to existing macroscopic methods, D2PTM can be applied to minute samples and involves a simple experimental setup.

The theoretical foundation of D2PTM is established by extending our previous analysis of nematic flow around a microrheological probe [54]. We determine the mutual hydrodynamic interactions between pairs of distant particles immersed in a nematic complex fluid, and we use this knowledge to generalize two-point particle-tracking microrheology [30] to these soft materials. This new analysis allows for calculating the three Miesowicz shear moduli from the measured cross-MSD of particle pairs by solving a system of three complex-valued equations at each frequency. To test this approach, we simulate the Brownian motion of several thousands of spheres embedded in a nematic complex fluid in which we prescribe the Miesowicz shear moduli as functions of the frequency. We then apply the D2PTM analysis to the trajectories of the particles and recover the Miesowicz moduli, which result to be in close agreement with the prescribed ones.

To demonstrate the experimental application of D2PTM for nematic complex fluids and to investigate the rheological properties of these fluids, we perform particle-tracking experiments on F-actin solutions where the actin filaments are aligned by flow shear. The one-point statistics of particle motion obtained in our experiments are consistent with those previously reported for similar F-actin solutions [58]. Moreover, D2PTM provides direct information about the microstructure of the material that is not accessible from one-point measurements of particle mobility. Specifically, we observe that the microrheological response of F-actin solutions is predominantly viscous in the direction parallel to the nematic probably due to filament-solvent sliding, whereas this response is predominantly elastic in the perpendicular direction due to fiber distortions and fiber bending. This two-point analysis of particle trajectories reveals important differences between the actual directional shear moduli of nematic F-actin solutions, and the so-called effective

directional shear moduli derived from previously proposed one-point analyses [57, 34, 58]. In addition to not being able to capture the rotational shear modulus of the nematic, one-point PTM does not correctly determine the direction of maximum viscosity in nematic F-actin solutions, and underestimates the anisotropy in their elastic response.

The theoretical framework employed here to develop D2PTM is based on a number of simplifications that could potentially limit the applicability of this new microrheology technique. Specifically, we work with a continuum incompressible formulation that assumes small deformations. Thus, the accuracy of D2PTM is expected to deteriorate in experiments that cause large deformations, for strongly non-linear materials, and for materials that are heterogeneous at the length scale of the distance between particle pairs. It is important to note, however, that these simplifications are common to most if not all existing PTM methods [138].

An additional important simplification made in this chapter is that the orientation of the nematic remains uniform over the length scale of the inter-particle distance. This assumption is reasonable in the present experiments, where actin filaments are externally aligned as part of the sample preparation, and their persistence length ξ_p is approximately twice their total length and 80 times the particle radius. The assumption of uniform nematic orientation can be particularly delicate in the vicinity of the particle due to surface effects [127]. Likewise, when probing polymer solutions with $\xi_p \gg a$ the particle may alter the local orientation of filaments near itself [131]. However, these near-field effects have a negligible influence on the hydrodynamic interaction of pairs of distant particles, and thus the ability of D2PTM to quantify the bulk response of the fluid remains largely unaffected [88]. Distortions of the nematic orientation could be incorporated into the D2PTM analysis by considering static non-uniform nematic fields that include defects near the particle surface [140]. Alternatively, the dynamics of the nematic could be solved taking into account its Frank elasticity constants [44], or using the Poisson-bracket approach [139]. Nonetheless, these refinements would introduce additional material parameters unknown *a priori*, and a two-particle protocol would be insufficient to determine these new parameters together with the Miesowicz shear moduli.

In conclusion, we have developed a new directional two-point particle tracking mi-

crorheology method (D2PTM) that provides important new information about the anisotropic viscoelastic response of nematic complex fluids, which is hidden to currently available microrheology techniques.

4.6 Appendix A - Single-Particle Response Function

This appendix provides the general form of the components of the response function (4.22) of a particle of radius a moving in a directional complex fluid, calculated from the integral (4.19) making use of equations (4.14)-(4.15). The singularities of the response function and its Taylor expansion around the isotropy point are also presented.

The components of the response function of nematic complex fluid with general values of the shear moduli α_1^*, $\tilde{G}_a$, $\tilde{G}_b$ and $\tilde{G}_c$ are

$$s\tilde{\zeta}_{||} = \frac{8\pi a\tilde{G}_b B(\vec{\mu})}{D_+(\vec{\mu})\frac{\arctan[C_+(\vec{\mu})]}{C_+(\vec{\mu})} - D_-(\vec{\mu})\frac{\arctan[C_-(\vec{\mu})]}{C_-(\vec{\mu})}}, \tag{4.49}$$

$$s\tilde{\zeta}_{\perp} = \frac{8\pi a\tilde{G}_a\left(\frac{\tilde{G}_b}{\tilde{\alpha}_1^*}\right)^2 C_-(\vec{\mu})^8\frac{E_+(\vec{\mu})}{E_-(\vec{\mu})}}{\frac{\arctan\left(\sqrt{\tilde{G}_c/\tilde{G}_a-1}\right)}{\sqrt{\tilde{G}_c/\tilde{G}_a-1}} + \frac{1}{B(\vec{\mu})}\frac{\tilde{G}_a}{\tilde{G}_b}\left[\frac{\arctan[C_-(\vec{\mu})]}{C_-(\vec{\mu})} - \frac{\arctan[C_+(\vec{\mu})]}{C_+(\vec{\mu})}\right]}. \tag{4.50}$$

where we have used the non-dimensional functions

$$A(\vec{\mu}) = \frac{\tilde{\alpha}_1^* + \tilde{G}_c}{\tilde{G}_b} - 1, \tag{4.51}$$

$$B(\vec{\mu}) = \sqrt{A(\vec{\mu})^2 + \frac{4\tilde{\alpha}_1^*}{\tilde{G}_b}}, \tag{4.52}$$

$$C_+(\vec{\mu}) = \sqrt{\frac{A(\vec{\mu}) + B(\vec{\mu})}{2}}, \tag{4.53}$$

$$C_-(\vec{\mu}) = \sqrt{\frac{A(\vec{\mu}) - B(\vec{\mu})}{2}}, \tag{4.54}$$

$$D_+(\vec{\mu}) = A(\vec{\mu}) + 2 + B(\vec{\mu}), \tag{4.55}$$

$$D_-(\vec{\mu}) = A(\vec{\mu}) + 2 - B(\vec{\mu}), \tag{4.56}$$

$$E_+(\vec{\mu}) = A(\vec{\mu})D_+(\vec{\mu}) - 2\left(\frac{\tilde{G}_c}{\tilde{G}_b} - 1\right), \tag{4.57}$$

$$E_-(\vec{\mu}) = A(\vec{\mu})D_-(\vec{\mu}) - 2\left(\frac{\tilde{G}_c}{\tilde{G}_b} - 1\right). \tag{4.58}$$

Equations (4.49)-(4.50) degenerate in the limit $B(\vec{\mu}) \to 0$, which occurs whenever

$$\frac{\tilde{G}_c}{\tilde{G}_b} \to \left(1 \pm \sqrt{\frac{-\tilde{\alpha}_1^*}{\tilde{G}_b}}\right)^2. \tag{4.59}$$

In this limit, $C_+ \to C_-$, $D_+ \to D_-$ and $E_+ \to E_-$, and the expressions that determine the two components of the response function (4.49)-(4.50) become undefined, although solving the limit yields $s\tilde{\zeta}_{||} = s\tilde{\zeta}_{\perp} = 0$. There is a change of sign of $s\tilde{\zeta}_{\perp}$, when crossing the limit (4.59) along the branch associated to the $-$ sign, only when $\tilde{\alpha}_1^* < -\tilde{G}_b$, yielding unphysical negative values of the response function. On the other hand, the sign of the response function does not change along the branch associated to the $+$ sign.

Equations (4.49)-(4.50) are singular for $\tilde{\alpha}_1^* = 0$. However, the response function can be calculated, for a complex fluid with $\tilde{\alpha}_1^* = 0$, as the limit

$$s\tilde{\zeta}_{||}\Big|_{\tilde{\alpha}_1^*=0} = \frac{4\pi a(\tilde{G}_c - \tilde{G}_b)}{\frac{\tilde{G}_c}{\tilde{G}_b}\frac{\arctan\left(\sqrt{\tilde{G}_c/\tilde{G}_b - 1}\right)}{\sqrt{\tilde{G}_c/\tilde{G}_b - 1}} - 1}, \tag{4.60}$$

$$s\tilde{\zeta}_{\perp}\Big|_{\tilde{\alpha}_1^*=0} = \frac{8\pi a(\tilde{G}_c - \tilde{G}_b)}{1 - \frac{\arctan\left(\sqrt{\tilde{G}_c/\tilde{G}_b - 1}\right)}{\sqrt{\tilde{G}_c/\tilde{G}_b - 1}} + \frac{\tilde{G}_c - \tilde{G}_b}{\tilde{G}_a}\frac{\arctan\left(\sqrt{\tilde{G}_c/\tilde{G}_a - 1}\right)}{\sqrt{\tilde{G}_c/\tilde{G}_a - 1}}}. \tag{4.61}$$

For complex fluids that are nearly isotropic, the response function can be approximated by the Taylor expansion of equations (4.49)-(4.50) around $\tilde{\alpha}_1^* = 0$ and $\tilde{G}_a = \tilde{G}_b = \tilde{G}_c = \tilde{G}$:

$$\frac{s\tilde{\zeta}_{\parallel}}{6\pi a\tilde{G}} \approx 1 + \frac{4}{35}\frac{\tilde{\alpha}_1^*}{\tilde{G}} + \frac{4}{5}\left(\frac{\tilde{G}_b}{\tilde{G}} - 1\right) + \frac{1}{5}\left(\frac{\tilde{G}_c}{\tilde{G}} - 1\right), \tag{4.62}$$

$$\frac{s\tilde{\zeta}_{\perp}}{6\pi a\tilde{G}} \approx 1 + \frac{3}{70}\frac{\tilde{\alpha}_1^*}{\tilde{G}} + \frac{1}{2}\left(\frac{\tilde{G}_a}{\tilde{G}} - 1\right) + \frac{1}{10}\left(\frac{\tilde{G}_b}{\tilde{G}} - 1\right) + \frac{2}{5}\left(\frac{\tilde{G}_c}{\tilde{G}} - 1\right). \tag{4.63}$$

Equation (4.50) is also singular for $\tilde{G}_a = \tilde{G}_c$. However, it presents the limit value:

$$s\tilde{\zeta}_{\perp}\Big|_{\tilde{G}_a=\tilde{G}_c} = \frac{8\pi a\tilde{G}_c\left(\frac{\tilde{G}_b}{\tilde{\alpha}_1^*}\right)^2 C_-(\vec{\mu})^8\frac{E_+(\vec{\mu})}{E_-(\vec{\mu})}}{1+\frac{1}{B(\vec{\mu})}\frac{\tilde{G}_c}{\tilde{G}_b}\left[\frac{\arctan[C_-(\vec{\mu})]}{C_-(\vec{\mu})}-\frac{\arctan[C_+(\vec{\mu})]}{C_+(\vec{\mu})}\right]}. \tag{4.64}$$

Equations (4.60)-(4.61) present other singularities, for different combinations of $\tilde{G}_a$, $\tilde{G}_b$ and $\tilde{G}_c$, with finite limits:

$$s\tilde{\zeta}_{||}\Big|_{\substack{\tilde{\alpha}_1^*=0\\ \tilde{G}_b=\tilde{G}_c}} = 6\pi a\tilde{G}_c, \tag{4.65}$$

$$s\tilde{\zeta}_{\perp}\Big|_{\substack{\tilde{\alpha}_1^*=0\\ \tilde{G}_a=\tilde{G}_c}} = \frac{8\pi a(\tilde{G}_c-\tilde{G}_b)}{2-\frac{\tilde{G}_b}{\tilde{G}_c}-\frac{\arctan\left(\sqrt{\tilde{G}_c/\tilde{G}_b-1}\right)}{\sqrt{\tilde{G}_c/\tilde{G}_b-1}}}, \tag{4.66}$$

$$s\tilde{\zeta}_{\perp}\Big|_{\substack{\tilde{\alpha}_1^*=0\\ \tilde{G}_b=\tilde{G}_c}} = \frac{24\pi a\tilde{G}_a}{\frac{\tilde{G}_a}{\tilde{G}_c}+3\frac{\arctan\left(\sqrt{\tilde{G}_c/\tilde{G}_a-1}\right)}{\sqrt{\tilde{G}_c/\tilde{G}_a-1}}}, \tag{4.67}$$

$$s\tilde{\zeta}_{\perp}\Big|_{\substack{\tilde{\alpha}_1^*=0\\ \tilde{G}_a=\tilde{G}_b=\tilde{G}_c}} = 6\pi a\tilde{G}_c. \tag{4.68}$$

4.7 Appendix B - Two-Particle Response Function

This appendix provides the general form of the components of the hydrodynamic interaction tensor $\tilde{\tilde{\mathcal{G}}}(\vec{r};s)$ (see equation 4.25) of pairs of distant particles moving in a directional complex fluid, calculated as the inverse Fourier transform of equations (4.14)-(4.15) when both particles are located in the same plane $z=0$. For the sake of completeness, we also provide the Green's function for the pressure, *i.e.* the inverse Fourier transform of (4.13).

The hydrodynamic interaction tensor in a nematic complex fluid, with general values of the shear moduli α_1^*, $\tilde{G}_a$, $\tilde{G}_b$ and $\tilde{G}_c$, is given by

$$\frac{\tilde{\mathcal{G}}_{11}}{s}\Big|_{z=0} = \frac{\sqrt{2}}{eb}\left(\frac{d+ex^2}{\sqrt{c-ey^2}}-\frac{d-ex^2}{\sqrt{c+ey^2}}\right), \tag{4.69}$$

$$\frac{\tilde{\mathcal{G}}_{12}}{s}\Big|_{z=0} = \frac{\tilde{G}_{21}}{s}\Big|_{z=0} = \frac{\sqrt{2}}{eb}\frac{x}{y}\left(\sqrt{c+ey^2}-\sqrt{c-ey^2}\right), \tag{4.70}$$

$$\frac{\tilde{\mathcal{G}}_{13}}{s}\Big|_{z=0} = \frac{\tilde{G}_{31}}{s}\Big|_{z=0} = 0, \tag{4.71}$$

$$\frac{\tilde{\mathcal{G}}_{22}}{s}\Big|_{z=0} = \frac{\sqrt{2}}{G_c y^2}\left[\sqrt{2}\sqrt{x^2+\frac{G_c}{G_a}y^2}+\frac{1}{eb}\cdot\left(\frac{m_-}{\sqrt{c-ey^2}}-\frac{m_+}{\sqrt{c+ey^2}}\right)\right], \tag{4.72}$$

$$\frac{\tilde{\mathcal{G}}_{23}}{s}\Big|_{z=0} = \frac{\tilde{G}_{32}}{s}\Big|_{z=0} = 0, \tag{4.73}$$

$$\frac{\tilde{\mathcal{G}}_{33}}{s}\Big|_{z=0} = \frac{\sqrt{2}}{G_c y^2}\left[-\frac{\sqrt{2}x^2}{\sqrt{x^2+\frac{G_c}{G_a}y^2}}+\frac{b}{e}\cdot\left(\frac{n_+}{\sqrt{c+ey^2}}-\frac{n_-}{\sqrt{c-ey^2}}\right)\right], \tag{4.74}$$

where x, y and z are the coordinates of the particle-particle separation in the Cartesian coordinate system defined in **Figure 4.2**, and

$$b(\vec{\mu};\vec{r}) = \sqrt{\left(\tilde{\alpha}_1^* + \tilde{G}_b + \tilde{G}_c\right)x^2y^2 + \tilde{G}_b x^4 + \tilde{G}_c y^4}, \tag{4.75}$$

$$c(\vec{\mu};\vec{r}) = \left(\tilde{\alpha}_1^* + \tilde{G}_b + \tilde{G}_c\right)y^2 + 2\tilde{G}_b x^2, \tag{4.76}$$

$$d(\vec{\mu};\vec{r}) = \left(\tilde{\alpha}_1^* + \tilde{G}_b + \tilde{G}_c\right)x^2 + 2\tilde{G}_c y^2, \tag{4.77}$$

$$e(\vec{\mu}) = \sqrt{\left(\tilde{\alpha}_1^* + \tilde{G}_b + \tilde{G}_c\right)^2 - 4\tilde{G}_b\tilde{G}_c}, \tag{4.78}$$

$$m_+(\vec{\mu};\vec{r}) = (c - G_b x^2)(d + ex^2 - 2G_c y^2) - 2G_b G_c x^2 y^2, \tag{4.79}$$

$$m_-(\vec{\mu};\vec{r}) = (c - G_b x^2)(d - ex^2 - 2G_c y^2) - 2G_b G_c x^2 y^2, \tag{4.80}$$

$$n_+(\vec{\mu};\vec{r}) = \tilde{\alpha}_1^* + \tilde{G}_b + \tilde{G}_c + e, \tag{4.81}$$

$$n_-(\vec{\mu};\vec{r}) = \tilde{\alpha}_1^* + \tilde{G}_b + \tilde{G}_c - e. \tag{4.82}$$

It should be noted here that all (4.69), (4.70), (4.72) and (4.74) depend on $\tilde{G}_b$ and $\tilde{G}_c$, while only (4.72) and (4.74) depend on $\tilde{G}_a$. The Green's function for the pressure has the form

$$\tilde{\mathcal{P}}_1\Big|_{z=0} = \frac{2\sqrt{2}x}{eb^3}\left[G_c\left(3\tilde{G}_b h + ly^4\right)\left(\frac{1}{\sqrt{c+ey^2}}-\frac{1}{\sqrt{c-ey^2}}\right) - G_b\left(\frac{q_-}{(c+ey^2)^{3/2}}-\frac{q_+}{(c-ey^2)^{3/2}}\right)\right], \tag{4.83}$$

$$\tilde{\mathcal{P}}_2\Big|_{z=0} = \frac{2\sqrt{2}y}{eb^3}\left[G_c\left(3\tilde{G}_b h + ly^4\right)\left(\frac{1}{\sqrt{c+ey^2}}-\frac{1}{\sqrt{c-ey^2}}\right) - G_b\left(\frac{q_-}{(c+ey^2)^{3/2}}-\frac{q_+}{(c-ey^2)^{3/2}}\right)\right], \tag{4.84}$$

$$\tilde{\mathcal{P}}_3\Big|_{z=0} = 0, \tag{4.85}$$

where

$$h(\vec{\mu};\vec{r}) = \left(\tilde{\alpha}_1^* - \tilde{G}_a + \tilde{G}_b + \tilde{G}_c\right) x^2 y^2 + \tilde{G}_b x^4 + \tilde{G}_c y^4, \tag{4.86}$$

$$l(\vec{\mu}) = \left(\tilde{\alpha}_1^* - \tilde{G}_a + \tilde{G}_b + \tilde{G}_c\right)\left(\tilde{\alpha}_1^* + \tilde{G}_b + \tilde{G}_c\right) - 4\tilde{G}_b\tilde{G}_c \tag{4.87}$$

$$p(\vec{\mu};\vec{r}) = 2\tilde{G}_c y^2\left[\left(h + 2\tilde{G}_b x^4\right)\left(\tilde{\alpha}_1^* + \tilde{G}_b + \tilde{G}_c\right) + \tilde{G}_c y^2\left(2\tilde{G}_b x^2 - \tilde{G}_a y^2\right)\right] \tag{4.88}$$

$$q_+(\vec{\mu};\vec{r}) = p + \tilde{G}_b x^6\left(\tilde{G}_a m_+ + 4\tilde{G}_b\tilde{G}_c\right), \tag{4.89}$$

$$q_-(\vec{\mu};\vec{r}) = p + \tilde{G}_b x^6\left(\tilde{G}_a m_- + 4\tilde{G}_b\tilde{G}_c\right). \tag{4.90}$$

For a complex fluid with $\tilde{\alpha}_1^* = 0$, equations (4.69)-(4.84) are simplified into

$$\frac{\tilde{\mathcal{G}}_{11}}{s}\Big|_{\substack{z=0\\ \tilde{\alpha}_1^*=0}} = \frac{2}{\tilde{G}_b - \tilde{G}_c}\left(\frac{1}{\sqrt{x^2+y^2}} - \frac{\tilde{G}_c}{\tilde{G}_b}\frac{1}{\sqrt{x^2 + \frac{\tilde{G}_c}{\tilde{G}_b}y^2}}\right), \tag{4.91}$$

$$\frac{\tilde{\mathcal{G}}_{12}}{s}\Big|_{\substack{z=0\\ \tilde{\alpha}_1^*=0}} = \frac{2}{\tilde{G}_b - \tilde{G}_c}\frac{x}{y}\left(\frac{-1}{\sqrt{x^2+y^2}} + \frac{1}{\sqrt{x^2 + \frac{\tilde{G}_c}{\tilde{G}_b}y^2}}\right), \tag{4.92}$$

$$\frac{\tilde{\mathcal{G}}_{22}}{s}\Big|_{\substack{z=0\\ \tilde{\alpha}_1^*=0}} = \frac{2}{\tilde{G}_b - \tilde{G}_c}\frac{x^2}{y^2}\left[\frac{1}{\sqrt{x^2+y^2}} - \frac{\tilde{G}_b}{\tilde{G}_c}\frac{1}{\sqrt{x^2 + \frac{\tilde{G}_c}{\tilde{G}_b}y^2}} + \frac{1}{x^2}\left(\frac{\tilde{G}_b}{\tilde{G}_c} - 1\right)\sqrt{x^2 + \frac{\tilde{G}_c}{\tilde{G}_a}y^2}\right], \tag{4.93}$$

$$\frac{\tilde{\mathcal{G}}_{33}}{s}\Big|_{\substack{z=0\\ \tilde{\alpha}_1^*=0}} = \frac{2}{\tilde{G}_b - \tilde{G}_c}\frac{1}{y^2}\left[-\sqrt{x^2+y^2} + \frac{\tilde{G}_b}{\tilde{G}_c}\sqrt{x^2 + \frac{\tilde{G}_c}{\tilde{G}_b}y^2} - \left(\frac{\tilde{G}_b}{\tilde{G}_c} - 1\right)\frac{x^2}{\sqrt{x^2 + \frac{\tilde{G}_c}{\tilde{G}_a}y^2}}\right], \tag{4.94}$$

$$\tilde{\mathcal{P}}_1\Big|_{\substack{z=0\\ \tilde{\alpha}_1^*=0}} = \frac{2x}{\tilde{G}_b - \tilde{G}_c}\left(\frac{\tilde{G}_a - \tilde{G}_c}{\left(x^2+y^2\right)^{3/2}} - \frac{\tilde{G}_c}{\tilde{G}_b}\frac{\tilde{G}_a - \tilde{G}_b}{\left(x^2 + \frac{\tilde{G}_c}{\tilde{G}_b}y^2\right)^{3/2}}\right), \tag{4.95}$$

$$\tilde{\mathcal{P}}_2\Big|_{\substack{z=0\\ \tilde{\alpha}_1^*=0}} = \frac{2y}{\tilde{G}_b - \tilde{G}_c}\left(\frac{\tilde{G}_a - \tilde{G}_c}{\left(x^2+y^2\right)^{3/2}} - \frac{\tilde{G}_c}{\tilde{G}_b}\frac{\tilde{G}_a - \tilde{G}_b}{\left(x^2 + \frac{\tilde{G}_c}{\tilde{G}_b}y^2\right)^{3/2}}\right). \tag{4.96}$$

For nearly isotropic complex fluids, the particle-particle interaction can be approximated

by its Taylor expansion around $\tilde{\alpha}_1^* = 0$ and $\tilde{G}_a = \tilde{G}_b = \tilde{G}_c = \tilde{G}$ as

$$\frac{\tilde{G}\tilde{\mathcal{G}}_{11}}{s}\Big|_{z=0} \approx \frac{2x^2+y^2}{(x^2+y^2)^{3/2}} - \frac{y^2}{8}\frac{8x^4+4x^2y^2+y^4}{(x^2+y^2)^{7/2}}\frac{\tilde{\alpha}_1^*}{\tilde{G}} - \frac{1}{4}\frac{8x^4+8x^2y^2+3y^4}{(x^2+y^2)^{5/2}}\left(\frac{\tilde{G}_b}{\tilde{G}}-1\right) - \frac{y^2}{4}\frac{4x^2+y^2}{(x^2+y^2)^{5/2}}\left(\frac{\tilde{G}_c}{\tilde{G}}-1\right), \tag{4.97}$$

$$\frac{\tilde{G}\tilde{\mathcal{G}}_{12}}{s}\Big|_{z=0} \approx xy\left[\frac{1}{(x^2+y^2)^{3/2}} - \frac{y^2}{8}\frac{6x^2+y^2}{(x^2+y^2)^{7/2}}\frac{\tilde{\alpha}_1^*}{\tilde{G}} - \frac{1}{4}\frac{4x^2+y^2}{(x^2+y^2)^{5/2}}\left(\frac{\tilde{G}_b}{\tilde{G}}-1\right) - \frac{3}{4}\frac{y^2}{(x^2+y^2)^{5/2}}\left(\frac{\tilde{G}_c}{\tilde{G}}-1\right)\right], \tag{4.98}$$

$$\frac{\tilde{G}\tilde{\mathcal{G}}_{22}}{s}\Big|_{z=0} \approx \frac{x^2+2y^2}{(x^2+y^2)^{3/2}} - \frac{5}{8}\frac{x^2y^4}{(x^2+y^2)^{7/2}}\frac{\tilde{\alpha}_1^*}{\tilde{G}} - \frac{1}{\sqrt{x^2+y^2}}\left(\frac{\tilde{G}_a}{\tilde{G}}-1\right) - \frac{3}{4}\frac{x^2y^2}{(x^2+y^2)^{5/2}}\left(\frac{\tilde{G}_b}{\tilde{G}}-1\right) - \frac{y^2}{4}\frac{x^2+4y^2}{(x^2+y^2)^{5/2}}\left(\frac{\tilde{G}_c}{\tilde{G}}-1\right), \tag{4.99}$$

$$\frac{\tilde{G}\tilde{\mathcal{G}}_{33}}{s}\Big|_{z=0} \approx \frac{1}{\sqrt{x^2+y^2}} - \frac{1}{8}\frac{y^4}{(x^2+y^2)^{5/2}}\frac{\tilde{\alpha}_1^*}{\tilde{G}} - \frac{x^2}{(x^2+y^2)^{3/2}}\left(\frac{\tilde{G}_a}{\tilde{G}}-1\right) - \frac{1}{4}\frac{y^2}{(x^2+y^2)^{3/2}}\left(\frac{\tilde{G}_b}{\tilde{G}}-1\right) - \frac{3}{4}\frac{y^2}{(x^2+y^2)^{3/2}}\left(\frac{\tilde{G}_c}{\tilde{G}}-1\right), \tag{4.100}$$

$$\tilde{\mathcal{P}}_1\Big|_{z=0} \approx \frac{x}{(x^2+y^2)^{3/2}}\left[2 - \frac{3}{4}\frac{4x^2-y^2}{(x^2+y^2)^2}y^2\frac{\tilde{\alpha}_1^*}{\tilde{G}} + \frac{2x^2-y^2}{x^2+y^2}\left(\frac{\tilde{G}_a}{\tilde{G}}-1\right) + \frac{2x^2-y^2}{x^2+y^2}\left(\frac{\tilde{G}_b}{\tilde{G}}-1\right)\right], \tag{4.101}$$

$$\tilde{\mathcal{P}}_2\Big|_{z=0} \approx \frac{y}{(x^2+y^2)^{3/2}}\left[2 - \frac{3}{4}\frac{4x^2-y^2}{(x^2+y^2)^2}y^2\frac{\tilde{\alpha}_1^*}{\tilde{G}} + \frac{2x^2-y^2}{x^2+y^2}\left(\frac{\tilde{G}_a}{\tilde{G}}-1\right) + \frac{2x^2-y^2}{x^2+y^2}\left(\frac{\tilde{G}_b}{\tilde{G}}-1\right)\right]. \tag{4.102}$$

Equations (4.69)-(4.84) are also singular for other combinations of the viscoelasticity parameters. Here we list their limit values. For $\tilde{\alpha}_1^* = \tilde{\alpha} = -\left(\sqrt{\tilde{G}_b} - \sqrt{\tilde{G}_c}\right)^2$, we have:

$$\frac{\tilde{\mathcal{G}}_{11}}{s}\Big|_{\substack{z=0\\ \tilde{\alpha}_1^*=\tilde{\alpha}}} = \frac{1}{\tilde{G}_b}\frac{2x^2+\sqrt{\frac{\tilde{G}_c}{\tilde{G}_b}}y^2}{\left(x^2+\sqrt{\frac{\tilde{G}_c}{\tilde{G}_b}}y^2\right)^{3/2}}, \tag{4.103}$$

$$\frac{\tilde{\mathcal{G}}_{12}}{s}\Big|_{\substack{z=0\\ \tilde{\alpha}_1^*=\tilde{\alpha}}} = \frac{1}{\tilde{G}_b}\frac{xy}{\left(x^2+\sqrt{\frac{\tilde{G}_c}{\tilde{G}_b}}y^2\right)^{3/2}}, \tag{4.104}$$

$$\frac{\tilde{\mathcal{G}}_{22}}{s}\Big|_{\substack{z=0\\ \tilde{\alpha}_1^*=\tilde{\alpha}}} = \frac{1}{\tilde{G}_c y^2}\left(2\sqrt{x^2+\frac{\tilde{G}_c}{\tilde{G}_a}y^2} - x^2\frac{2x^2+3\sqrt{\frac{\tilde{G}_c}{\tilde{G}_b}}y^2}{\left(x^2+\sqrt{\frac{\tilde{G}_c}{\tilde{G}_b}}y^2\right)^{3/2}}\right), \tag{4.105}$$

$$\frac{\tilde{\mathcal{G}}_{33}}{s}\Big|_{\substack{z=0\\ \tilde{\alpha}_1^*=\tilde{\alpha}}} = \frac{1}{\tilde{G}_c y^2}\left(\frac{-2x^2}{\sqrt{x^2+\frac{\tilde{G}_c}{\tilde{G}_a}y^2}}+\frac{2x^2+\sqrt{\frac{\tilde{G}_c}{\tilde{G}_b}}y^2}{\sqrt{x^2+\sqrt{\frac{\tilde{G}_c}{\tilde{G}_b}}y^2}}\right), \tag{4.106}$$

$$\tilde{\mathcal{P}}_1\Big|_{\substack{z=0\\ \tilde{\alpha}_1^*=\tilde{\alpha}}} = \frac{x}{\tilde{G}_b\left(x^2+\sqrt{\frac{\tilde{G}_c}{\tilde{G}_b}}y^2\right)^{5/2}}\left[3\tilde{G}_c y^2+\tilde{G}_a\sqrt{\frac{\tilde{G}_c}{\tilde{G}_b}}y^2\frac{5x^4-\frac{\tilde{G}_c}{\tilde{G}_b}y^4}{\left(x^2+\sqrt{\frac{\tilde{G}_c}{\tilde{G}_b}}y^2\right)^2}\right.$$
$$\left.+2\tilde{G}_a x^4\frac{x^4-\frac{\tilde{G}_c}{\tilde{G}_b}y^4}{\left(x^2+\sqrt{\frac{\tilde{G}_c}{\tilde{G}_b}}y^2\right)^3}\right], \tag{4.107}$$

$$\tilde{\mathcal{P}}_2\Big|_{\substack{z=0\\ \tilde{\alpha}_1^*=\tilde{\alpha}}} = \frac{y}{\tilde{G}_b\left(x^2+\sqrt{\frac{\tilde{G}_c}{\tilde{G}_b}}y^2\right)^{5/2}}\left[3\tilde{G}_c y^2+\tilde{G}_a\sqrt{\frac{\tilde{G}_c}{\tilde{G}_b}}y^2\frac{5x^4-\frac{\tilde{G}_c}{\tilde{G}_b}y^4}{\left(x^2+\sqrt{\frac{\tilde{G}_c}{\tilde{G}_b}}y^2\right)^2}\right.$$
$$\left.+2\tilde{G}_a x^4\frac{x^4-\frac{\tilde{G}_c}{\tilde{G}_b}y^4}{\left(x^2+\sqrt{\frac{\tilde{G}_c}{\tilde{G}_b}}y^2\right)^3}\right]. \tag{4.108}$$

For $\tilde{\alpha}_1^*=\tilde{\alpha}=-\left(\sqrt{\tilde{G}_b}+\sqrt{\tilde{G}_c}\right)^2$:

$$\frac{\tilde{\mathcal{G}}_{11}}{s}\Big|_{\substack{z=0\\ \tilde{\alpha}_1^*=\tilde{\alpha}}} = \frac{1}{\tilde{G}_b}\frac{2x^2-\sqrt{\frac{\tilde{G}_c}{\tilde{G}_b}}y^2}{\left(x^2-\sqrt{\frac{\tilde{G}_c}{\tilde{G}_b}}y^2\right)^{3/2}}, \tag{4.109}$$

$$\frac{\tilde{\mathcal{G}}_{12}}{s}\Big|_{\substack{z=0\\ \tilde{\alpha}_1^*=\tilde{\alpha}}} = \frac{1}{\tilde{G}_b}\frac{xy}{\left(x^2-\sqrt{\frac{\tilde{G}_c}{\tilde{G}_b}}y^2\right)^{3/2}}, \tag{4.110}$$

$$\frac{\tilde{\mathcal{G}}_{22}}{s}\Big|_{\substack{z=0\\ \tilde{\alpha}_1^*=\tilde{\alpha}}} = \frac{1}{\tilde{G}_c y^2}\left(2\sqrt{x^2+\frac{\tilde{G}_c}{\tilde{G}_a}y^2}-x^2\frac{2x^2-3\sqrt{\frac{\tilde{G}_c}{\tilde{G}_b}}y^2}{\left(x^2-\sqrt{\frac{\tilde{G}_c}{\tilde{G}_b}}y^2\right)^{3/2}}\right), \tag{4.111}$$

$$\frac{\tilde{\mathcal{G}}_{33}}{s}\Big|_{\substack{z=0\\ \tilde{\alpha}_1^*=\tilde{\alpha}}} = \frac{1}{\tilde{G}_c y^2}\left(\frac{-2x^2}{\sqrt{x^2+\frac{\tilde{G}_c}{\tilde{G}_a}y^2}}+\frac{2x^2-\sqrt{\frac{\tilde{G}_c}{\tilde{G}_b}}y^2}{\sqrt{x^2-\sqrt{\frac{\tilde{G}_c}{\tilde{G}_b}}y^2}}\right), \tag{4.112}$$

$$\tilde{\mathcal{P}}_1\Big|_{\substack{z=0\\ \tilde{\alpha}_1^*=\tilde{\alpha}}} = \frac{x}{\tilde{G}_b\left(x^2-\sqrt{\frac{\tilde{G}_c}{\tilde{G}_b}}y^2\right)^{5/2}}\left[3\tilde{G}_c y^2-\tilde{G}_a\sqrt{\frac{\tilde{G}_c}{\tilde{G}_b}}y^2\frac{5x^4-\frac{\tilde{G}_c}{\tilde{G}_b}y^4}{\left(x^2-\sqrt{\frac{\tilde{G}_c}{\tilde{G}_b}}y^2\right)^2}\right.$$
$$\left.+2\tilde{G}_a x^4\frac{x^4-\frac{\tilde{G}_c}{\tilde{G}_b}y^4}{\left(x^2-\sqrt{\frac{\tilde{G}_c}{\tilde{G}_b}}y^2\right)^3}\right], \tag{4.113}$$

$$\tilde{\mathcal{P}}_2\Big|_{\substack{z=0\\ \tilde{\alpha}_1^*=\tilde{\alpha}}} = \frac{y}{\tilde{G}_b\left(x^2-\sqrt{\frac{\tilde{G}_c}{\tilde{G}_b}}y^2\right)^{5/2}}\left[3\tilde{G}_c y^2-\tilde{G}_a\sqrt{\frac{\tilde{G}_c}{\tilde{G}_b}}y^2\frac{5x^4-\frac{\tilde{G}_c}{\tilde{G}_b}y^4}{\left(x^2-\sqrt{\frac{\tilde{G}_c}{\tilde{G}_b}}y^2\right)^2}\right.$$
$$\left.+2\tilde{G}_a x^4\frac{x^4-\frac{\tilde{G}_c}{\tilde{G}_b}y^4}{\left(x^2-\sqrt{\frac{\tilde{G}_c}{\tilde{G}_b}}y^2\right)^3}\right]. \tag{4.114}$$

When $\tilde{\alpha}_1^*=0$ and $\tilde{G}_b=\tilde{G}_c$:

$$\frac{\tilde{\mathcal{G}}_{11}}{s}\Big|_{\substack{z=0\\ \tilde{G}_b=\tilde{G}_c}} = \frac{1}{\tilde{G}_c}\frac{2x^2+y^2}{\left(x^2+y^2\right)^{3/2}}, \tag{4.115}$$

$$\frac{\tilde{\mathcal{G}}_{12}}{s}\Big|_{\substack{z=0\\ \tilde{G}_b=\tilde{G}_c}} = \frac{1}{\tilde{G}_c}\frac{xy}{\left(x^2+y^2\right)^{3/2}}, \tag{4.116}$$

$$\frac{\tilde{\mathcal{G}}_{22}}{s}\Big|_{\substack{z=0\\ \tilde{G}_b=\tilde{G}_c}} = \frac{1}{\tilde{G}_c y^2}\left(2\sqrt{x^2+\frac{\tilde{G}_c}{\tilde{G}_a}y^2}-x^2\frac{2x^2+3y^2}{\left(x^2+y^2\right)^{3/2}}\right), \tag{4.117}$$

$$\frac{\tilde{\mathcal{G}}_{33}}{s}\Big|_{\substack{z=0\\ \tilde{G}_b=\tilde{G}_c}} = \frac{1}{\tilde{G}_c y^2}\left(\frac{2x^2+y^2}{\sqrt{x^2+y^2}}-\frac{2x^2}{\sqrt{x^2+\frac{\tilde{G}_c}{\tilde{G}_a}y^2}}\right), \tag{4.118}$$

$$\tilde{\mathcal{P}}_1\Big|_{\substack{z=0\\ \tilde{G}_b=\tilde{G}_c}} = \frac{x\left[2\tilde{G}_a+3\left(\tilde{G}_c-\tilde{G}_a\right)\frac{y^2}{x^2+y^2}\right]}{\tilde{G}_c\left(x^2+y^2\right)^{3/2}}, \tag{4.119}$$

$$\tilde{\mathcal{P}}_2\Big|_{\substack{z=0\\ \tilde{G}_b=\tilde{G}_c}} = \frac{y\left[2\tilde{G}_a+3\left(\tilde{G}_c-\tilde{G}_a\right)\frac{y^2}{x^2+y^2}\right]}{\tilde{G}_c\left(x^2+y^2\right)^{3/2}}. \tag{4.120}$$

When $\tilde{\alpha}_1^*=0$ and $\tilde{G}_a=\tilde{G}_b=\tilde{G}_c$:

$$\frac{\tilde{\mathcal{G}}_{22}}{s}\Big|_{\substack{z=0\\ \tilde{G}_a=\tilde{G}_b=\tilde{G}_c}} = \frac{1}{\tilde{G}_c}\frac{x^2+2y^2}{\left(x^2+y^2\right)^{3/2}}, \tag{4.121}$$

$$\frac{\tilde{\mathcal{G}}_{33}}{s}\Big|_{\substack{z=0\\ \tilde{G}_a=\tilde{G}_b=\tilde{G}_c}} = \frac{1}{\tilde{G}_c}\frac{1}{\sqrt{x^2+y^2}}, \tag{4.122}$$

$$\tilde{\mathcal{P}}_1\Big|_{\substack{z=0\\ \tilde{G}_a=\tilde{G}_b=\tilde{G}_c}} = \frac{2x}{\left(x^2+y^2\right)^{3/2}}, \tag{4.123}$$

$$\tilde{\mathcal{P}}_2\Big|_{\substack{z=0\\ \tilde{G}_a=\tilde{G}_b=\tilde{G}_c}} = \frac{2y}{\left(x^2+y^2\right)^{3/2}}. \tag{4.124}$$

Another singularity arises when $y = 0$, independently of the viscoelasticity coefficients:

$$\frac{\tilde{\mathcal{G}}_{12}}{s}\Big|_{\substack{z=0\\y=0}} = 0, \tag{4.125}$$

$$\frac{\tilde{\mathcal{G}}_{22}}{s}\Big|_{\substack{z=0\\y=0}} = \frac{1}{\tilde{G}_a x}, \tag{4.126}$$

$$\frac{\tilde{\mathcal{G}}_{33}}{s}\Big|_{\substack{z=0\\y=0}} = \frac{1}{\tilde{G}_a x}. \tag{4.127}$$

4.8 Appendix C - Numerical Implementation of Laplace Transforms

Laplace transforms are calculated using the Fast Laplace Transform (FLT) approach [65]. The FLT is based on the observation that the complex Laplace frequency s is related to the Fourier frequency ω as $s = c + i\omega$, so that the Laplace transform can be calculated by using the coefficients of the Fast Fourier Transform. We use an efficient implementation of the Fast Fourier Transform called the FFTW [46, 47]. The accuracy of the FLT has been characterized as a function of the free frequency parameter c [65], being $c = 4\pi/T$ the optimal value, which we have employed throughout the simulations. We have found the errors introduced by the FLT for the specific data of our simulations to be $\sim 10^{-6}\%$ (data not shown). We dismissed the implementation of an improved Talbot approximation to the Inverse Laplace Transform [145, 156, 35] because, while it would provide a smoother result, it is singular at $\tau = 0$.

4.9 Appendix D - Validation of D2PTM by Numerical Simulation. Additional Data.

The parameters used in the simulation presented in **§4.3** were deliberately chosen so that the MSD would display isotropic features at high frequencies and anisotropic characteristics at low frequencies, and thus illustrate the applicability of D2PTM to differentiate these two behaviors. Here, we present additional validation data for a more generic example fluid where the 6 viscoelastic parameters are different from each other, *i.e.* $\mu_a = 0.1$ Pa, $\mu_b = 0.4$ Pa, $\mu_c = 0.3$ Pa,

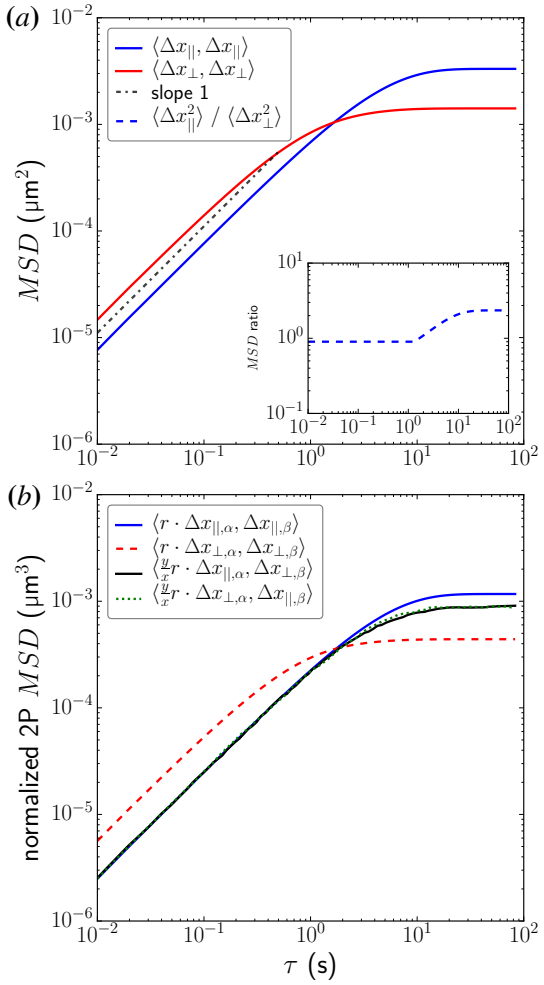

Figure 4.14: One- and two-point MSD of $N = 1,000$ simulated particles and $M = 2,000$ particle pairs in the principal directions of an additional nematic Kelvin-Voigt fluid. (*a*) One-point MSD in the principal directions of a nematic Kelvin-Voigt fluid with $\mu_a = 0.1$ Pa, $\mu_b = 0.4$ Pa, $\mu_c = 0.3$ Pa and $\eta_a = 0.6$ Pa·s, $\eta_b = 0.2$ Pa·s, $\eta_c = 0.4$ Pa·s, projected along the $||$ (——) and $\perp$ (– –) directions. A line of unit slope is plotted as reference (·····). The inset shows the MSD ratio, $\langle \Delta x_{||}, \Delta x_{||} \rangle / \langle \Delta x_{\perp}, \Delta x_{\perp} \rangle$. (*b*) Renormalized two-point cross-MSD of the same simulated trajectories: $\langle r \cdot \Delta x_{||,\alpha}, \Delta x_{||,\beta} \rangle$ (——), $\langle r \cdot \Delta x_{\perp,\alpha}, \Delta x_{\perp,\beta} \rangle$ (– –), $\langle \frac{y}{x} r \cdot \Delta x_{||,\alpha}, \Delta x_{\perp,\beta} \rangle$ (– · –) and $\langle \frac{y}{x} r \cdot \Delta x_{\perp,\alpha}, \Delta x_{||,\beta} \rangle$ (·····). The data are plotted versus the time separation τ.

$\eta_a = 0.6$ Pa·s, $\eta_b = 0.2$ Pa·s and $\eta_c = 0.4$ Pa·s, and show that they can also be recovered by D2PTM. In **Figure 4.14** we show the MSD of individual microparticles and the cross-MSD of pairs of interacting particles embedded in the simulated material. It can be seen that the shapes of the MSD curves are qualitatively similar to those shown in **Figure 4.7**, but here the anisotropy is present at all frequencies. In **Figure 4.15** we show the directional shear moduli prescribed to the simulation, along with the values recovered by the D2PTM implementation. Although the shape

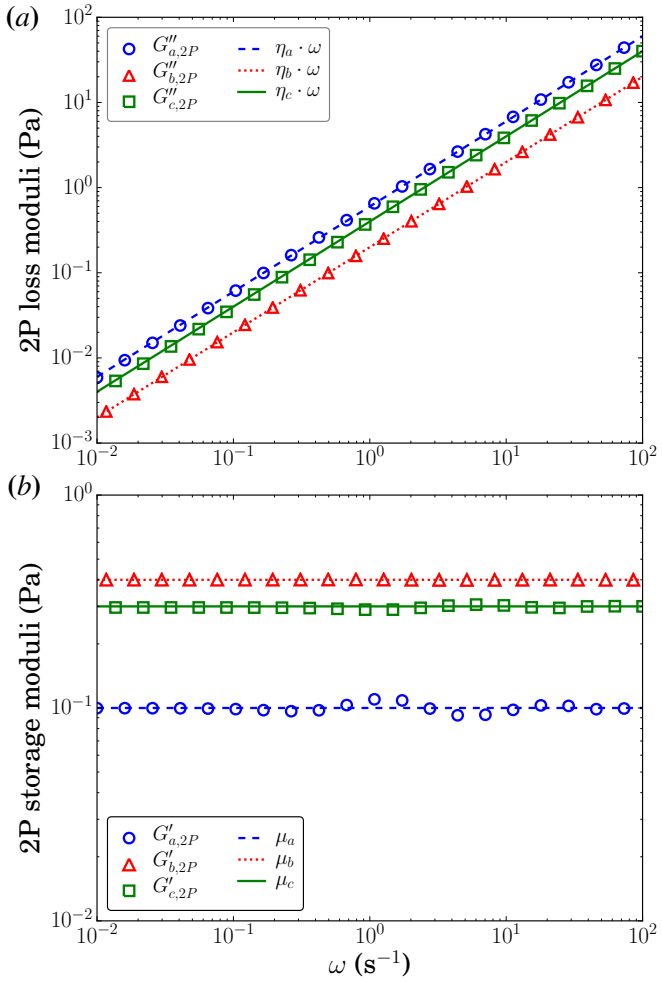

Figure 4.15: Prescribed and recovered loss and storage moduli of an aditional simulated fluid, calculated by applying the D2PTM analysis (*a*) Symbols: G''_a (○), G''_b (Δ) and G''_c (□). Lines: actual loss moduli of the material (– –, ····· and ——). (*b*) Symbols: G'_a (○), G'_b (Δ) and G'_c (□). Lines: actual storage moduli of the material (– –, ····· and ——).

of the loss moduli is qualitatively similar to those shown in **Figure 4.8**, the numerical values of every coefficient are now different. As one can see, the shear moduli are recovered with an accuracy similar to **§4.3**.

4.10 Appendix E - Validation of the Particle Tracking Setup

To characterize the accuracy of the imaging platform and particle tracking algorithm implemented for our experiments, we performed PTM in a solution of glycerol and water, which is a well characterized system with isotropic Newtonian rheology. We prepared control isotropic samples of 50% (v/v) glycerol in water, which results in a bulk viscosity consistent with MSD values that span the range of MSD measured in the F-actin experiments.

Figure 4.16 shows the MSD of the probing particles in principal directions as well as the total MSD. For the whole range of representative frequencies of the experiment, the MSD follow a straight line with unit slope down to the lowest values of τ. This result indicates that our particle tracking setup has sufficient spatial resolution to track particle displacements at our experimental sampling frequency. Furthermore, we calculated the viscosity of the sample from the MSD by applying standard PTM (equation 4.35), and obtained a viscosity coefficient of $\eta \approx 6.5$ mPa·s, consistent with a 50% (v/v) solution of glycerol in water, at 20°C. Another important result stemming from **Figure 4.16** is that, although the isotropic samples were confined in the same

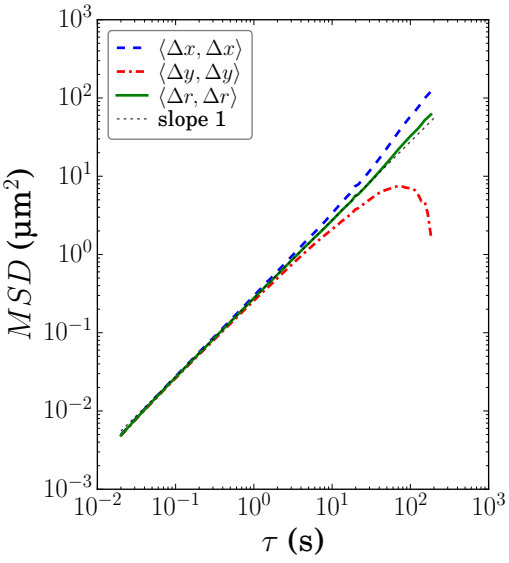

Figure 4.16: MSD of 0.5 μm diameter particles embedded in a 50% (v/v) solution of glycerol in water, plotted as a function of time separation τ. Total (——) MSD as well as MSD in principal directions of maximal (– –) and minimal (– · –) mobility are shown. A line with unit slope has been included for reference (· · · · ·).

capillary tubes than the F-actin solutions, the measured MSD are isotropic up to time separations $\tau \sim 10s$. Thus, the spatial confinement induced by the walls of the capillary tube does not induce anisotropic particle mobility in the range of frequencies of interest.

Chapter 4 has been in part submitted for peer review under the title "Two-Point Particle Tracking Microrheology of Nematic Complex Viscoelastic Fluids", by M. Gómez-González and J. C. del Álamo. The dissertation author is the primary investigator in this publication.

Chapter 5

Particle Tracking Microrheology of Live Cell Membranes

5.1 Introduction

In this chapter, we study the microrheological properties of the membrane-cortex complex of live Red Blood Cells (RBC). To that end, we apply PTM in a similar manner we did in previous chapters, by using probing particles embedded in the membrane-cortex complex of the RBC (note that, from here on, we will interchangeable use the expressions membrane-cortex complex and "membrane", as opposed to the "cell membrane").

RBC are the cells in charge of delivering oxygen to the body tissues. To that end, they need to squeeze through the body's capillaries, and thus their deformability, stability and other mechanical properties are key to their correct function [19]. Their viscoelasticity and deformability can be highly influenced by different pathophysiological conditions [19, 71], such as age, the invasion of the Malaria parasite [25], the sickle cell disease [97], Thalassemia, etc., and thus modifying the blood viscosity, circulation and RBC function. Similarly, the processing and storage of transfusion blood greatly affect their deformability and viscoelasticity, and thus the quality and performance of the donated RBC[160, 23]. Because of this interplay between mechanical

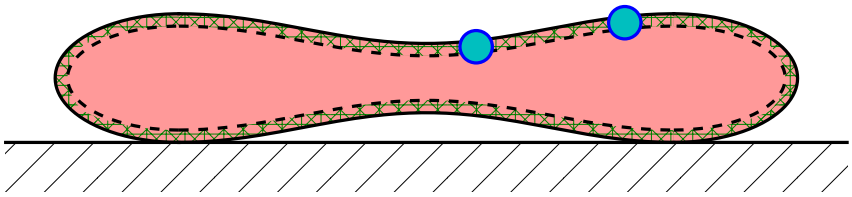

Figure 5.1: Side-view schematic representation of the RBC's membrane PTM experiment. Individual RBC (depicted in red) are attached to a solid surface. Probing polylysine-coated microparticles (shown in blue) are embedded in the cell's membrane (solid line)-cortex (green hatch) complex.

properties and cell function, a quantitative analysis of the RBC structural microrheology is key to understanding different diseases and conditions of the blood and RBC.

RBC transport oxygen by making use of the oxygen-binding protein hemoglobin. In order to maximize the amount of hemoglobin they carry, adult mammalian RBC lack a cell nucleus and most organelles. Their structure, integrity and viscoelasticity is mostly provided by the cell membrane and the spectrin cortex laying underneath it, and thus it is paramount to design an experimental tool to measure the viscoelasticity of this structure. In [19, 71], the authors provide extensive reviews of the experimental approximations taken to measure the microrheological characteristics of RBC.

In **Figure 5.1** we show a side-view schematic representation of a RBC mechanical structure and the PTM experimental setup that we used to probe its local microrheological properties. The RBC's cell membrane is depicted as a solid black line, and the spectrin cortex is delimited by a dashed black line, and hatched in green. Individual RBC are attached to a solid surface, and polylysine-coated microparticles are embedded into its membrane. This experimental system presents the defining characteristic that the probed material is a thin viscoelastic membrane, surrounded by buffer and the cell cytoplasm, and the probing particles cannot freely move in three dimensions, but their motion is restricted to the surrounding membrane. Furthermore, the particle motion is also affected by the fluid surrounding the membrane. Thus, we cannot apply the GSER (1.17) to the measured particle MSD in order to obtain the membrane shear modulus, but we will need to correctly model the diffusivity of the particles in this complex

system. Consequently, this is a perfect example of the importance of having a correct description of the fluid mechanics of the experimental system, and the need to adapt the GSER to the physical characteristics of the specimen under study.

In the following sections, we will provide the drag force of a particle embedded in this system, the interaction of pairs of distant embedded particles, and we will use them to modify the GSER to correctly measure the membrane viscoelasticity. Furthermore, we will provide some experimental examples of their application, *i.e.* we will measure the viscoelasticity of the membrane-cortex complex of RBC by applying membrane one-particle and two-point PTM.

5.2 One-Point PTM of 2D Membranes Embedded in Surrounding Fluids

Lets consider a viscoelastic 2D membrane of thickness h and shear modulus $\tilde{G}_m$ embedded in a viscoelastic fluid of shear modulus $\tilde{G}_f$, as depicted in **Figure 5.2**. This membrane contains a cylindrical inclusion, α, of radius a_α and height not smaller than h. We are interested in the mobility of the inclusion, with motion parallel to the membrane surface. In the low Reynolds number regime and in the frequency domain, a force $\tilde{F}_\alpha$ acting on the particle and its induced velocity $\tilde{v}_\alpha$ are related by the particle's translational mobility $\tilde{b}_{T,\alpha}$ as

$$\tilde{v}_\alpha = \tilde{b}_{T,\alpha} \cdot \tilde{F}_\alpha, \tag{5.1}$$

where the particle mobility is the inverse of the particle resistance, in the frequency domain, $\tilde{b}_{T,\alpha}(s) = \tilde{\zeta}_\alpha^{-1}(s)$. Saffman and Delbrück [129, 128] calculated the mobility of an inclusion bounded to a purely viscous membrane which is embedded in a purely viscous liquid. Here, we will apply analytical continuation to their results and study the case of complex viscoelastic membranes embedded in a viscoelastic fluid. In the case $\left(\tilde{G}_m \cdot h / \tilde{G}_f \cdot a_\alpha\right) \gg 1$ and assuming a no-slip boundary condition on the inclusion, the translational mobility of the particle takes the

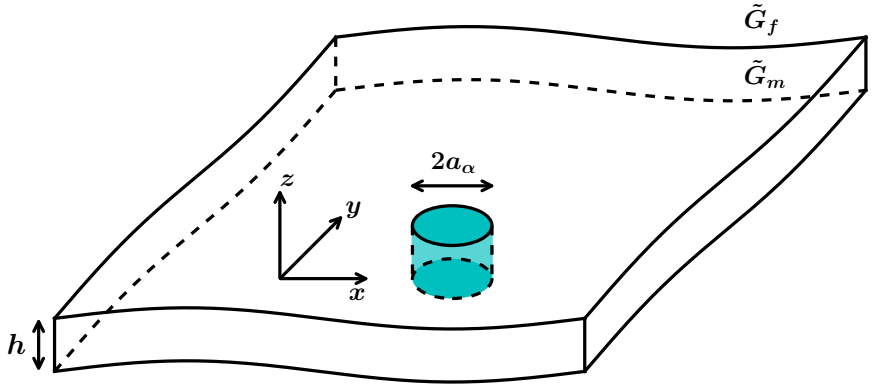

Figure 5.2: Schematic representation of the hydrodynamic model for the mobility of inclusions submerged on a 2D viscoelastic membrane which is simultaneously embedded in a different viscoelastic fluid. The membrane is defined by a shear modulus $\tilde{G}_m$ and a thickness h and the surrounding fluid by a shear modulus $\tilde{G}_f$. The inclusions, modeled as cylinders of radius a_α and height not smaller than h, can freely move in the xy plane but not in the z direction.

form

$$\tilde{b}_{T,\alpha} = \frac{s}{4\pi\tilde{G}_m \cdot h}\left[\ln\left(\frac{\tilde{G}_m \cdot h}{\tilde{G}_f \cdot a_\alpha}\right) - \gamma\right], \tag{5.2}$$

where $\gamma \approx 0.5772$ is the Euler-Mascheroni constant. This is the equivalent to the Stokes equation (1.3) when we are quantifying the drag force of a particle submerged on a 2D viscoelastic membrane, which is embedded in a second viscoelastic fluid. If instead of a no-slip boundary condition on the particle surface we impose a zero tangential stress condition, the translational mobility takes the form

$$\tilde{b}_{T,\alpha} = \frac{s}{4\pi\tilde{G}_m \cdot h}\left[\ln\left(\frac{\tilde{G}_m \cdot h}{\tilde{G}_f \cdot a_\alpha}\right) + \frac{1}{2} - \gamma\right]. \tag{5.3}$$

In the specific case where the fluids above and bellow the membrane present different shear moduli, $\tilde{G}_{f,a}$ and $\tilde{G}_{f,b}$, equations (5.2) and (5.3) should be modified to include the effective fluid shear moduli $\tilde{G}_f = \left(\tilde{G}_{f,a} + \tilde{G}_{f,b}\right)/2$ [89]. Interestingly, equations (5.2)-(5.3) are independent on the amount the inclusion sticks out of the membrane. This allows spherical particles of radius larger than the membrane thickness, *i.e.* $a_\alpha \gg h$, to be locally modelled as disks embedded in a membrane, with hemispherical protrusions projecting into the surrounding fluid. In the reminder

of this section, we will consider no-slip on the particle surface.

Similar to the analysis carried out in previous chapters, we can relate the MSD in the frequency domain, $\langle \Delta\tilde{r}_\alpha^2(s)\rangle$, of inclusion α subjected to Brownian thermal excitations and its translational mobility through the Einstein equation (1.16)

$$\langle \Delta\tilde{r}_\alpha^2(s)\rangle = \frac{2nk_BT}{s^2}\tilde{b}_{T,\alpha}(s), \tag{5.4}$$

where n is the number of dimensions of the motion, $k_B = 1.3806488 \times 10^{-23} m^2 kg/s^2 K$ is the Boltzmann constant and T is the absolute temperature. We then obtain an equation equivalent to the GSER that can be applied to our model system

$$\langle \Delta\tilde{r}_\alpha^2(s)\rangle = \frac{nk_BT}{2\pi s\tilde{G}_m \cdot h}\left[\ln\left(\frac{\tilde{G}_m \cdot h}{\tilde{G}_f \cdot a_\alpha}\right) - \gamma\right]. \tag{5.5}$$

The ensemble average of the MSD of N particles takes the form

$$\langle \Delta\tilde{r}^2(s)\rangle = \frac{nk_BT}{2\pi s\tilde{G}_m \cdot h}\left[\ln\left(\frac{\tilde{G}_m \cdot h}{\tilde{G}_f \cdot \overline{a}}\right) - \gamma\right], \tag{5.6}$$

where

$$\langle \Delta\tilde{r}^2(s)\rangle = \frac{1}{N}\sum_{\forall\alpha}\langle \Delta\tilde{r}_\alpha^2(s)\rangle, \tag{5.7}$$

is the ensemble average of the MSD of N individual particles and

$$\overline{a} = \frac{1}{N}\sum_{\forall\alpha} a_\alpha. \tag{5.8}$$

is their average radius.

Equation (5.6) present certain particularities. It is a transcendental equation, and thus it needs to be solved iteratively, and we need to prescribe an initial guess. However, it is a fairly smooth function, and we can use, as initial guess, the result provided by (1.17) or an estimation similar to the one shown below, and the iterative solver will quickly converge. A second possible

source of problems is that it contains the logarithm of a complex number, and hence it should be treated carefully. In our implementation, we have defined the following non-dimensional parameters and variables

$$\tilde{A}(s) = \frac{2\pi}{nk_BT}\langle\Delta\tilde{r}^2(s)\rangle \cdot s \cdot \overline{a} \cdot \tilde{G}_f(s), \tag{5.9}$$

$$\tilde{G}(s) = \frac{\tilde{G}_m(s)\cdot h}{\tilde{G}_f(s)\cdot \overline{a}}, \tag{5.10}$$

and solved the non-dimensional equation

$$\tilde{F}_{\log}(s) \equiv \ln\left[\tilde{G}(s)\right] - \gamma - \tilde{A}(s)\cdot\tilde{G}(s) = 0. \tag{5.11}$$

At this point, we can make an order-of-magnitude estimation of the error incurred on when applying the GSER (1.17) to a system that actually follows (5.6). If we define the shear modulus provided by the GSER as

$$\tilde{G}_{3D}(s) = \frac{nk_BT}{3\pi\overline{a}s\langle\Delta\tilde{r}^2(s)\rangle}, \tag{5.12}$$

and combine it with equation (5.6), we obtain the relation

$$\tilde{G}_{3D}(s) = \frac{2}{3}\frac{h}{\overline{a}}\frac{\tilde{G}_m(s)}{\ln\left(\frac{\tilde{G}_m\cdot h}{\tilde{G}_f\cdot\overline{a}}\right) - \gamma}, \tag{5.13}$$

In a typical live-cell membrane PTM experiment, the surrounding fluid will consist on a water based buffer, with shear modulus $\tilde{G}_f(s) \sim \tilde{G}_{\mathrm{H_2O}}(s)$. The membrane complex will typically consist on an oily substance with a shear modulus such that $\tilde{G}_m(s) \sim 10^3\tilde{G}_{\mathrm{H_2O}}(s)$. The membrane thickness will be in the range of tenths of nanometers, while the probing particle diameter will be a fraction of a micron. For these values, $\left|\tilde{G}_m(s)\cdot h/\tilde{G}_f(s)\cdot\overline{a}\right| \sim 10^3$. Since a logarithm is applied to this parameters, a fairly large variation of the parameters will have a relative small influence in

our estimations. It follows that

$$\frac{2}{3}\left|\ln\left(\frac{\tilde{G}_m \cdot h}{\tilde{G}_f \cdot \overline{a}}\right) - \gamma\right| \sim 10, \tag{5.14}$$

and thus

$$\tilde{G}_m(s) \sim 10 \cdot \frac{\overline{a}}{h} \cdot \tilde{G}_{3D}(s). \tag{5.15}$$

As we already indicated, the above statement is an order-of-magnitude estimation, and any deduction extracted from it should be regarded as a rough estimation. In the light of equation (5.15), we can expect that the shear modulus provided by the GSER and the membrane formulation will be simmilar when the particle radius is one tenth of the membrane thickness. However, for that geometry, the experimetnal particles that we use in this study would probably not be well described by a cylindrical inclusion, and the membrane formulation would break. We will be testing this order-of-magnitude estimation with our experimental results.

5.3 Two-Point PTM of 2D Membranes Embedded in Surrounding Fluids

In [138] the authors provide an extensive review of the conditions under which the assumptions that lead to the GSER (1.17) might break. Specifically, the Einstein relation (1.16) will break if the system is not in thermodynamic equilibrium or if the equipartition theorem doesn't hold, *i.e.* if the driving force has an average energy content different than $k_B T/2$, as happens in active PTM. The Stokes equation (1.3) will not be applicable if the material cannot be described as a continuous, homogeneous and isotropic fluid, *i.e.* if the far-field assumptions don't hold, or if the local mechanical or electrochemical interactions between the particle and the medium alter the local environment, *i.e.* if the near-field hypothesis breaks. In **§5.2**, we focused on why the far field assumptions of the GSER don't hold in our experimental system, and we modified the Stokes formula to take into account the actual hydrodynamics of the problem. In this

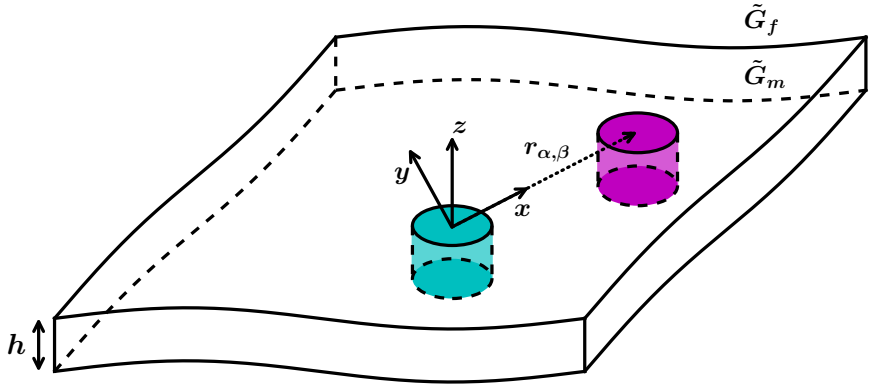

Figure 5.3: Schematic representation of the hydrodynamic model for interactions of pairs of distant inclusions submerged on a 2D viscoelastic membrane which is simultaneously embedded in a different viscoelastic fluid. The membrane is defined by a shear modulus $\tilde{G}_m$ and a thickness h and the surrounding fluid by a shear modulus $\tilde{G}_f$. The inclusions, modeled as cylinders of radius a_i and height not smaller than h, can freely move in the xy plane but not in the z direction. Each pair of particles are located at a distance $r_{\alpha,\beta} \gg a_i$.

section, we will focus on the breaking of the near-field assumptions, as happens when the probing particles induce local compressibility, when there are electrochemical interactions between the particle and the probed material, when there is partial or total slip in the particle surface, etc. As stated before, these conditions will have an effect in the mobility of individual particles. However, their effect will be negligible in the cross-correlated motion of pairs of distant particles, and thus they will not affect 2PPTM.

Lets consider two distant inclusions α and β, as depicted in **Figure 5.3**, embedded in the model viscoelastic system, and separated a distance $r_{\alpha,\beta} \gg a_i$. We define a Cartesian coordinate system with the x-direction defined by the line that connects the particle centers, the z-direction perpendicular to the membrane, and the y-direction defining a right orthonormal system. When an in-plane point force $\tilde{\vec{f}}_\alpha$ is applied to one inclusion, the second inclusion experiences an in-plane velocity $\tilde{\vec{v}}^{\,I}_{\alpha,\beta}$ of the form

$$\tilde{\vec{v}}^{\,I}_{\alpha,\beta}(s) = \frac{\tilde{\tilde{\mathcal{G}}}(r_{\alpha,\beta};s)\cdot\tilde{\vec{f}}_\alpha(s)}{8\pi} \tag{5.16}$$

where $\tilde{\tilde{\mathcal{G}}}(r_{\alpha,\beta};s)$ is the Green's function for the velocity. In the coordinate system so defined, the

Green's function tensor has the form, up to first order,

$$\tilde{\overline{\mathcal{G}}}(r_{\alpha,\beta};s) = \begin{bmatrix} \tilde{\mathcal{G}}_{xx} & 0 \\ 0 & \tilde{\mathcal{G}}_{yy} \end{bmatrix}. \tag{5.17}$$

In [89, 115] the authors provide the general form of $\tilde{\mathcal{G}}_{xx}$ and $\tilde{\mathcal{G}}_{yy}$ by using Bessel and Struve functions. In [115] they also provide approximations for different ranges of the problem parameters. Specifically, we are interested in a membrane that is much more viscous than the surrounding fluid, and particles that are separated a distance large compare to their radius, *i.e.*

$$\left|\tilde{k}\cdot\frac{a_i}{h}\right|^{-1} \ll \frac{r_{\alpha,\beta}}{a_i} \ll \left|\tilde{k}\cdot\frac{a_i}{h}\right|^{-3/2}, \tag{5.18}$$

where

$$\tilde{k} = 2\cdot\frac{\tilde{G}_f}{\tilde{G}_m}. \tag{5.19}$$

For this range of parameters

$$\tilde{\mathcal{G}}_{xx}(r_{\alpha,\beta};s) = \frac{2s}{\tilde{G}_m\cdot h}\left\{\ln\left(\frac{2}{\tilde{k}}\cdot\frac{h}{r_{\alpha,\beta}}\right) - \gamma + \frac{1}{2} + \frac{2}{3}\tilde{k}\cdot\frac{r_{\alpha,\beta}}{h}\right\}, \tag{5.20}$$

$$\tilde{\mathcal{G}}_{yy}(r_{\alpha,\beta};s) = \frac{2s}{\tilde{G}_m\cdot h}\left\{\ln\left(\frac{2}{\tilde{k}}\cdot\frac{h}{r_{\alpha,\beta}}\right) - \gamma - \frac{1}{2} + \frac{4}{3}\tilde{k}\cdot\frac{r_{\alpha,\beta}}{h}\right\}. \tag{5.21}$$

By combining equations (5.20)-(5.21) with the *two-particle* Einstein equation (4.39) we obtain the form of the cross-MSD of a pair of interacting particles

$$\langle \Delta x_\alpha(0), \Delta\tilde{x}_\beta(s)\rangle = \frac{k_B T}{2\pi s\tilde{G}_m\cdot h}\left\{\ln\left(\frac{2}{\tilde{k}}\cdot\frac{h}{r_{\alpha,\beta}}\right) - \gamma + \frac{1}{2} + \frac{2}{3}\tilde{k}\cdot\frac{r_{\alpha,\beta}}{h}\right\}, \tag{5.22}$$

$$\langle \Delta y_\alpha(0), \Delta\tilde{y}_\beta(s)\rangle = \frac{k_B T}{2\pi s\tilde{G}_m\cdot h}\left\{\ln\left(\frac{2}{\tilde{k}}\cdot\frac{h}{r_{\alpha,\beta}}\right) - \gamma - \frac{1}{2} + \frac{4}{3}\tilde{k}\cdot\frac{r_{\alpha,\beta}}{h}\right\}, \tag{5.23}$$

that don't depend on the size of the particles. It is important to note that, while interacting particles

embedded in a 3D isotropic material present coss-MSD that are related as

$$\left.\frac{\langle \Delta x_\alpha(0), \Delta x_\beta(\tau)\rangle}{\langle \Delta y_\alpha(0), \Delta y_\beta(\tau)\rangle}\right|_{3D} = 2, \tag{5.24}$$

interacting particles embedded in our membrane system will present a ratio of cross-MSD that is more complicated, and in general dependent on the shear moduli ratio of the membrane and surrounding fluids, as well as other geometric parameters of the problem.

In a typical 2PPTM experiment, we will calculate the ensemble average of the cross-MSD of M pairs of distant particles. For the system under study, they take the form

$$\langle \Delta r_1(0), \Delta \tilde{r}_2(s)\rangle = \frac{k_B T}{2\pi s \tilde{G}_m \cdot h}\left\{\ln\left(\frac{2}{\tilde{k}\cdot\hat{r}}\right) - \gamma + \frac{1}{2} + \frac{2}{3}\tilde{k}\cdot\bar{r}\right\}, \tag{5.25}$$

$$\langle \Delta \theta_1(0), \Delta \tilde{\theta}_2(s)\rangle = \frac{k_B T}{2\pi s \tilde{G}_m \cdot h}\left\{\ln\left(\frac{2}{\tilde{k}\cdot\hat{r}}\right) - \gamma - \frac{1}{2} + \frac{4}{3}\tilde{k}\cdot\bar{r}\right\} \tag{5.26}$$

where

$$\langle \Delta r_1(0), \Delta \tilde{r}_2(s)\rangle = \frac{1}{M}\sum_{\substack{\forall \alpha,\beta \\ \alpha\neq\beta}} \langle \Delta x_\alpha(0), \Delta \tilde{x}_\beta(s)\rangle, \tag{5.27}$$

$$\langle \Delta \theta_1(0), \Delta \tilde{\theta}_2(s)\rangle = \frac{1}{M}\sum_{\substack{\forall \alpha,\beta \\ \alpha\neq\beta}} \langle \Delta y_\alpha(0), \Delta \tilde{y}_\beta(s)\rangle \tag{5.28}$$

are the ensemble averages of the cross-MSD of M pairs of interacting particles in the directions parallel and perpendicular to the lines of centers,

$$\bar{r} = \frac{1}{M}\sum_{\substack{\forall \alpha,\beta \\ \alpha\neq\beta}} \frac{r_{\alpha,\beta}}{h} \tag{5.29}$$

is the average inter-particle distance divided by the membrane thickness and

$$\hat{r} = \left(\prod_{\substack{\forall \alpha,\beta \\ \alpha\neq\beta}} \frac{r_{\alpha,\beta}}{h}\right)^{1/M} \tag{5.30}$$

is the geometric mean of the inter-particle distances divided by the membrane thickness. By knowing the physical and geometrical parameters of the experiment, both equation (5.25) and (5.26) independently provide the shear modulus of the embedded membrane $\tilde{G}_m$. In practice, we will solve both equations and average the obtained shear moduli. However, it is important to be aware that the radial particle interactions $\langle \Delta r_1(0), \Delta \tilde{r}_2(s) \rangle$ will frequently be higher and contain less noise than the transversal interactions $\langle \Delta \theta_1(0), \Delta \tilde{\theta}_2(s) \rangle$, and thus there might be experimental circumstances where we only want to use one of the equations.

The inter-particle interactions (5.25)-(5.26) are weaker in nature than the single particle MSD (5.6), and thus more prone to be affected by experimental noise. In order to obtain statistically significant 2PPTM results, one needs to average over a comparatively large number of pairs of particles, *i.e.* $M \gg N$. On top of that, the inter-particle distance will not be uniform, but it greatly vary from pair to pair. This poses a problem on its own, because the inter-particle interaction decreases with the particle distance $r_{\alpha,\beta}$, and averaging over noisy data with very different values will introduce numerical errors. One can mitigate this by normalizing the cross-MSD with the distance, and obtaining data with similar order of magnitude that we can average with more confidence. The normalized cross-MSD of pairs of distant particles in our model system take the form

$$\langle r \cdot \Delta r_1(0), \Delta \tilde{r}_2(s) \rangle = \frac{k_B T}{2\pi s \tilde{G}_m} \left\{ \bar{r} \cdot \left[\ln\left(\frac{2}{\tilde{k}}\right) - \gamma + \frac{1}{2} \right] - \ln\left(\widehat{r^r}\right) + \frac{2}{3} \tilde{k} \cdot \overline{r^2} \right\}, \tag{5.31}$$

$$\langle r \cdot \Delta \theta_1(0), \Delta \tilde{\theta}_2(s) \rangle = \frac{k_B T}{2\pi s \tilde{G}_m} \left\{ \bar{r} \cdot \left[\ln\left(\frac{2}{\tilde{k}}\right) - \gamma - \frac{1}{2} \right] - \ln\left(\widehat{r^r}\right) + \frac{4}{3} \tilde{k} \cdot \overline{r^2} \right\} \tag{5.32}$$

where

$$\langle r \cdot \Delta r_1(0), \Delta \tilde{r}_2(s) \rangle = \frac{1}{M} \sum_{\substack{\forall \alpha,\beta \\ \alpha \neq \beta}} r_{\alpha,\beta} \cdot \langle \Delta x_\alpha(0), \Delta \tilde{x}_\beta(s) \rangle, \tag{5.33}$$

$$\langle r \cdot \Delta \theta_1(0), \Delta \tilde{\theta}_2(s) \rangle = \frac{1}{M} \sum_{\substack{\forall \alpha,\beta \\ \alpha \neq \beta}} r_{\alpha,\beta} \cdot \langle \Delta y_\alpha(0), \Delta \tilde{y}_\beta(s) \rangle \tag{5.34}$$

are the ensemble averages of the cross-MSD, normalized with the inter-particle distance $r_{\alpha,\beta}$, of

M pairs of interacting particles in the directions parallel and perpendicular to the lines of centers,

$$\overline{r^2} = \frac{1}{M} \sum_{\substack{\forall \alpha,\beta \\ \alpha \neq \beta}} \left(\frac{r_{\alpha,\beta}}{h} \right)^2 \tag{5.35}$$

is the average of the square of the inter-particle distances divided by the membrane thickness and

$$\widehat{r^r} = \left[\prod_{\substack{\forall \alpha,\beta \\ \alpha \neq \beta}} \left(\frac{r_{\alpha,\beta}}{h} \right)^{r_{\alpha,\beta}/h} \right]^{1/M} \tag{5.36}$$

is the geometric mean of the inter-particle distance divided by the membrane thickness, to the power of the inter-particle distance divided by the membrane thickness.

Correspondingly to the results given in **§5.2**, equations (5.31)-(5.32) are nonlinear and have to be solved iteratively. By defining the following non-dimensional parameters

$$\tilde{A}(s) = \frac{2\pi}{k_B T} \langle r \cdot \Delta r_1(0), \Delta \tilde{r}_2(s) \rangle \cdot s \cdot \tilde{G}_f(s), \tag{5.37}$$

$$\tilde{B}(s) = \frac{2\pi}{k_B T} \langle r \cdot \Delta \theta_1(0), \Delta \tilde{\theta}_2(s) \rangle \cdot s \cdot \tilde{G}_f(s), \tag{5.38}$$

$$\tilde{G}(s) = \frac{\tilde{G}_m(s)}{\tilde{G}_f(s)}, \tag{5.39}$$

the system of equations to solve are

$$\tilde{F}_r(s) \equiv \tilde{G}(s) \cdot \left\{ \tilde{A}(s) \cdot \tilde{G}(s) - \bar{r} \cdot \left[\ln\left(\tilde{G}(s)\right) - \gamma + \frac{1}{2} \right] + \ln\left(\widehat{r^r}\right) \right\} - \frac{4}{3}\overline{r^2} = 0, \tag{5.40}$$

$$\tilde{F}_\theta(s) \equiv \tilde{G}(s) \cdot \left\{ \tilde{B}(s) \cdot \tilde{G}(s) - \bar{r} \cdot \left[\ln\left(\tilde{G}(s)\right) - \gamma - \frac{1}{2} \right] + \ln\left(\widehat{r^r}\right) \right\} - \frac{8}{3}\overline{r^2} = 0. \tag{5.41}$$

5.4 One- and Two-Point Particle Tracking Microrheology of the Membrane-Cortex Complex of Red Blood Cells

In this section, we illustrate the application of membrane one-point and two-point PTM to experimental data acquired from adult human RBC. The RBC were suspended in a water based

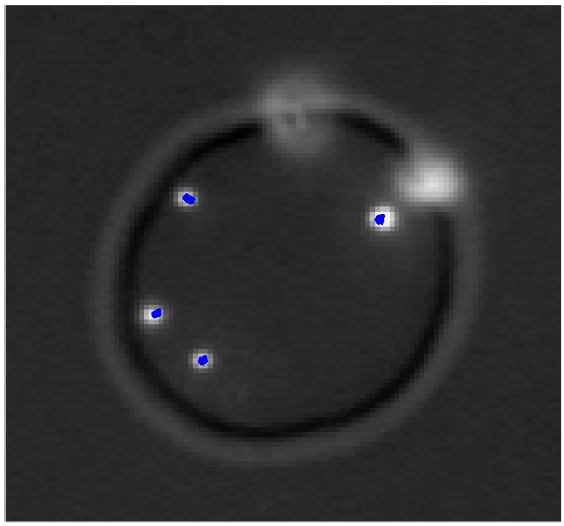

Figure 5.4: Experimental image of a RBC with microparticles embedded in its membrane-cortex complex. The microparticles are the white bright spots. The particle trajectories (—) are overlaid on on top of each particle.

buffer, and attached to a rigid cover-slip. 0.1 μm diameter carboxilated fluorescent beads were coated with polylysine and embedded in the membrane-cortex complex of the RBC. A more detailed specific experimental protocol will be published elsewhere. Time snapshots of the RBC and the embedded microparticles were taken at a fixed frame rate of 100 Hz. In **Figure 5.4** we show an example of a typical experimental image of a RBC with four probing microparticles. In the image, we can clearly distinguish the cell outline and four embedded beads, depicted as bright spots. The center of the particle probes were tracked by using the tracking algorithm discussed in previous sections. The tracked trajectories are overlaid, as blue lines, in **Figure 5.4**.

From here on, we will show the data collected from five RBC, totalling $N = 31$ particles and $M = 91$ particle pairs. We calculate the *one-dimensional* MSD of individual particles as (2.1) and their cross-correlation as (2.2). For the analyzed RBC, the motion in the plane defined by the membrane is highly isotropic, and thus the MSD in orthogonal directions are equal. We can thus define the *two-dimensional* MSD of individual particles as

$$\langle \Delta r^2(\tau) \rangle = \langle \Delta x^2(\tau) \rangle + \langle \Delta y^2(\tau) \rangle. \tag{5.42}$$

In panel (*a*) from **Figure 5.5** we show the ensemble average of the *two-dimensional* MSD

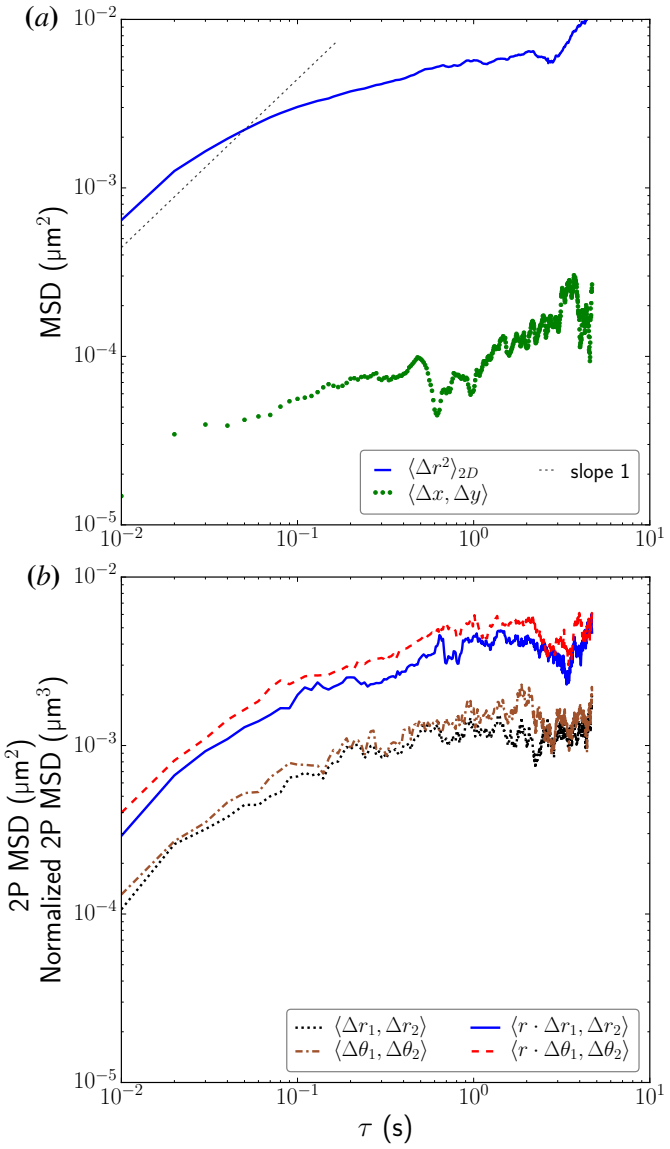

Figure 5.5: One-point and two-point MSD of probing particles embedded in the membrane-cortex complex of RBC. (*a*) Ensemble MSD of individual particles (——), cross-correlation of the MSD in orthogonal directions (• • •) and line of slope 1 (▪ ▪ ▪ ▪ ▪ ▪). (*b*) Ensemble two-particle cross-MSD of pairs of interacting particles along the line of centers (▪ ▪ ▪ ▪ ▪ ▪) and the normal direction (▬ ▪ ▬). Ensemble normalized two-particle cross-MSD along the line of centers (——) and the normal direction (– –).

of the probing particles, together with the cross-MSD in orthogonal directions. Theoretically, the displacements in orthogonal directions of particles undergoing Brownian motion should be uncorrelated, and thus the cross-MSD should be identically zero. For experimental results, they provide a measurement of the experimental noise-level of the tracking. It can be seen that, in the

results presented here, the nose level is far below the measured signal. As reference, we include a line of slope 1. We can see that the slopes of the MSD are larger than 0 in the whole domain and smaller than 1 for most time separations. The observation of these slopes points towards a more elastic behaviour of the system at most frequencies, while a more viscous response is displayed at high frequencies. However, since the MSD of the probing particles and the shear moduli of the membrane and fluid don't follow an inverse proportionality relation, as in a 3D isotropic fluid, interpretations based solely on the MSD of the probing particles are just rough descriptions of the viscoelasticity of the fluid.

In panel (*b*) from **Figure 5.5** we depict the ensemble average of the *two-particle* cross-MSD projected over the direction of the line of centers (5.27), and the orthogonal direction (5.28). The normalized cross-MSD (5.33)-(5.34) are also provided. We can highlight certain characteristics of these curves. The general shape of the four curves is similar between them, and much alike the *one-particle* MSD. However, as we explained above, we cannot immediately infer the viscoelastic characteristics of the fluid from them. We can also see that, as predicted, the normalized MSD are larger and smoother than the raw cross-MSD, and thus we will use them to calculate the microrheological parameters of the material.

An important characteristic readily recognizable in panel (*b*) of **Figure 5.5** is the asymmetry of the cross-MSD along the line of centers and the normal direction. As we mentioned above (5.24), the ratio of cross-MSD of pairs of particles freely diffusing in a three-dimensional fluid is 2. However, in our experimental model, this ratio of MSD is highly dependent on the viscoelasticity as well as the geometry of the system. In **Figure 5.6** we show the ratio of cross-MSD, as well as the ratio of normalized cross-MSD. We can clearly see that, for the pairs of particles tracked, the ratio of MSD is always lower or around 1, not being this ratio substantially affected by the normalization with the inter-particle distance. In contrast to the freely-diffusing 3D problem, the particles in this medium move slightly more in the direction perpendicular to the line of centers than in the direction of centers. A remarkable characteristic of the MSD ratio is that it remains considerably constant for the ratio of frequencies under study, and we would expect it to become even smoother when we study a larger number of particle pairs.

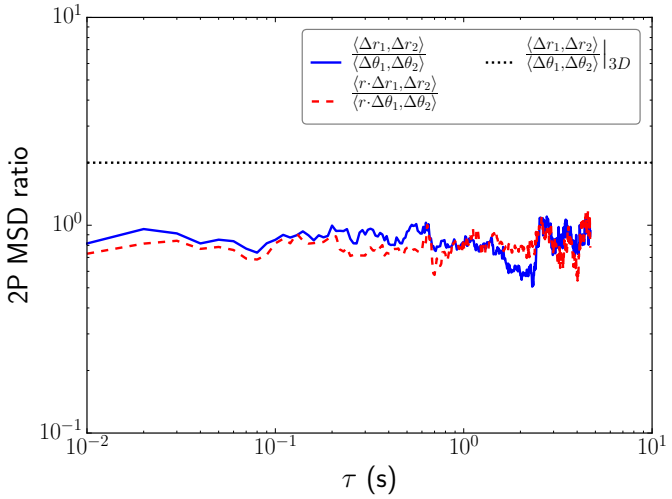

Figure 5.6: Ratio of two-point cross-MSD of pairs of interacting particles embedded in the membrane-cortex complex of RBC: unnormalized (——) and normalized (– –). Ratio of MSD of pairs of particles freely diffusing in a three-dimensional fluid (▪▪▪▪▪).

We will first analyze the MSD shown in **Figure 5.5** by using the isotropic formulae (1.17)-(1.19), as if the probing particles were freely diffusing in a 3D fluid, and investigate the results they provide. We name $\tilde{G}_{1P}$ and $\tilde{G}_{2P}$, respectively, to the shear moduli they yield, and they will be interpreted as effective friction coefficients and effective hydrodynamic interactions of the probing particles. In **Figure 5.7** we show the calculated effective shear moduli. We can point to several features which indicate that the isotropic model is not valid for the system under study. We can clearly see that the results provided by the one-point (1.17) and the two-point (1.19) formulae present manifestly similar shapes, but the one-particle effective moduli are uniformly ten times larger than the two-particle effective moduli. This large discrepancy would not be present in isotropic fluids. A second revealing detail comes from the foreknowledge of the system under study. The membrane-cortex complex of the RBC is mainly formed by lipids and a cross-linked spectrin network, that should present an effective shear modulus of around hundreds or thousands of times larger than the viscosity of water. However, the one-point effective shear modulus measured and provided in **Figure 5.7** is of the order of magnitude of the viscosity of water, while the two-point effective shear modulus is ten times lower. Having present all of the above, one can conclude that the isotropic GSER is not a valid model for the system under study.

Equations (5.11), (5.40) and (5.41) show that the hydrodynamics of the problem is highly

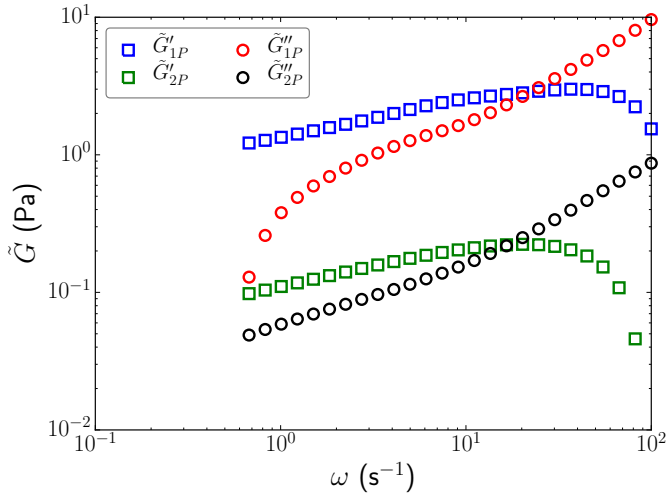

Figure 5.7: Effective shear moduli, as a function of frequency ω, obtained by applying the GSER (1.17) and the 2PPTM formulae (1.19) to the measured MSD and cross-MSD of individual and interacting pairs of distant probing particles embedded in the membrane-cortex complex of RBC: one-particle effective storage (□) and loss (○) moduli, two-particle effective storage (□) and loss (○) moduli.

dependent not only on the shear moduli of the membrane and surrounding fluids, but also on the thickness of the membrane-cortex complex. Furthermore, by just analyzing the mobility of probing particles and solving the above equations, without external measurements on the thickness of the membrane, we can only measure the product of the shear modulus with the membrane thickness, $\tilde{G}_m \cdot h$. However, this product is a significant physical measurement on its own, given that the mechanical characteristics of the system depend on it, rather than simply the shear modulus. As such, many previous studies measure and analyze this and related physical quantities [19, 71, 124].

As previously explained, the fluid surrounding the RBC is a buffer with zero elasticity and viscosity close to that of water, *i.e.* $\eta_{f,a} \approx 1$ mPa·s. The fluid below the membrane-cortex complex is the cell cytoplasm. The cytoplasm of a RBC is known to be composed mainly of an hemoglobin solution, with zero elasticity and viscosity in the range of 2-7 mPa·s at physiological conditions [19, 71]. Here, we have used an average value of $\eta_{f,b} \approx 4$ mPa·s. As a result, the effective shear modulus of the surrounding fluid used in our analysis is

$$\tilde{G}_f(s) = \frac{\tilde{G}_{f,a} + \tilde{G}_{f,b}}{2} \approx 2i\omega \text{ mPa}. \tag{5.43}$$

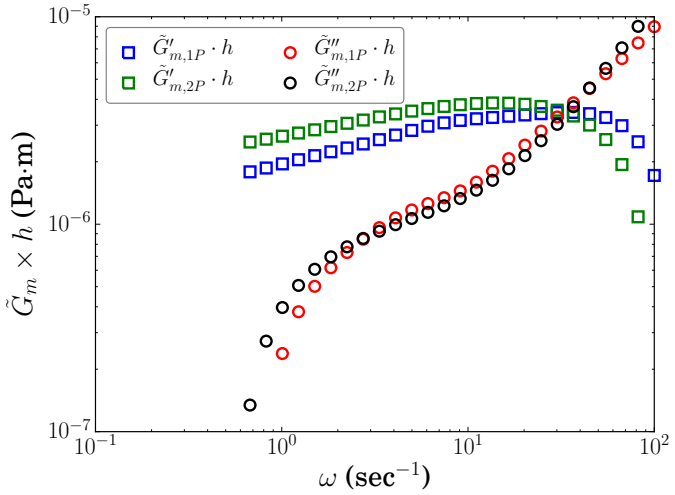

Figure 5.8: Product of the shear modulus and thickness of the membrane-cortex complex of RBC, as a function of frequency ω: storage (□) and loss (○) moduli measured using the one-point formulation, storage (□) and loss (○) moduli measured applying the two-point formulation.

In **Figure 5.8** we show the measured membrane shear moduli, times the membrane thickness, obtained by solving the non-linear one-point (5.11) and two-point (5.40)-(5.41) formulae. It is readily noticeable that both the one-point and two-point formulation provide very consistent results, further confirming the applicability of the membrane model. We can see that the material is highly viscous at high frequencies, while the elasticity dominates at low and moderate frequencies. Furthermore, the shapes of the storage and loss moduli are highly reminiscent of those of a Kelvin-Voigt material, as can be seen by inspecting **Figures 5.8** and **2.17** (as a reference, we should also compare **Figures 5.5** and **2.15**). This fact is particularly consistent with the experimental membrane system, composed of a viscous lipid membrane strongly attached to an elastic spectrin network. However, there are noticeable deviations from the Kelvin-Voigt model at low frequencies. This can be explained by the fact that, at lower frequencies, fewer experimental data points are available, and the averaged data tends to be noisier (see **Figure 5.5**). Furthermore, the lowest frequencies are more affected by experimental noise, sample drift and even cell movements, and thus more experimental data would be necessary to more accurately resolve the lowest frequency region.

In **Figure 5.9** we show the ratio between the effective storage and shear moduli calculated

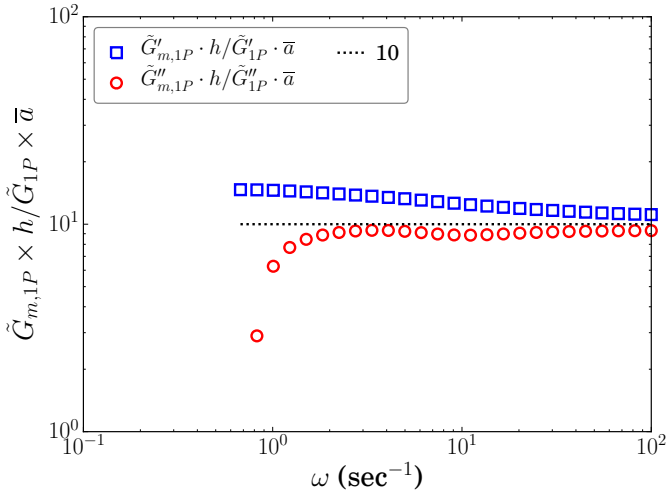

Figure 5.9: Ratio between the storage (□) and loss (○) moduli rendered by the isotropic GSER (1.17) and the membrane formulation (5.11). Comparison with the theoretical estimation for this ratio (5.15) (▪▪▪▪▪).

using the isotropic GSER (1.17) and the shear moduli obtained by applying the membrane formulation (5.11). As a reference, we include the theoretical estimation of this ratio shown in equation (5.15). It can be seen that the ratio of shear moduli, both for the real and imaginary parts, is of the order of magnitude predicted by our initial theoretical estimation.

By knowing the thickness of the membrane-cortex complex of the RBC, one can use the data shown in **Figure 5.8** and calculate the actual membrane viscoelasticity. An average value of 50 nm, previously reported in the literature [60], has been used from here on. The shear moduli of the membrane-cortex complex, calculated by using both the one-particle and two-particle data are reported in **Figure 5.10**. The values calculated are compatible with a viscous membrane attached to an elastic spectrin network, and they are comparable to measuremets performed with micropipete aspiration and other mocrorheology techniques and reported in the literature [111, 71]. By comparing with **Figure 5.8**, we can also see that the shear moduli of the membrane system is one to three orders of magnitude higher than the value provided by the isotropic GSER and the isotropic 2PPTM formulation. In **Figure 5.11** we show the ratio between the storage and loss moduli provided by the one-point and two-point membrane formulation, and the effective moduli calculated from the isotropic formulation. One can see that the effective one-point isotropic formulation greatly underestimates the shear moduli of the

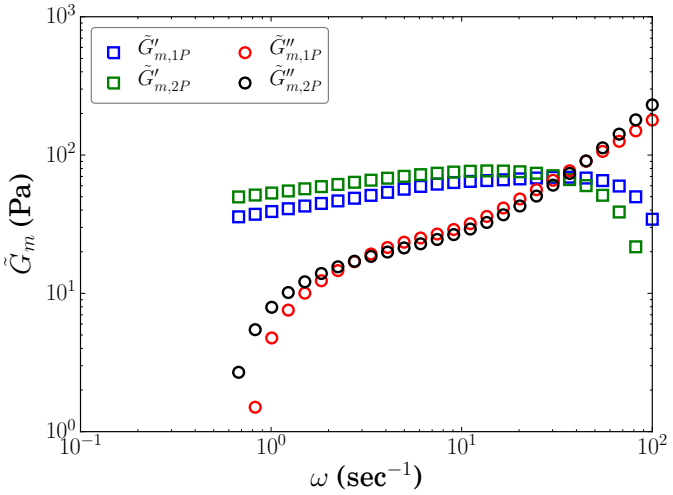

Figure 5.10: Shear modulus of the membrane-cortex complex of RBC, as a function of frequency ω: storage (□) and loss (○) moduli measured using the one-point formulation, storage (□) and loss (○) moduli measured applying the two-point formulation. An average value of 50 nm was used as the membrane thickness.

material, providing values around 20 times smaller than the membrane moduli. On the other hand, the results rendered by two-particle isotropic fomulation are even worse, providing effective hydrodynamic interactions that are 300-500 times smaller than the membrane shear moduli. It is also very noticeable that, given the physical and geometrical parameters of the experimental system, the isotropic and the membrane formulation provide virtually proportional numerical

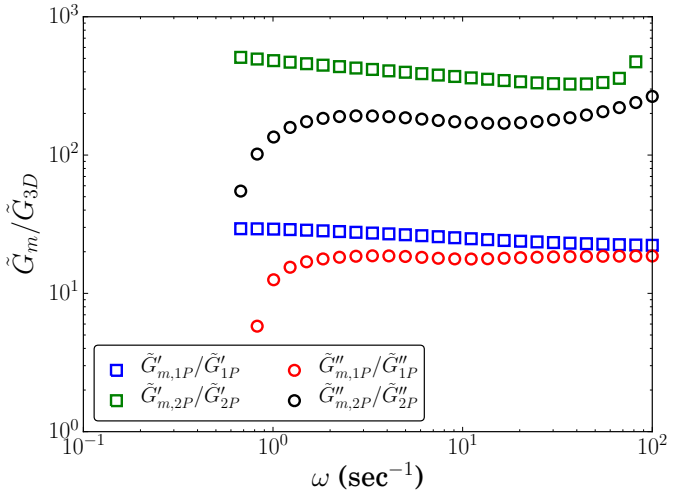

Figure 5.11: Ratio of the shear moduli provided by the membrane and the effective isotropic PTM formulations: ratio of storage (□) and loss (○) moduli calculated with the one-particle data, ratio of storage (□) and loss (○) moduli calculated with the two-particle interaction data.

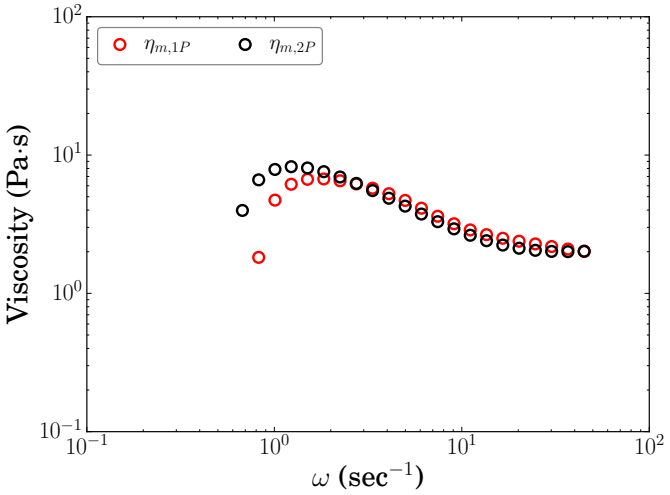

Figure 5.12: Viscosity coefficient of the membrane-cortex complex of RBC, as a function of frequency ω, calculated with the one-point (O) and two-point (O) experimental data.

results, with very low variation in the proportionality constant at the measured frequencies.

In **Figure 5.12** we depict the viscosity coefficient, defined as the ratio between the loss modulus and the complex frequency

$$\eta(s) = \frac{\tilde{G}''(s)}{s}, \tag{5.44}$$

measured from the one-pont and two-pint data, and both are virtually identical. It can ve seen that the viscosity coefficient display very low variation with the frequency, being its value between 1,000 and 10,000 times the viscosity of water.

5.5 Conclusions

In this chapter, we have reviewed the importance of the RBC deformability and viscoelasticity properties for the correct blood flow and RBC function. As a consequence, we proposed a PTM experiment capable of resolving the mechanical properties of their membrane-cortex complex, which is the one responsible for the RBC microrheological properties. We provided the formulation capable of relating the MSD of individual particles embedded in the membrane-cortex complex and the shear moduli and geometric parameters of the material. We also related the

measured interactions of pairs of distant particles with the physical parameters of the material. In the final part of the chapter, we applied both the one-particle and two-particle formulation to the membrane-cortex complex of live RBC. We found that, for this model system, the straight application of the isotropic PTM formulation provides results that are 10 to 1000 times smaller than the actual shear modulus of the system. The results here provided open the door to the use of this relatively inexpensive and high-throughput tool to study the microrheological influence of different RBC diseases and conditions.

It should finally be noted that there are sources of uncertainties in our experimental application. The membrane thickness is a key parameter in the hydrodynamics of the problem, to the point that the particle mobility is dominated by the product of the membrane shear modulus and thickness. In order to calculate the shear modulus, an independent measurement of the specific membrane thickness should be performed. Here, we have used an average value of 50 nm previously reported in the literature. However, the conditions that modify the RBC shear moduli might also modify the membrane-cortex thickness, and a rigorous quantitative analysis should include the *in situ* measurement of the sample membrane thickness. A second source of uncertainty is the viscoelasticity of the surrounding medium. Here, we have assumed a purely viscous buffer, with the viscosity of water, surrounding the RBC, and an average viscosity for the RBC cytoplasm at physiological conditions. However, the viscosity of the RBC cytoplasm can be greatly influenced by the cell conditions, and thus it should be independently measured in order to accurately quantify the shear moduli of the RBC membrane-cortex system.

Chapter 5 is currently being prepared for publication under the provisional title “Dynamic viscoelasticity of individual human RBCs measured by video-particle tracking microrheology”, by Y.F. Tseng, Y.Q. Chen, M. Gómez-González, J. C. del Álamo and A. Chiou.

Chapter 6

Concluding Remarks

In this dissertation we have analyzed the current practical limitations that hinder the applicability of PTM. We have addressed some of its most significant practical shortcomings, such as the accurate Laplace transform of the experimental measurements and the adequate physical modeling of the medium under study. We have provided mathematical alternatives that provide a more accurate approach to said limitations than the current isotropic formulation in use. Furthermore, we have applied these novel results to the study of the rheological properties of appropriate complex biomaterials.

In **chapter 2** we explained how PTM relies on the accurate Laplace transform of the particle tracking measurements in order to calculate the shear modulus of the material under study. We showed that, due to the fact that the experimental tracking data is only known in a given time interval and over discrete time points, the numerical Laplace transform is prone to be calculated with considerable numerical errors. We presented the approximations to the Laplace transform currently reported in the literature, and analyzed how the most extensively used method, the Γ-approach, breaks for many rheological models. In order to solve this issue, we proposed a novel strategy known as the Power-Exp approximation. It consists on performing a least square fit of the MSD data to a sum of power-exponential functions in the time domain. These functions present a known analytical Laplace transform, and making use of the linearity of

the problem, the Laplace transform of the sum is calculated. We then quantify the accuracy of this procedure by analyzing four theoretical materials: a simple viscous fluid, a simple elastic solid, a Kelvin-Voigt viscoelastic fluid and a Maxwell viscoelastic material. We found that the Power-Exp approximation is at least as accurate as the previous methods, and that it highly outperforms them in the most delicate regions of the frequency spectrum, where previous methods fail to correctly identify the Laplace transform of the particles' MSD and the Power-Exp approximation provides accurate numerical values.

In **chapter 3** we study the applicability of 1PPTM to directional samples. As summarized in **chapter 1**, the classical PTM formulation is only applicable to isotropic materials, and its use with directional fluids will provide, at most, viscoelastic friction coefficients that don't fully describe the directional fluid under study. In **chapter 3** we modelled the directional medium with the Leslie-Ericksen equations that, as we illustrated, hold when the driving thermal forces are weak enough to not perturb the global orientation of the nematic. We find that the fluid dynamics of the problem is fully described by three viscoelastic directional shear moduli, and obtain the form of the drag force of an embedded microparticle and the flow induced by it, as a function of these three shear moduli. The form of the drag force is a generalization of the Stokes formula for directional fluids, and is a tensorial equation that depends on the orientation of the particle velocity with respect to the nematic. We observe that, in this model system, the anisotropy of the dynamics is originated by two distinct mechanisms, *i.e.* the anisotropic diffusion of momentum and the bending of the fluid with respect to the nematic. Combining the formula of the drag force thus obtained with the Einstein equation, we are able to generalize the GSER to take into account the directionality of the fluid. However, we conclude that due to the symmetrical mechanical characteristics of the problem under study, following single microparticles will provide, at most, two independent equations, even in a fully three-dimensional experiment. Because a general directional medium is described by three shear moduli, we resolve that Directional 1PPTM doesn't provide sufficient information to fully characterize a nematic fluid.

In **chapter 4** we extend the work presented in **chapter 3** and we calculate the hydrodynamic interactions between pairs of distant particles embedded in a nematic fluid. By knowing the

analytical form of these interactions, we generalize 2PPTM to take into account the directionality of the medium under study, designing a technique named D2PTM. By cross-correlating the motion of pairs of distant particles, we obtain three independent equations that are sufficient to determine the three viscoelastic shear moduli of the nematic medium under study. In order to asses the feasibility and accuracy of D2PTM, we simulate the motion of groups of interacting particles embedded in a directional viscoelastic fluid. From the simulations we obtain the trajectory of each particle, to which we apply the novel D2PTM formulation. We conclude that the calculated shear moduli are in high agreement to the shear moduli initially prescribed to the simulated material, and thus establishing the applicability of the method. In the final part of the chapter, we describe a laboratory experiment where we prepare F-actin sample gels and shear them to induce a nematic alignment of the fluid. The samples are seeded with probing microparticles, and D2PTM is applied to the measured trajectories of the particles. We obtain the directional shear moduli of the material, which describe a complex dynamics that that is not properly describe by the previous isotropic formulation.

In **chapter 5** we analyze a different type of anisotropic material: we study the rheological properties of a membrane system embedded in a different fluid. We show the formulation of 1PPTM and 2PPTM when it is adapted to take into account the complex dynamics of this system, which is a good model for the membrane-cortex complex of RBC. We then embed microparticles in the membrane-cortex complex of live adult human RBC and track their motion by applying the tools developed in **chapter 4**. We first apply the GSER and the 2PPTM formulation to the MSD and cross-MSD of the tracked microparticles, obtaining shear moduli that are one or two orders of magnitude lower than the expected values, and in high discrepancy between the one- and two-point formulation. We finally apply the membrane formulation of 1PPTM and 2PPTM, obtaining highly consistent results, and values that are in good agreement to the viscoelasticity of the system measured with previous microrheological methods.

The results and methods reported in this dissertation open the door to compelling new studies on biological and technological materials. The directional PTM has been here formulated and applied to a model biomaterial, a nematic F-actin solution. However, directionality is a

key factor in many biological processes and technological materials, and as such D2PTM is an interesting new tool to study their directional rheology. Among those materials, we can list nematic liquid crystals, nematic viscoelastomers, the live cell cytoplasm, etc.; and a deeper understanding of their behaviour can only be achieved if we correctly model their directional dynamics. On the other hand, many samples of interest present non-directional anisotropy or other characteristics not accurately described by the isotropic GSER. Because of this reason, future rheological studies should take an approach similar to the methodology presented in this dissertation, and correctly model the dynamics of the system in order to accurately quantify the sample's rheology.

Bibliography

[1] URL http://www.micro-manager.org/.

[2] B. Alvarez-Gonzalez, R. Meili, E. Bastounis, R. A. Firtel, and J. C. Lasheras. Three-Dimensional Balance of Cortical Tension and Axial Contractility Enables Fast Amoeboid Migration. *Biophysical Journal*, 108(4):821–832, 17 Feb. 2015.

[3] F. Amblard, A. C. Maggs, B. Yurke, A. N. Pargellis, and S. Leibler. Subdiffusion and anomalous local viscoelasticity in actin networks. *Physical Review Letters*, 77(21):4470–4473, 18 Nov. 1996.

[4] A. Ashkin. Forces of a Single-Beam Gradient Laser Trap on a Dielectric Sphere in the Ray Optics Regime. *Biophysical Journal*, 61(2):569–582, Feb. 1992.

[5] J. T. Beale and M.-C. Lai. A method for computing nearly singular integrals. *SIAM Journal on Numerical Analysis*, 38(6):1902–1925, February 2001.

[6] W. W. Beens and W. H. de Jeu. Flow-measurements of the viscosity coefficients of 2 nematic liquid-crystalline azoxybenzenes. *Journal de physique*, 44(2):129–136, 1983.

[7] S. Behnel, R. Bradshaw, C. Citro, L. Dalcin, D. S. Seljebotn, and K. Smith. Cython: The best of both worlds. *Computing in Science & Engineering*, (13):31–39, 2011.

[8] V. V. Belyaev. Physical Methods for Measuring the Viscosity Coefficients of Nematic Liquid Crystals. *Physics-Uspekhi*, 44(3):255–284, 2001.

[9] K. Berg-Sorensen and H. Flyvbjerg. The colour of thermal noise in classical Brownian motion: a feasibility study of direct experimental observation. *New Journal of Physics*, 7 (38), 1 Feb. 2005.

[10] G. Binning, C. F. Quate, and C. Gerber. Atomic Force Microscope. *Physical Review Letters*, 56(9):930–933, 3 Mar. 1986.

[11] S. M. Block. Making Light Work with Optical Tweezers. *Nature*, 360(6403):493–495, 3 Dec. 1992.

[12] J. M. Brake, M. K. Daschner, Y.-Y. Luk, and N. L. Abbott. Biomolecular interactions at phospholipid-decorated surfaces of liquid crystals. *Science*, 302(5653):2094–2097, December 2003.

[13] R. Brown. *The miscellaneous botanical works of Robert Brown, Esq., D.C.L., F.R.S.*, chapter Additional remarks on active molecules, pages 479–486. Robert Hardwicke, 1866.

[14] R. Brown. *The miscellaneous botanical works of Robert Brown, Esq., D.C.L., F.R.S.*, chapter A brief account of microscopical observations made in the months of June, July and August, 1827, on the particles contained in the pollen of plants; and on the general existence of active molecules in organic and inorganic bodies, pages 463–479. Robert Hardwicke, 1866.

[15] I. C. Carpen and J. F. Brady. Microrheology of colloidal dispersions by brownian dynamics simulations. *Journal of Rheology (1978-present)*, 49(6):1483–1502, 2005.

[16] P. M. Chaikin and T. C. Lubensky. *Principles of Condensed Matter Physics*. Cambridge University Press, 1994.

[17] C. S. Chen, J. Tan, and J. Tien. Mechanotransduction at cell-matrix and cell-cell contacts. *Annual Review of Biomedical Engineering*, 6:275–302, 2004.

[18] Y.-Q. Chen, P.-T. Su, Y.-H. Chen, M.-T. Wei, C.-H. Huang, K. Osterday, J. C. del Álamo, W.-J. Syu, and A. Chiou. The effect of enterohemorrhagic e. coli infection on the cell mechanics of host cells. *PloS one*, 9(11):e112137, 2014.

[19] S. Chien. Red-Cell Deformability and its Relevance to Blood Flow. *Annual Review of Physiology*, 49:177–192, 1987.

[20] S. Chien. Mechanotransduction and endothelial cell homeostasis: the wisdom of the cell. *American Journal of Physiology - Heart and Circulatory Physiology*, 292(3):H1209–H1224, 2007.

[21] S. Chien, K. L. P. Sung, R. Skalak, and S. Usami. Theoretical and Experimental Studies on Viscoelastic Properties Erythrocyte-Membrane. *Biophysical Journal*, 24(2):463–487, 1978.

[22] F. C. Chretien. Involvement of the glycoproteic meshwork of cervical mucus in the mechanism of sperm orientation. *Acta Obstetricia et Gynecologica Scandinavica*, 82(5): 449–461, 2003.

[23] J. C. A. Cluitmans, V. Chokkalingam, A. M. Janssen, R. Brock, W. T. S. Huck, and G. J. C. G. M. Bosman. Alterations in Red Blood Cell Deformability during Storage: A Microfluidic Approach. *Biomed Research International*, 2014.

[24] P. J. Collings and M. Hird. *Introduction to Liquid Crystals: Chemistry and Physics*. The Liquid Crystals Book Series. Taylor & Francis, 1997.

[25] B. M. Cooke, J. Stuart, and G. B. Nash. The Cellular and Molecular Rheology of Malaria. *Biorheology*, 51(2-3):99–119, 2014.

[26] R. Cortez. The method of regularied stokeslets. *SIAM Journal on Scientific Computing*, 23 (4):1204–1225, December 2001.

[27] F. H. C. Crick. The physical properties of cytoplasm: A study by means of the magnetic particle method Part 2. Theoretical Treatment. *Experimental Cell Research*, 1(4):505–533, 1950.

[28] F. H. C. Crick and A. F. W. Hughes. The physical properties of cytoplasm: A study by means of the magnetic particle method Part I. Experimental. *Experimental Cell Research*, 1(1):37–80, 1950.

[29] J. C. Crocker and B. D. Hoffman. Multiple-particle tracking and two-point microrheology in cells. *Methods in Cell Biology*, 83:141–178, 2007.

[30] J. C. Crocker, M. T. Valentine, E. R. Weeks, T. Gisler, P. D. Kaplan, A. G. Yodh, and D. A. Weitz. Two-point microrheology of inhomogeneous soft materials. *Physical Review Letters*, 85(4):888–891, July 2000.

[31] B. R. Daniels, B. C. Masi, and D. Wirtz. Probing single-cell micromechanics in vivo: The microrheology of C-elegans developing embryos. *Biophysical Journal*, 90(12):4712–4719, June 2006.

[32] B. R. Daniels, C. M. Hale, S. B. Khatau, S. Kusuma, T. M. Dobrowsky, S. Gerecht, and D. Wirtz. Differences in the Microrheology of Human Embryonic Stem Cells and Human Induced Pluripotent Stem Cells. 99(11):3563–3570, Dec. 2010.

[33] P. G. De Gennes and J. Prost. *The Physics of Liquid Crystals*. Oxford University Press, second edition, 1993. ISBN 0 19 851785 8 (Pbk).

[34] J. C. del Álamo, G. N. Norwich, Y. J. Li, J. C. Lasheras, and S. Chien. Anisotropic rheology and directional mechanotransduction in vascular endothelial cells. *Proceedings of the National Academy of Sciences of the United States of America*, 105(40):15411–15416, October 2008.

[35] B. Dingfelder and J. A. C. Weideman. An improved talbot method for numerical laplace transform inversion, April 2013.

[36] D. E. Discher, P. Janmey, and Y. L. Wang. Tissue cells feel and respond to the stiffness of their substrate. *Science*, 310(5751):1139–1143, 18 Nov. 2005.

[37] A. Edelstein, N. Amodaj, K. Hoover, R. Vale, and N. Stuurman. Computer control of microscopes using manager. *Current Protocols in Molecular Biology*, pages 14.20.1–14.20.17, October 2010.

[38] A. Einstein. Die Plancksche Theorie der Strahlung und die Theorie der spezifischen Wärme. *Annalen der Physik*, 327(1):180–190, 1906.

[39] A. Einstein. Berichtigung zu meiner Arbeit: "Die Plancksche Theorie der Strahlung etc.". *Annalen der Physik*, 22(4):800, 1907.

[40] A. J. Engler, S. Sen, H. L. Sweeney, and D. E. Discher. Matrix elasticity directs stem cell lineage specification. *Cell*, 126(4):677–689, 25 Aug. 2006.

[41] J. L. Ericksen. Anisotropic fluids. *Archive for Rational Mechanics and Analysis*, 4(15): 231–237, 1960.

[42] E. A. Evans. Structure and Deformation Properties of Red Blood-Cells - Concepts and Quantitative Methods. *Methods in Enzymology*, 173:3–35, 1989.

[43] J. D. Ferry. *Viscoelastic Properties of Polymers*. Wiley, New York, 1980.

[44] F. C. Frank. On the theory of liquid crystals. *Discussions of the Faraday Society*, (25): 19–28, 1958.

[45] H. Freundlich and W. Seifriz. On the elasticity of soles and gels. *Zeitschrift für physikalische Chemie, Stöchiometrie und Verwandtschaftslehre*, 104(3/4):233–261, March 1923.

[46] M. Frigo and S. G. Johnson. URL http://www.fftw.org.

[47] M. Frigo and S. G. Johnson. The design and implementation of fftw3. *Proceedins of the IEEE*, 93(2):216–231, February 2005.

[48] H. C. Fu, V. B. Shenoy, and T. R. Powers. Role of slip between a probe particle and a gel in microrheology. *Physical Review E*, 78(6):061503, Dec 2008. doi: 10.1103/PhysRevE.78.061503.

[49] C. Gähwiller. The viscosity coefficients of a room-temperature liquid crystal (mbba). *Physics Letters A*, 36(4):311–312, 1971.

[50] C. G. Galbraith, R. Skalak, and S. Chien. Shear stress induces spatial reorganization of the endothelial cell cytoskeleton. *Cell Motility and the Cytoskeleton*, 40(4):317–330, 1998.

[51] M. L. Gardel, M. T. Valentine, and D. A. Weitz. *Microscale Diagnostic Techniques*, chapter Microrheology, pages 1–50. Springer, 2005.

[52] F. Gittes, B. Mickey, J. Nettleton, and J. Howard. Flexural Rigidity of Microtubules and Actin Filaments Measured from Thermal Fluctuations in Shape. *Journal of Cell Biology*, 120(4):923–934, Feb. 1993.

[53] F. Gittes, B. Schnurr, P. D. Olmsted, F. C. MacKintosh, and C. F. Schmidt. Microscopic viscoelasticity: Shear moduli of soft materials determined from thermal fluctuations. *Physical Review Letters*, 79(17):3286–3289, October 1997.

[54] M. Gómez-González and J. C. del Álamo. Flow of a viscous nematic fluid around a sphere. *Journal of Fluid Mechanics*, 725:299–331, June 2013.

[55] M. Guo, A. J. Ehrlicher, M. H. Jensen, M. Renz, J. R. Moore, R. D. Goldman, J. Lippincott-Schwartz, F. C. Mackintosh, and D. A. Weitz. Probing the Stochastic, Motor-Driven Properties of the Cytoplasm Using Force Spectrum Microscopy. *Cell*, 158(4):822–832, 14 Aug. 2014.

[56] M. Guo, A. J. Ehrlicher, M. H. Jensen, M. Renz, J. R. Moore, R. D. Goldman, J. Lippincott-Schwartz, F. C. Mackintosh, and D. A. Weitz. Probing the stochastic, motor-driven properties of the cytoplasm using force spectrum microscopy. *Cell*, 158(4):822–832, 2014.

[57] I. A. Hasnain and A. M. Donald. Microrheological characterization of anisotropic materials. *Physical Review E*, 73(3):031901, March 2006.

[58] J. He, M. Mak, Y. Liu, and J. X. Tang. Counterion-dependent microrheological properties of f-actin solutions across the isotropic-nematic phase transition. *Physical Review E*, 78(1): 011908, July 2008.

[59] A. Heilbronn. Eine neue methode zur bestimmung der viskosität lebender protoplasten. *Jahrbuch der Wissenschaftlichen Botanik*, 61:284–338, 1922.

[60] V. Heinrich, K. Ritchie, N. Mohandas, and E. Evans. Elastic Thickness Compressibilty of the Red Cell Membrane. *Biophysical Journal*, 81(3):1452–1463, Sept. 2001.

[61] H. Herba, A. Szymanski, and A. Drzymala. Experimental test of hydrodynamic theories for nematic liquid-crystals. *Molecular Crystals and Liquid Crystals*, 127(1):153–158, 1985.

[62] W. Hess and R. Klein. Generalized Hydrodynamics of Systems of Brownian Particles. *Advances in Physics*, 32(2):173–283, 1983.

[63] H. Heuer, H. Kneppe, and F. Schneider. Flow of a nematic liquid-crystal around a sphere. *Molecular Crystals and Liquid Crystals*, 214:43–61, April 1992.

[64] J. D. Hunter. Matplotlib: A 2d graphics environment. *Computing in Science & Engineering*, (9):90–95, 2007.

[65] H. Inoue, M. Kamibayashi, K. Kishimoto, T. Shibuya, and T. Koizumi. Numerical laplace transform and inversion using fast fourier transform. *JSME International Journal Series 1 - Solid Mechanics Strength of Materials*, 35(3):319–324, July 1992.

[66] J. Janik, J. K. Moscicki, K. Czuprynski, and R. Dabrowski. Miesowicz viscosities study of a two-component thermotropic mixture. *Physical Review E*, 58(3):3251–3258, September 1998.

[67] E. Jones, T. Oliphant, P. Peterson, and others. SciPy: Open source scientific tools for Python, 2001–. URL http://www.scipy.org/.

[68] R. Kaunas, P. Nguyen, S. Usami, and S. Chien. Cooperative effects of Rho and mechanical stretch on stress fiber organization. *Proceedings of the National Academy of Sciences of the United States of America*, 102(44):15895–15900, November 2005.

[69] D. B. Khismatullin. The Cytoskeleton and Deformability of White Blood Cells. *Leukocyte Adhesion*, 64:47–111, 2009.

[70] S. Kim and S. J. Karrila. *Microhydrodynamics - Principles and Selected Applications*. Dover Publications, Inc., 2005.

[71] Y. Kim, K. Kim, and Y. Park. *Blood Cell - An Overview of Studies in Hematology*, chapter 10. Measurement Techniques for Red Blood Cell Deformability: Recent Advances, pages 167–194. InTech.

[72] H. Kneppe and F. Schneider. Determination of the viscosity coefficients of the liquid-crystal mbba. *Molecular Crystals and Liquid Crystals*, 65(1-2):23–37, 1981.

[73] H. Kneppe, F. Schneider, and B. Schwesinger. Axisymmetrical flow of a nematic liquid crystal around a sphere. *Molecular Crystals and Liquid Crystals*, 205:9–28, August 1991.

[74] G. M. Koenig, R. Ong, A. D. Cortes, J. A. Moreno-Razo, J. J. de Pablo, and N. L. Abbott. Single nanoparticle tracking reveals influence of chemical functionality of nanoparticles on local ordering of liquid crystals and nanoparticle diffusion coefficients. *Nano Letters*, 9 (7):2794–2801, July 2009.

[75] T. P. Kole, Y. Tseng, I. Jiang, J. L. Katz, and D. Wirtz. Intracellular mechanics of migrating fibroblasts. *Molecular Biology of the Cell*, 16(1):328–338, 2005.

[76] R. Kubo. The fluctuation-dissipation theorem. *Reports on progress in physics*, 29:255–284, 1966.

[77] O. A. Ladyzhenskaya. *The Mathematical Theory of Viscous Incompressible Flow*. Gordon and Breach Science Publishers, second english edition, 1969.

[78] M. Laitl. URL https://github.com/strohel/Ceygen.

[79] J. Lammerding and R. T. Lee. The nuclear membrane and mechanotransduction: impaired nuclear mechanics and mechanotransduction in lamin a/c deficient cells. *Novartis Found. Symp.*, 264:264–273, 2005.

[80] J. Lammerding, P. C. Schulze, T. Takahashi, S. Kozlov, T. Sullivan, R. D. Kamm, C. L. Stewart, and R. T. Lee. Lamin A/C deficiency causes defective nuclear mechanics and mechanotransduction. *Journal of Clinical Investigation*, 113(3):370–378, Feb. 2004.

[81] L. D. Landau and E. M. Lifshitz. *Fluid Mechanics*, volume 6 of *Course of theoretical physics*. Pergamon Press, second english edition, 1987.

[82] D. Langevin. Spectrum analysis of light scattered from free-surface of a nematic liquid-crystal - surface-tension and viscosity measurements. *Journal de physique*, 33(2-3): 249–256, 1972.

[83] R. G. Larson. *The Structure and Rheology of Complex Fluids*. Oxford University Press, 1999.

[84] H.-H. Lee, H.-C. Lee, C.-C. Chou, S. S. Hur, K. Osterday, J. C. del Álamo, J. C. Lasheras, and S. Chien. Shp2 plays a crucial role in cell structural orientation and force polarity in response to matrix rigidity. *Proceedings of the National Academy of Sciences*, 110(8): 2840–2845, February 2013.

[85] J. S. H. Lee, M. I. Chang, Y. Tseng, and D. Wirtz. Cdc42 mediates nucleus movement and mtoc polarization in swiss 3t3 fibroblasts under mechanical shear stress. *Molecular Biology of the Cell*, 16(2):871–880, February 2005.

[86] F. M. Leslie. Some constitutive equations for anisotropic fluids. *Quarterly Journal of Mechanics and Applied Mathematics*, 19(3):357–370, 1966.

[87] A. J. Levine and T. C. Lubensky. One- and two-particle microrheology. *Physical Review Letters*, 85(8):1774–1777, April 2000.

[88] A. J. Levine and T. C. Lubensky. Response function of a sphere in a viscoelastic two-fluid medium. *Physical Review E*, 63(4):041510, March 2001.

[89] A. J. Levine and MacKintosh. F. C. Dynamics of Viscoelastic Membranes. *Physical Review E*, 66(6), Dec. 2002.

[90] A. Lin, G. Krockmalnic, and S. Penman. Imaging Cytoskeleton Mitochondrial-membrane Attachments by Embedment-free Electron-microscopy of Saponin-extracted Cells. *Proceedings of the National Academy of Sciences of the United States of America*, 87(21): 8565–8569, November 1990.

[91] N. Liron and E. Barta. Motion of a rigid particle in stokes flow: a new second-kind boundary-integral equation formulation. *Journal of Fluid Mechanics*, 238:579–598, May 1992.

[92] C. M. Lo, H. B. Wang, M. Dembo, and Y. L. Wang. Cell movement is guided by the rigidity of the substrate. *Biophysical Journal*, 79(1):144–152, July 2000.

[93] J.-C. Loudet, P. Barois, and P. Poulin. Colloidal ordering from phase separation in a liquid-crystalline continuous phase. *Letters to Nature*, 407(6804):611–613, August 2000.

[94] J. C. Loudet, P. Hanusse, and P. Poulin. Stokes drag on a sphere in a nematic liquid crystal. *Science*, 306(5701):1525–1525, November 2004.

[95] K. Luby-Phelps. Cytoarchitecture and physical properties of cytoplasm: Volume, viscosity. diffusion, intracellular surface area. In *International Review of Cytology - A survey of Cell Biology, vol 192*, volume 192 of *International Review of Cytology - A survey of Cell Biology*, pages 189–221. Academic Press Inc, San Diego, CA 92101-4495 USA, 2000.

[96] K. Luby-Phelps, D. L. Taylor, and F. Lanni. Probing the Structure of Cytoplasm. *Journal of Cell Biology*, 102(6):2015–2022, 1986.

[97] J. L. Maciaszek, B. Andemariam, and G. Lykotrafitis. Microelasticity of Red Blood Cells in Sickle Cell Disease. *Journal of Strain Analysis for Engineering Design*, 46(5):368–379, July 2011.

[98] M. Mak, R. D. Kamm, and M. H. Zaman. Impact of dimensionality and network disruption on microrheology of cancer cells in 3d environments. *PLoS computational biology*, 10 (11):e1003959, 2014.

[99] R. R. Markwald, T. P. Fitzharris, D. L. Bolender, and D. H. Bernanke. Structural analysis of cell:Matrix association during the morphogenesis of atrioventricular cushion tissue. *Developmental Biology*, 69(2):634–654, 1979.

[100] S. L. Marple Jr. *Digital Spectral Analysis With Applications*. Prentice-Hall Series in Signal Processing. Prentice-Hall, NJ, 1987.

[101] T. G. Mason. Estimating the viscoelastic moduli of complex fluids using the generalized stokes-einstein equation. *Rheologica Acta*, 39(4):371–378, August 2000.

[102] T. G. Mason and D. A. Weitz. Optical measurements of frequency-dependent linear viscoelastic moduli of complex fluids. *Physical Review Letters*, 74(7):1250–1253, February 1995.

[103] T. G. Mason, K. Ganesan, J. H. van Zanten, D. Wirtz, and S. C. Kuo. Particle tracking microrheology of complex fluids. *Physical Review Letters*, 79(17):3282–3285, October 1997.

[104] J. C. Maxwell. On the Dynamical Evidence of the Molecular Constitution of Bodies. *Nature*, 11:357–359, 4 Mar. 1875.

[105] J. L. McGrath, J. H. Hartwig, and S. C. Kuo. The mechanics of f-actin microenvironments depend on the chemistry of probing surfaces. *Biophysical Journal*, 79(6):3258–3266, December 2000.

[106] A. Meyer, A. Marshall, B. G. Bush, and E. M. Furst. Laser tweezer microrheology of a colloidal suspension. *Journal of Rheology (1978-present)*, 50(1):77–92, 2006.

[107] M. Miesowicz. Influence of the magnetic field on the viscosity of liquids in the nematic phase. *Bulletin International de l'Academie Polonaise des Sciences et des Lettres*, (5-6): 228–247, May 1936.

[108] M. Miesowicz. The three coefficients of viscosity of anisotropic liquids. *Nature*, 158 (4001):27–27, 1946.

[109] A. A. Minin, A. V. Kulik, F. K. Gyoeva, Y. Li, G. Goshima, and V. I. Gelfand. Regulation of mitochondria distribution by rhoa and formins. *Journal of Cell Science*, 119(4):659–670, February 2006.

[110] D. Mizuno, D. Head, F. MacKintosh, and C. Schmidt. Active and passive microrheology in equilibrium and nonequilibrium systems. *Macromolecules*, 41(19):7194–7202, 2008.

[111] N. Mohandas and E. Evans. Mechanical Properties of the Red Cell Membrane in Relation to Molecular Structure and Genetic Defects. *Annual Review of Biophysics and Biomolecular Structure*, 23:787–818, 1994.

[112] J. A. Moreno-Razo, E. J. Sambriski, G. M. Koenig, E. Díaz-Herrera, N. L. Abbott, and J. J. de Pablo. Effects of anchoring strength on the diffusivity of nanoparticles in model liquid-crystalline fluids. *Soft Matter*, 7(15):6828–6835, 2011.

[113] P. Mörters and Y. Peres. *Brownian Motion*. Cambridge Series in Statistical and Probabilistic Mathematics. Cambridge University Press, 2010.

[114] H. Nyquist. Thermal agitation of electric charge in conductors. *Physical Review*, 32(1): 110–113, July 1928.

[115] N. Oppenheimer and H. Diamant. Correlated Diffusion of Membrane Proteins and Their Effect on Membrane Viscosity. *Biophysical Journal*, 96(8):3041–3049, 22 Apr. 2009.

[116] Orsay Liquid Crystal Group. Viscosity measurements by quasi elastic light scattering in p-azoxyanisol. *Molecular Crystals and Liquid Crystals*, 13(2):187–191, 1971.

[117] K. Osterday, T. Chew, P. Loury, J. Haga, M. Gómez-González, J. C. del Álamo, and S. Chien. Viscoelastic Properties of Vascular Endothelial Cells Exposed to Stretch. *arXiv preprint arXiv:1309.2683*, 2013.

[118] J. D. Pardee and J. A. Spudich. Purification of muscle actin. *Methods in Enzymology*, 85 (B):164–181, 1982.

[119] O. Parodi. Stress tensor for a nematic liquid crystal. *Le Journal de Physique*, 31(7): 581–584, July 1970.

[120] R. Parthasarathy. Rapid, accurate particle tracking by calculation of radial symmetry centers rapid, accurate particle tracking by calculation of radial symmetry centers rapid, accurate particle tracking by calculation of radial symmetry centers. *Nature Methods*, 9(7): 724–726, 2012.

[121] V. N. Pokrovskii and A. A. Tskhai. Slow motion of a particle in a weakly anisotropic viscous fluid. *PMM Journal of Applied Mathematics and Mechanics*, 50(3):391–394, 1986.

[122] T. D. Pollard and G. G. Borisy. Cellular motility driven by assembly and disassembly of actin filaments. *Cell*, 112(4):453–465, February 2003.

[123] P. Poulin, H. Stark, T. C. Lubensky, and D. A. Weitz. Novel colloidal interactions in anisotropic fluids. *Science*, 275(5307):1770–1773, March 1997.

[124] M. Puig-De-Morales-Marinkovic, K. T. Turner, J. P. Butler, J. J. Fredberg, and S. Suresh. Viscoelasticity of the Human Red Blood Cell. *American Journal of Physiology-Cell Physiology*, 293(2):C597–C605, Aug. 2007.

[125] Python Software Foundation. URL https://www.python.org.

[126] S. S. Rogers, T. A. Waigh, and J. R. Lu. Intracellular microrheology of motile amoeba proteus. *Biophysical Journal*, 94(8):3313–3322, April 2008.

[127] R. W. Ruhwandl and E. M. Terentjev. Friction drag on a particle moving in a nematic liquid crystal. *Physical Review E*, 54(5):5204–5210, November 1996.

[128] P. G. Saffman. Brownian motion in thin sheets of viscous fluid. *Journal of Fluid Mechanics*, 73(4):593–602, 1976.

[129] P. G. Saffman and M. Delbrück. Brownian Motion in Biological Membranes. *Proceedings of the National Academy of Sciences of the United States of America*, 72(8):3111–3113, 1975.

[130] P. Scherp and K. H. Hasenstein. Anisotropic viscosity of the Chara (Characeae) rhizoid cytoplasm. *American Journal Of Botany*, 94(12):1930–1934, DEC 2007. ISSN 0002-9122. doi: {10.3732/ajb.94.12.1930}.

[131] F. G. Schmidt, B. Hinner, and E. Sackmann. Microrheometry underestimates the values of the viscoelastic moduli in measurements on F-actin solutions compared to macrorheometry. *Physical Review E*, 61(5):5646–5653, May 2000.

[132] B. Schnurr, F. Gittes, F. C. MacKintosh, and C. F. Schmidt. Determining microscopic viscoelasticity in flexible and semiflexible polymer networks from thermal fluctuations. *Macromolecules*, 30(25):7781–7792, December 1997.

[133] C. Selhuber-Unkel, P. Yde, K. Berg-Sorensen, and L. B. Oddershede. Variety in intracellular diffusion during the cell cycle. *Physical Biology*, 6(2), June 2009.

[134] K. Skarp, S. T. Lagerwall, and B. Stebler. Measurements of Hydrodynamic Parameters for Nematic 5CB. *Molecular Crystals and Liquid Crystals*, 60(3):215–236, 1980.

[135] K. Skarp, S. T. Lagerwall, and B. Stebler. Measurements of hydrodynamic parameters for nematic 5cb. *Molecular Crystals and Liquid Crystals*, 60(3):215–236, 1980.

[136] T. M. Squires. Nonlinear microrheology: bulk stresses versus direct interactions. *Langmuir*, 24(4):1147–1159, February 2008.

[137] T. M. Squires and T. G. Mason. Tensorial generalized stokes-einstein relation for anisotropic probe microrheology. *Rheologica Acta*, 49(11-12):1165–1177, December 2010.

[138] T. M. Squires and T. G. Mason. Fluid mechanics of microrheology. *Annual Review of Fluid Mechanics*, 42:413–438, 2010.

[139] H. Stark and T. C. Lubensky. Poisson-bracket approach to the dynamics of nematic liquid crystals. *Physical Review E*, 67(6):061709, June 2003.

[140] H. Stark and D. Ventzki. Stokes drag of spherical particles in a nematic environment at low ericksen numbers. *Physical Review E*, 64(3):031711, August 2001.

[141] O. Stenull and T. C. Lubensky. Dynamics of nematic elastomers. *Physical Review E*, 69 (5):051801, May 2004.

[142] N. Stuurman, N. Amdodaj, and R. Vale. manager: Open source software for light microscope imaging. *Microscopy Today*, 15(3):42–43, 2007.

[143] J. Su, X. Jiang, R. Welsch, G. M. Whitesides, and P. T. C. So. Geometric Confinement Influences Cellular Mechanical Properties I - Adhesion Area Dependence. *Molecular & Cellular Biomechanics*, 4(2):87–104, June 2007.

[144] K. L. P. Sung, G. W. Schmidschonbein, R. Skalak, G. B. Schuessler, S. Usami, and S. Chien. Influence of Physicochemical Factors on Rheology of Human-Neutrophils. *Biophysical Journal*, 39(1):101–106, 1982.

[145] A. Talbot. The accurate numerical inversion of laplace transforms. *Journal of the Institute of Mathematics and its Applications*, 23(1):97–120, 1979.

[146] H. C. Tseng, D. L. Silver, and B. A. Finlayson. Application of the continuum theory to nematic liquid crystals. *The Physics of fluids*, 15(7):1213–1222, July 1972.

[147] Y. Tseng, T. P. Kole, and D. Wirtz. Micromechanical mapping of live cells by multiple-particle-tracking microrheology. *Biophysical Journal*, 83(6):3162–3176, December 2002.

[148] T. Turiv, I. Lazo, A. Brodin, B. I. Lev, V. Reiffenrath, V. G. Nazarenko, and O. D. Lavrentovich. Effect of collective molecular reorientations on brownian motion of colloids in nematic liquid crystal. *Science*, 342(6164):1351–1354, 2013.

[149] M. T. Valentine, Z. E. Perlman, M. L. Gardel, J. H. Shin, P. Matsudaira, T. J. Mitchison, and D. A. Weitz. Colloid surface chemistry critically affects multiple particle tracking measurements of biomaterials. *Biophysical Journal*, 86(6):4004–4014, June 2004.

[150] S. van der Walt, S. C. Colbert, and G. Varoquaux. The numpy array: A structure for efficient numerical computation. *Computing in Science & Engineering*, 13:22–30, 2011.

[151] C. Y. Wang. Stokes slip flow through square and triangular arrays of circular cylinders. *Fluid Dynamics Research*, 32(5):233–246, May 2003.

[152] H. Wang, T. X. Wu, S. Gauza, J. R. Wu, and S.-T. Wu. A method to estimate the leslie coefficients of liquid crystals based on mbba data. *Liquid crystals*, 33(1):91–98, January 2006.

[153] N. Wang, J. P. Butler, and D. E. Ingber. Mechanotransduction across the cell surface and through the cytoskeleton. *Science*, 260(5111):1124–1127, 1993.

[154] M. Warner and E. M. Terentjev. *Liquid Crystal Elastomers*. International Series of Monographs on Physics. Oxford Science Publications, 2003.

[155] J. J. Waterston and Lord Rayleigh. On the Physics of Media that are Composed of Free and Perfectly Elastic Molecules in a State of Motion. *Philosophical Transactions of the Royal Society of London. A*, 183:1–79, 1892.

[156] J. A. C. Weideman. Optimizing talbot's contours for the inversion of the laplace transform. *SIAM Journal on Numerical Analysis*, 44(6):2342–2362, 2006.

[157] L. Wilson, A. Harrison, A. Schofield, J. Arlt, and W. Poon. Passive and active microrheology of hard-sphere colloids. *The Journal of Physical Chemistry B*, 113(12):3806–3812, 2009.

[158] D. Wirtz. Particle-tracking microrheology of living cells: principles and applications. *Annual review of biophysics*, 38:301–326, 2009.

[159] D. Wirtz, K. Konstantopoulos, and P. C. Searson. The physics of cancer: the role of physical interactions and mechanical forces in metastasis. *Nature Reviews Cancer*, 11(7): 512–522, July 2011.

[160] O. Yalcin, D. Ortiz, A. G. Tsai, P. C. Johnson, and P. Cabrales. Microhemodynamic aberrations created by transfusion of stored blood. *Transfusion*, 54(4):1015–1027, Apr. 2014.

[161] M. Yanai, J. P. Butler, T. Suzuki, H. Sasaki, and H. Higuchi. Regional rheological differences in locomoting neutrophils. *American Journal of Physiology - Cell Physiology*, 287(3):C603–C611, September 2004.